THE UNIVERSITY OF READING

School of the Built Environment

A rasterized numerical model of outdoor thermal climate simulation for strategic urban planning based on Geographic Information System (GIS)

Wenbo Wang

A thesis submitted for the degree of Doctor of Philosophy

January 2023

DECLARATION

I confirm that this is my own work and the use of all material from other sources has been properly and fully acknowledged.

Wenbo Wang

ABSTRSCT

A consequence of the rapid urbanization process around the world has been the deterioration of the urban environment caused by climate change, air pollution, the increasing demand for energy, etc. Numerical models can assist sustainable urban environmental planning and strategic solutions. This thesis documents a series of developments aimed at improving the practicality and ability of climate models to assess and optimize urban planning using outdoor thermal climate simulations based on a Geographic Information System (GIS). The research focuses on efficiently representing the physical and behavioural processes of heat exchange at the neighbourhood scale.

Major contributions and key findings include:

1) A new urban surface feature description scheme based on raster data was developed. By integrating the representation of urban surface properties into a multi-band raster dataset, the new scheme can more briefly and comprehensively reflect the morphological features of urban surfaces. It can also use map algebra algorithms integrated into climate simulation models to reduce computational expense. Also, the input data acquisition method to describe the urban surface features has been improved by combining it with the multi-data source fusion method. Improvements have been made to the pre-processing of input data for urban climate simulations.
2) A new scheme for simulating surface thermal radiation interactions based on a 2.5D urban structure model was developed. The scheme provides additional façade information for the 2.5D building model by the gradient analysis of raster data. This makes up for the lack of vertical surface results when analysing solar radiation distribution in traditional 2.5D models. The algorithm for calculating the solar radiation distribution within districts based on the 2.5D model has been improved.

3) A new numerical simulation framework for neighbourhood thermal climates using the GIS spatial analysis method was developed. The new framework includes important urban surface energy transfer processes, as well as new algorithms based on geographic information system spatial analysis. The framework integrates the raster data map algebra algorithm as the main body to simulate the energy exchange process at the urban neighbourhood scale and realizes a novel wind direction judgment in a short time with the help of the raster data flow direction algorithm. The new framework has been evaluated and compared with experimental data to confirm that it can accurately and quickly represent the outdoor thermal environment of different urban morphologies.

These developments are compiled into a free open-source model using the Python language. The integrated model tool has the ability to efficiently quantify neighbourhood thermal climate values under different urban morphologies during the planning stage. The outputs should help improve urban environmental design solutions and promote sustainable urban development.

ACKNOWLEDGEMENTS

Four years have passed in a flash, and along with the busy research work, the day of finalizing my PhD thesis has finally arrived. During the process of writing my thesis, I have experienced the hardships of academic research, I have been confused, depressed, and overwhelmed, but I am glad to have the final draft of my thesis, which also means that my four-year PhD research career is coming to an end. Looking back on my four years, whenever I walk around the Reading campus, the air is always fresh. I love this beautiful green campus, which has marked a distinctive part of my life and has recorded my rewards and gratitude. During my time at Reading, I have not only gained a wealth of expertise, but I have also honed my resilience. I know that receiving a PhD is the end of a period of study, but also the beginning of a new one.

I would like to thank my first supervisor, Professor Yao Runming. Over the past four years, under the guidance of my supervisor, I have been able to enrich my knowledge and broaden my horizons by developing my understanding of my field of study from an inexperienced one to an in-depth study of a particular aspect. In the process of writing my thesis, including the selection of the topic, the adjustment of the content, and the revision of the text, the guidance of my supervisor was evident everywhere. My supervisor's rigorous and untiring spirit, solid theoretical skills, and writing skills have left an indelible impression on me and have benefited me for life.

A heartfelt thank you to my second supervisor, Professor Sue Grimmond She has provided crucial guidance on urban climate. This has given me a more comprehensive knowledge of urban climate. This has also provided me with the basic theoretical knowledge for my research.

My sincere thanks to all the teachers who reviewed and taught me during my doctoral studies. My heartfelt thanks to Professor Shao Li, Professor Zhiwen Luo, Professor Libby Schweber, Dr. Florence Phua, and all the other teachers for their help and guidance. The profound academic attainments of the teachers and their moral and artistic qualities have enriched my knowledge and broadened my horizons.

My heartfelt thanks to my family for all the love and tolerance they have given me! Thank you to my parents who are far away from home, you have supported me in my studies, work, and life with the simplest of actions, giving me selfless support and encouragement when I was lost and making me feel the warmth from my loved ones at all times. Thank you to my wife, who has always been there for me during difficult time in a foreign country, and who has steadfastly supported me in my pursuit of education. With your understanding, tolerance, and support, I was able to focus on my thesis and complete my studies successfully. It was your company and support that gave me the courage and perseverance to study. I can say that the completion of my studies is also a result of your efforts.

On the occasion of graduation, I would like to express my sincere gratitude and best wishes to all the teachers, students, friends, and family who have educated, supported, helped, and cared for me.

Finally, I would like to express my sincere gratitude to all the experts and scholars who reviewed my thesis and participated in the defence of my thesis during my busy schedule.

CONTENTS

List of Figures:

Chapter 2

Chapter 3

Chapter 4

Chapter 5

Chapter 6

List of Tables

Chapter 1

Introduction

1.1 Motivation

Cities are the main habitats of human beings in modern society. People often choose to settle in cities in pursuit of better employment, education, or economic opportunities. The United Nations (2022) reported that the global population will reach 8 billion by the end of 2022, with more than half of the population living in cities (nearly 6 times the figure in 1950). This will be especially pronounced in Asia, with India, China and, in Africa, Nigeria alone projected to add 900 million urban dwellers by 2050 (United Nations, 2019).

While cities provide opportunities for people, continued urbanization will inevitably lead to profound changes in the urban environment, especially in deteriorating environmental conditions. The poor outdoor environment of residential areas has a series of direct and indirect negative impacts on the health and social economy of urban residents. Ambient air pollution caused more than 4 million premature deaths annually as of 2019, a 66% increase over the previous 20 years (Fuller *et al.*, 2022). Overheating in cities is another major threat. Large numbers of deaths due to extreme heat events have been recorded worldwide, including in Chicago, USA (1995), a European-wide heat wave (2003) and South-eastern Australia (2009) (Campbell *et al.*, 2018). Locally intensified heatwaves due to the urban heat island effect will undoubtedly lead to increased urban mortality (Wong *et al.*, 2013; Taylor *et al.*, 2015). The economic risk is mainly reflected in the increase in urban energy demand. Due to the deterioration of the outdoor thermal environment, the energy consumption of air conditioning in various aspects of urban life (including in buildings, vehicles, etc.) has risen (Santamouris, 2014, 2016). This not only increases the cost of energy but can also lead to energy shortages (Su *et al.*, 2021).

Climate change is likely to bring more frequent and severe heatwaves, which will amplify the effects of urban heat. The greater concentration of people, traffic and equipment will also increase the urban heat emission (anthropogenic heat) and further exacerbate the urban heat island effect (Du *et al.*, 2016; Yuan *et al.*, 2020). Meanwhile, more sophisticated urban textures alter the distribution of wind and turbulence in urban streets (Zhang *et al.*, 2018). The breeze is slowed down due to the increased friction, which is detrimental to the ventilation of the street and hinders the diffusion of pollutants or heat (Von Glasow *et al.*, 2013; Zhang *et al.*, 2018). These different elements of local climate, urban structure and functional zoning interact in complex ways, creating different local climate change conditions for each community, city and region. Thus, urban climate risks are both regional and localized.

Good urban planning often plays a key role in helping to mitigate climate change. To ensure sustainable urban designs are appropriately addressed by architects, urban planners and environmental assessors, the neighbourhood thermal climate and environmental conditions should be taken into account carefully (Allegrini *et al.*, 2015; Lin *et al.*, 2017). The neighbourhood thermal conditions will affect building heating, cooling and thermal comfort needs. A single building decision may vary between simple early design indicators to detailed stage simulation software. Despite recent developments in solar performance assessment methods for design support (Beckers and Rodríguez, 2009; Reinhart *et al.*, 2013), few target early design at neighbourhood or district scales. Typically, if building context and neighbourhood morphology are fixed early, the required climate variables for the building site should be easy to derive and are essential to support early decision-making. Ideally, these can be obtained by architects and environmental assessors using quick simulations based on neighbourhood morphology and location within the city for other atmospheric influences (e.g., UHI intensity expected within a neighbourhood) and therefore design mitigation strategies for the neighbourhood setting can be incorporated during the early planning stage. Facing such a complex, multi-dimensional and multi-objective decision-making environment in an urban context, it is crucial for these stakeholders to obtain intuitive, clear and decision-relevant information during the urban planning and design stage (Hidalgo *et al.*, 2019).

In developing planning strategies, quantitative design tools for neighbourhood thermal climate assessment purposes can better support sustainable urban environmental design, as traditional design processes are mostly based on experience rather than science (Evins, 2013; Czmoch and Pękala, 2014). Modelling techniques can provide the expected spatial distributions of wind speed and direction, air and surface temperatures and scalar fields inside complex urban areas at the district scale, which can help sustainable environment design associated with outdoor thermal climate. A single building is the most basic unit to study the outdoor thermal environment and many mature models currently exist. However, as the outdoor thermal environment needs to take full account of the influence of adjacent buildings and the environment. The basic object of outdoor thermal environment research is no longer individual buildings but groups of buildings, which makes the process of analysing the outdoor thermal environment very complicated. However, the development and utilization of climate models for urban planning optimization is still affected by various factors such as computing power, urban surface complexity and urban information data integrity. Specifically, existing models for simulating and analysing urban microclimates (mainly the Urban Canopy Model and Computational Fluid Dynamics tools) are not suitable for the first-cut calculation by urban planners, architects and environmental assessors, who may require rapid comparisons between different urban forms and textures, the climate environment for UHI mitigation strategies in cities and an assessment of the impact of microclimates on building energy consumption. Therefore, it is worth exploring further how to analyse urban climate more comprehensively and efficiently for urban planning purposes in a limited computing environment.

In order to better solve this complex problem, on the one hand, it is necessary to start with mathematical models of these problems and to make continuous theoretical improvements. On the other hand, it is also necessary to find more advanced analytical means and methods. Only simultaneous development on both these necessities will make it possible to tackle these problems at their root. This also means that numerical climate models for the purpose of urban planning processes need to explore new analytical approaches for outdoor thermal climate simulations. In other words, to realize an urban microclimate simulation that rapidly addresses existing design problems or compares feasible solutions, a more robust and practical modelling method is required.

1.2 Aim and objectives

The overarching aim of this research is to develop a new practical and robust urban microclimate model based on the raster data operation analysis method for simulating neighbourhood thermal climates. The proposed model introduces new raster forms of data representation and storage for a more efficient representation of urban surface properties. A faster and more practical model for outdoor urban thermal climate analysis is expected to be achieved by means of raster-based operations. It is expected to be able to conduct a preliminarily assessment of the impact of urban planning/renovation schemes (such as urban structure, vegetation coverage, functional zoning, etc.) on the outdoor thermal climate during the planning stage. This overarching aim will be achieved through the following objectives:

- Develop a novel multi-data-source analysis method to establish an urban surface properties database in raster data format. This is a more efficient method of building input data files for the simulation model.
- Establish the microclimate model based on the GIS platform using a raster data spatial analysis method with sub-models of radiation, airflow, thermal energy transfer, anthropogenic heat and surface energy balance.
- Build a new 2.5D-based radiation simulation method with the analysis results of vertical surfaces.
- Build a simple airflow analysis based on a raster data flow direction algorithm (i.e., each pixel represents an airflow area) to complete a wind flow simulation.
- Build the thermal heat transfer model by adopting a basic formula based on the physics of different surface characteristics from the map algebra algorithm.
- Estimate anthropogenic heat for the simulation model based on building usage information from the established urban information dataset in raster format.

Validate the proposed model by comparing simulation results with experimental results based on field measurements.

1.3 Thesis structure

A brief summary of each chapter is provided to guide the reader as follows:

Chapter 2: Urban climate research

In order to explore new models for the rapid simulation of the urban outdoor thermal environment, understanding the theory and state-of-the-art urban climate modelling is necessary. Chapter 2 mainly reviews past urban climate research methods and modelling techniques, discusses the characteristics of different urban models and their main uses and identifies the shortcomings of the current generation of urban models in practical production scenarios.

Chapter 3: A rasterized method for describing the properties of urban surfaces

The characteristic properties of urban surfaces are often complex and variable. How these urban surface properties are described in the urban climate model will directly affect the quality of the simulation results. To make this process more efficient, Chapter 3 outlines an urban surface properties representation method based on the raster data format. Meanwhile, it proposes a new urban surface properties acquisition framework. With the help of multi-data source analysis, the new framework can obtain parameters used to describe urban surface properties more quickly and comprehensively and provide more new analytical ideas or subsequent urban climate simulations.

Chapter 4: A novel 2.5D-based radiation simulation model

Solar radiation is one of the main sources of energy on the urban surface. Fast and accurate simulation of the radiation distribution in urban environments can provide useful data to support relevant urban climate studies. This chapter records a new method for calculating urban solar radiation distribution based on a 2.5D urban structure model, which quickly analyses urban solar potential with the help of grid spatial analysis methods. Unlike the traditional 2.5D model calculation method, the new solution provides vertical plane simulation results.

Chapter 5: A novel raster-based outdoor thermal climate simulation model

Making urban climate modelling more practical for the early planning/renovation assessment phase of cities can contribute to a greener and more sustainable urban environment. A new numerical model based on raster data operations to analyse the outdoor thermal climate is proposed. Chapter 5 describes this newly developed urban microclimate model for rapidly simulating neighbourhood-scale outdoor thermal climatic conditions. Multiple models such as radiation, airflow and anthropogenic heat simulations are developed and integrated, primarily using raster data spatial analysis and map algebra algorithms. A new solution is proposed for strategic decision-making at the planning stage of a built-environment design.

Chapter 6: Case study and discussion

To illustrate the usefulness of the model in practical production, a simple case study is presented in Chapter 6. This chapter describes the practical role of the newly proposed model in the early design stage.

Chapter 7: Conclusion and contributions

Chapter 7 provides conclusions and summarizes the contributions and limitations of the current work; it also suggests possible future research.

Chapter 2

Urban Climate Research

2.1 Urban thermal climate studies

Due to increasingly frequent extreme climate events, the urban ecological environment and climate issues have begun to receive more attention. The unique land-air-water characteristics of cities undoubtedly reflect the influence of human activities on the climate of a building complex, especially the increasing urban high temperatures and the heat island effect. The Urban Heat Island (UHI) phenomenon was first observed in the 19th century by meteorologist Luke Howard based on the comparisons of temperatures between cities, such as London in this case, and undeveloped rural surroundings (Mills, 2008). A UHI effect of approximately 2℃ (warming) during the night and -0.2℃ (cooling) was observed during the day. By the middle of the 1960s, an average difference of 4-6℃ in nocturnal temperature between central London and its surroundings was evident. More recently, urban climatologists have noted extreme UHI intensities in excess of 7℃ (Azevedo, Chapman and Muller, 2016). For example, during the August 2003 heatwave in London, the UHI intensity reached 9℃ on one occasion (Mavrogianni *et al.*, 2011). This strongly suggests that global warming has speeded up urban climate change. Therefore, exploring the cause of the higher temperatures in urban areas also became an attractive topic in the early research on urban climate change with Oke (1988) proposing the use of the surface energy balance equation to explore the principle behind the UHI phenomenon, which allowed some conclusions to be drawn. Myrup, McGinn and Flocchini (1993) proposed the urban heat island energy balance model by studying the urban thermal energy exchange and found that the decrease in urban evaporation, the increase of dynamic volume, the high thermal properties of building envelope materials and changes in wind speed are the main reasons for the heat island effect. Thus, according to the current research on the physical process of urban heat exchange (as shown in Figure 2.1), the phenomenon whereby the temperature of urban areas is higher than rural areas should be attributed to the following three major factors:

1)Urban forms: due to the uneven height of the buildings, the long-wave radiation reaching the ground is limited and the walls of the buildings are also subjected to long-wave radiation, some of which is directed downward, to supplement the atmospheric reverse radiation (Takebayashi and Moriyama, 2009). This exchange of long-wave radiation increases the net radiation in the urban canopy layer (Rizwan, Dennis and Liu, 2008). At the same time, buildings of different shapes and heights change the distribution of wind and turbulence in urban streets, which is not conducive to the diffusion of pollutants within them (Zhang, Gu and Yu, 2018). Additionally, some researchers also studied the relationship between the urban form and climate by introducing the sky view factor (SVF) (Zhu *et al.*, 2013; Dirksen *et al.*, 2019), which indicates the ratio between the radiation received by a planar surface from the sky to the radiation hitting the entire hemispheric radiating environment. The relationship between urban geometry and the UHI has been commonly adopted in urban climatology studies (Unger, 2004).

2)Urban surface textures include building and road materials, vegetation and water features (ponds, lakes, rivers, etc). Taking building materials as an example, since the urban ground is mainly made of reinforced concrete with its large thermal capacity, high thermal conductivity (Arya, 2001; Bokaie *et al.*, 2016) and low moisture content, it can absorb a large amount of solar radiation. In contrast, vegetation could directly impact the urban climate by reducing surface and local air temperatures or indirectly modify it by reducing heat exchange with occupied spaces thereby reducing mechanical cooling loads or any other anthropogenic heat patterns linked to rising temperatures (Gunawardena, Wells and Kershaw, 2017).

3) Anthropogenic heat includes the heat emitted from transport, people, buildings etc. Due to the dense urban population and concentrated economic activities, the heat released during the burning of fossil fuels in industrial production, home stoves and transportation, as well as the waste heat emitted by air conditioners and vehicles, is far greater than in the suburbs (Sailor, 2011).

In addition to the above three factors, the urban heat island effect may be influenced by wind speed, cloud cover, air pollution and other factors, such as global warming, which tend to have an effect on the urban climate (Li *et al.*, 2018).

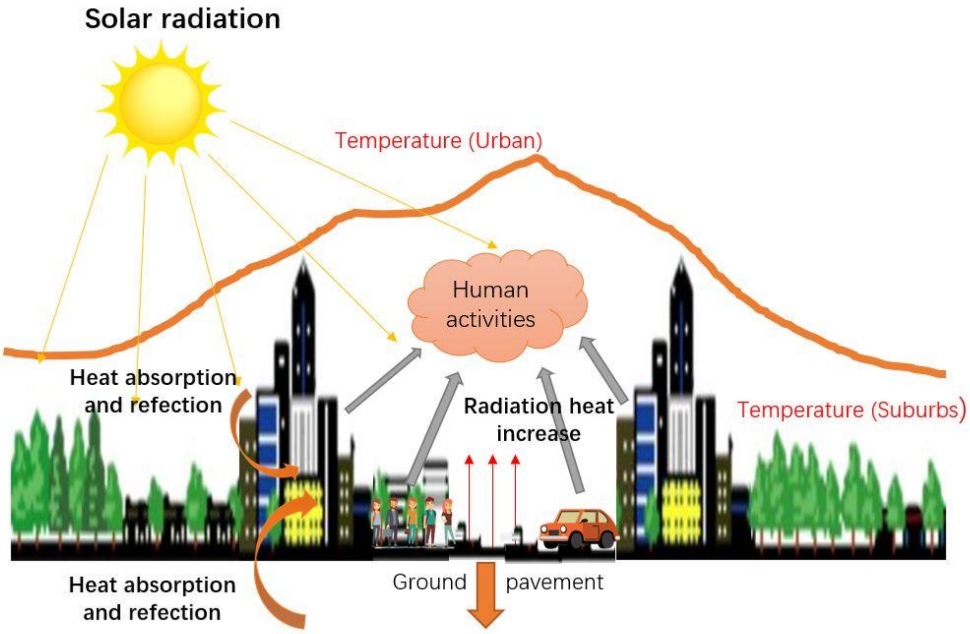

Figure 2.1: Factors affecting urban thermal environments. The figure simply shows the effect of the city shape, materials, and human activities on the heat exchange in the city.

In general, differences in underlying surface characteristics and the intensity of human activities between cities and suburbs cause variations in urban energy balance, which forms the basis of urban climate change. Thus, the research on the interaction between different urban constituent elements and the urban climate could effectively map the migration strategies of the UHI and its side effects. At the same time, studies on the topic of UHIs have also been widely carried out internationally to gain more knowledge about preventing urban climate change, such as in Japan (Hirano and Fujita, 2012), the USA (Debbage and Shepherd, 2015; Vahmani and Ban-Weiss, 2016), Canada (Wang, Berardi and Akbari, 2016), China (Zhou *et al.*, 2016; Li *et al.*, 2018) and some European cities (Doick, Peace and Hutchings, 2014; Noro and Lazzarin, 2015; Salata *et al.*, 2017).

2.2 Typical urban climate research methods

To study the causes, effects, and migration strategies of urban heat island effects, a variety of research methods have been adopted, which can be divided into three main categories (Deilami, Kamruzzaman and Liu, 2018): a) Applied statistical models with data from field measurement by instruments set up in the urban area to monitor environmental parameters such as temperature, humidity, wind speed, etc. at different locations (Tan *et al.*, 2010; Alves and Lopes, 2017; Sobstyl *et al.*, 2018); b) Remote sensing by using satellite, airborne and aircraft platforms to obtain images and analyze them (Yusuf, Pradhan and Idrees, 2014; Tsou *et al.*, 2017); c) Computer simulations by developing mathematical models; these include the energy balance model, the Computational Fluid Dynamics (CFD) model, Meso-scale modelling, Micro-scale modelling, and so on (Tominaga *et al.*, 2015; Derakhshan and Shaker, 2017). The strengths and weaknesses of these methods are briefly summarized in Table 2.1. Regarding the field measurement method, fixed or mobile stations are usually used, which are very expensive and time-consuming. The data collected are hardly simultaneously measured. The thermal remote sensing method is a very expensive approach whose limitations include 1) it is not possible to have steady images from the urban surface; 2) limited time over one specific region and inaccurate data due to the complexity of urban spaces (Zhao, 2003). Furthermore, computer simulation modelling has certain shortcomings due to its inability to cover the phenomena creating the entire UHI thereby leading to theoretical weaknesses (Jones and Lister, 2009; Li *et al.*, 2009). In general, the field measurement and the remote sensing methods are more often used to reveal the principle and impact of the UHI whilst computer simulation modelling is more suitable for the discussion of migration strategies. Furthermore, due to the advances in information technology, numerical models have been widely used for migration strategies in recent years, which has also promoted the development of urban climate modelling. Therefore, the computing simulation modelling method is mainly adopted in this research.

Table 2.1: Urban climate research methods feature summary.

METHODS	PROS	CONS
FIELD MEASUREMENT	Easy to operate. Various types of data can be collected.	Time-consuming. High labour costs. Data quality is affected by the observer.
REMOTE SENSING	Time-saving. Easy to operate for a large area. Multiple technical solutions.	High costs. Low accessibility and resolution. Interpretation of results is complex. Imitated types for results.
NUMERICAL MODELS	Quick solution for complex interacting systems. Flexible application scenarios.	Accuracy of results. Limited capability for climate-related strategic decision-making.

2.3 The scale of urban climate models

The complex combination of structures, materials and human activity features on urban surfaces makes initial microclimate changes difficult to interpret. Their complexity and spatial variability extend from a few metres (facades or canyons) to tens of kilometres (entire city-wide). Therefore, scale issues should be initially considered in urban climate measurement, modelling and the application of scenario designs.

Additionally, the scale of urban climate research varies from building-scale (usually used to investigate the impact of UHI on the thermal comfort of pedestrians) to city-scale (normally used to explore the effects of synoptic winds on urban ventilation).

a) Building-scale

Building-scale models, also known as building energy models (BEM), are mainly limited to isolated building envelopes and generally ignore the impact of neighbouring buildings on their energy performance. This means that outdoor weather parameters such as air temperature, solar radiation, long-wave radiation and humidity are usually inputted through an external dataset since BEM is developed based on the energy balance applied to the building's control volume. These tools (e.g. EnergyPlus, ESP-r, and TRNSYS) are often used to investigate the response of building envelopes to possible future climate changes and extreme weather conditions (Lauzet *et al.*, 2019). Obviously, BEM tools are too simple in expressing the interaction between a building and its surrounding area. Therefore, when studying the impact of UHI on the energy performance of buildings, they should be integrated with other climate models or data.

b) Street-scale

A structure formed by the arrangement of a street and its flanking buildings is often referred to as an urban canyon or street canyon. Its biggest feature lies in its unique geometry. Canyons are described by their 2D cross-sections, expressed as the ratio of the height of buildings near the street to the width of the street (i.e., H/W, where H is the height of the building and W is the width of the street). H/W is also known as the canyon aspect ratio. Its value affects many characteristics of an urban climate, including solar potential, shading and trapping, outdoor thermal comfort, wind corridors and the spread of vehicular pollutants. Since it is most clearly defined in dense central areas of cities, the canyon aspect ratio is the most basic unit in urban microclimate simulations along with the Urban Canyon Model (UCM) which the most commonly used tool to characterize urban microclimates (Masson, 2000). It is worth mentioning that the airflow situation in UCM is decoupled and then coupled with the calculation of the energy budget model.

c) Block-scale

A city block unit consists of a road network, usually with multiple, simply-structured, adjacent street canyons. Due to the various arrangements of the road network, blocks may be regular shapes such as triangles, squares or circles, or irregular shapes such as crescents and five-pointed stars. The combination of these different blocks produces a variety of climates and is large enough to generate localized breeze systems (such as parks) or clouds (such as factory complexes). However, block units can be difficult to identify in all cities.

d) Neighbourhood-scale

Unlike block scales, neighbourhood scales are broader in scope and contain more complex surface features including urban planning information on land-use areas, such as industrial, commercial, residential, public land and undeveloped land. The numerical model of neighbourhood scales was developed based on the interaction of a building with its surroundings at the surface layer. In principle, such models include physical quantities such as solar radiation, heat exchange and convection on the building and land surfaces. In many numerical models for microclimate simulation, the CFD technique, which deals with the equations governing the flow (Navier-Stokes equations), is applied to describe the airflow patterns around and inside buildings. In general, microclimate models (MCMs) are widely used by architects and building scientists to study the effects of different urban elements at neighbourhood scales (e.g. building orientation, street canyon aspect ratios, surface materials, vegetation coverage, pedestrian comfort and urban ventilation) (Haghighat and Mirzaei, 2011; Tominaga *et al.*, 2015).

e) City-scale

Investigation of the large-scale UHI variation within a city is broadly adopted in urban climatology and meteorology fields. The impact of urban-scale policies to mitigate the UHI, e.g. urban ventilation, pollution dispersion management and greening, is mostly analysed using meso-scale tools (Lemonsu and Masson, 2002). The developed models are based on the equations governing fluid dynamics with equally important models such as radiation, cloud cover and soil integrated into the calculations. As the major limitation, the mesoscale models are applied to very coarse cells, implying a weak resolution on the surface layer to observe interactions between buildings and their environment.

In summary, predictive models at various scales often serve different purposes. In contrast, neighbourhood-scale numerical models are the most conducive to exploring the relationship between different urban constituent elements and urban climate as well as building-energy-consumption related to local climate, which could be used to compare early strategic decision-making in urban planning and design. Therefore, this research focuses on the development of numerical models at the neighbourhood scale.

2.4 Types of land surface parametrizations for urban climate models

In order to better understand the numerical model of an urban climate and develop a model suitable for more practical urban and environmental design analysis, urban surface climate simulation methods in the last three decades have been reviewed (as shown in Table 2.2) and divided into three general categories (Figure 2.2): i) Representing urban surfaces with improved heat capacity, surface albedo, thermal conductivity, roughness length and water supply in bare soil (or adaptive vegetation scheme). ii) A simple building average urban canopy model. This is usually subdivided into (a) a single-layer urban canopy model (SLUCM) and (b) a multi-layer urban canopy model (MLUCM). iii) Resolving models of the building. In the following sections, discussions will be based on each of the modelling methods, the level of detail and complexity of the urban surface features they represent and their advantages and limitations.

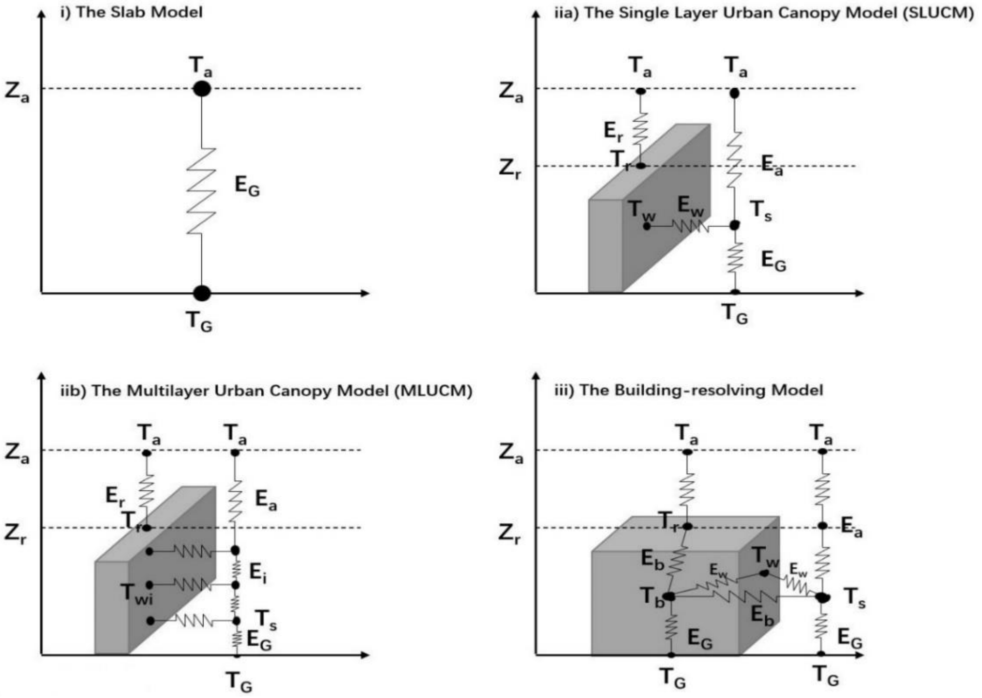

Figure 2.2: Schematic diagram of different urban surface parameterization for climate models. T_a, T_G, T_w, T_b, T_s and T_r represents temperature of the air, ground, wall, building, surface and roof respectively. E_a, E_G E_w, E_b, E_r and Tr represents energy from the air, ground, wall, building and roof respectively.

Table 2.2: Summary of the historical development of land surface numerical models for urban climate research in the last three decades in chronological order.

References	**Model description**	**Model type**	**Model scale**
(Bruse and Fleer, 1998)	Urban block parameterization	ENVI-met	Neighbourhood
(Taha, 1999)	Modifying a mesoscale meteorological model to better incorporate urban heat storage: A bulk parameterization approach.	A simple bulk-parameterization scheme.	City
(Masson, 2000)	Town Energy Balance (TEB) models.	TEB (SLUCM)	Street
(Arnfield, 2000)	A simple model of an urban canyon energy budget.	UCP (SLUCM)	Street
(Montavez, Jimenez and Sarsa, 2000)	A Monte Carlo model for urban canyon temperature.	Monte Carlo model	Street
(Thielen *et al.*, 2000)	Influence of urban surfaces on rainfall development.	A spatially-variable	City

		parameterization scheme	
(Kusaka *et al.*, 2001)	A single-layer canopy model for energy and momentum exchange between the urban surface and the atmosphere.	SLUCM	street
(Grimmond and Oke, 2002)	Local-scale urban meteorological parameterization (LUMPS).	LUMPS	Street
(Shashua-bar and Hoffman, 2002)	The Green Cluster Thermal Time Constant (CTTC).	CTTC	Neighbourhood
(Martilli, Clappier and Rotach, 2002)	Urban building effect parameterization (BEP) model for mesoscale models.	BEP	Street
(Kikegawa *et al.*, 2003)	Coupled mesoscale model (MM) - one-dimensional urban canopy model (UCM) - building energy analysis model (BEM)	UCM	Neighbourhood
(Kusaka and Kimura, 2004)	Coupled single-layer urban canopy model with a simple atmospheric model.	SLUCM	Street
(Otte *et al.*, 2004)	An urban canopy parameterization (UCP) implemented into the fifth-generation Pennsylvania State University–National Center for Atmospheric Research Mesoscale Model (MM5).	UCP-MM5	City
(Harman, Barlow and Belcher, 2004)	The surface energy balance and boundary layer over urban street canyons.	SLUCM	Street
(Dupont, Otte and Ching, 2004)	Urban canopy parameterization.	UCM-MM5	City
(Kondo *et al.*, 2005)	A multi-layer urban canopy model for the analysis of energy consumption in a big city.	MLUCM	Neighbourhood
(Baklanov *et al.*, 2005)	This model parameterizes the urban roughness sublayer and surface exchange fluxes and the role of the urban soil layers.	DMI-HIRLAM NWP model	City
(Fortuniak, 2005)	A slab surface energy balance model.	A slab model	City
(Best, 2005)	Representing urban areas in NWPs.	SLUCM	City
(Bonacquisti *et al.*, 2006)	An urban canopy layer model applied in Rome.	SLUCM	Neighbourhood
(Dupont and Mestayer, 2006;	Parameterization of the urban energy budget (SM2_U) and integration with the sub-mesoscale soil model (ISBA).	SLUCM	Neighbourhood

Dupont *et al.*, 2006)			
(Harman and Belcher, 2006)	The surface energy balance and boundary layer over urban street canyons.	UCM	Street
(Hamdi and Schayes, 2007)	Validation of Martilli's urban boundary layer scheme.	UCP	Street
(Krayenhoff and Voogt, 2007)	Temperatures of Urban Facets in 3-D (TUF-3D) for predicting urban surface temperatures.	Building resolving model	Street
(Matzarakis *et al.*, 2007)	A micro-scale RayMan model for the calculation and estimation of solar potential.	Building resolving model	Neighbourhood
(Robinson *et al.*, 2007)	A unique model to support designers in optimizing the sustainability of urban communities (SUNtool).	Building resolving model	Neighbourhood
(Tian *et al.*, 2007)	Building integrated photovoltaics (PV) on the microclimate of the urban canopy layer.	SLUCM	Street
(Lee and Park, 2008)	A vegetated urban canopy model for meteorological and environmental modelling.	SLUCM	Street
(Oleson *et al.*, 2008)	A single layer urban canopy model coupled with a global climate model.	SLUCM	Street
(Hamdi and Masson, 2008)	Representation and implementation of an urban canopy model into TEB.	MLUCM	Street
(Salamanca *et al.*, 2010)	A new building energy model (BEM) coupled with an urban canopy parameterization (UCP) for mesoscale models.	BEM	Street
(Chen *et al.*, 2011)	The integrated WRF/urban modelling system.	Synthesis of different software	City
(Yao *et al.*, 2011)	A simplified mathematical model for urban microclimate simulations (UMsim).	Building resolving model	Neighbourhood
(Yang *et al.*, 2012)	A simple temporal 3D air and surface temperature model for an ideal courtyard.	Building resolving model	Neighbourhood
(Trusilova *et al.*, 2013)	Implementation of an urban canopy model into a Regional Climate Model COSMO-CLM.	UCP-COSMO	City

(Huszar *et al.*, 2014)	Representing urban canopy model in RCMs.	SLUCM	Street
(Yang *et al.*, 2015)	Enhancing hydrologic modelling in the coupled Weather Research and Forecasting (WRF).	SLUCM	Street
(Morille, Lauzet and Musy, 2015)	A tool to evaluate the energy consumption efficiency of envelopes at the district scale.	SOLENE-microclimate	Neighbourhood
(Li, Malyshev and Shevliakova, 2016)	A new urban canopy model that characterizes urban physical and biogeochemical processes within the sub-grid tiling framework.	SLUCM	Street
(Best and Grimmond, 2016)	The partitioning of turbulent fluxes at urban sites with varying vegetation cover.	A slab model	City
(Ward *et al.*, 2016)	Surface urban energy and water balance scheme.	SUEWS	City
(Mauree *et al.*, 2017)	An interface between mesoscale and a micro-scale atmospheric models.	CIM	Street
(Liu *et al.*, 2017)	Evaluation of an urban canopy model with tree evapotranspiration.	SLUCM	Street
(Wang *et al.*, 2020)	A multi-layer urban canopy meteorological model with trees.	BEP-Tree	Street
(Wang *et al.*, 2020)	An advanced geometric model to simulate thermal anisotropy time series for simplified urban neighbourhoods.	GUTA-T	Neighbourhood

2.4.1 Slab models

The slab model typically treats urban geometry as a flat surface or similar to a vegetation canopy with a large roughness length and small albedo, which usually represents the urban surface with an improved soil vegetation transfer scheme (Brown, 2000). Hence, a building and a road are normally set to the same temperature, as well as the height and coverage of the buildings being implicitly processed in the surface layer. In this type of model, the geothermal flux is treated as having the same value as the surface temperature. The urban geometry (e.g. surface roughness length, thermal inertia, albedo and moisture availability) represented in this model is modified until the best simulation output is achieved (Kusaka *et al.*, 2001). Furthermore, this type of model is based on the surface layer scheme of the Monin-Obukhov similarity theory, the surface heat balance and a vertical diffusion equation, which could estimate bulk transfer coefficients, surface temperature and urban temperature separately (Kusaka *et al.*, 2001). Most field observations indicate that this representation of urban surfaces is not sufficient to reproduce the large heat storage linked with the different characteristics of urban surfaces (Rotach, 1993). Another problem is that this scheme cannot represent the heterogeneity that exists in urban areas, which is highly variable in space and time from the neighbourhood to the local scale. Therefore, it is recommended to parameterize the surface in detail and estimate its surface and geometric properties, rather than simply modifying the vegetation canopy model to represent the city surface as in earlier studies such as Seaman *et al.*, 1989; Menut *et al.*, 1999 and Brown, 2000.

2.4.2 Canopy models

Oke and colleagues developed the concept of the Urban Canyon Model (UCM), which involves urban streets and roads bordered by two-facing walls (Oke, 1979). This method simply averages the urban geometry such as the height, width and impervious surface of the building, thereby effectively representing the urban surface with minimal computational cost. UCM usually takes two different approaches: (a) the single-layer urban canopy model (SLUCM) and (b) the multi-layer urban canopy model (MLUCM).

The SLUCM is based on simplified urban geometry, which is as close as possible to the actual urban surface. In this model, the building is considered to have a 3D shape, and the scheme calculates separate energy budgets for roofs, walls and roads and then aggregates at the canopy level. Specifically, the turbulent sensible heat flux from the roof to the air, the heat energy flux from the building wall to the canopy and the surface-to-ground flux were calculated based on the temperature difference at different locations. These fluxes are then calculated together to give the energy flux transferring to the air. In addition, compared to the flat model, the physics handled by the SLUCM scheme is relatively complete since it takes into account the reflection and shielding of the sun. At the same time, the heat conduction method is applied to obtain the stored energy for each different layer of the roof, walls and roads. Moreover, this type of model reduces the computational cost by averaging the direction of the overall orientations in a grid cell with building heights and has become the most widely used urban canopy model. Kusaka *et al.* (2001) developed a simple SLUCM that only considered the energy conversion between different faces in the canopy but ignored the differences in the surface material. In order to further improve the effect of SLUCM, Kikegawa *et al.* (2003) proposed a method of connecting BEM and UCM to take into account the influence of the building's interior on the urban canopy. Also considering the impact of buildings, Tian *et al.* (2007) proposed a SLUCM specifically for the study of the effect of building-integrated photovoltaics. In addition, in order to better reflect the impact of different covers on the canopy climate, Lee and Park (2008) introduced the calculation of vegetation cover into SLUCM. Yang *et al.* (2015) proposed further improvements in the model of the hydrological process to better show the urban energy and water balance. Later, Liu *et al.* (2017) added the effects of tree evaporation in models that Yang *et al.* (2015) proposed to enhance the hydrological process. Ward *et al.* (2016) designed a climate simulation tool divided into seven surface types to better reflect the impact of different land cover on canopy temperature. Due to the relatively complete physical calculation process and simplified geometric model of SLUCM, it is widely used to combine mesoscale climate models to improve simulation results (Dupont, Otte and Ching, 2004; Otte *et al.*, 2004; Mauree *et al.*, 2017). However, the urban canopy model normally treats the urban area as typical urban canopies, which neglects the diversity of the urban texture. The purpose of the urban canopy model is to allow its incorporation into large meteorological models to better represent urban effects, so it focuses more on vertical than horizontal resolution. Thus, it is difficult to use the model to examine the micro-level impact on the climate of different urban forms.

The other method is called the Multi-layer Urban Canopy Model (MLUCM). Unlike SLUCM, this method treats the canopy as a single layer but subdivides it into many sub-layers. Therefore, it is more representative of the atmosphere in urban canyons than the SLUCM and slab models. Martilli *et al.* (2002) proposed an MLUCM (called Building Effect Parameterization (BEP)) that allows direct interaction with the boundary layer, recognizes the three-dimensional nature of urban surfaces and captures the vertical distribution of heat, moisture and momentum across the urban canopy. Chen *et al.* (2011) assert that this representation can better simulate the mechanical and thermodynamic structure of the urban roughness sublayer and thus that of the urban boundary layer. Since it can simulate the most observed urban features (e.g. UHI and enhanced inversion layers above urban surfaces), this method is adopted for temperature and wind profiles within the urban canopy layer (Chen *et al.*, 2011). However, it is only suitable for detailed urban studies with unrestricted computing resources since the higher resolution of MLUCM requires more computing resources than the current mesoscale climate models.

2.4.3 Building-resolving models coupled with CFD

Building-analytical models allows the detailed examination of specific processes such as radiation effects and air ducts. Most analytical models of buildings use computational fluid dynamics (CFD) to accurately simulate thermal and airflow conditions inside and outside urban canopies (Fernando *et al.*, 2001). Unlike other UCMs, CFD can clearly analyse multi-scale turbulence at the boundary layer arising from a single building, thus representing the impact of the city on the atmosphere more realistically. Bruse and Fleer (1998) proposed a widely-used CFD-based tool called ENVI-met, which simulates surface-plant-air interactions to assess the impact of the green building vision on local thermal comfort conditions. On the other hand, Morille, Lauzet and Musy (2015) adopted Code-Saturne (a CFD open-source code developed by EDF) and SOLENE proposed SOLENE-

Microclimate, which can calculate outdoor air temperature, humidity, wind speed and surface temperature in a grid, so that the impact of planning on local climate characteristics can be evaluated along with more comprehensive indicators, such as comfort indicators (MRT, PET, UTCI). However, such models are currently in the experimental stage and are rarely used because they require extensive computing resources and huge initial and boundary conditions, making them difficult to use for regional or global climate model simulations. However, CFD models are useful during the testing and validation of urban models, because they allow spatial averaging as opposed to potentially incorrect point measurements (Martilli, Clappier and Mathias W. Rotach, 2002).

2.4.4 Urban climate modelling associated with GIS

Additionally, some urban climate studies have used GIS to quickly provide reliable data to support urban climate modelling analysis. This is because GIS-based urban spatial data can quickly and accurately help to delineate the distribution of green, blue and grey spaces in cities (Michaelides *et al.*, 2009). This is why a number of urban climate studies have used GIS as an aid to describe the surface conditions of cities. For example, Xiao *et al.* (2007) used a GIS-based surface classification model and a regression tree model (CART) to examine the impact of spatial patterns of impervious surfaces (IS) on the land surface temperature (LST) in Beijing. Buyadi, Mohd and Misni (2013) similarly assessed the impact of vegetation growth on the distribution of surface temperature (LST) in urban areas with the help of GIS. Zhao *et al.* (2020) also used elastic net regularised regression with GIS information to decompose the thermal contribution of six urban land cover types in urban areas (i.e. water bodies, urban trees, grass, bare ground, impervious surfaces and buildings). In contrast to the above studies using GIS information as input data only, Lindberg *et al.* (2018) proposes a GIS-based climate tool for exploring urban-scale issues of outdoor thermal comfort, wind, urban energy consumption and climate change mitigation. In general, a large number of urban climate modelling studies are currently using GIS more as a source of input data. In general, a large number of urban climate modelling studies are currently using GIS more as a source of input data. Meanwhile, with the rapid maturation of GIS technology and the widespread use of geospatial data, more researchers and practitioners are experimenting with the introduction of GIS in specific applications of in-depth urban modelling (Tao, 2013). It is worth exploring further how to take advantage of GIS platforms to enhance the capabilities of urban climate models.

In a word, the slab model and the canopy model achieve the analysis and prediction of micro-scale climates by simplifying the structure of existing cities and introducing corresponding physical models. However, due to this simplification of urban morphology, these two models are insufficient for the analysis of urban planning strategies at the microscale. In contrast, the CFD-based method is not suitable for rapid guidance to address urban design problems due to its overly complicated calculation process and considerable computation costs. Furthermore, the appropriate integration of GIS with urban climate models is a direction worth exploring.

2.5Numerical models for modelling neighbourhood thermal climates

As described above, there is a wide range of modelling approaches for urban areas. These different numerical simulation methods are designed by researchers to use different tools for microclimate simulation according to different purposes that may require only limited processing (e.g. radiative (Matzarakis *et al.*, 2007)) and focus on flow (e.g. computational fluid dynamics (CFD) (Toparlar *et al.*, 2017)). However, the simulation of outdoor thermal climates is often more complex and requires the consideration of multiple heat exchange processes in the neighbourhood environment. The building-resolving 3-D models are typically constrained by unrealistic boundary conditions or unrealistic assumptions about atmospheric stability. An alternative approach is to use large grid cells and to parameterise the sub-grid scale processes. This approach is taken for urban climate and weather modelling across cities. These models diagnose the profiles within the urban canopy layer and roughness sublayer as they normally assume the lowest layer is at the blending height or the inertial sub-layer (Masson, Grimmond and Oke, 2002; Chen *et al.*, 2011; Hertwig *et al.*, 2021). They model the urban energy balance fluxes by assuming the urban areas consist of a canyon composed of building roofs and walls with a road in between, with vegetation also accounted for. An example of this is the Town Energy Budget (TEB) (Masson, 2000; Lemonsu *et al.*, 2012; Stavropulos-Laffaille *et al.*, 2018). The Cluster Thermal Time Constant (CTTC) model is another type of model that uses the building thermal time constant to calculate the 3D lumped parameter of the air temperature in the local building environment changing with external heat disturbances (Swaid and Hoffman, 1990; Shashua-Bar and Hoffman, 2002). The development of the green-CTTC also considers the vegetation. The CTTC model benefits from its simplicity and computational efficiency but its inherent limitations restrict its use in complex situations. However, building the above schemes following the canyon approach simplifies individual building shapes but may ignore the detailed examination of specific processes (e.g., radiative effects) between buildings. Therefore, these schemes are unsuitable for direct use in evaluating urban designs. Furthermore, some research efforts have been made to simulate the urban microclimate considering three-dimensional buildings. Yang, Li and Yang (2012) proposed a simple temporal 3D air and surface temperature model of an ideal courtyard, which includes transient heat conduction of the ground and building walls, solar radiation and thermal radiation exchanges between surfaces and the detailed heat loss/increase caused by courtyard ventilation. It can analyse the air temperature in a courtyard and its surface temperature distribution minute-by-minute over a day or longer with the help of the temporal ambient air temperature and weather data. The RayMan model is also a radiation calculations-based tool with three-dimensional surroundings for the simulation of radiation flux densities and mean radiant temperatures in simple and complex environments

(Matzarakis *et al.*, 2007). It allows calculating sunshine duration with or without sky view factors; estimating the daily mean, max or summing of global radiation; calculating shadows for existing or future complex environments and estimating the outdoor thermal comfort for humans. The Temperature of Urban Facets Indoor–Outdoor Building Energy Simulator (TUF-IOBES) simulates indoor and outdoor building surface temperatures and heat fluxes in a district area using a 3-D raster-type geometry model (Yaghoobian and Kleissl, 2012). The above models all use three-dimensional geometric patterns to reflect the climatic conditions between buildings more realistically and can, to a certain extent, help architects and urban planners to learn and explore the interactions between buildings and urban microclimates. However, all the newly-developed models mentioned above are subject to the simple assumption that vegetation or wind profiles can be neglected, which may be not true for situations involving complex building arrangements.

More complicated models are also available in the literature. The building-resolving model allows detailed simulation of microclimates including radiative effects, wind channelling, plant distribution and outdoor thermal comfort conditions. The SOLENE-microclimate model which can calculate outdoor air temperature, humidity, wind speed and surface temperature in a grid is dedicated to modelling urban microclimates and the thermal behaviour of buildings (Morille *et al.*, 2015). In addition, it can evaluate the impact on planning local climate characteristics and more comprehensive indicators such as comfort indicators (MRT, PET, UTCI). The CFD-based ENVI-met tool can simultaneously simulate most of the essential physical phenomena of the urban microclimate including shortwave and longwave radiation, the heat and vapour exchange processes of vegetation and heat exchange with the soil as well as models of fluid and thermodynamics (Bruse and Fleer, 1998). In fact, ENVI-Met is the most applied software for urban microclimate analysis at district scales (Toparlar *et al.*, 2017). These building resolving models coupled with CFD have proved a great help in the assessment of urban microclimates, thereby enabling researchers or environmental assessors to study and evaluate the urban environment under different scenarios in detail. However, these models are usually designed from the perspective of a detailed assessment of the urban microclimate and are not perfect for assisting the design phase of work due to their overly complicated setting parameters and calculation procedures. At the same time, in the early stages of design, it is usually necessary to quickly check a series of options, so simplifying the process as much as possible. For this purpose, a few simplified microclimate simulation models have been developed especially for urban design. The sustainable urban neighbourhood modelling tool (SUNtool) is a model designed to support urban designers or architects when optimizing their planning proposals for sustainable designs at the district scale. It enables the users to adjust the layout, form and fabric design of buildings to choose the optimum combination for the urban design. However, the model currently does not include the thermal microclimate model and only considers short-wave radiation. Furthermore, Yao *et al.* (2011) proposed a simplified nodal network model (UMsim) to simulate urban microclimates for design purposes and the simulation results were validated against field measurements in Chongqing. The limitation of this simplified model is that it does not include the effects of anthropogenic heat and the effects of vegetation are only considered by introducing a fixed coefficient. Moreover, it is not compatible with other city model files (hence the need to build a morphological model separately) and may not apply to high-rise buildings. Thus, this method is still not a complete and applicable rapid urban design analysis tool. The modelling characteristics of the above models are also briefly summarised in Table 2.3.

Table 2.3: A brief summary of neighbourhood/district scales numerical microclimate model capabilities in last three decades.

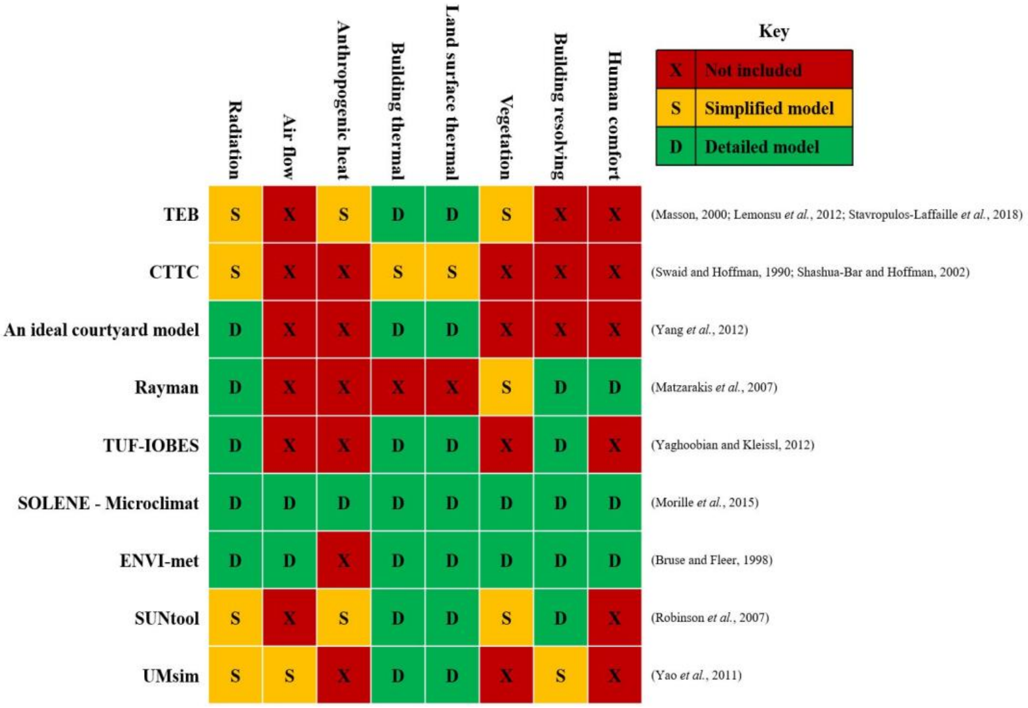

	Radiation	Air flow	Anthropogenic heat	Building thermal	Land surface thermal	Vegetation	Building resolving	Human comfort	
TEB	S	X	S	D	D	S	X	X	(Masson, 2000; Lemonsu *et al.*, 2012; Stavropulos-Laffaille *et al.*, 2018)
CTTC	S	X	X	S	S	X	X	X	(Swaid and Hoffman, 1990; Shashua-Bar and Hoffman, 2002)
An ideal courtyard model	D	X	X	D	D	X	X	X	(Yang *et al.*, 2012)
Rayman	D	X	X	X	X	S	D	D	(Matzarakis *et al.*, 2007)
TUF-IOBES	D	X	X	D	D	X	D	X	(Yaghoobian and Kleissl, 2012)
SOLENE - Microclimat	D	D	D	D	D	D	D	D	(Morille *et al.*, 2015)
ENVI-met	D	D	X	D	D	D	D	D	(Bruse and Fleer, 1998)
SUNtool	S	X	S	D	D	S	D	X	(Robinson *et al.*, 2007)
UMsim	S	S	X	D	D	X	S	X	(Yao *et al.*, 2011)

Key

X	Not included
S	Simplified model
D	Detailed model

2.6 Summary and conclusion

As the characteristics of the urban climate in the late 19th and early 20th centuries began to be gradually revealed, the need for a better understanding of urban climate mechanisms and the use of more applicable climate modelling tools which can help future urban planners to mitigate the negative effects of climate change became apparent (Section 2.1). With the massive progress of computing power in recent years, numerical simulation plays a more flexible and important role in the process of climate research (Section 2.2). Considering the characteristics of different climate research scales, neighbourhood-scale numerical models are most beneficial in explaining the relationship between different urban components and local climate-related building-energy-consumption (Section 2.3). They can help the governor/planner intuitively establish an appropriate urban planning scheme in the early strategic decision-making and planning stages.

Due to the complexity of urban climate simulation, a variety of surfaceparameterized numerical simulation schemes have been used in urban climate research (Section 2.4). Slab models were widely used in early climate simulations due to their lightweight computational advantages. With their superior balance, UCMs have become the most widely used urban climate research tool since they preserve the urban surface features as much as possible while lightening the calculation process. Contrary to the previous two models, building-resolving models aim to reflect the urban surface climate characteristics more realistically and comprehensively. However, the huge calculations required mainly restrict their use to microclimate research.

Nevertheless, performing the outdoor thermal-climate-related environmental planning optimization and assessment tasks required by existing microclimate numerical models (whether based on parametrization approaches of slab models, UCMs or building-resolving models) is challenging in practice (Section 2.5). This is mainly due to the current microclimate models being developed for two research purposes. One is to interface with mesoscale climate models to represent the influence of urban texture on the Urban Boundary Layer (UBL) climate. Microclimate models for this purpose are usually based on slab models and UCMs, therefore, they use an average parametric approach to represent the morphological features of the city, which, whilst reducing computing costs, makes it impossible for them to distinguish in detail the differences brought about by urban form. For example, the building features in a climate model are considered the same regardless of whether the blocks are arranged in a diamond or square shape, as long as the width of the streets and the height of the buildings are the same. Thus, numerical models based on slab models and UCMs cannot be used to plan micro-scale improvements to the built environment.

The second purpose is to carry out a detailed parametric study of the microclimate in different building arrangements. Models built for this purpose usually restore the real physical situation as much as possible. Building-resolving models in combination with CFD is the most typical approach; however, this often makes the simulation process very complex whilst failing to provide an efficient output which can assist real-world urban planning optimization. In general, the current microclimate models seem to be at two extremes. They are either too simplified to provide sufficient information or too complex to achieve effective, timely output. None of them is capable of climate modelling for the purpose of supporting early-stage urban planning related to thermal climate. A gap that currently exists is the lack of urban climate analysis methods that fall between these two types of modelling scheme. Such methods should achieve the most critical outdoor heat exchange simulations at minimal computational cost without losing details of urban surface features.

Therefore, if it is expected that a microclimate simulation model can serve the built environment planning process more practically and effectively, a new numerical simulation scheme is indispensable. By building on previous work, the following chapters explore and propose a novel simulation method using rasterized urban models for urban microclimate prediction (Chapters 3-5) which can rapidly support a range of urban environmental planning options on a district scale.

Chapter 3

A Rasterized Method for Describing the Properties of Urban Surfaces

3.1 Introduction

3.1.1 Numerical models to describe the properties of surfaces

Building geometry plays an important role in addressing changes in urban climate. For instance, on clear nights, building geometry and land cover determine the thermal contrast situation (Oke *et al.*, 2017). Building geometry and land cover albedo are also related to the urban energy/water balance and urban air corridors (Oke, 1988). They contribute to urban climate change through the shape and orientation of buildings, roads and other man-made surfaces that affect the mechanical, thermal and radiative properties of the atmospheric boundary layer. In addition, the values of these parameters depend on the shape and materials of the building, the thermal structure, the vegetation coverage on the roof and road, the sky view factor and the heating source inside the building, which vary for different building shapes, sizes and types. Hence, accurate descriptions of urban surface properties should improve the output of numerical models for simulating urban climates. The canopy model, for example, requires input on the width of the street, the height of the street valley and the proportions of the surface materials to characterise the urban surface. The closer these input parameters are to the real surface conditions the more reliable the simulation results will be.

Urban surface feature parameters are often used to refine specific urban surfaces in such canopy models. Such parameters usually vary according to the simulation focus of different models. For example, some studies may pay more attention to the impression of differences in surface coverage and mainly consider parameters such as surface albedo and emissivity and heat capacity (Salleh *et al.*, 2013) while other studies may focus on the role of the urban fabric on urban climate and pay more attention to parameters such as average building height, orientation and street width (Whitehand *et al.*, 2011). Parameterizing these urban surface geographies is a critical necessity in urban climate simulations.

The thermal and radiative properties of urban surfaces are determined primarily by the composition of the urban structures (such as the proportion of wood, brick and stone in walls, the percentage of asphalt shingle, wood shingle and vegetation in roofs). Different compositions of pavement materials are also worth considering in the study of urban thermal and radiation environments. In regional studies, the classification of coverage with the same building and road construction materials is significant. In addition, urban morphology depends to a certain extent on culture and geography. For example, buildings in some areas are entirely brick and cement. In other regions, walls are built with mud and bricks. Therefore, accurate representation of urban areas in urban climate models cannot generally ignore the geographic knowledge of the studied area.

Urban surface properties vary greatly in space and time. However, static urban surfaces that do not reflect urban growth are what most current urban canopy models use. Urban land cover never stays the same due to population growth in urban environments. This also makes urban land cover increase both horizontally and vertically, which simultaneously changes the thermal, radiative and hydrological properties of a city. Inaccurate representations of urban surfaces will undoubtedly affect predictions of future urban climates under looming urbanization and climate change. Therefore, it is of great significance to strengthen the updated and accurate representation of urban surface geographic data for urban climate simulation.

Treitz *et al.* (1992) claimed that the geometry and morphological parameters of cities can usually be extracted using ground observation or remote sensing satellite information. Furthermore, thanks to the development of machine learning in computer vision recognition, remote sensing image classification could overcome the limitation of customer service restrictions and subjective choices, as well as making the classification of remote sensing images more convenient and accurate (Reichstein *et al.*, 2019). In a word, different building shapes and sizes, the materials of building walls, internal heat sources, thermal structure, materials/coverings of roofs and roads and even sky viewing coefficients, etc. determine the parameters of urban surface properties. Therefore, only accurate observations of these parameters can ensure the quality of the output from urban climate models.

3.1.2 The types of urban surface properties

An authentic description of urban surface properties is the essential input element for correctly simulating the urban climate and showing its characteristics at different locations. According to Oke *et al.* (2017), urban surface properties can be grouped into three major categories: urban structure, urban surface textures and urban function zones. These three types affect different aspects of the urban climate and have the following features (Figure 3.1):

1) **Urban structure** refers to the dimensions of urban elements (mainly buildings)

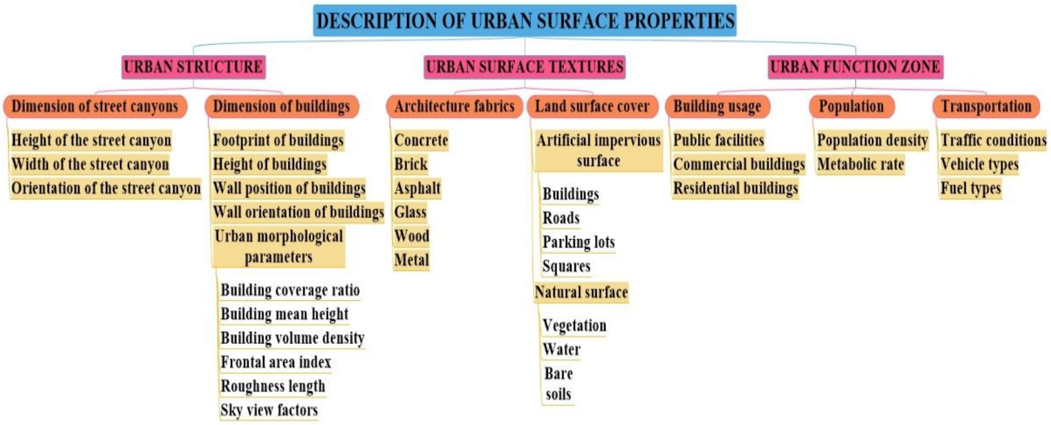

Figure 3.1: Simple description of urban surface properties for urban climate simulation.

and their spatial arrangement. Simply put, urban valleys generally gain more net radiation due to the uneven heights of buildings (Rizwan *et al.*, 2008; Takebayashi and Moriyama, 2009). In addition, as previously stated, the increased number of buildings increases the coefficient of friction of the urban canopy resulting in a reduction in urban breezes as well as the effectiveness of urban ventilation.

2) **Urban Surface textures** include building and road materials, vegetation, and water features (ponds, lakes, rivers, etc). Taking building materials as an example, the urban ground, mainly made of reinforced concrete, can absorb a large amount of solar radiation due to its large thermal capacity, high thermal conductivity and low moisture content (Arya, 2001; Bokaie *et al.*, 2016). In contrast, vegetation covering can affect urban climate directly and indirectly by evapotranspiration cooling and reducing heat exchange with occupied spaces, thereby mitigating urban thermal stress (Gunawardena *et al.*, 2017; Herath *et al.*, 2018).

3) **Urban function zone (UFZ)** refers to the basic urban area divisions that carry specific socio-economic activities (such as commercial, industrial and residential) (Qin *et al.*, 2022). It was originally an urban economics concept and is now widely recognized as one of the morphological parameters affecting urban climate due to its high correlation with anthropogenic heat (Yu *et al.*, 2021). In simple terms, the same UFZ usually presents similar energy consumption and outdoor thermal environment features including similar spectral characteristics as well as a specific functional composition (Sun *et al.*, 2013).

Nevertheless, it is a challenge to build datasets that can comprehensively and accurately describe all the above-mentioned data types for urban climate research. This is because data on urban surface properties are not only diverse but also change with the construction of the city. Complex data types make it more difficult to establish a dataset since different data types often require appropriate means of access due to their different characteristics. For example, although building outlines can be effectively extracted using full-colour optical aerial imagery, it is difficult to distinguish between features with similar spectral characteristics such as pools and grass (Hao *et al.*, 2016). A further complication is that changes in the surface properties of cities brought about by urban construction make it necessary to constantly update the data to ensure the authenticity of the dataset. These two characteristics of urban surface properties data may further increase the time and economic cost of building the dataset since an amount of time is required to collect and update the data. In addition, the form in which the data is stored and expressed is also an issue. For example, building geometry can be expressed in 3D forms as well as using Digital Elevation Models (DEMs). Such non-uniform data formats will undoubtedly add more time to the pre-processing of the data before it can be used. Therefore, a systematic approach to providing reliable and convenient datasets of urban surface properties for urban climate studies is needed.

This chapter aims to develop a method to characterize urban surface properties based on raster data models to improve the efficiency and practicality of urban climate simulations. The simple structure of the raster data (points, lines and surfaces are stored in the same form) makes it easier to store large amounts of surface property data. The special overlay algorithm also facilitates better spatial analysis and surface simulation, which provides new analytical approaches for subsequent urban climate simulations. To realize this method, (1) More realistic and comprehensive information on urban surface properties need to be obtained. This ensures the reliability of the input data for urban climate studies. (2) A novel approach to data updating brings urban surface information data closer to real urban characteristics. (3) Information on urban surface properties can be obtained at a low economic cost. (4) Systematic data processing solutions provide comprehensive datasets describing urban surface characteristics in a uniform format. This new method provides a convenient solution for data pre-processing in the early stage of urban climate research and can improve the overall efficiency of urban climate simulation.

3.2 Representing urban surface properties with the raster data model

In order to create a systematic dataset of urban surface properties, a uniform representation of urban surface information is essential. The digital representation of geospatial data usually takes the form of vector data and raster data (Figure 3.2). Vector data models use points, lines and polygons to represent spatial features with clear spatial locations and boundaries, such as rivers, building layouts and vegetation cover. Each vector feature is assigned an identification code to be associated with its attributes. Raster data models use grids and grid cells to represent spatial features. Point features are represented by a single cell, line features are represented by a series of adjacent cells and polygonal elements are represented by a collection of consecutive cells. The cell value represents the attribute of the spatial feature at this cell location. Raster data models are suitable for representing continuous features such as elevation and land cover classifications. Much of the data used in GIS is encoded in raster formats, such as Digital Elevation Models (DEMs) and satellite imagery. Although there are certain errors in the spatial features represented by raster data, its unique advantage is that it has a fixed cell location which enables efficient operation and analysis of raster data models in computational algorithms. Since the purpose of this research is to quickly and efficiently simulate the urban climate under different built environments, the description of urban surface features in raster format is more conducive to the establishment of later simulation algorithms. In addition, the simpler data structure of raster data also makes it more suitable for storing complex data types since a multi-band data structure can quickly integrate multiple data types. The following section will discuss in detail how to establish the urban surface properties dataset based on the raster data model.

3.2.1 Principle of the raster data model for storing geospatial data

The raster format is also called grids or images in GIS. A raster represents a continuous surface, but when used for data storage and analysis, a raster consists of rows, columns and cells (also called pixels of an image). The rows and columns start from the upper left corner of the grid. In a two-dimensional coordinate system, the row is the y coordinate, and the column is the x coordinate. Each cell in the raster is strictly defined by its row and column position.

As shown in Figure 3.2, raster data represent points, lines and polygons in a specific manner to single or multiple adjacent cells. Although the raster data model has disadvantages in representing the precise location boundaries of spatial features, it

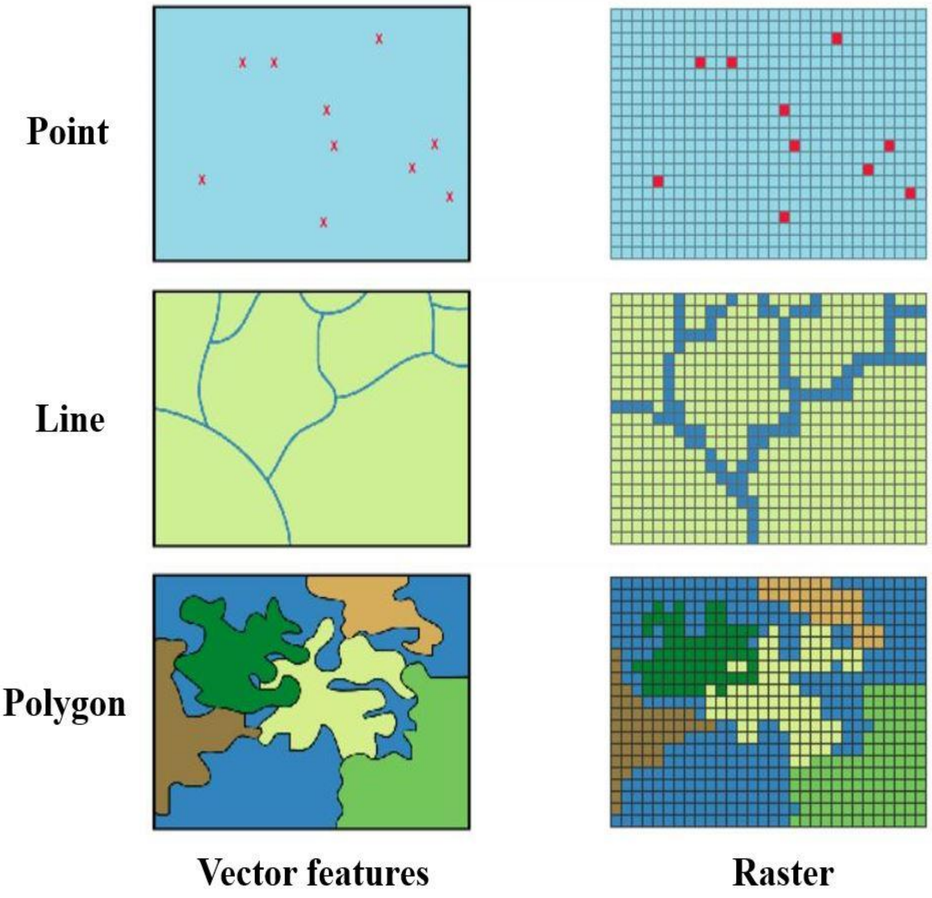

Figure 3.2: Schematic representation of features in raster and vector formats. (Source: ArcMap 10.8)

has distinct advantages in having fixed grid locations (Peuquet and Duan, 1995). Algorithmically, a raster can be viewed as a matrix with rows and columns and its cell values can be stored as a two-dimensional array and processed as a permutation variable expressed in code. Therefore, raster data is easier to manipulate, aggregate and analyse than vector data. When building a raster data model, the following elements are the most basic to consider:

Cell values can be categories or numbers. Taking the land cover raster as an example, the categories it contains can be: 1- urban land, 2- forest land, 3- water body, etc. A land cover raster is also an example of an *integer raster* because its cell values have no decimal places. In addition, the digital elevation raster contains numeric data such as 30.5, 15.66, etc. The digital elevation raster is a floating-point raster since its cell values include decimal places. In summary, the specific data-type of a cell value is determined by the type of geospatial data represented.

Cell size refers to the size of the area represented by a single cell. If a grid cell is 100 sqm in size, this means that each side of each cell is 10m long. The cell size determines the spatial resolution of the raster data (smaller values mean higher spatial resolution). Cells that are too large cannot represent the precise location of spatial features and increase the chance of having mixed features in a single cell. With smaller cells, these problems are alleviated, but small cells increase the amount of data and data processing time. Therefore, it is very important to select the appropriate pixel size according to the characteristics of the data type and the content to be analysed.

Raster bands can be single or multiple. There is only one cell value per cell in a single-band raster. Normally, elevation data is a single band of data, which has only one elevation value at each pixel location. Each cell in a multiband raster is associated with more than one cell value. Satellite imagery is a typical example of multiband raster data. It can have multiple bands at each cell location representing different cell values. Reasonable multi-band raster data fusion can increase the dimension of data types to comprehensively represent spatial information.

Spatial reference information is necessary for the GIS data model since it enables GIS data to be spatially registered with each other. For example, if overlaying one elevation raster on top of another land cover classification raster, it is necessary to ensure that both datasets are based on the same coordinate system. Therefore, the need for a unified and suitable coordinate system according to the analysis needs cannot be ignored.

It is essential to design a suitable raster data structure according to the characteristics of the geospatial data and the above elements. Therefore, it is important to understand the form of spatial data that needs to be displayed or analysed when building a raster dataset.

3.2.2 Build essential urban surface properties units in raster format

In order to build a reasonable raster data model for describing urban surface properties, it is significant to understand the basic unit used to describe urban surfaces as input data. As mentioned above, urban surface features can be divided into three main categories. The following sections will explore the most basic units based on these three classes of surface properties.

(1) Urban structure

Airflow and radiation exchange in the urban canopy are mainly influenced by the size of urban elements (buildings and trees) and their spatial arrangement. Therefore, the urban form information is usually the basis for the study of such problems. The simplest way to describe the geometry of a city is to measure the size of the elements: width, length (L), height (H) and the distance between different elements (D).

Furthermore, to reflect the relationship between urban spatial layouts and climate in greater detail, some more complex urban morphological parameters are widely used, namely building coverage ratio (BCR), building height (BH), building volume density (BVD), frontal area index (FAI), roughness length (RL) and sky view factor (SVF) respectively (Xu *et al.*, 2017). These parameters are considered to have important implications related to urban heat and wind (See Appendix I for details).

To a large extent, these parameters can support research into the urban environment. The equations in Appendix I reveal that the footprint and height of the building are the basic elements for calculating these parameters. Therefore, in this study, the parameters used to build the urban structure are defined as footprint and height attributes.

(2) Urban surface textures

Cities are usually constructed using a wide variety of materials, including man-made materials such as concrete, brick, wood, asphalt, stone, glass, metal, etc. as well as natural materials such as vegetation, soil and water. Due to their unique physical properties (albedo, emissivity, heat capacity, etc.), urban surfaces composed of various materials in varying proportions exhibit unique climatic behaviours. At the same time, the composition of the land cover has been widely recognized as influencing land surface temperature (LST) (Weng, 2009). Lower percentage coverage of buildings and higher coverage of woody vegetation are considered to be the most important factors in mitigating the effects of UHI (Zhou *et al.*, 2011). Impervious surface and tree canopy percentages correlate with temperature changes for most of the day in cities (Coseo and Larsen, 2014). In addition, recent studies have shown that changes in the urban surface coverage ratio can also indirectly affect the urban wind environment by influencing the urban thermal environment (Ngarambe *et al.*, 2021). Thus, data on urban surface coverage types is essential for this study. Meanwhile, since building surface materials are usually not used as necessary input data and are difficult to distinguish using remote sensing images, this study does not directly obtain such data.

(3) Urban Function Zone

The Urban Functional Zone (UFZ) concept was originally used in urban economics but is now widely considered among the morphological parameters that affect urban climate. It is considered to indirectly change the urban climate because it influences urban emission types. The additional emission from human activities consists primarily of the release of large amounts of sensible heat from fuel combustion, the release of additional water in the form of vapour or liquid during the combustion process as well as particulate and gaseous air pollutants (Oke, 1979). These emissions are mainly affected by the characteristics of regional human activities including population, traffic and urban functional zoning. However, since the population and traffic conditions in an area are highly real-time and need to be collected by researchers according to actual needs, only data involving urban functional zoning will be extracted in this study, which will be reflected in classifying the use of individual buildings.

To sum up, in this study, building footprints and heights, urban land cover types and building usage types will be collected as the most basic urban surface information in a raster format. This study builds a gridded urban surface properties model based on the above basic units, which stores the information on the building geometries and urban morphology within a digital matrix. This raster data model forms the basic framework for all the urban surface properties. Furthermore, the process of calculating the thermal environment parameters of buildings involved in a simulation are all based on these digital matrices and expressed in raster form. The building layout, height, shape and other information in the raster data correspond to the cells of the raster data one-to-one, which clearly expresses the building group information stored in the multiple band raster (the specific data structure is shown in Figure 3.3). Therefore, to adjust the parameters such as the layout, height, shape and even physical properties of the building, it is only necessary to adjust the input parameters from the interface, which greatly simplifies the establishment and adjustment of the parameters of the urban building group. This rasterized urban dataset provides a convenient representation for modelling a complex building environment and subsequent analysis. Additionally, in order to quickly establish a rasterized urban surface properties model, the research also proposes a method to establish an urban surface information dataset by comprehensively utilizing and analysing geographic information data and remote sensing data, as described in the following section.

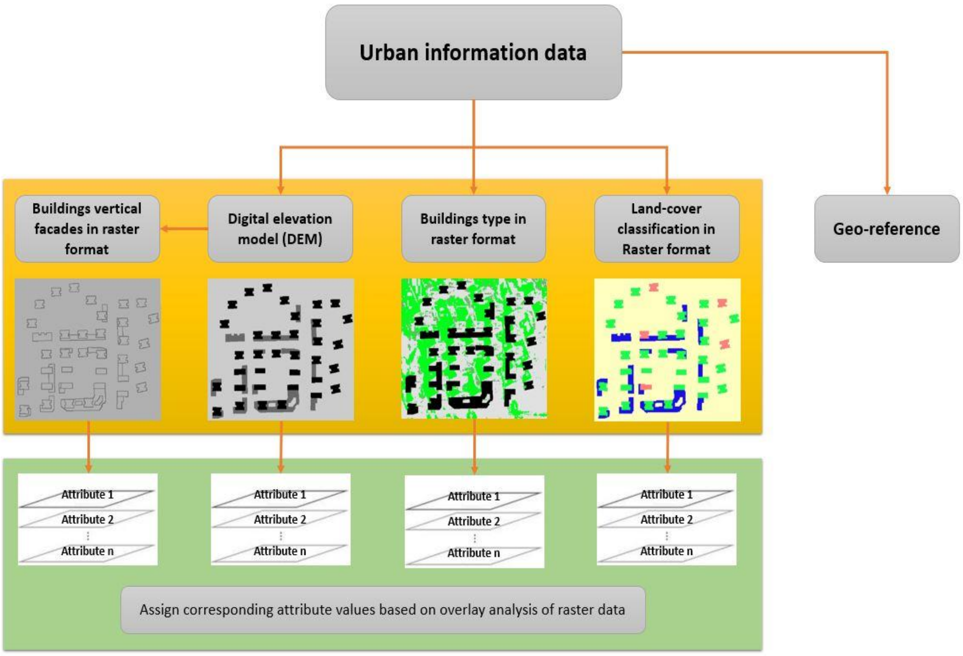

Figure 3.3: Schematic diagram of the urban information dataset based on a raster data format.

3.3 A new multi-source data fusion method for extracting urban surface properties

3.3.1 The framework of the new method

This section presents the characteristics of different types of data to establish reliable input to urban surface properties datasets for urban climate modelling based on information from multiple data sources. A novel raster format method for describing urban surface properties by the fusion of data from multiple sources is proposed. The framework of the proposed method is shown in Figure 3.4. Firstly, this study addresses the most basic urban surface properties that need to be described in urban climate simulations, namely 1) the geometry of buildings, 2) the classification of land cover types (such as green infrastructure, rivers, bare soils). 3) the classification of building types. Secondly, this study uses open-source data as raw data for analysis and processing to achieve low-cost data collection. A total of four kinds of open-source data are obtained from different datasets. Then, combining image analysis and GIS spatial analysis methods of remote sensing data not only reduces the identification error of surface attributes but also provides a novel data-update method. At the same time, comprehensive urban surface attribute data can be quickly extracted using multiple data sources. Finally, all the results obtained by this method are compared with the field survey data to verify their accuracy and reliability. Moreover, the specific processing flow chart for these urban information data is also shown in Figure 3.4. The specific principles and processes used to obtain these three types of data will be described in detail below.

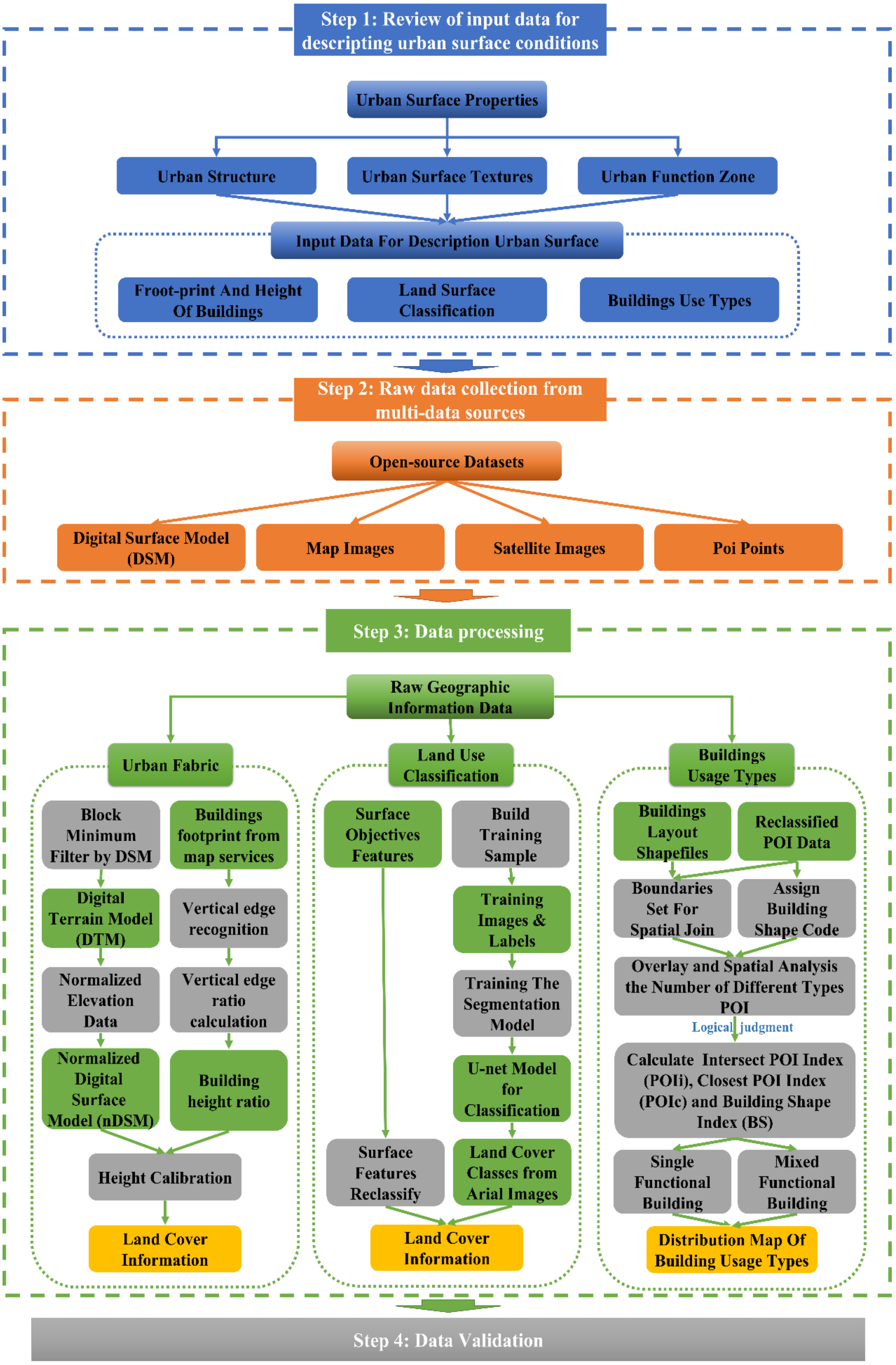

Figure 3.4: The research framework for urban information extraction. In the flowchart, the blue box is the reviewing part; the orange box is the raw data extracted from GIS services; the green box is files created during data processing; the grey box is the data processing and validating steps and the yellow box is the final output data.

3.3.2 Building-geometry data

The process of extracting urban morphology information includes two major steps: 1) building-layout extraction and 2) building-height extraction. The building layout extraction process was based on the styled maps obtained from the Maps Static API, while the building heights were generated from the AW3D30 DSM aid with satellite image recognition.

(1) Building-footprint data

The image processing method based on the existing open map services data is adopted to establish the building-footprint data. Currently, most map data service applications (Google, Baidu, Gaode, etc.) provide Application Programming Interface (API) interfaces, which allow users to obtain some geographic information data. Take Google as an example, the Maps Static API provides users with Google map data. Users can directly obtain map pictures with georeferencing such as road maps, satellite images and topographic maps and can also obtain urban element features such as points of interest (POI), roads and water bodies through the API interface. Unfortunately, there is currently no map data service application that provides an open interface for building-footprint data even if the data is already present in the map provided. Thus, this study applies the image processing method combined with geographic information data processing to extract the building layout features based on the accessible map data.

To create building-footprint information, a map within the selected area is obtained using the Map Static API. According to the introduction to the Map Static API, the zoom level should be set to 17 (This represents the zoom level of the image on the map). When at level 17, the area covered by the building on the map can be displayed in data layers. The image is formatted as a .tif file, which provides geographic information for the map and is stored in the form of raster data in the RGB format colour model. The three colour features are represented by a numerical

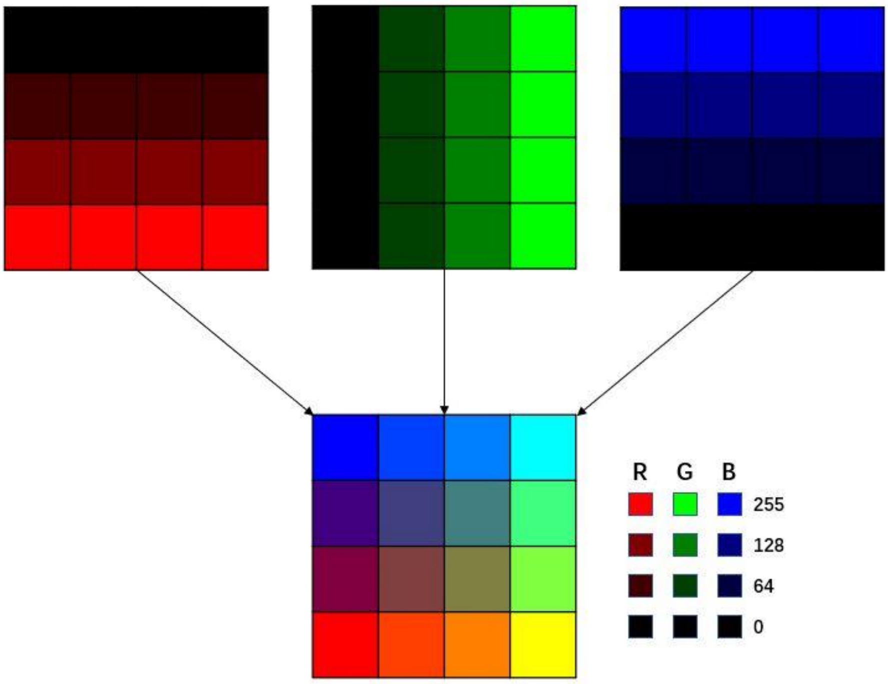

Figure 3.5: Raster data RGB colour synthesis principle, where RGB represents Red, Green, and Blue respectively.

grid from 0 to 255 in three different layers as shown in Figure 3.5. Then, the data of the three layers are displayed together as an RGB composite image in which similar colours have similar numerical codes. Therefore, after filtering out these data and reassigning them (according to the logical relationship in Eq. 3.1), an area of a specific colour can be extracted. Specifically, this logical algorithm identifies the part with an RGB value of (155, 155, 155) (i.e., grey) as the building area and the other RGB numerical values as non-building areas for reclassification.

$$Outputs = \begin{cases} buildings\ covering,\ if\ colour\ RGB = (155{,}155{,}155) \\ other\ surfaces,\ if\ colour\ RGB = else \end{cases} \tag{3.1}$$

After obtaining the corresponding map image, the method of band analysis and raster reclassification is applied to make the map re-define feature parameters to set the building coverage to black and set the background (including water and road features) to white to emphasize the buildings' footprint in the map. Finally, the ArcScan tool in ArcGIS is used to digitally convert the building footprint into a vector format in a fast and automatic way. The specific process of the above method is shown in Figure 3.6.

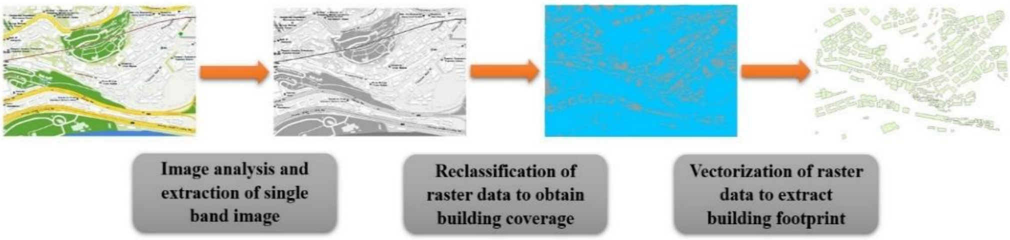

Figure 3.6: Schematic diagram of the building footprint extraction process.

(2) Building-height data

The building-height (BH) data at the city scale is not always straightforward. There is currently no open-source data to directly obtain building heights in many cities. The commonly used methods to obtain the BH data includes ground survey field measurement, satellite image stereo and radar data (such as SAR and LiDAR), which are normally expensive and time-consuming. In this study, the AW3D30 DSM data (an elevation model that represents the altitude of all objects on the surface of the earth including trees and buildings.) is used to extract basic building height information, meanwhile, the image recognition technology is applied for secondary calibration of the height data. The whole processing workflow for extracting the building height consists of three stages. The first stage is the generation of a normalized Digital Surface Model (nDSM), which only contains the height of objects higher than the ground. To build the nDSM data for separating non-ground objects from the ground, it is essential to build a data model of bare ground (continuous ground terrain, called a digital terrain model, DTM). The block minimum filtering method is usually used to obtain the minimum elevation in a certain area, allowing DTM data to be generated (Wimmer and Wack, 2002). Considering the resolution of the original DSM images (30m), the block minimum filter was applied with a grid size of 600m. The difference between the original DSM and the approximated DTM is the value of the normalized DSM (nDSM), which contains the height information of all non-ground objects. The calculation method for nDSM is shown in Eq. 3.2.

$$nDSM = DSM - DTM \tag{3.2}$$

Since the AW3D30 DSM images were collected in 2011, buildings built after 2011 are not accommodated. Therefore, the second step is to combine the stereo images method for eliminating deviations caused by the time of data collection. Generally speaking, the relationship between the height of a certain building and the satellite elevation angle is shown in Figure 3.7, which can be expressed as Eq. 3.3. Therefore, the height relationship of different buildings in the same satellite image can be expressed as Eq. 3.4. According to the spatial relationship between the satellite and the earth, the altitude angle can be expressed by Eq. 3.5.

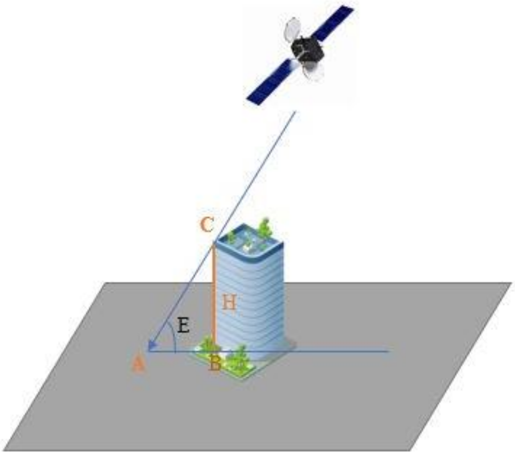

Figure 3.7: Spatial relationship between building height and satellite elevation.

$$L_{AB} = \frac{H_n}{\tan{(E_{sat})}} \tag{3.3}$$

$$\frac{H_1}{H_2} = \frac{L_{AB1}}{L_{AB2}} * \frac{\tan{(E_{sat1})}}{\tan{(E_{sat2})}} \tag{3.4}$$

$$E_{sat} = arctan\frac{\cos(lon_{sat} - lon_{site}) * \cos{(lat_{site})} - 0.1512}{\sqrt{1 - cos^2(lon_{sat} - lon_{site}) * cos^2(lat_{site})}} \tag{3.5}$$

where L_{AB} is the length of the building height reflecting on the view panel of the satellite, H_n is the building height, E_{sat} is the satellite elevation angle, lon_{sat} is the satellite's longitude in degrees, lon_{site} is the site longitude in degrees, lat_{site} is the site latitude in degrees.

Since the latitude and longitude values of the features in the same satellite image have a small difference, the tangent ratio of the elevation angle in Eq. 3.3 is approximately equal to 1. Thus, the height relationship of the buildings to each other can be determined by simply calculating the proportion of the vertical side of the building in the satellite image. To detect the vertical edge of buildings from satellite images for height estimation, the Canny edge detection and Hough transform (the feature extraction technology in image processing) are introduced in this study. The basic outline of the ground objects in the satellite image is first extracted by the edge detection of the Canny operator. Secondly, the vertical edge segment of the building is fitted by the Hough transform. Finally, the ratio of the edge of the building is calculated with the help of geographic coordinates. Canny edge detection adopts the method of first smoothing and then derivation to suppress noise and accurately locate edges. It first smooths the image using a Gaussian filter to remove noise, see Eq. 3.6.

$$G(x,y)=\frac{1}{2\pi{\sigma_G}^2}e^{\frac{-(x^2+y^2)}{2{\sigma_G}^2}} \tag{3.6a}$$

$$f_s(x,y)=f(x,y)*G(x,y) \tag{3.6b}$$

where $f(x,y)$ represents the input source data (original images), $G(x,y)$ represents the two-dimensional Gaussian function, $f_s(x,y)$ is the image after convolution and smoothing, σ_G is the standard deviation of the Gaussian distribution, x is the x-axis coordinate of the pixel in the image and y is the y-axis coordinate of the pixel in the image.

The gradient magnitude and direction were calculated when the image is smoothed. The Sobel operator (performs non-normalized Gaussian smoothing in the direction of one coordinate axis and makes a difference in the direction of the other coordinate axis) was used to return the first derivative values of the horizontal G_x and the vertical G_y to calculate the gradient strength and the gradient direction using Eq. 3.7.

$$G=\sqrt{G_x^2+G_y^2} \tag{3.7a}$$

$$\theta_{grad}=arctan\frac{G_y}{G_x} \tag{3.7b}$$

$$G_x = f_s(x, y) * Sobel_x(x, y) \tag{3.7c}$$

$$G_y = f_s(x, y) * Sobel_y(x, y) \tag{3.7d}$$

where G is the magnitude of the gradient, θ_{grad} is the direction of the gradient, G_x is the gradient in the x-axis direction, G_y is the gradient in the y-axis direction, $Sobel_x(x, y)$ is the Sobel operator in the x-axis direction and $Sobel_y(x, y)$ is the Sobel operator in the y-axis direction.

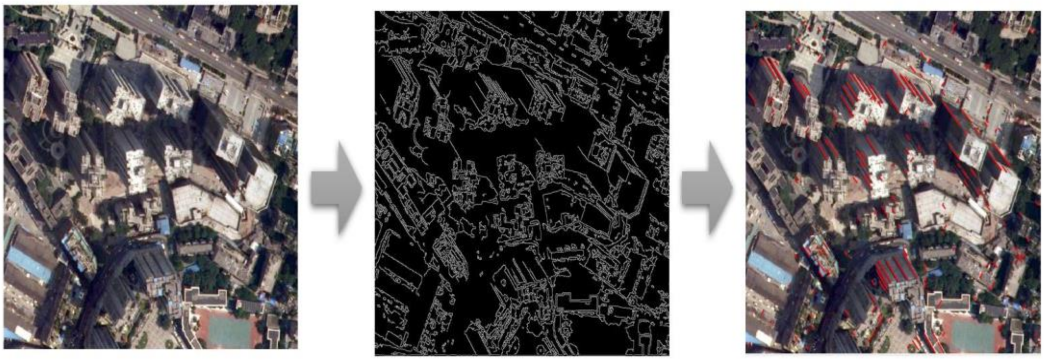

Figure 3.8: Results of the building contour extracted after edge detection.

The amplitude image is then non-maximally suppressed to remove pixels that are not considered edges (leaving only thin lines considered candidate edges). Finally, double-threshold detection is performed to identify the edges of the object and connect them (Results are shown in Figure 3.8). The Hough transform will be used to identify the vertical sides of the building after the outline of the object is identified. It detects objects with specific shapes such as lines or circles through a voting algorithm. In fact, a straight line is a collection of discrete points in an image. Therefore, a discrete polar formula (Eq. 3.8.) for a line can also be used to express each pixel in the line:

$$\rho = x * cos\theta_{polar} + y * sin\theta_{polar} \tag{3.8}$$

where ρ is the geometrical perpendicular to the line and θ_{polar} refers to the angle between ρ and the x-axis.

Since the pixel coordinates (x, y) of the image are fixed, each $(\rho,\ \theta_{polar})$ value can be drawn according to the pixel coordinates (x, y) values, which convert from the Cartesian coordinate system of the image to the polar coordinate Hough space system. The transform divides or accumulates the lattice by quantizing the Hough parameter space into a finite number of intervals. When the Hough transform algorithm starts, each pixel coordinate point (x, y) is converted to the curve point $(\rho,\ \theta_{polar})$ and accumulated to the corresponding grid data point. When a wave peak appears, it means that there is a straight line. After the transformation, the vertical edges of the building can be extracted. Then, the length of the vertical side of the building on the view panel of the satellite projection can be further measured by the coordinate system combined with the raster data. By comparing the vertical side projection lengths of different buildings, the height ratio between different

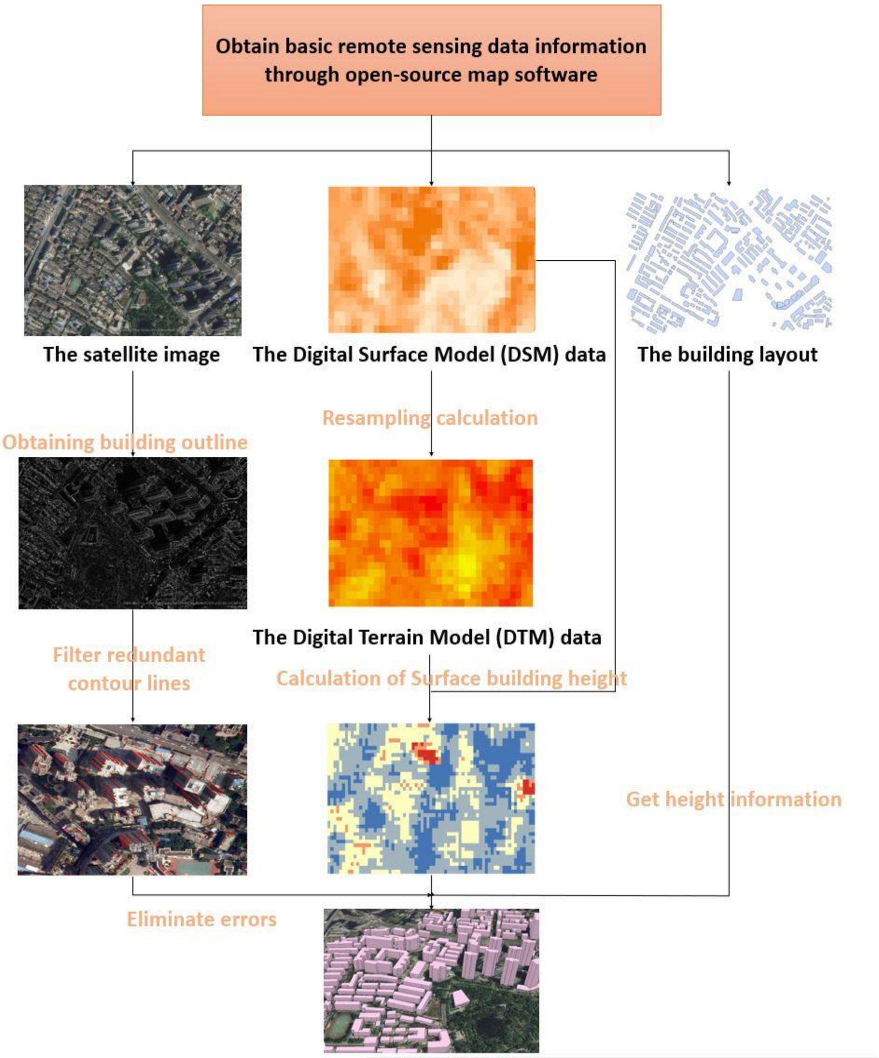

Figure 3.9: 3D city layout information acquisition process.

buildings can be obtained. Finally, using the building height obtained by nDSM to perform proportional conversion, the height of all buildings can be obtained. The last stage of the building height extraction is to separate buildings from other objects by assigning the height to each building footprint using the building shapefiles acquired from the Maps API. In this study, BH refers to the average building height of an individual building. The entire building height estimation process is shown in Figure 3.9.

3.3.3 Land-cover classification data

Recognition and re-segmentation of aerial images is the most common method of obtaining land-cover features (Treitz *et al.*, 1992). However, the urban surface information is usually more complex, manifesting as the overlapping of the different surface objects, such as the sheltering of the road by trees or the green roof. Thus, it is difficult to accurately extract the type of surface cover only by reclassifying the aerial image. To reflect the surface type more comprehensively, a multisource data analysis method similar to the extraction approach to building geometric data is adopted. According to the characteristics of the urban land cover, a total of seven land cover categories are classified as buildings, trees, grasses, water, roads, bare soil and other artificial surfaces (e.g., pavements and squares). The extraction of ground cover types can be divided into three steps: (1) extraction of building coverage and road coverage with the help of Map Static API (the same method used for building footprint extraction), (2) reclassification of satellite images with the help of supervised classification and (3) the combination of the data obtained through the map API services and the results of satellite image recognition. Additionally, in terms of supervised classification, the U-Net model, an improved semantic segmentation network based on the full convolutional network (FCN), is introduced for land cover classification. The U-net was originally invented and first used for biomedical image segmentation. Its architecture can be broadly thought of as an encoder network followed by a decoder network. Generally, the U-net model consists of two parts as shown in Figure 3.10 (Weng and Zhu, 2021). The first part is feature extractions (convolution layers) and the second part is the up-sampling (up-sampling layers). In the feature extraction part, there is one scale for each pooling layer and there are 5 scales including the scale of the original image as shown in the right part of Figure 3.10. In the up-sampling part, each up-sampling is fused at the same scale as the number of channels corresponding to the feature extraction part, but it must be cropped before fusion (left part of Figure 3.10). Furthermore, compared with traditional FCN models, U-Net is more successful in architecture and pixel-based image segmentation; in particular, it is more effective for images with limited data sets, which makes it very suitable for land cover classification. On the other hand, to achieve the aims of land cover classification for this research, two aspects are modified based on the original model. Firstly, deep learning requires a lot of training data which is normally solved by data

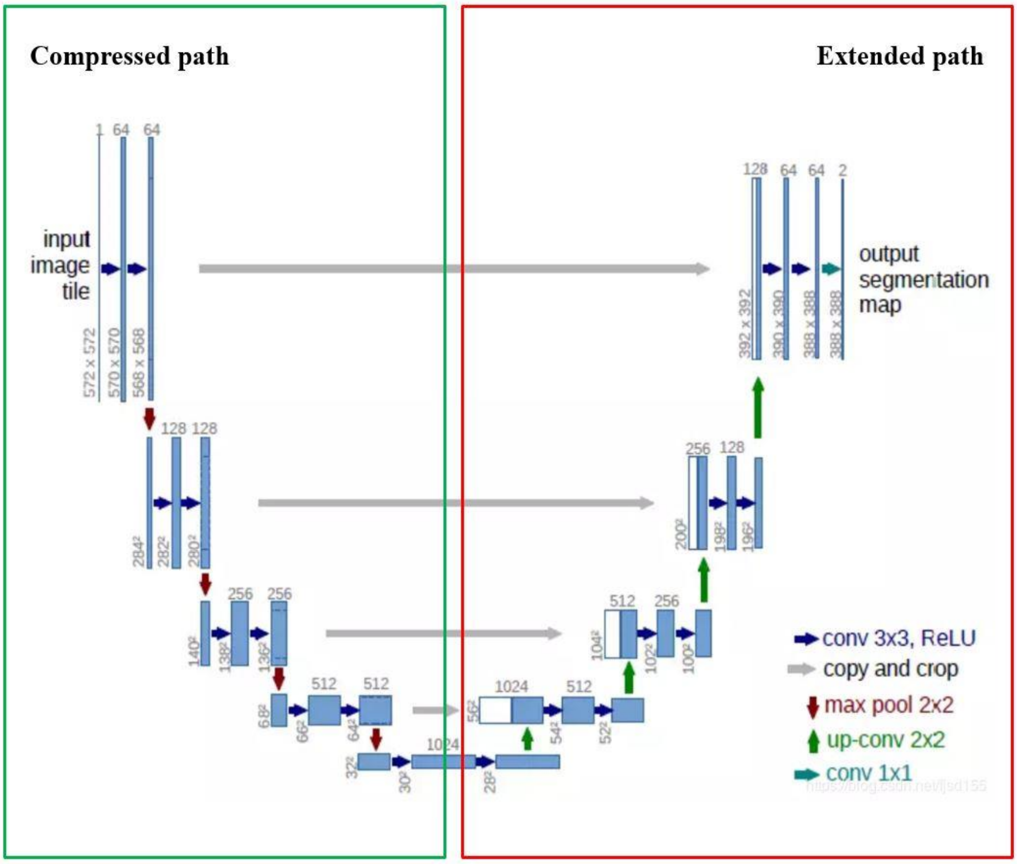

Figure 3.10: 32x32 pixel U-net architecture schematic. The blue and white squares represent the multi-channel feature map and the replicated feature map, respectively. Arrows correspond to different actions.

augmentation technology. However, since the original model was used for image segmentation of medical pictures which have different image features from land cover images, different data augmentation strategies are adopted. Then, since the data volume is not as huge as the original dataset used, some redundant parameters are removed from the U-Net model to improve the performance. Finally, a detailed scheme is provided in Figure 3.11 presenting the resulting land-cover map.

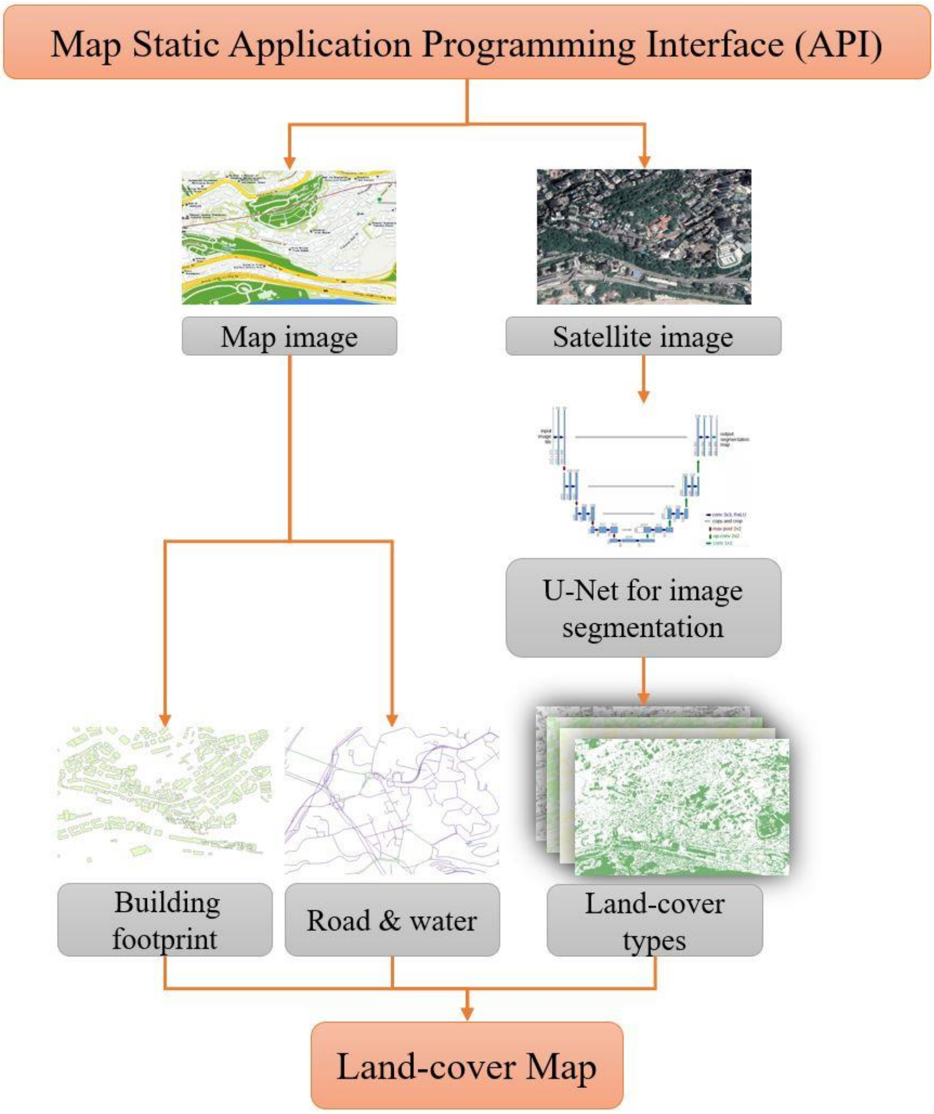

Figure 3.11: A brief flowchart for obtaining land-cover maps.

3.3.4 Building-type classification data

The concept of an Urban Functional Zone (UFZ) is often introduced to explore the impact of different functional areas of the city on its environment or other factors.

In theory, the basic unit of UFZ analysis should be the type of use of an individual building. This is because the UFZ is determined by analysing the proportion of each building or site type within a certain area. Therefore, the type of use of a building is usually the most basic unit of analysis when performing UFZ analysis. To build the most basic urban surface properties information dataset, this research tends to focus on the functional analysis of a building's use type rather than considering land use. On the other hand, accurate building-use information is difficult to obtain from remote sensing images (Heiden *et al.,* 2012). To solve this problem, point of interest (POI) data is used as the basic research object of buildings using category analysis. POI data are easily available in most open-source geographic information platforms and allow the identification of object categories based on human cognition at spatial, temporal and semantic granularity. They often include educational institutes, commercial points, residential buildings, parks, companies and public services, which are different from land cover types, e.g., vegetation, soil, water and buildings; thus, they are fundamental to analysing functional categories of buildings. However, the qualities of POIs vary among categories. For example, there are significantly more commercial POIs than other types e.g., residential and public institutions. The reason is that the POI data is produced by human activities and focuses mainly on commercial institutes more than others. This will cause an unbalanced distribution of POIs, which makes it difficult to represent volumes and spatial distributions of geographic objects with the original POIs. Accordingly, the POI data need to be reclassified and spatially processed to achieve consistency with the ground truth, which enables POIs to be used as classification samples to build a classifier for labelling building categories. For each building, filter out the POIs that fall within the scope of the building according to its spatial scope and then construct the closest POI field value (POIc), the intersect POI field value (POIi) and the building shape index (BS) to judge the building based on the types of these POI functions. Specifically, POIc and POIi represent two different relationships between POI points and building outline vector data that are closest and intersecting, respectively, as shown in Figure 3.12. BS stands for the building shape by calculating its area, perimeter and number of line segments. Hence, the same shape buildings will share the same BS value, otherwise, it will be 0. The specific calculation logic is shown in Eq. 3.9.

$$B_t = \begin{cases} POIi, \ POIi > 0 \\ POIi, \ POIi = 0 \cap BS > 0 \\ POIc, \ POIc = 0 \cap BS = 0 \end{cases} \tag{3.9}$$

Where B_t is the buildings use types, $POIi$ is the intersect POI value, $POIc$ is the closest POI value and BS is the building shape index.

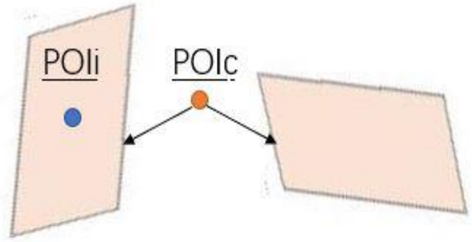

Figure 3.12: Schematic diagram of the positional relationship between POI points and building vector outlines; the blue point is POIi, (the intersection relationship) and the orange point is POIc, (the closest relationship).

Additionally, in this study, 10 categories of building-use types - determined by the classification contained in the original POI data acquired - were established to consider both the ecological impacts of different socioeconomic activities and the national standards for land-use classification: repast, office buildings, residential quarters, shopping centres, financial services, rest and entertainment, scientific research and education, medical services, government agencies and accommodation. Then, based on the functional differences of buildings, they can be classified into three categories: public facilities, commercial and residential (see Figure 3.13). Finally, the normalized kernel densities of the POIs for each building were then extracted. After that, the category of each building was identified through analysis of the POI data, with the aid of building layout shapefiles to show functional maps for each building. In general, through the above analysis and processing of different data types, basic urban morphology information can be obtained. Finally, all the above data will be merged into a raster dataset and stored in the form of different bands.

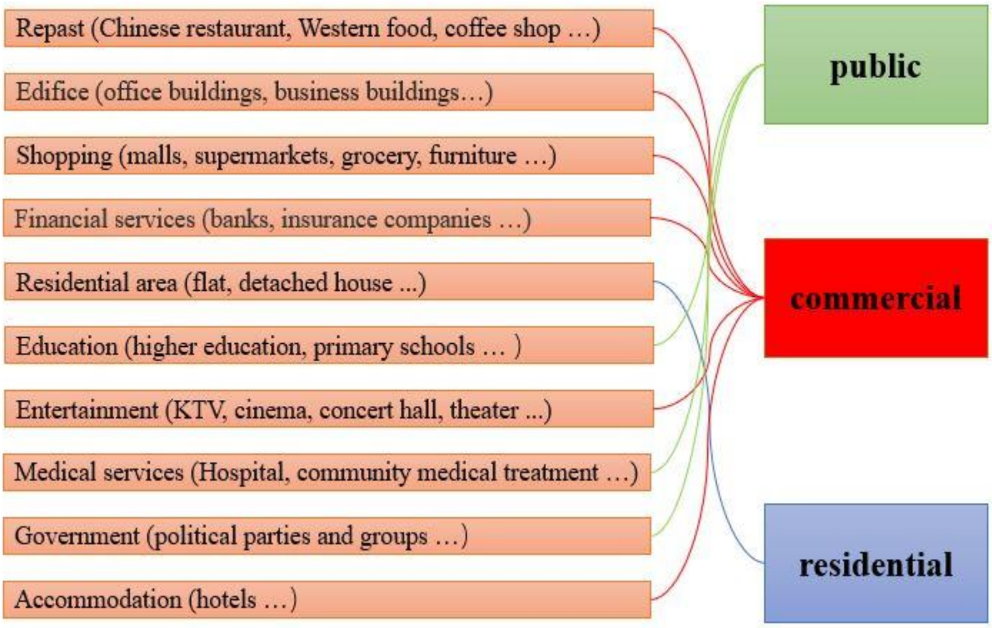

Figure 3.13: Categories for the building-use types based on POIs.

3.4 Method verification

3.4.1 Observational data area

To demonstrate the practicability and reliability of the proposed method, Chongqing (106°N, 29°E) was selected as an experimental area for data validation. Chongqing is a comprehensive transportation hub and the largest industrial city in Southwest China. By the end of 2020, Chongqing had a built-up area of 82,400 square kilometres and a permanent population of 32.0542 million making it one of the most compact cities in China. At the same time, with the characteristics of building on mountains, Chongqing has shaped its unique urban form. Because of this high density, Chongqing is facing undesirable externalities such as thermal comfort issues, overcrowding, urban heat island effects, poor air ventilation and high air pollution concentrations in deep street canyons. In order to improve the urban environment and promote a green city, the strategic research of the 14th five-year plan for green buildings in Chongqing (2021-2025) (Chongqing Commission of

Housing and Urban-Rural Development, 2021) defines the key strategic planning direction in the future as the full completion of urban green buildings. This includes improving the construction quality of green buildings, improving the energy efficiency level of new buildings, promoting the integrated development of green buildings, promoting regional green and low-carbon development. In this study, a total of 5 areas (300m*300m in size) located in the south, east, north, west and middle of the city were selected for data validation in the urban area of Chongqing. The specific locations of the selected areas are shown in Figure 3.14.

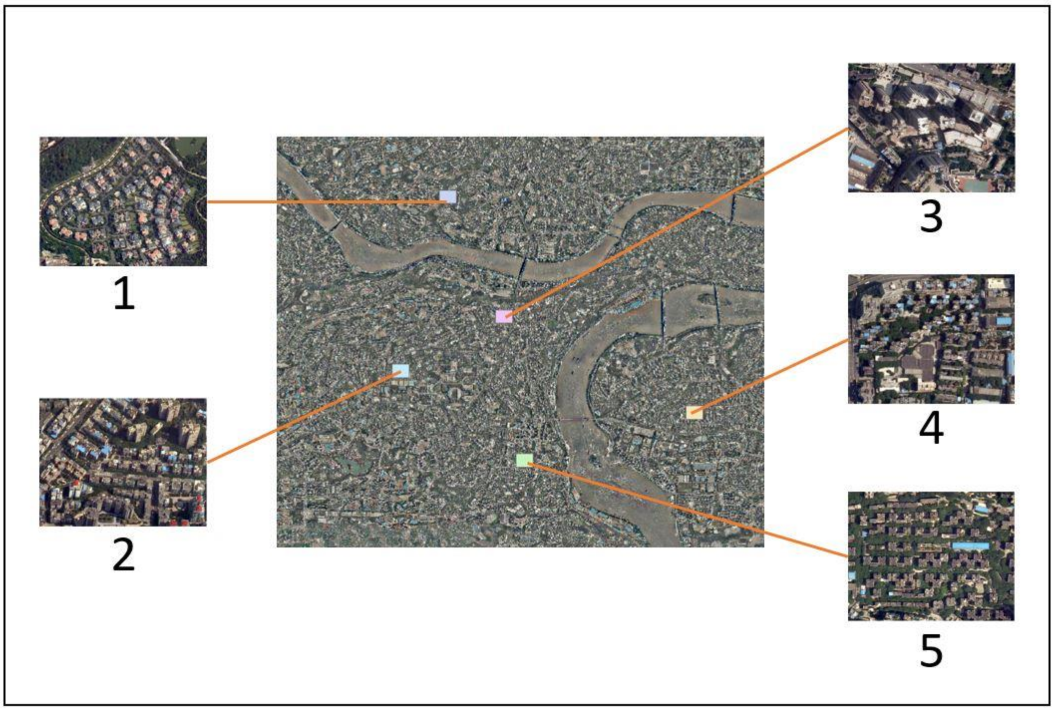

Figure 3.14: The 5 sample site locations in Chongqing.

3.4.2 Input data

As described in Section 2, to obtain the urban morphology data of the study area, four types of data need to be obtained: city POI data, high-resolution satellite images, urban map images and DSM data. Of these, the POI data, high-definition satellite images and map images of the urban area can be obtained through the API provided by Google. In addition, POI data, satellite imagery and map imagery used in this study all date from 2021. For DSM data, the Advanced Land Observing

Satellite (ALOS) World 3D – 30m (AW3D30) DSM is the most up-to-date global DEM dataset currently available for free to the public. It was created from raw images acquired from 2006 to 2011 on the 5-metre grid ALOS dataset, considered the most accurate free elevation dataset (Tadono *et al.*, 2014). Hence, the AW3D30 dataset was chosen to extract building height information in this study. Furthermore, all datasets were resampled to 2m resolution raster data for further analysis and calculations. Finally, to verify and validate the results, manual identification and field measurement in all study areas was adopted to obtain actual urban form data for comparison.

3.4.3 Data validation

In this study, the reliability of the method is validated by comparing the field measurement data with the results calculated by the above method (The data for comparison includes land coverage type and building-layout, -height and -function). Additionally, all the results were compared in the form of raster data, that is, the values of their corresponding cells are compared. Two quantitative indices - the average absolute deviation (AAD) between the estimated results and the actual observations and the correlation coefficient (CC) - were introduced to assess the quality of the estimated results of the method proposed in this study. The two indices are calculated as follows:

$$AAD = \frac{1}{n_{samp}} \sum_{i=1}^{n_{samp}} |y_i - x_i| \tag{3.10a}$$

$$CC = \frac{n_{samp} \sum x_i y_i - (\sum x_i)(\sum y_i)}{\sqrt{(n \sum x_i{}^2) - (\sum x_i)^2} * \sqrt{(n \sum y_i{}^2) - (\sum y_i)^2}}$$

(3.10b)

where y_i and x_i represent the estimated and actual morphological values at location i respectively, n_{samp} is the total number of validation samples.

Better prediction results are usually presented as smaller average absolute deviation (AAD) or percentage AAD values and higher CC. At the same time, building a linear regression analysis using the R-squared and root mean squared error (RMSE) goodness-of-fit statistics can also explore the relationship between predictions and actual observations. Higher R-squared and smaller RMSE reflect a better-fitted model. This will help to establish a quantitative relationship between estimated parameters and actual parameters for practical use and better-eliminate errors. In addition, since the final results of land cover classification and building use classification are dummy values, which are expressed as single numbers (like 0,1,2), these two results are not suitable for performing linear regression. Also, since all results will be validated as raster data, all results will be resampled to 30m resolution to validate the average value within each pixel.

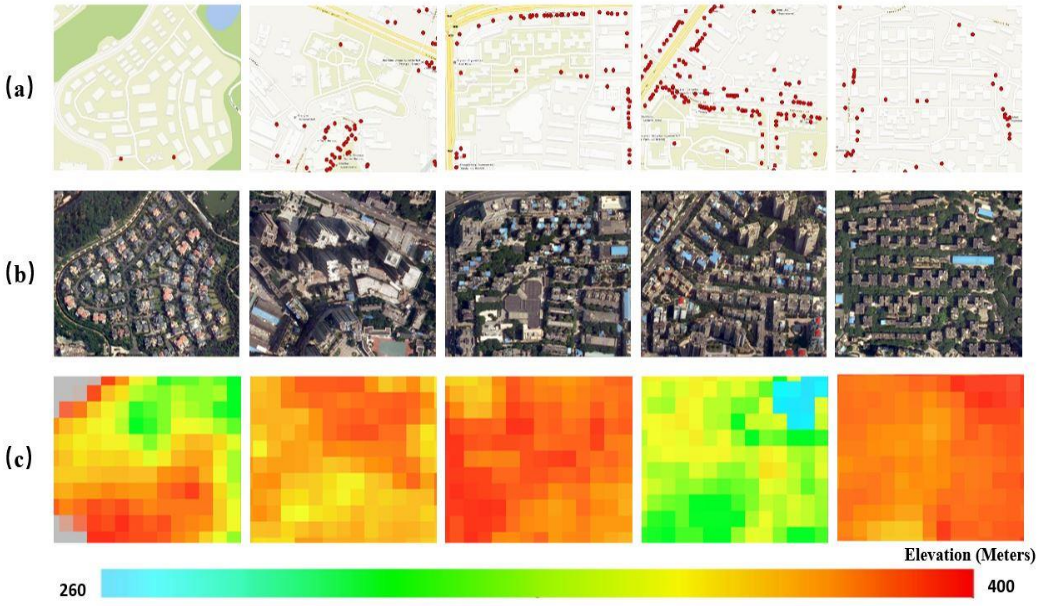

Figure 3.15: Input data for the proposed approach: (a) map image and POI data, (b) optical satellite image, (c) Digital Surface Model (DSM) data (Different pixel colours represent different absolute elevations of the surface, from blue to red corresponding to the elevation values from low to high).

City POI data, map images, satellite images and DSM data are used to extract urban morphological information. Figure 3.15 shows the input data for each area used for data validation. Figure 3.15(a) shows the map image data and POI data obtained through the map API service. Figures 3.15(b) and 3.15(c) show the city satellite image and the DSM data, respectively. By applying all the above input data according to the method described in the previous section, we can obtain the basic information for the overall urban morphology, which includes the footprint of buildings, the height of buildings, the classification of land cover and the classification of building uses. The basic information of a city can be completely displayed after combining the above information and visualizing, as shown in Figure 3.16.

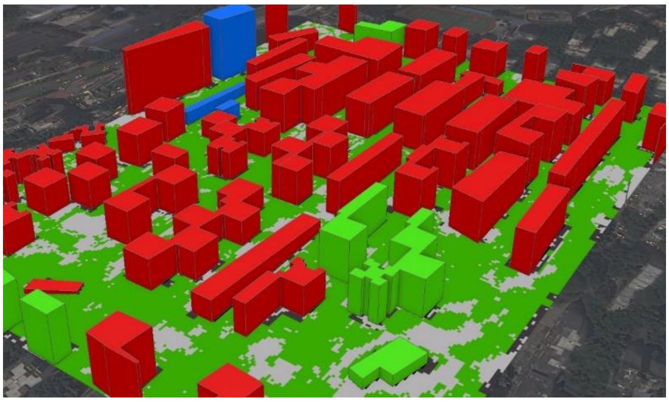

Figure 3.16: The obtained results show the urban morphology information after visualization in Chongqing. (The building outline colours in the figure represent different building usage types, blue, green, and red, corresponding to residential, public, and commercial buildings respectively. The plane colours correspond to the different ground cover, green for trees, grey for roads, and black for man-made surfaces.).

For validation purposes, parameters from real urban morphology (extracted from actual observations) were used to compare the results obtained above to calculate the mean absolute difference and CC. These two quantitative indicators are used to reveal the gap between the predicted results and the actual observations, which can reflect the quality of the estimated results. As mentioned before, better estimation results normally reflect a higher CC and a smaller AAD (or percentage AAD value). All the indices of the accuracy statistics (with a spatial resolution of 30m) are shown in Table 3.1. From Table 3.1, it can be seen that all of the estimated results had relatively low-percentage AAD values (below 0.1) compared with the actual observations data and also presented high correlation coefficients (above 0.85) with the actual parameters.

Table 3.1: Statistical Results for the Estimated and Actual Data.

Parameters	***Building footprint***	***Building height***	***Land-cover classification***	***Building usage***
Mean	0.58	60.15	1.79	0,57
CC	0.98	0.93	0.87	0.99
AAD	0.02	4.3	0.09	0.02
Percentage AAD	3%	7%	5%	3%

At the same time, the relationship between estimated data and actual data is more intuitively displayed by generating scatter plots, as shown in Figure 3.17, in which the x-coordinate and y-coordinate represent the estimated morphological parameters and actual morphological parameters respectively. The scatter plots of the extracted building footprint and building height data are shown in Figures 3.17(a) and 3.17(b) respectively. The variables estimated using the open-source geographic-information-based method are similar to the actual morphological

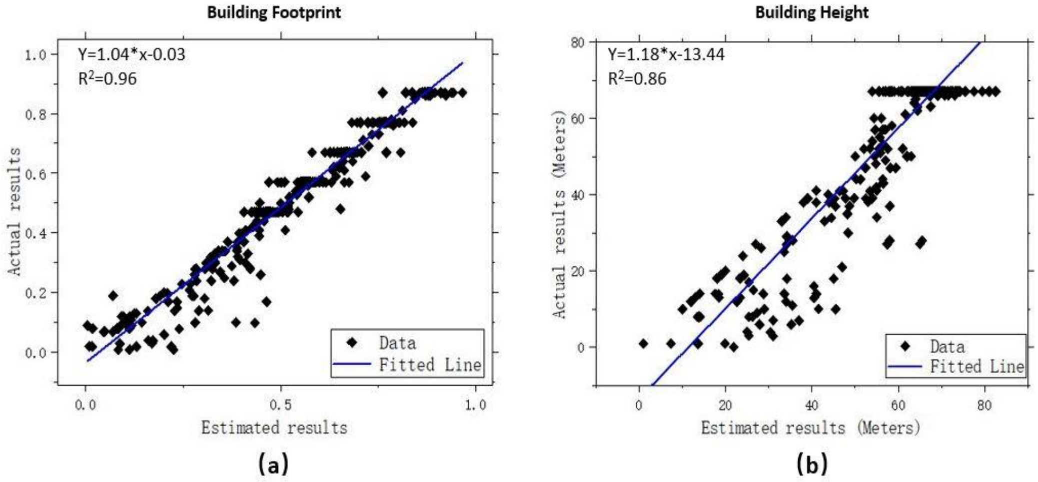

Figure 3.17: Scatter plot of comparison between the actual observed results and the predicted results of building geometric information: (a) Building footprint displayed by coverage ratio; (b) Building height.

information since the data scattering is close to the 1-1 line. The quantitative indices shown in Table 3.1 are consistent with the results shown in the scatterplot.

3.5 Discussion

3.5.1 Building-footprint

Validation of the results based on the above 30m grid shows good agreement between the actual and estimated building footprints with $R^2=0.96$. This also shows that the method can quickly provide building-footprint data for urban climate and urban environment studies, which can be used to calculate building coverage ratios. In addition, since this method uses the secondary image processing method to obtain the building coverage area on the existing map image, the result of the data acquisition is relatively stable. In other words, it is generally not affected by the quality of the input image. For example, when extracting the contour of a building through satellite image recognition, the output may be affected by the presence of vegetation occlusions, etc. However, the original data is provided by the map service API and the reliability of its data will directly affect the output result. Therefore, it is crucial to choose a reliable map service data source.

3.5.2 Building height

The estimated building height has a reasonable relationship with an R^2 value of 0.86 for a grid size of 30m. This also indicates that the method can reliably extract the height data of buildings. Combining the extracted building-height data with the building-footprint data can further calculate urban morphological indices such as building volume density, sky view factor, frontal area index, roughness length, etc. which can provide more useful data support for the study of the urban climate or environment. Additionally, unlike the extraction method for building-footprints, building-height data adopts a method that combines multiple data types and analysis methods. This also largely makes up for the computational deviation brought about by a single data source. Specifically, if only the data from the AW3D30 dataset is used to obtain building heights, the height data of all buildings built after 2010 will be lost. Therefore, the introduction of satellite image recognition calculation can greatly reduce the error caused by the date that the AW3D30 dataset was acquired, since the latest satellite images are relatively easier to obtain. As shown in Figure 3.18, through Google historical satellite imagery, it can be found that the building in the red line area in the selected area 2 in the northern part of Chongqing was built after 2010. The height data of these newly built buildings is lost when directly using the calculated height values from the AW3D30 dataset. However, the data results for this area obtained by the methods used in this study are accurate and complete. This also shows that this method can provide more accurate real-time building-height data.

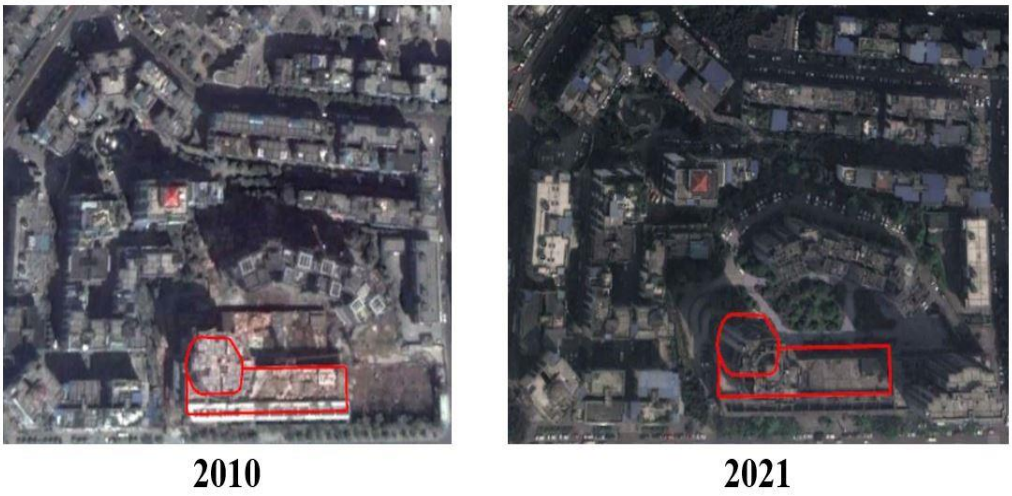

Figure 3.18: Satellite imagery of selected area 2 in the Chongqing case study in 2010 and 2021. Source: Google earth.

3.5.3 Land-cover classification

For the relationship between land cover classification based on actual observations and that based on geographic information data analysis, the CC is 0.87 and AAD is less than 0.1. All results demonstrate a high degree of consistency and can provide support for the division of local climate zones. Like building-height data, the division of land cover types also adopts the method of a comprehensive analysis of diverse types of geographic information data. As with the building height extraction method, the combination of multiple data types can largely eliminate errors caused by the use of a single data point. Therefore, this study achieves efficient land cover classification by combining satellite image recognition with map service data. For example, it is sometimes difficult to separate objects of similar colour through image recognition classification alone. The water bodies (shown as red lines) in case study area 1 (see Figure 3.14) are similar in colour to the vegetation, as shown in Figure 3.19. This has led to the misclassification of this type of water as a vegetated area. However, the occurrence of such errors can be reduced by using the existing map data for auxiliary identification, which has been identified in the map image.

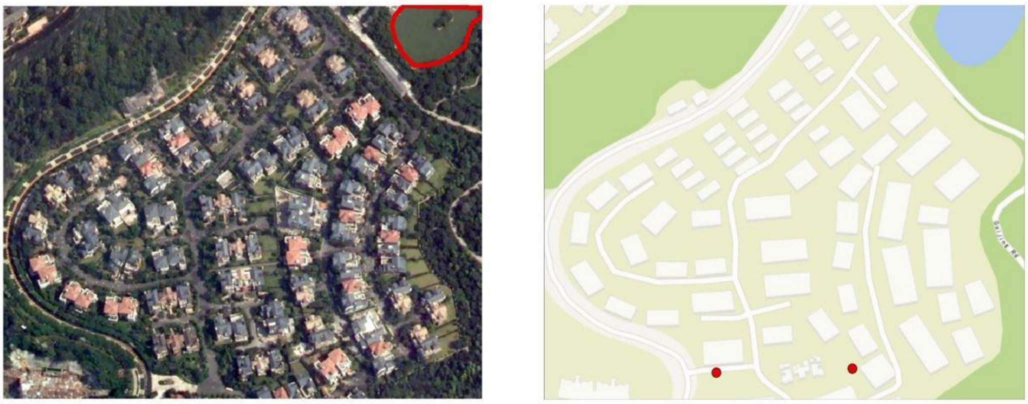

Figure 3.19: Satellite image (right) and map image (left) of selected area 1 in the Chongqing case study.

3.5.4 Types of building

As with all the parameters obtained above, the predicted results of the building usage type and the actual data also show a high degree of consistency, with a Correlation Coefficient (CC) of 0.99. A simple classification of building occupancy types by leveraging POI data that can associate with calculating a building's anthropogenic heat in relation to the urban climate can be obtained. Furthermore, instead of using POI data to calculate zonal functions in the city, this study used the spatial analysis of POI data to classify the usage type of each building. This provides more accurate data support for studies related to the urban environment.

3.5.5 Limitations

Although the newly developed overall urban morphology information extraction method performs well in the validation of the results, it still shows a slight overestimation and underestimation of the results when the method is applied to extract building heights in the study areas. After locating the deviation on maps, it seems that these cases are caused by the position of the satellite when the photo was taken. It is believed that this can be improved by checking the shooting angle of images. More specifically, although this study makes up for the error in the acquisition date of the AW3D30 dataset by introducing image analysis technology, it still fully relies on the acquisition location and quality of satellite images. Since some urban areas have high building densities, the obtained satellite images may sometimes have buildings obscured by other buildings or vegetation due to the shooting angle, which can lead to the failure to extract building edge proportions. All the above findings suggest that future research could consider fine-tuning the methods for handling building edges in satellite images to further improve building height estimation in some specific scenarios, especially since satellite photos were taken from a low angle (which may lead to some features being obscured). At the same time, future research should also focus on testing and validation in more situations, which can make the applicability and practicality of the proposed method clearer.

Additionally, due to the different shooting angles and dates of different satellite images, the colour difference presented by the satellite images may cause a large deviation. Therefore, when using this method to extract classification information of land cover, it is suggested that a small area test based on the input satellite image should take place. It recommends that replacing the input satellite image or retraining the recognition model when there is a large deviation in the results would improve the accuracy.

Finally, roofs are also usually considered an important part of urban form in urban environments research. However, due to the rough spatial resolution of the AW3D30 dataset and the structural characteristics of the raster data, it is currently difficult to accurately represent the geometric shape and coverage type of the roof. Therefore, this study focuses only on the footprint and height of the building.

3.6 Conclusion

To meet the challenges of data acquisition in complex and variable urban surface properties data for urban microclimate simulation, a unique multi-band raster data model has been developed in this chapter. This model combines the raster data model structure and multiple GIS data-source processing technologies to establish a novel urban surface properties dataset. In order to verify the reliability of the proposed model, the data from the field observations were compared one-by-one with the data extracted from the model. The validation results show good comparative results for all data, with correlation coefficient values close to or above 0.9. This indicates that the results of the dataset provided by the model are plausible.

The rasterised and multi-data fusion analysis allows the model to have the following features:

- The newly proposed raster data model can display and store urban surface feature information more concisely and comprehensively. This is mainly due to the raster data structure and the use of multi-source fusion analysis approaches. The multi-band storage structure of the raster data allows the dataset to be easily overlaid with different types of data. The analysis of multi-source data also makes it possible to obtain almost all required basic urban surface information units.
- A new way of updating data allows the model to provide information about the surface of the city that is closer to the real situation. This is due to the combination of image analysis methods and multi-source geographic

information data analysis. Real-time satellite imagery provides a realistic picture of the ground surface, while the database provides baseline data. This combination effectively reduces data analysis time and increases analytical accuracy.

- The model is also a low-cost means of accessing urban surface property data. This low-cost feature is largely attributed to the use of fully open-source data.
- This new model provides a systematic and uniform data format for building a complete raster model of urban surface properties. This allows the model's output to be used subsequently to save more time in data pre-processing.

Overall, the model is expected to provide comprehensive and reliable data on urban surface properties in an efficient and convenient way for urban climate studies, especially urban climate simulations.

Although the rasterized spatial data display method leads to a certain degree of ambiguous spatial data characteristics (without a clear boundary of objects), the data performance of this method is still more conducive to the representation of local/mesoscale urban characteristics and climate simulation. First of all, the error brought by the high-resolution raster data model is very small and can be ignored. Secondly, the multi-band storage raster format can be a more systematic and efficient way to store and recall the required urban surface information. Additionally, raster data has fixed pixel locations, which makes it possible to effectively mimic and analyse urban climate in computational algorithms (See Chapter 4 for details). These overall improvements provide the basic data structure framework for subsequent efficient and practical urban climate simulation schemes.

The new urban surface model acquisition and representation scheme succeeded in simplifying the process of describing surface properties and in including basic surface property information. Nevertheless, it is still impossible to cover all urban geometry and morphology information. According to different research needs, some parameters still need to be obtained by researchers/users separately. However, it is also possible to integrate these individual parameters through the proposed raster data model. A more complete presentation of the urban environment and even the interior spaces, may be considered beneficial in the future.

Chapter 4

A Novel 2.5D-Based Radiation Simulation Model

4.1 Introduction

Solar radiation is the most important factor in driving the near-surface urban climate. In a city, dynamic patterns of light and shadow in outdoor spaces are a prominent feature in situations where the sun's rays are blocked by obstacles such as buildings and trees. When it is hot, pedestrians usually choose to walk in the shade rather than on the sunny side of the street, and *vice versa*. The mutual shade provided by buildings is therefore a useful urban feature in areas with hot climates. Conversely, in many places, homeowners fight hard for their access to sunlight, which may be enshrined in local design regulations (Hraška, 2019).

However, what is not actually visible but equally important is the exchange of infrared radiation between the urban façade, the plane and the atmosphere. At some points in urban street valleys, the Sky View Factor (SVF) is reduced by the shadow of buildings or vegetation. This usually results in changes in the relative amounts of diffuse solar radiation and thermal infrared radiation received from the sky and by surrounding buildings. These phenomena show that the surface structure, the orientation of objects towards the sun and sky, and the radiative properties of the surface cannot be ignored in order to understand urban radiation exchange. In detail, the shadowing effects of buildings and the urban surface albedo can reduce the amount of solar radiation received by the Urban Canopy Layer (UCL). The urban structure and the composition of the surface material determine the amount of attenuation. Current studies have all shown that in urban areas where building facades are dominated by glass curtain walls and high-rise buildings are concentrated, the amount of solar radiation reaching the urban surface is low (Khodakarami and Ghobadi, 2016). Take Hong Kong, China, as an example, its solar irradiance is influenced by sky view factors due to dense, towering buildings that block some of the incoming solar radiation (Yuan *et al.*, 2020). The same problem occurs in other areas such as Dhaka (Kakon and Nobuo, 2009). At the same time, an increase in the urban heat island (UHI) or amplification of pollutants is also accompanied by an increase in incoming long-wave radiation (Oke, 1981).

The reflected radiation is also a crucial factor in the radiation balance of a city. This mainly includes multiple reflections between canopy walls and diffuse reflections from roof walls and roads. Generally speaking, albedo values are lower in urban areas than in rural areas due to differences in the radiative and thermal properties of the building materials used. The radiation balance can also be affected by snowfall, which is mainly seen in the winter months in mid and high latitudes (Grenfell *et al.*, 1994).

In short, the increase in urban energy may be caused by lower urban surface albedo and higher long-wave radiation. Conversely, the shading and attenuation of air pollutants can reduce solar radiation and hence urban energy concentrations. Undoubtedly, in the urban radiation environment, parameters such as direct solar energy distribution, scattered energy distribution, long-wave radiation, reflected radiation, underlying surface material distribution, the building-structure and sunshine hours distribution all directly affect the distribution of outdoor radiation within the built environment.

Thus, one of the most fundamental tools for architects, urban planners and landscape designers to optimize microclimates is the management of radiation exchange through architecture and landscape design. It is important to note that the design-specific parameters of the building (e.g., height and geometry) are defined by the designer at an early design stage. For a building-scale design, designers can combine their intuition and experience with widely available simulation tools and software (ranging from simple early design stage indicators to complex later operation and maintenance stages) to better manage radiation exchange conditions for a single building (Beckers and Rodríguez, 2009; Bragança, Vieira and Andrade, 2014; Méndez Echenagucia *et al.*, 2015; Negendahl, 2015; Kamari, Kotula and Schultz, 2022). In contrast, for larger scales such as a neighbourhood, the situation becomes quite different, as the variability of neighbourhood morphologies greatly increases the complexity of design parameters. This also makes it necessary for building designers to use simulation software in order to manage neighbourhood-wide radiant heat exchange at an early design stage. Nevertheless, Nault *et al.* (2015) state that although more models and tools are available to assess radiation within a neighbourhood, they are still not up to the task of working in the early design phase.

4.1.1 Existing numerical models for environmental radiation simulation within building complexes

The impact of urban form on the potential for solar energy access has been studied previously with different focuses. In this study, the focus will be on existing models for neighbourhood assessment of solar radiation, which are more applicable to earlier radiation-related design assessments. In simple terms, the current solar radiation simulation methods used at the neighbourhood scale can be divided into three types according to the way in which building models are established. The three methods available for solar radiation analysis are as follows: (1) by coupling 3D building models generated from CAD files; (2) by combining a Geographic Information System (GIS) and 3D Models and (3) by utilizing Digital Elevation Models (DEMs) based on GIS.

For the comprehensive and accurate simulation in neighbourhoods, applying 3D urban models produced from CAD files to achieve 3D solar radiation analysis has been explored by many researchers. Compagnon (2004) proposed a method for quantifying the active and passive solar heating, photovoltaic power generation and daylighting potential of facades and roofs located in urban areas based on the RADIANCE lighting simulation model. TOWNSCOPE is a tool derived from the POLIS project to support solar access decision-making from a sustainable built environment perspective (Teller and Azar, 2001). This tool combines a 3D city information system and a solar energy assessment model to construct a computer system for solar access visualization or assessment purposes in urban areas. SOLENE is another numerical model that can be used to simulate natural light and solar radiation in urban forms and interior spaces (Miguet and Groleau, 2002). It is a finite element-based 3D model that integrates multiple calculation modules for taking into account the solar, luminous or thermal effects between urban forms and their environmental and climatic dimensions. In addition, there are some systems that also use 3D models combined with several novel algorithms to simulate and evaluate the incidence of the sun in a city. Mardaljevic and Rylatt (2003) proposed a method for generating accurate building surface irradiance maps in urban contexts using sophisticated modelling based on a physically-based rendering approach, the output of which can be presented directly to planners and designers for detailed analysis. Carneiro (2011) mentioned a radiation simulation method using 3D city models involving pre-existing façade models and performing separate calculations only for the vertical faces. Erdélyi *et al.* (2014) refer to an approach for a three-dimensional SOlar RAdiation Model (SORAM) to assess the potential direct and diffuse solar radiation concentrated at a point location in an urban area. Nevertheless, it will be difficult for those models to provide effective assistance for strategic urban planning mainly because of the computing power they require. All of the above models are time consuming when applied to a group of buildings within a neighbourhood. The time they take makes their application in real production projects impracticable, especially in the early design phase when the need is for quick multi-scene comparisons.

To optimise the computing power requirements, some studies started to combine the 3D model with a Geographic Information System (GIS) to provide an efficient urban area solar energy access simulation with superior spatial analysis capability. Similarly, Redweik *et al.* (2013) explained a method to estimate solar potential in urban environments by estimating building shadow maps and facade shadow maps, as well as sky view factor maps and facade sky view factors based on Lidar data. Similarly, Chow *et al.* (2014) and Desthieux *et al.* (2018) applied 3D cadastral data in GIS to implement tools for assessing the potential of solar energy in developing smart net-zero energy communities with fine spatial resolution and evaluating the solar radiation of downtown building roofs and vertical facades, respectively. Indeed, with the help of the spatial information processing capability of GIS, the computational efficiency of solar radiation simulations is greatly improved. However, they are still not competent to assess radiation-related neighbourhood design in the early design phase. This is due to their lack of flexibility in the actual simulation process. Their simulation of a case requires a lot of time for the pre-modelling of the built environment. This prevents these models from enabling flexible multi-scene comparison tasks, which are most needed in the early design stages.

Other studies have tried to use the 2.5D digital elevation model (DEM) model in GIS to simulate the solar radiation within the built environment. Moreover, the application of ArcGIS Solar Analyst (Fu and Rich, 1999) and the GRASS r.sun (Hofierka and Súri, 2002) models is the most typical example. These models work on raster-based geographic information layers and were originally designed for neighbourhood radiant energy assessments. However, as the accuracy of geographic information continues to improve, they have also been successfully used to assess solar energy potential in urban environments (Hofierka and Kaňuk, 2009; Nguyen and Pearce, 2012) and the potential of urban canopies based on roof geometry (Brito *et al.*, 2012). Unfortunately, since 2.5D models store information based on planes, these models ignore solar radiation to the vertical façade. Therefore, Mahmoud *et al.* (2019) proposed a façade solar radiation analysis based on a 2.5D model, which is still too simplistic due to the lack of interaction between the plane and the façade. Although the simulation method of the 2.5D model can maximize the computational power, the rough simulation results limit the scope of its application. For instance, these methods are not applicable when the effect of vertical planes needs to be considered. This also prevents them from being used in the early design stages of neighbourhoods, even though they can quickly provide comparative results for scenarios. This is because they do not provide enough reference information for designers.

In general, current 3D, model-based, neighbourhood-level, solar radiation distribution analysis is complex, either through CAD files or GIS platform simulations. As Ekici and Aksoy (2009) pointed out, "most programs are oriented to analysis and not to design. Thus, they are mainly used at the final step of the project, when the principal ideas are already defined, and all their possibilities are not apprehended". Therefore, these tools do not provide flexible usage paths in real-world circumstances. For example, in the early stages of design, it provides rapid strategy comparison analysis to optimize the initial design or provides rapid assessment/analysis in the urban renewal stage to effectively implement the defects of the existing urban design. Although the simulation method based on 2.5D is more practical, the output lacks detailed information. For instance, most of the calculations of DEM models solve the problem of solar incident radiation distribution on the horizontal plane of the building complex but do not solve the solar radiation distribution on the vertical plane of the building. The 2.5D-based approach is also inadequate for the task of strategic planning of solar radiation at the community scale. This study, therefore, advocates the development of a flexible and rapid method for assessing solar potential in the neighbourhood built environment in order to assist in the early design phase.

To achieve such a method, this chapter proposes a raster operations-based method for solar radiation analysis for the neighbourhood built environment. The introduction of raster analysis can improve the effectiveness of the model's operations by applying a special algorithm, which will be described later. Furthermore, the rasterised representation allows more flexible modelling of the urban environment, as described in Chapter 3. Thus, by introducing raster operations, the model is: (1) an enhanced 2.5D-based model for neighbourhood-scale solar radiation analysis; (2) a fast and relatively detailed simulation method for outdoor solar radiation distribution at neighbourhood scales and (3) a more flexible and practical simulation method for mimicking radiation conditions in different urban environments. The model is expected to assist in strategic urban planning by improving the urban climate model during the early design/renewal phase and allowing it to be more effectively integrated with urban surface climate models for rapid design optimization and problem-solving.

4.2 A novel radiation simulation based on raster analysis

After rasterising the urban surface properties in Chapter 3, the raster data operations

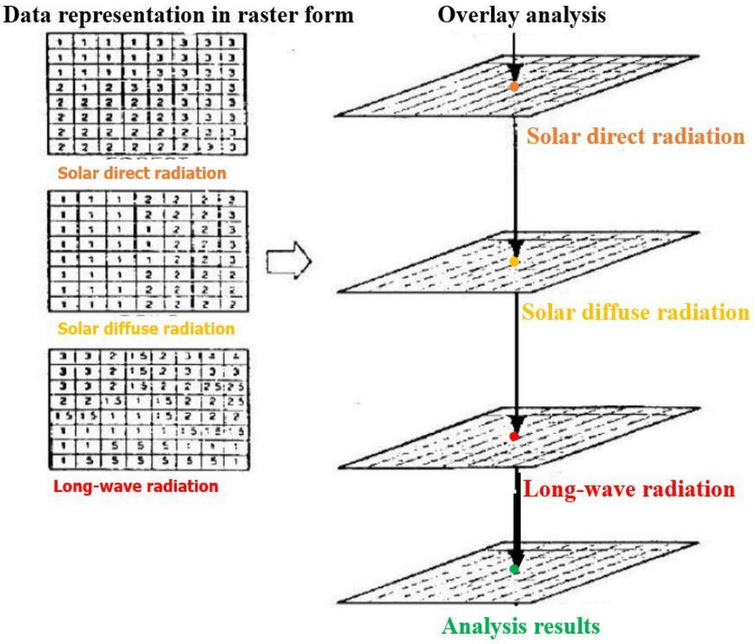

Figure 4.1: Schematic diagram of raster data overlay analysis. (Each layer in the diagram represents a different data type. They form new analyses by superimposing them together.).

method can be applied for simulating the radiation distribution in building groups. The calculation of all physical processes can be realised by means of a map overlay algorithm of raster data based on four basic arithmetic operations, Boolean operations, and complex function operations. As mentioned in the previous chapter, raster datasets can be composed of different data types. Specifically, a raster dataset can have different layers e.g., solar direct radiation, diffuse radiation and shadow maps. By superimposing these different data and assigning a certain weighting algorithm or function, the corresponding analysis results can be obtained, as shown in Figure 4.1. Therefore, the method of analysis of the urban environment can also be used as a reference to obtain the corresponding analysis results by superimposing different urban information layers. The most basic overlay analysis uses point-to-point overlay, which means that only phase metadata for the same location will be overlaid, as shown in Figure 4.1. As mentioned above, the superposition process of raster data allows the performance of not only simple addition and subtraction but also functions and logical operations. This is the most obvious advantage of raster computing in the analysis of environmental and surface problems. It is no longer necessary to re-match the data to be associated by traversal or encoding. Different data can be connected simply by their location. Therefore, the parameters used in the radiation model are also connected in this way in this study. The following is the introduction to the principle of overlay analysis of raster data used for this study and how it is connected with the radiation model, which is the most important method of raster data processing in the proposed model.

4.2.1 Raster data analysis operations

The raster data model uses a regular grid to cover the entire space. Each cell value of the grid corresponds to the characteristics of the spatial phenomenon at that cell location. This simple data structure with fixed cell locations is not only computationally efficient but can also be applied to a variety of data analyses. Therefore, raster data is often used in computationally intensive GIS projects, which also provides a usable framework for efficient urban climate simulations.

Unlike vector data analysis, which is based on point, line and polygon geometric objects, raster data analysis is based on raster cells and grids. Thus, raster data analysis can be performed at different levels at individual cells, groups of cells, or all cells in the entire raster. Some raster operations use a single raster layer, while others use two or more raster layers. Additionally, pixel data types need to be considered in raster data analysis. For example, whether raster data is analysed as numeric or categorical values. Various types of data are stored in a raster format (See Chapter 3). However, the operation of raster data analysis needs to be selected according to the raster data type. Therefore, this chapter creates a new built environment radiation analysis model based on the raster dataset established in Chapter 3. The raster data analysis operations used in this research will be introduced in the following:

(1) Data analysis environment

Since two or more raster layers may be involved, raster operations need to define the data analysis environment by specifying its area extent or output cell size, where the extent of the area used for analysis is the specified grid or an area defined by the minimum and maximum x, y coordinates. In addition, it may be an area generated by overlapping multiple raster layers. The size of the output cells is another essential element of the analysis environment. In general, the output cell size is set to be equal to, or larger than, the largest cell in the input raster. This is consistent with the rationale that the output resolution corresponds to the lowest resolution of the input raster. Since this research has established a unified raster dataset in Chapter 3, the analysis environment of the data has been unified. The default analysis area is the area contained in the satellite image and the output unit size is 1m. In actual analysis, users can also adjust the area according to their own needs.

(2) Local operation

Local operation is a pixel-by-pixel operation that establishes the core of raster data analysis. Local operations generate a new raster layer from single or multiple input raster layers. The cell value of the new raster layer can be calculated by the relationship function between the input and output raster layers or assigned by the classification table. This is also the main raster operation used in this study to build the physical model for climate simulation. The different physical parameters are represented by a single layer of data and these layers are then connected according to physical formulas by means of local operations. This is consistent with the process illustrated in Figure 4.1. The procedure and rules for this operation are as follows:

Local operations on a single raster layer:

Assuming that a single raster is used as the source data, based on the cell value of the input raster, the local operation calculates the value of each cell of the output raster through the spatial function. Therefore, the values of the input raster and the output raster have a one-to-one correspondence in space. As shown in Table 4.1, the local operation of raster data based on the GIS platform usually includes basic mathematical algorithms.

Table 4.1: Arithmetic functions used in local operations and examples of their operation statements.

Algorithm	***Calculating signs***
Count	+, -, *, /, abs, int, float
Logarithm	exp, log
Trigonometric function	sin, cos, tan, arcsin, arccos, arctan
Power function	pow, sqrt

For example, multiplying the value in the original raster data by 2 to get a new numeric raster is a simple local operation. It performs a uniform calculation for each pixel using the basic multiplication rule. As shown in Figure 4.2, to convert raster data A from original data to doubled data B can use an expression like: $Raster\ B = Raster\ A * 2$. Such operations are important for processing individual physical parameter data cases. For example, data pre-processing in which all physical parameter values are retained to two decimal places.

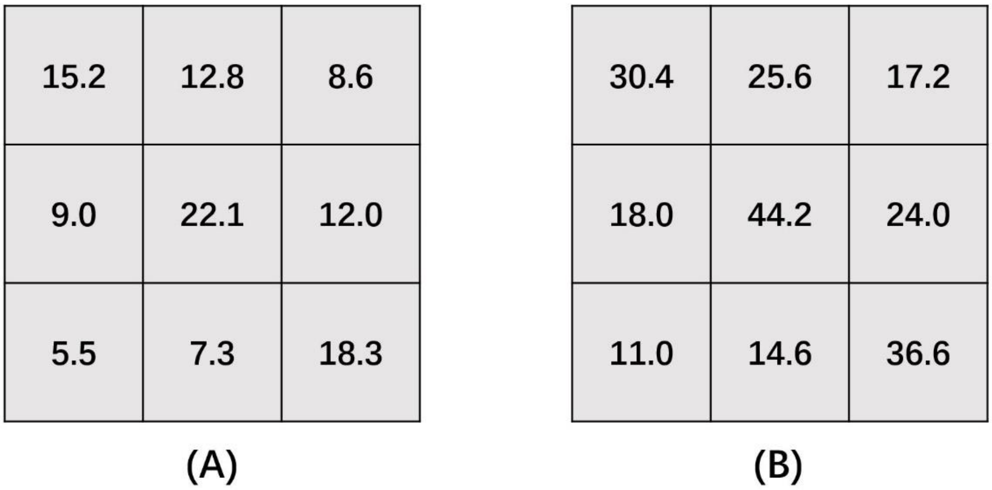

15.2	12.8	8.6
9.0	22.1	12.0
5.5	7.3	18.3

(A)

30.4	25.6	17.2
18.0	44.2	24.0
11.0	14.6	36.6

(B)

Figure 4.2: Basic multiplication operations from data A to data B with double values based on local operations.

Reclassification:

Reclassification is a local operation method that generates the new raster data by classification. There are two methods of reclassification. The first method is to change the one-to-one correspondence. For example, in the output raster, assign a value of 1 to the forest land cell in the land use type raster. The second method is to assign new values to a range of cell values in the input raster. For example, when analysing the building elevation raster in the city, the value of the building cell over 100 meters is assigned 1 and the others are assigned 2. The classification principles of these two methods are shown in Figure 4.3. Integer raster data can be reclassified by either of the above two methods, but floating-point raster data can only be reclassified by the second method.

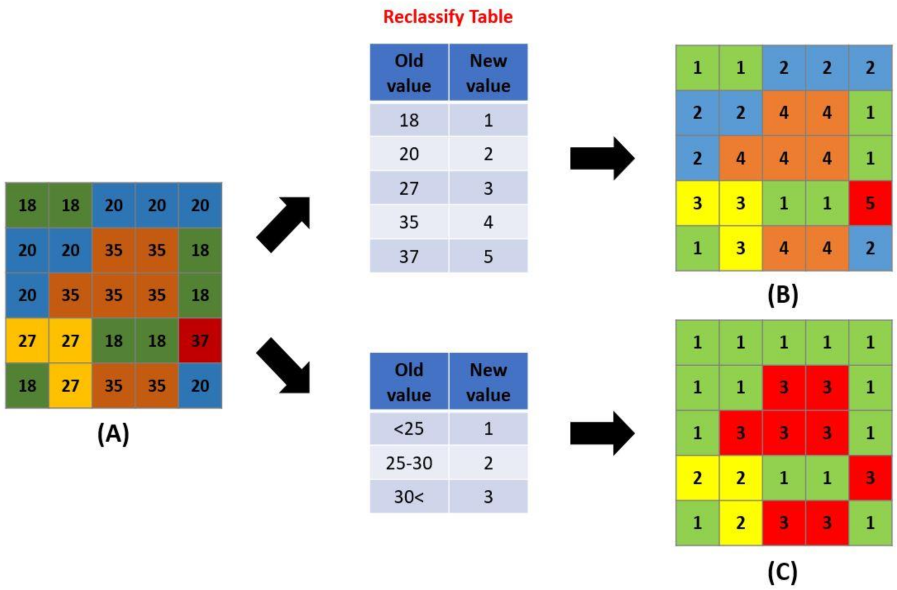

18	18	20	20	20
20	20	35	35	18
20	35	35	35	18
27	27	18	18	37
18	27	35	35	20

(A)

Reclassify Table

Old value	New value
18	1
20	2
27	3
35	4
37	5

1	1	2	2	2
2	2	4	4	1
2	4	4	4	1
3	3	1	1	5
1	3	4	4	2

(B)

Old value	New value
<25	1
25-30	2
30<	3

1	1	1	1	1
1	1	3	3	1
1	3	3	3	1
2	2	1	1	3
1	2	3	3	1

(C)

Figure 4.3: Two methods of reclassification based on local operations. Data A to data B represents one to one change; Data A to data C represents a range of cells change.

Reclassifying a raster typically serves three purposes. Firstly, it is designed to create simplified raster data. For example, raster data can use 1 to represent an elevation of 0-30 meters, use 2 to represent an elevation of 30-60 meters, and so on, to replace a series of continuous elevation values. The second produces a new raster containing unique categories or values, such as extracting building pixel blocks with a height of 30-100 meters. The third produces a new raster representing the sorted results of the input raster's cell values. For example, reclassification results can represent a suitability ranking of 1-5, with 1 being the most suitable and 5 being the least suitable. Nevertheless, in this study, the one-to-one classification method of reclassification was mainly applied. This operation is also mainly used for data pre-processing. In this study, the corresponding physical parameter raster data layer was produced by reclassifying different surface classifications. In this way, the input database for the numerical simulation can be quickly created. It can also be used directly in subsequent calls to complete the calculation in the overlay method. It should be noted that the anthropogenic heat calculation set up in Chapter 5 utilises the same approach.

Local operations on multiple raster layers:

The local operation of multiple raster layers involves operations such as compositing, overlaying or superimposing. Since operations can be performed with multiple raster layers, local operations are equivalent to vector-based, layer overlay, operations.

Many local operations use multiple input raster layers simultaneously instead of just a single input raster layer. In addition to the numerical operations available on individual raster layers, other metrics based on the input raster pixel values or their frequencies can also be stored in the output raster. However, some of these metrics are limited to the raster of numerical data.

Statistics such as maximum, minimum, range, sum, mean, median and standard deviation are all metrics applied to a numeric raster. For example, Figure 4.4 shows an example of a local operation that calculates the average of three input raster layers. In Figure 4.4, it averages the values in layers A, B and C to form layer D. Fig 4.4 shows that the local overlay operation for raster layers is very specific with

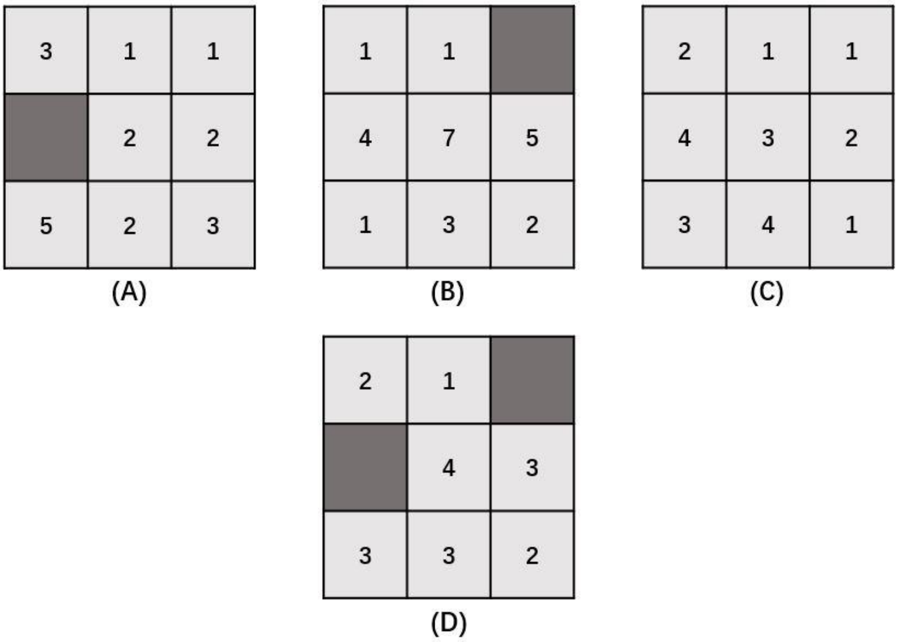

3	1	1
▨	2	2
5	2	3

(A)

1	1	▨
4	7	5
1	3	2

(B)

2	1	1
4	3	2
3	4	1

(C)

2	1	▨
▨	4	3
3	3	2

(D)

Figure 4.4: The cell in (D) is the average value calculated by the local operation of the 3 input raster layers (A, B and C), where the dark grey cell has no data.

the calculation based on the position of the cells in the raster data. For example, the number in the top-left corner of raster data D is obtained by averaging the numbers in the top-left corners of the three layers A, B and C. The data in the other grids correspond to each other in the same way. Additionally, due to the special rules of raster data operations, if a cell in the input raster has no data, the cell in the output raster also has no data.

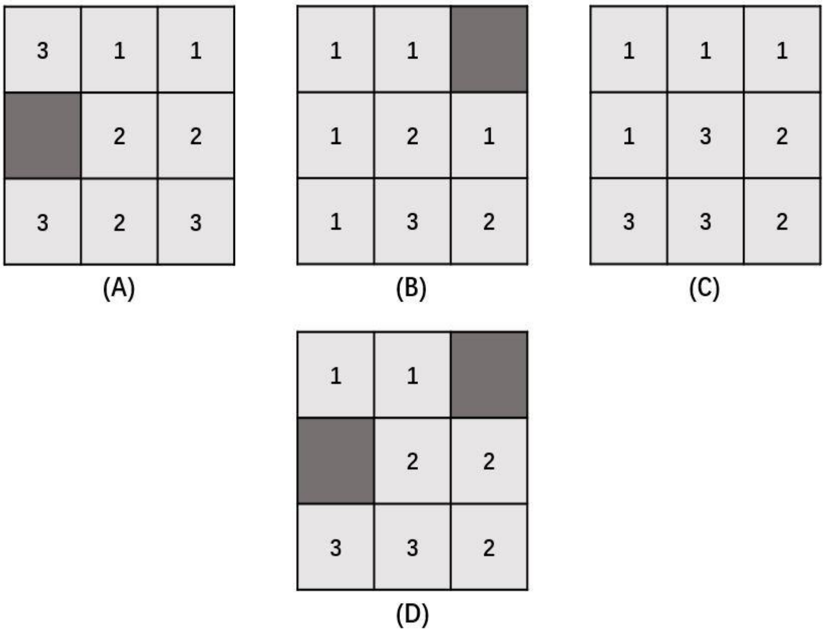

Figure 4.5: The cell in (D) is the majority of statistical values calculated by the local operation of the 3 input raster layers (A, B and C), where the dark grey cell has no data.

Other metrics are suitable for numerical or categorical raster data, e.g., statistical values such as majority, minority and the number of unique values. The majority represents the pixel value with the highest output frequency, the minority represents the pixel value with the lowest output frequency and the categorical raster outputs the number of different pixel values. For example, Figure 4.5 shows the output raster for the mode statistics obtained from the 3 input raster layers. The data in Figure 4.5 and the data in Figure 4.4 have the same rule of correspondence between the image elements in the operation. They differ only by the use of different algorithms. Figure 4.4 shows the average of the three raster data layers, while Figure 4.5 shows the majority of the three raster data layers. Therefore, in this study, the local operation on multi-layer raster data is the main approach used to connect the different physical parameters and build a numerical simulation model based on raster data operations. It sets different physical parameters to different raster data layers. The different physical parameter raster layers are then connected in a similar way, as in Figures 4.4 and 4.5, according to the required physical algorithms. This constitutes the most basic numerical model for the study based on raster operations. In addition, other operations still exist for raster data and they were also used in this study. However, due to the characteristics of these algorithms, they are only used to a small extent for some specific data analysis processes. In general, the local raster operation is the most basic operation for building this model.

(3) Neighbourhood operation

Neighbourhood operations, sometimes called focus operations, involve a focus cell and a set of surrounding cells. Surrounding cells are selected by their distance and

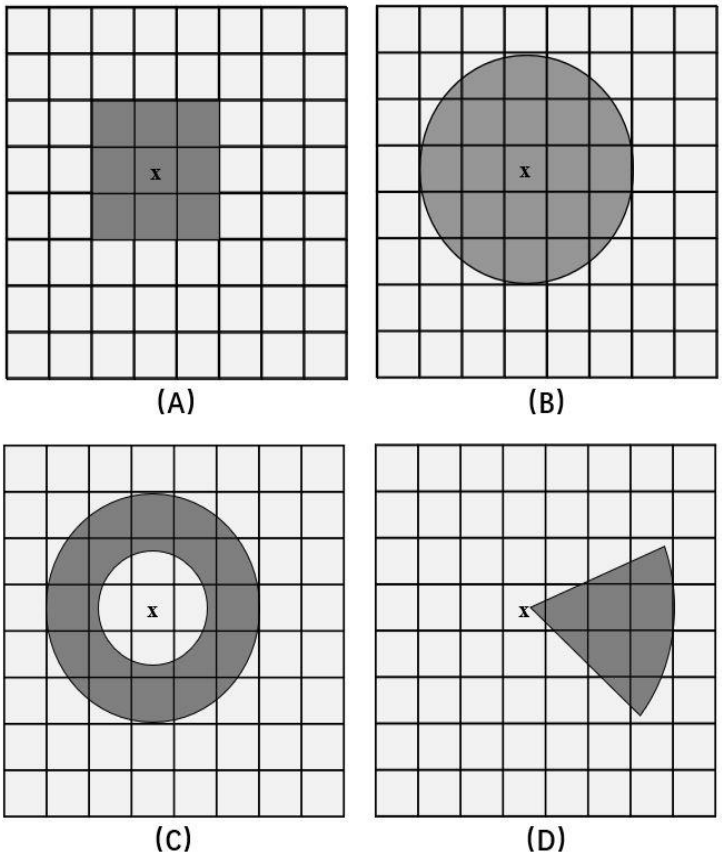

Figure 4.6: Four common neighbourhood types: rectangle (A), circle (B), ring (C) and wedge (D), where x is the focus pixel.

directional relationship to the focus cell. A required parameter of the neighbourhood operation is the neighbourhood type. Neighbourhood types generally include rectangles, circles, rings and wedges (Figure 4.6). A rectangular neighbourhood is defined by width and height in units of cells, such as a 3×3 window centred on the focal cell. A circular neighbourhood takes the focal cell as the centre and extends outward with a specified radius. A ring or donut-shaped neighbourhood consists of a circular area enclosed by a small circle and a large circle both centred on the focal cell. A wedge-shaped neighbourhood is a sector of a circle centred at the focus cell. As shown in Figure 4.6, within the defined neighbourhood, some pixels are only partially covered. In this regard, the general processing principle is: if the centre of the pixel is in the neighbourhood, then include it. In addition, according to some studies on data analysis requirements, special irregular neighbourhoods have also been proposed (Guan and Clarke, 2010).

Neighbourhood operations usually use the pixel values in the area to calculate and then assign the calculated value to the focal pixel. To complete a neighbourhood operation on a raster, it is necessary to move the focus cell from one cell to another until all cells have been visited. The GIS software has also designed different rules to deal with a focal pixel at the edge of the grid, which are not applicable to the 3*3 rectangular neighbourhood. Although the neighbourhood operation is performed on a single raster, its processing is similar to the local operation on multiple raster data. The difference is that the neighbourhood operation uses the cell values from the defined neighbourhood, rather than cell values from another raster data. From the output raster, the results obtained by the neighbourhood operation can be statistical values such as minimum value, maximum value, value range, sum, average value, median value, standard deviation, etc., as well as the values of metrics such as the majority, minority and a number of categories. These statistics and metrics are the same as the multiple raster local operation. Block operation is a neighbourhood operation using rectangles (blocks). It assigns the resulting value to all block cells in the output raster. Therefore, block operations differ from normal neighbourhood operations in that the operation does not move from cell to cell, but from block to block.

Neighbourhood operations are mainly used in data simplification, image processing and terrain analysis. In this study, neighbourhood operations are mainly used in terrain analysis to calculate specific urban morphological parameters which will be used as parameters to describe the surface characteristics of the city to cooperate with the simulation of the urban climate. See below for specific applications.

(4) Zonal operation

Zonal operations are used to process groupings of cells of the same value or similar features. These groups are called a zone. Zones can be contiguous or non-contiguous. Contiguous zones contain cells that are spatially connected, while non-contiguous zones contain separated regions of cells. A watershed raster is an example of a continuous zone where cells belonging to the same watershed are spatially connected. A land use raster is an example of a non-contiguous zone, where one type of land use can appear in different regions of the raster.

Zonal operations can operate on one or two raster layers. For a single input raster, the zonal operation measures the geometric characteristics of each zone, such as area, perimeter, thickness and centre of gravity. The area is the product of the number of cells in the zone and the cell size. The perimeter of a contiguous zone is the length of its boundary, while the perimeter of a discontinuous zone is the sum of the lengths of each part. Thickness is calculated as the radius of the largest circle that can be drawn within each zone. The centroid is the geometric centre of the zone, that is, the intersection of the major and minor axes of the ellipse that best matches the zone.

When given two raster layers (an input raster and a zonal raster), it is required to perform a zonal operation on the input raster within the area of the zonal raster to generate an output raster. The output raster summarizes the cell values of the input raster for each zone of the zonal raster. Summary statistical metrics include area, minimum, maximum, sum, range, mean, standard deviation, median, majority, minority and the number of species (if the input raster is a floating-point raster, the last 4 metrics are not available). Figure 4.7 shows the zonal operation process for calculating the average by zone. Figure 4.7 (A) is the zonal raster with regions, Figure 4.7 (B) is the input raster and Figure 4.7 (C) is the output raster. Take the grid labelled 1 in Figure 4.7 (B) as an example, it corresponds in position to the four smaller grids in the upper left corner of 4.7 (A) (the first two grids in the first row counting from left to right and the first two grids in the second-row counting from left to right). The grid value in the top left corner of Figure 4.7(C) is then the average of the four values circled by grid 1 of 4.7(B) in 4.7(A). This is the basic principle

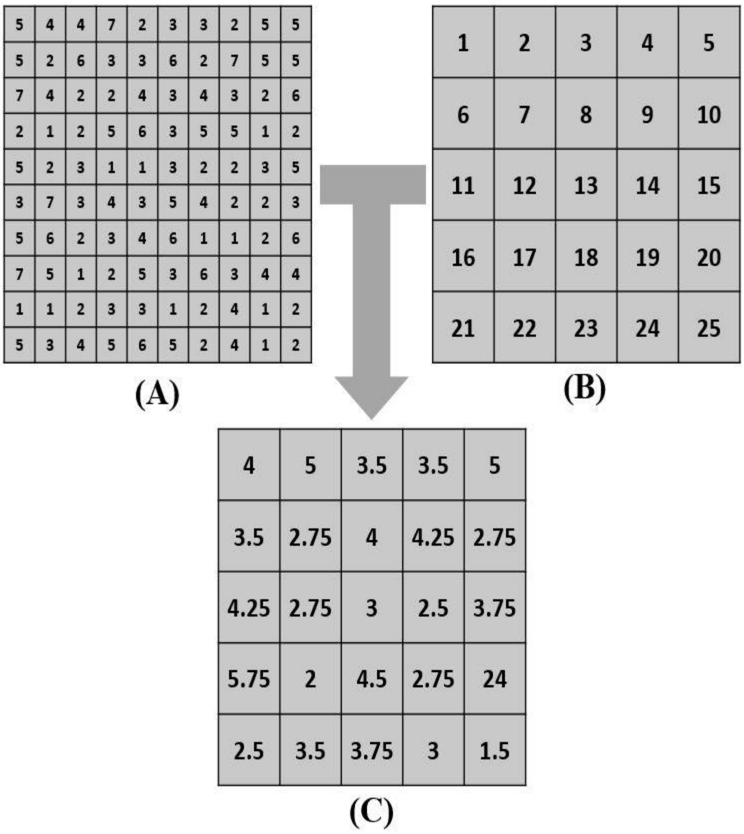

5	4	4	7	2	3	3	2	5	5
5	2	6	3	3	6	2	7	5	5
7	4	2	2	4	3	4	3	2	6
2	1	2	5	6	3	5	5	1	2
5	2	3	1	1	3	2	2	3	5
3	7	3	4	3	5	4	2	2	3
5	6	2	3	4	6	1	1	2	6
7	5	1	2	5	3	6	3	4	4
1	1	2	3	3	1	2	4	1	2
5	3	4	5	6	5	2	4	1	2

(A)

1	2	3	4	5
6	7	8	9	10
11	12	13	14	15
16	17	18	19	20
21	22	23	24	25

(B)

4	5	3.5	3.5	5
3.5	2.75	4	4.25	2.75
4.25	2.75	3	2.5	3.75
5.75	2	4.5	2.75	24
2.5	3.5	3.75	3	1.5

(C)

Figure 4.7: The cell value in data C is the average value of the zonal operation by input raster A and zonal raster B. e.g., 4 is the mean of (2, 4, 5, 5) for zone 1.

of zonal raster operations, where a range of raster data values is targeted by a zonal grid (i.e., 4.7(B)) for a particular calculation. In contrast to the one-to-one correspondence in local operations, each grid in Figure 4.7(B) corresponds to the four smaller grids in 4.7(A).

The zonal operation of two raster layers yields descriptive statistics for comparison purposes. For example, to compare surface temperature characteristics of different surface albedos, a classified raster containing vegetation, bare soil and artificial surface types can be used as the zonal raster and a raster of surface temperature or urban heat island intensity can be used as the input raster. Through a series of zonal operations, the surface temperature or urban heat island intensity characteristics of various surface albedo types can be summarised. In this study, the classification of partition operations is also used to show the advantages of features. In part of the simulation operation, the zonal operation is used to simplify the amount of operational data while retaining the regional characteristic parameters. For example, when counting the impact of reflected radiation on the surrounding environment within a certain area, the zonal raster operation can be used to effectively partition the calculation area and obtain results for a specific area. The specific application process is mentioned in the construction of the physical model.

(5) Physical distance measure operation

In GIS operations, distance can be expressed as physical distance and cost distance. Physical distance measures the straight-line distance or Euclidean distance, while cost distance measures the cost of traversing the physical distance. The distinction between these two distance measurements is important for practical applications. For example, taxi drivers are more interested in the time and fuel consumption to traverse a route than in its natural distance. In this case, the expended distance is not only related to the physical distance, but also to the speed limit and road conditions. Since this research mainly involves the analysis of urban structure, it focuses on the measurement of physical distance.

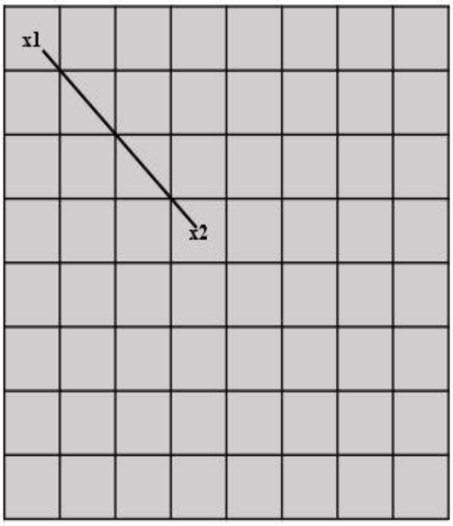

Figure 4.8: Straight line distance measures the distance from the centre of one cell to the centre of another. This figure represents the straight-line distance between cells (1, 1) and (4, 4).

The physical distance measure operation calculates the straight-line distance from the source cell. For example, in Figure 4.8, the distance formula can be used to obtain the distance between cells (1, 1) and (4, 4). In addition to calculating straight-line distances, physical distance measure operations can also generate allocation and direction raster data (see Figure 4.9). The cell value of the allocation raster corresponds to the source cell closest to the target cell. The cell value in the

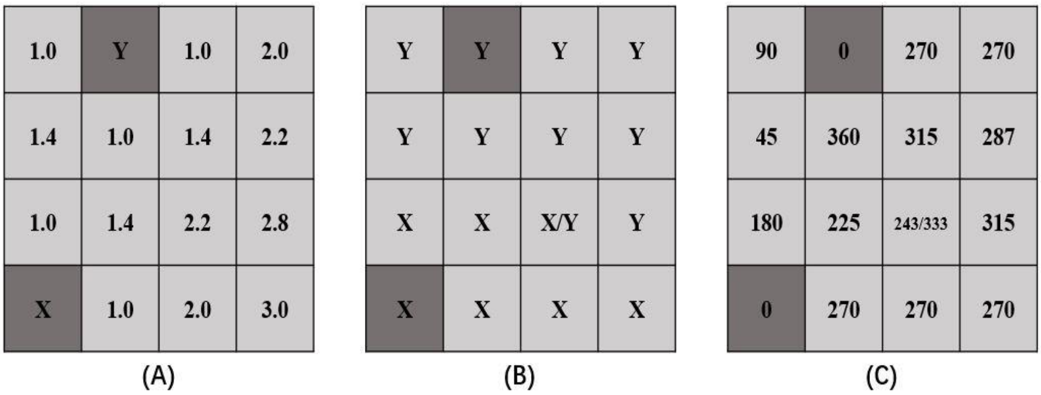

1.0	Y	1.0	2.0
1.4	1.0	1.4	2.2
1.0	1.4	2.2	2.8
X	1.0	2.0	3.0

(A)

Y	Y	Y	Y
Y	Y	Y	Y
X	X	X/Y	Y
X	X	X	X

(B)

90	0	270	270
45	360	315	287
180	225	243/333	315
0	270	270	270

(C)

Figure 4.9: Based on the source cells marked X and Y in the figure (X and Y are specific values in the actual calculation), (A) represents the natural distance measurement (in units of 1) of each cell to the nearest source cell; (B) represents the allocation between each cell and the nearest source cell; (C) represents the direction (in degrees) of each cell to the nearest source cell. The cell in row 3 and column 3 is equidistant from both source cells, so this cell can be assigned to either source cell.

direction raster corresponds to the direction value (in degrees) of its closest source cell. The direction value is based on the compass direction: 90°- east, 180°- south, 270°- west and 360°- north (0° is reserved for source cells).

Similar to building buffers around vector features, physical distance measure operations are widely used. For example, they can create equally spaced partitions from a river network or regional fault line map. In this study, they focus on the calculation of the direction allocation to analyse the urban DEM further. By analysing the orientation characteristics of each representative elevation value in the DEM, the orientation and position of the walls of different buildings can be determined. Practical applications and algorithms are shown in model-building.

(6) Map algebra

Map algebra is an informal language with an algebra-like syntax that can be used to facilitate the processing and analysis of raster data. Map algebra operations use expressions to link inputs and outputs. In addition to inputs and outputs, expressions can consist of GIS tools, mathematical operators and constants. GIS tools can include not only basic tools such as local, focus, zone and distance measurement operations, but also special tools, such as Slope for deriving a slope raster from the DEM raster. The structure of the expression must follow the rules set in the GIS software package, which is actually a computer language. Thus, all calculations in this study are based on the laws of map algebra and utilize basic raster operations.

4.2.2 Radiation simulation of the building environment based on raster analysis operation

In general, this chapter enhances the 2.5D DEM model using the multi-band properties of the raster dataset (see Chapter 3). This operation allows the DEM data to be dimensionally enhanced. It will not only include information on the height and footprint of the building but also information on the vertical plane of the building and information on all surface materials of the building. Along with the enhanced dimensional 2.5D model, the spatial analysis of raster data and the new radiation numerical model are combined to provide an effective tool that can support building planning at neighbourhood scales. Further, all operations of this model use the map algebra calculation mode (An informal raster data language) to process raster data. This allows users to efficiently predict solar radiation in a neighbourhood environment by simply entering incident radiation parameters and building geometry.

The new radiation model is constructed entirely based on the rules of the raster analysis operation described above. Overall, the novel model includes three parts: (1) inputs masking for facades and surface cover files, (2) view factors casting and (3) radiation modelling. (1) Masking of inputs was used to increase the dimension of space and physical properties of 2.5D models. After processing the masking of inputs, features of vertical faces and surface materials can be demonstrated in geometric models as an independent layer for calculation, which makes up for the DEM model's lack of facade presentation. Masking outputs serve as inputs for view factors casting which was developed to build up urban-geometry-related factors such as the shadow map and the sky view factor (SVF) for the simulation of the transmission of direct and isotropic radiation in a building complex. By inputting view factors casting results and meteorological data into the radiation modelling, the solar radiation and thermal radiation condition of building groups can be simulated. In this model, a new raster-based geometric model is proposed for the simulation of the radiation in a building's neighbourhood in GIS. Finally, the raster analysis processing method was applied to calculate radiation results and the model has been validated by comparing it with experimental data. The framework of this model is shown in Figure 4.10.

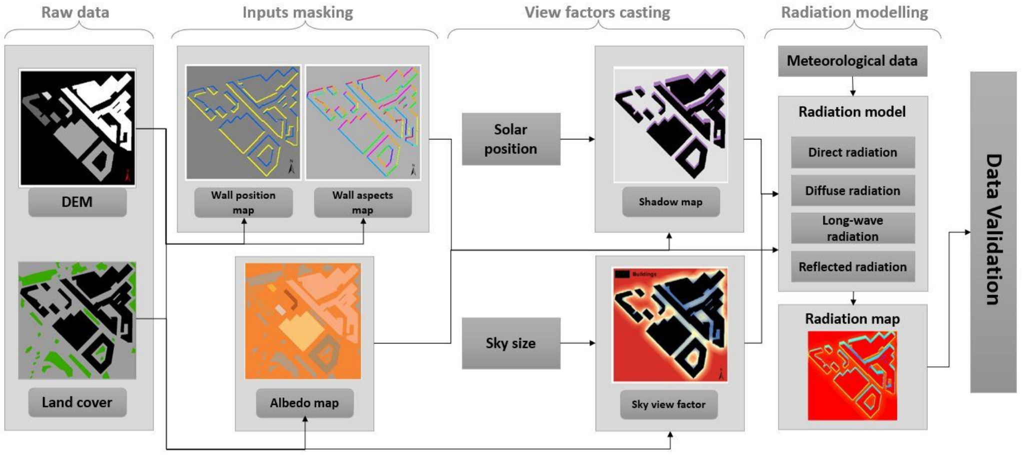

Figure 4.10: The framework of the proposed raster-based radiation simulation method.

(1) Enhanced 2.5D model based on raster analysis

As mentioned above, although 3D model-based solar potential simulation can obtain accurate results at the neighbourhood scale, it cannot efficiently assist strategic decision-making in the early stages of building or urban design due to its time-consuming and complex calculation process. Thus, in this study, a more agile 2.5D DEM data method was selected to increase the dimension with the help of the characteristics of raster data storage to make up for the lack of vertical plane data. As mentioned in Chapter 3, raster data (e.g., DEM data) is a space-filling data structure that divides space into blocks of uniform size and shape (grid) and the entire area is composed of grid cells (pixels). It can usually only describe one kind of information per layer. Nevertheless, multiple types of information located at the same location can be stored and processed by superimposing multiple layers. As shown in Figure 4.9, this study adds the location distribution, orientation and material information for building facades, as well as surface coverage (including building roofs) material information to the basic DEM data to form a new multi-dimensional urban morphological dataset with the same geo-transform. Moreover, unlike the storage method for 3D data (point cloud), although the geometric accuracy of raster data is low, its simple data structure and multi-layer data management mode are more conducive to rapid spatial and attribute analysis.

Generation of building-facade information based on DEM

As mentioned in Section 4.1.1, the analytical method of the DEM model only calculates the solar incident radiation distribution in the horizontal plane (ignoring the calculation of the solar radiation distribution in the vertical plane). For a vertical wall, since the direct solar radiation energy received by the wall at the same time is affected by the orientation of the wall, the distribution of the direct solar radiation energy is different in each orientation. Therefore, the establishment of the wall file should not only contain its location information but also determine its orientation. To this end, it is necessary to distinguish the building area and the non-building area in the raster data and find their dividing lines in order to identify the position of the outer envelope structure of the building facade. Since the DEM model used in this study does not consider the terrain factor, its data characteristics show that where the ground is located, the corresponding data is "0", and where the building area is located, the corresponding data are greater than "0". In other words, the values of elements in DEM are divided into "0" and "non-0" with the junction position of all "0" and "non-0" elements in the pixel forming the boundary line between the building area and the non-building area (the location of the outer wall). With the help of physical distance measure operation in raster data analysis (accessing each pixel in the input image with a 3*3 window), the derivative value of the boundary line in the X and Y directions can be calculated and the orientation value of the boundary line can be obtained, i.e., the wall orientation. Specifically, the following equation can be used when calculating the wall orientation of the centre pixel in Figure 4.11 (Each grid is marked with A-I from left to right and top to bottom):

The rate of change of cell E in the x direction:

$$\frac{dz}{dx} = \frac{(C+2F+I)-(A+2D+G)}{8*cellsize} \tag{4.1}$$

The rate of change of cell E in the y direction:

$$\frac{dz}{dy} = \frac{(G+2H+I)-(A+2B+GC)}{8*cellsize} \tag{4.2}$$

Orientation of the wall:

$$A_{wall} = arctan2(\frac{dz}{dy}, -\frac{dz}{dx}) \tag{4.3}$$

Where A-I represents the elevation value of the corresponding grid, with the cell size as the grid area and arctan2 as the function used to return the azimuth.

A	B	C
D	E	F
G	H	I

Figure 4.11: An example of the 3*3 window in the wall orientation calculation.

In this process, the position distribution and orientation of the wall in raster data could be produced (Figure 4.12) and the corresponding data file was established to lay the foundation for the calculation of the direct solar radiation energy distribution in the building complex. Using the geometric relationship between the direct sunlight and the orientation of the wall, the direct solar radiation energy is converted

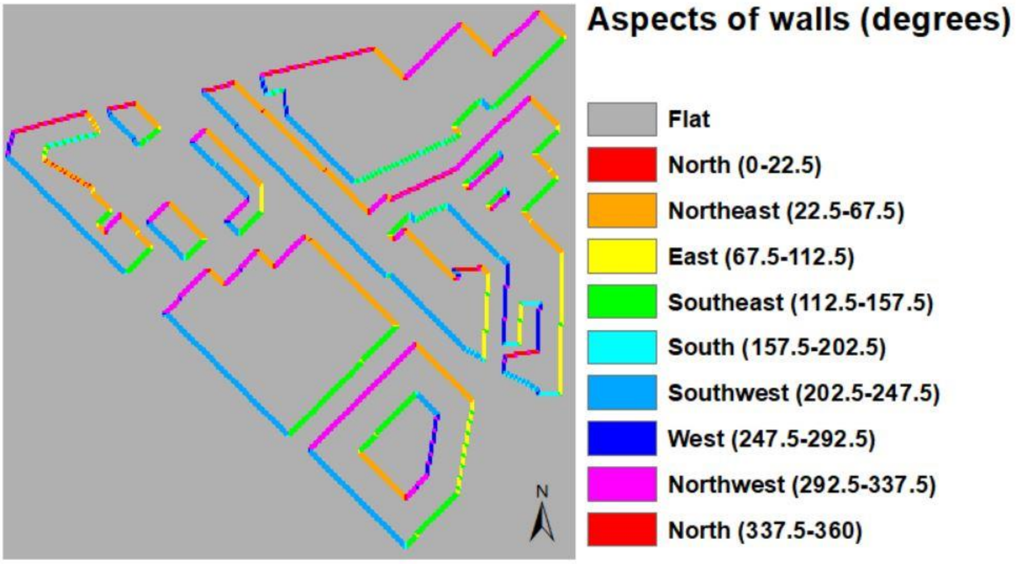

Figure 4.12: Position and orientation of building walls based on raster data gradient calculations. The direction in which the walls are facing is indicated by the different colours. (Refer to the legend, north is 0 degrees).

to the vertical walls with different orientations. In the direct energy distribution image, the corresponding energy value can be found for each pixel representing the position of the wall, ground and roof.

Establishment of surface cover albedo information

To analyse the reflected radiation for each underlying surface unit in the building complex, it is necessary to obtain the raster data distribution of parameters related to the albedo. For existing physical building groups, these data can be obtained through field research; if it is a building group in the design process, these parameters can be obtained from the design information and can be stored in the corresponding pixel positions. In this study, the raster local operation reclassification was carried out with the help of the existing land cover classification and building type data to establish the surface albedo information. The specific principle is described in section 4.2.1. The same type of values will be given the same numerical code in the raster data. Thus, by assigning cells with the same number to their corresponding albedo values, a data layer of surface reflectance features can be established.

Through the above raster data processing, a set of multi-band raster models containing urban surface properties will be obtained. Unlike the common raster data (e.g., DEM data) used to represent urban surface geospatial information, the newly established input dataset not only includes basic building geometry and surface coverage classification but also includes the specific location and orientation of walls and some physical attribute values for surface materials, which allows this raster-based radiation simulation method to calculate more useful outputs. The following will further introduce how to combine the proposed raster model with the basic radiation model to achieve efficient radiation distribution simulation in urban environments.

(2) Urban surface radiation budget

Solar radiation plays a major role in outdoor comfort and surface energy balance. The net total radiation in an urban microclimate is affected by the geometry (i.e. the location, orientation and shape of the building) (Shishegar, 2013). The total net solar radiation received on the surface is:

$$Q_R = K\downarrow - K\uparrow + L\downarrow - L\uparrow \tag{4.4}$$

Where Q_R is net radiation, $K\downarrow$ is incoming direct and diffuse short-wave radiation, $K\uparrow$ is reflected short-wave radiation, $L\downarrow$ is incoming long-wave radiation from the atmosphere, $L\uparrow$ is outgoing long-wave radiation from the surface.

The net radiation energy absorbed by the surface in a street canyon could be expressed as (Figure 4.13):

$$Q_R = (1-\alpha)(Q_B + Q_D + Q_{env}) + Q_L \tag{4.5}$$

Where Q_R is net radiation, α is the surface albedo, Q_B is the direct beam radiation on a plane surface, Q_D is diffuse radiation, Q_L is surface-absorbed long-wave radiation and Q_{env} is the radiation reflected from the surrounding urban environment.

The direct beam radiation on a plane surface, diffuse radiation and surface-absorbed long-wave radiation is determined on the assumption that the sky diffuse radiation and reflected solar radiation are isotropic (Figure 4.13). Since this study mainly studies the radiation distribution and absorption inside the building complex, the direct and diffuse solar radiation on the urban surface is provided by the measured data. Moreover, results from other models used to calculate total solar radiation (such as MRM and RRTM) can also be set as input parameters (Clough and Iacono, 1995; Kambezidis *et al.*, 2017)

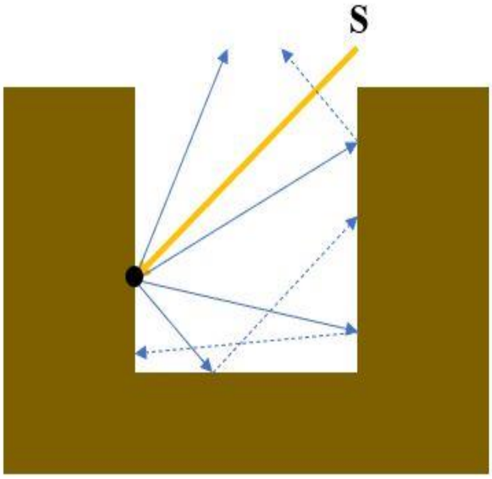

Figure 4.13: The effect of street canyon geometry on radiation exchange. The yellow arrow is the direct beam irradiation received by the street canyon; The solid blue arrow is the first reflection from the building surface; The blue dotted arrow is the second reflection from the canyon surface.

(3) Analysis of direct solar radiation

Direct solar radiation is one of the most important factors in the process of analysing the outdoor thermal environment of a building complex and directly affects the distribution of the outdoor thermal environment due to the different distribution of direct sunlight positions. Direct solar radiation is not only affected by the parameters of the single building itself, such as building shape, orientation, location and other factors but also by the overall planning and design of urban building groups (Méndez Echenagucia *et al.*, 2015). Thus, the position of every single building relative to other buildings is a dynamic parameter and changes to these dynamic parameters (e.g., the height, orientation and shapes) directly affect the reception of direct solar radiation by other buildings, thereby affecting the overall outdoor thermal environment of the building complex. This sophisticated relationship between buildings in a neighbourhood leads to the complexity of the 3D geometric analysis methods for analysing direct solar radiation. The use of DEM based on raster data analysis can easily analyse the distribution of direct solar radiation energy at different times in the building complex. Moreover, it can quantitatively analyse the relationship between the distribution of direct solar radiation energy and the building height, location and other factors in the planning of neighbourhoods.

Generation of building shadows in raster data

In order to determine the distribution of direct solar radiation energy in the building group, the grid value distribution of the sun shading by the building arrangement at the corresponding time should be calculated first. After the analysis location is determined, its corresponding longitude and latitude parameters and the distribution of building shadows in the building complex can be determined according to the sun zenith and azimuth at different analysis times. According to Duffie and Beckman (2013), the calculation equations for the solar zenith and azimuth angles are as follows:

$$sinH_s = sin\emptyset * sin\delta + cos\emptyset * cos\delta * cost \tag{4.6}$$

$$cosA_s = \frac{(sinH_s * sin\emptyset - sin\delta)}{(cosH_s * cos\emptyset)} \tag{4.7}$$

Where H_s is the solar zenith angle, A_s is the solar azimuth angle, $\emptyset$ is the geographic latitude, δ is the sun declination and t is the solar hour angle.

Moreover, the respective values of δ and t can be calculated by the following equations:

$$\delta = 0.006918 - 0.399912\cos(b) + 0.070257\sin(b) - 0.006758\cos(2b) + 0.000907\sin(2b) - 0.002697\cos(3b) + 0.00148sin(3b) \tag{4.8}$$

$$t = (solar\ time - 12) * 15° \tag{4.9}$$

Where b=2*pi*(N-1)/365, N is the number of days from January 1 to the calculation day in a year.

After calculating the sun azimuth at a certain location at a certain time, combined with the building wall orientation calculated above (Figure 4.12), the light-backing and light-facing walls of the building can be further judged. Specifically, the wall orientation in the range of [A-90, A+90] is the light-facing surface and the opposite is the light-backing surface (as shown in Figure 4.14).

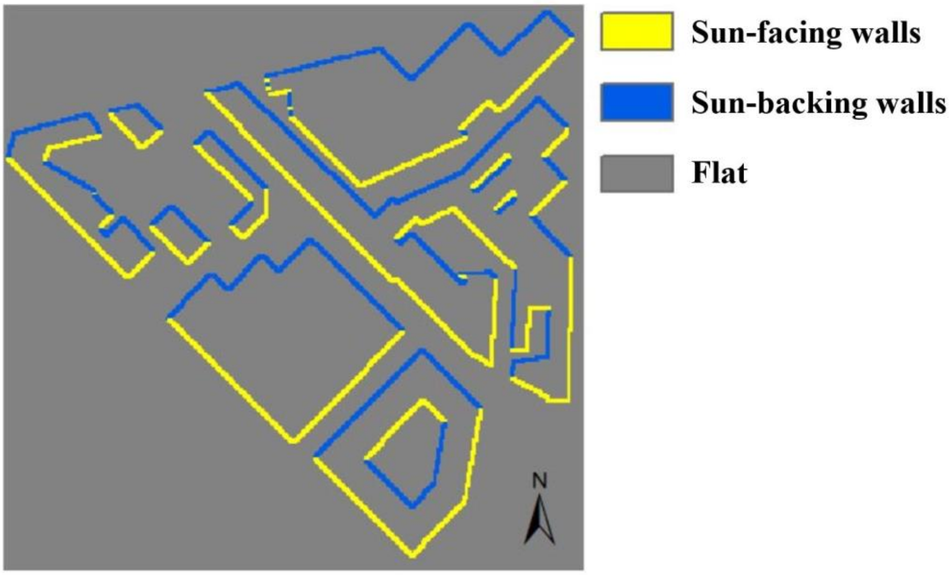

Figure 4.14: The solar exposure of walls in the building complex at 12 o'clock.

Furthermore, the backlit wall position raster layer is combined with the DEM raster layer to generate the backlit wall raster layer with height. Then the window in Figure 4.11 is also used to traverse the new raster layer (i.e., neighbourhood operation) to obtain the distribution of the building shadows according to the following equations:

$$Shade = 255 * (\cos H_s * \cos A_{slope}) + (\sin H_s * \sin A_{slope} * \cos(A_s - A_{wall})) \tag{4.10}$$

Where A_{slope} is the slope angle and can be calculated as:

$$A_{slope} = \operatorname{atan}\left(height * \sqrt{(\frac{dz}{dx})^2 + (\frac{dz}{dy})^2}\right) \tag{4.11}$$

Finally, the shadow distribution of the building complex at different times can be obtained as shown in Figure 4.15.

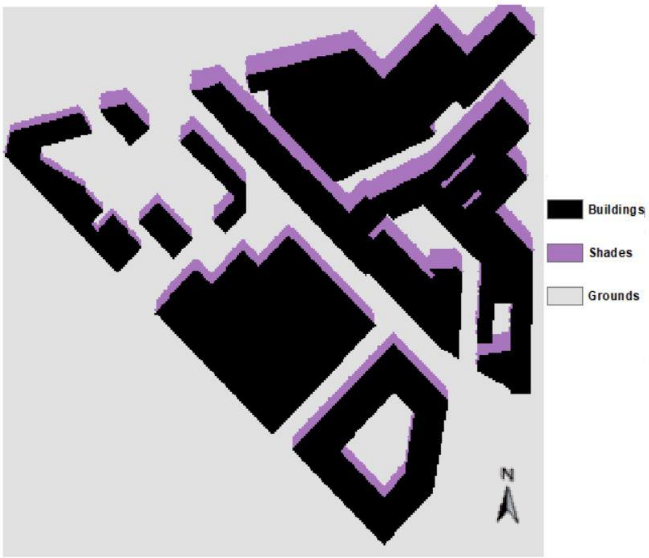

Figure 4.15: The output showing the shadows in the buildings complex at 12 o'clock.

Calculation of direct solar radiation energy distribution

The measured direct radiation I_B is the direct solar radiation intensity at the surface of the earth in a plane perpendicular to the sun's rays, depending on the specific site of the study (Figure 4.15). The direct solar radiation energy received by the horizontal surface in the building complex can be expressed as (Oke *et al.*, 2017a):

$$Q_{BH} = I_B * sinH_s \tag{4.12}$$

The intensity of direct solar radiation received on the vertical plane of the building is:

$$Q_{BV} = I_B * cosH_s * \cos{(A_s - A_{wall})} \tag{4.13}$$

Where I_B is direct radiation intensity on a horizontal plane, H_s is the solar zenith angle, A_s is the solar azimuth angle and A_{wall} is the orientation of the wall.

Eq. 4.12 and Eq. 4.13, respectively provide the shadow distribution in the building group, the building facade position and the orientation of the raster layer for the calculation based on the local operation of multiple raster layers. The direct solar radiation will be converted to the horizontal plane and the building facade in each direction and the corresponding raster layer established as shown in Figure 4.16. These grid layers can be superimposed to realize the distribution of direct radiation energy for a whole day as the image and the direct radiation distribution results can also be output separately for each hour.

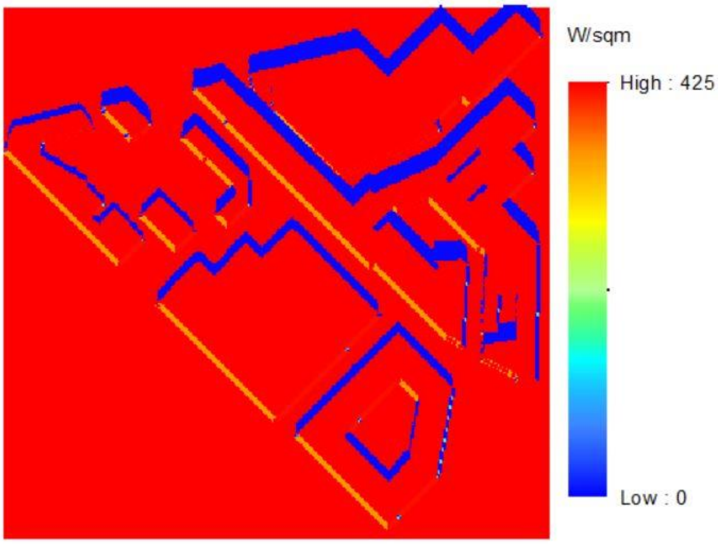

Figure 4.16: The output of the solar direct radiation map at 12 o'clock.

(4) Analysis of diffuse solar radiation

Diffuse radiation is also an important part of radiation in neighbourhoods and will have a significant impact on the outdoor thermal environment, especially when there are clouds in the sky. The diffuse radiation energy can be determined by the following equation (Lee *et al.*, 2013; 2020):

$$Q_D = I_D * SVF \tag{4.14}$$

Where I_D is diffuse radiation intensity and SVF is the sky view factor (i.e. the viewing angle coefficient of the plane facing the sky).

Generation of SVF maps in raster data

There are many factors affecting the viewing angle coefficient of the urban ground facing the sky. For example, it is affected by factors such as the layout, height and shape of the building. Thus, the viewing angle coefficient at any point on the ground is different making the solution process for the Sky View Factor (SVF) quite complicated. Nevertheless, DEM data is also widely used in the calculation of SVF due to the raster data analysis method having an excellent ability to analyse spatial relationships.

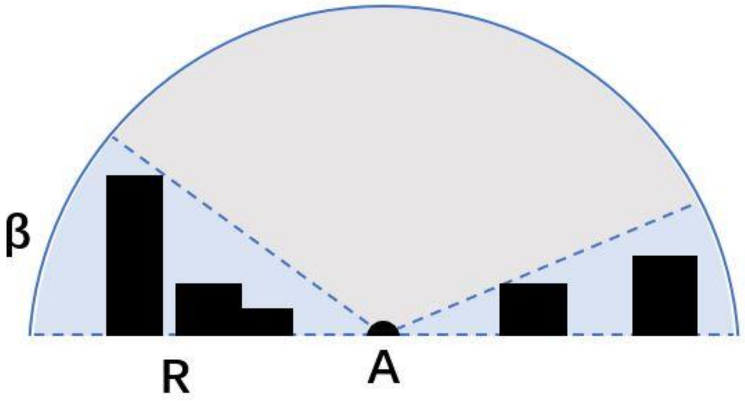

Figure 4.17: View of the sky from point A on the ground affected by surrounding buildings.

Figure 4.17 is a schematic diagram of the viewing angle range of the sky when a certain point A on the ground is affected by surrounding buildings. If there is no influence from surrounding buildings, then point A's view of the sky is a regular hemisphere. Its boundary is a circle existing on the ground plane with its centre at point A. In addition, if there is no occlusion by surrounding buildings, it is easy to know that the viewing factor of point A to the sky is 1. On the contrary, when the surrounding buildings block the sky, the viewing angle coefficient of point A to the sky will become smaller. Thus, calculating the ratio of the hemisphere that represents the non-occluded area is based on the specific layout, height and shape of the buildings around point A. According to the schematic diagram in Figure 4.17, the SVF can be calculated by the following equation:

$$SVF = 1 - \int_{\theta=0}^{2\pi} \sin\left(\beta(R,\theta)\right) d\theta \qquad (4.15)$$

Where the angle from the centre point to the maximum obstacle height at the maximum distance is equal to the constant search radius (R).

In addition, since the actual calculation is performed through a finite number of discrete grid values based on zonal operation, the discrete calculation formula is as follows:

$$SVF = 1 - \frac{\sum_{i=1}^{n} sin\beta_i}{n} \tag{4.16}$$

Where β_i is the terrain height angle of azimuth angle i, and n is the number of calculated azimuth angles.

At the same time, in order to calculate the SVF value more effectively, this study uses a certain number of ground observation points as the central calculation point. Finally, similar to the building shadow calculation, the SVF result for a certain central grid value is also calculated according to Equation 4.16 with the help of raster proximity analysis. The calculated result is shown above in Figure 4.18.

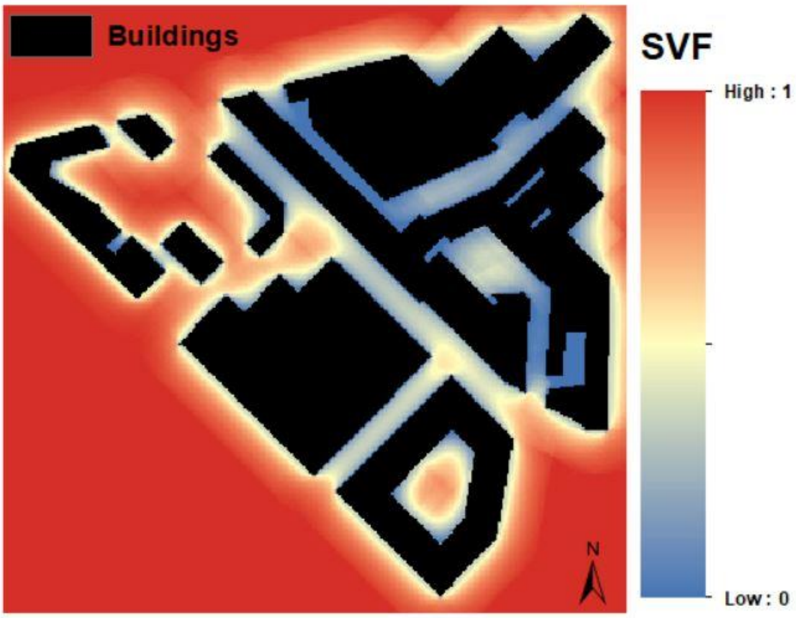

Figure 4.18: The output of sky view factor (SVF) in building complexes.

Calculation of diffuse solar radiation energy distribution

As with the calculation of direct radiation, after obtaining the SVF map for the building complex, the amount of diffuse radiation received at any location in the building neighbourhood can be calculated according to Equation 4.14 based on the local operation of multiple raster layers to establish the corresponding raster data layer. Figure 4.19 shows the result for the solar diffuse radiation distribution.

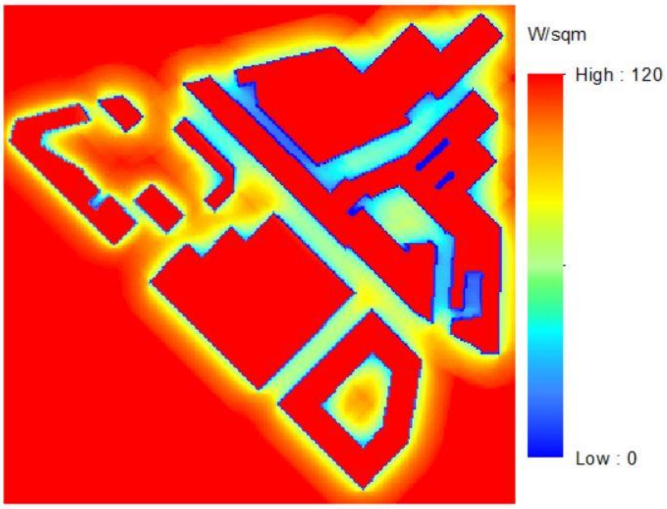

Figure 4.19: The output of the solar diffuse radiation map at 12 o'clock.

(5) Analysis of longwave radiation

The thermal environment within the complex is not only affected by solar radiation, but also by long-wave radiation between the ground and building facades. This effect is quite complicated because the location of any point on the surrounding buildings is variable depending on its location, size, height and other factors linked to the various building facades. Meanwhile, quantitative analysis of long-wave radiation in the building complex is critical for the accuracy of outdoor thermal environment analysis. Theoretically speaking, the long-wave radiation heat obtained by the surface i of a building (or the ground) from the surface j of the surrounding environment can be expressed by the following equation:

$$Q_{Li} = \sum_{j=1}^{n} B_{ji}(\varepsilon_j A_j \sigma T_j^4) \tag{4.17}$$

Where B_{ji} is the angular coefficient of the radiated energy from the surface j to surface i, ε_j is the emissivity of the surface j, A_j is the area of the surface j, σ is the Stefan-Boltzmann constant and T_j is the surface temperature of surface j.

Due to the interchangeability of the radiation heat transfer between the two surfaces, the two planes at surface i and surface j have the following relationship:

$$B_{ij}A_i = B_{ji}A_j \tag{4.18}$$

Therefore:

$$\sum_{j=1}^{n} B_{ij}A_i = \sum_{j=1}^{n} B_{ji}A_j \tag{4.19}$$

and

$$A_i \sum_{j=1}^{n} B_{ij} = A_j \sum_{j=1}^{n} B_{ji} \tag{4.20}$$

can be obtained from Equation 4.18.

At the same time, in order to simplify the calculation of the long-wave radiation for each surface by expressing it in an area-averaged way, the emissivity and surface temperature of the surrounding buildings are averaged in Equation 4.17 to obtain:

$$Q_{Li} = \varepsilon_{ave}\sigma T_{env}^4 A_i \sum_{j=1}^{n} B_{ij} \tag{4.21}$$

Where ε_{ave} is the average emissivity of surrounding surfaces and T_{env} is the effective environment temperature of surrounding objects.

Since $\sum_{j=1}^{n} B_{ij}$ represents the angle coefficient of surface I relative to the surrounding building face, the angle coefficient of the surrounding building face in the analysis here is (1 − SVF), which is exactly 1 when added to the angle coefficient of the building complex to the sky. Therefore, Equation 4.21 can be further expressed as:

$$Q_{Li} = \varepsilon_{ave}\sigma T_{env}^4 A_i (1 - SVF) \tag{4.22}$$

Thus, the long-wave radiation heat balance of the surface of a building (or ground) can be expressed as:

$$Q_L = (\varepsilon_{ave}\sigma T_{env}^4 (1 - SVF) - \varepsilon_i \sigma T_{sur}^4) A_i \tag{4.23}$$

Where ε_i is the emissivity of the surface and T_{sur} is the surface temperature.

The solution of the average temperature is to complete the solution of the surrounding average temperature by analysing the temperature values corresponding to each pixel in different directions around it and then taking the average value (i.e., raster zonal operation). Figure 4.20 is an analysis of the raster distribution of the corner coefficients of the surrounding buildings (that is the distribution of coefficients facing the surrounding buildings. It can be described as 1-SVF at any position in the building group.

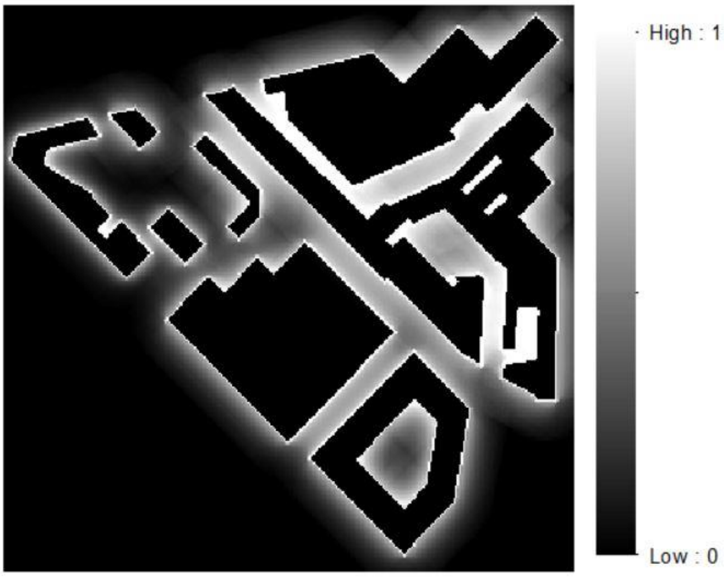

Figure 4.20: The distribution of the corner coefficients of the surrounding buildings.

(6) Analysis of reflected radiation

Additionally, unlike smooth surfaces, the direct, diffuse and long-wave radiation received in the urban canyon will be reflected. At this time, the reflected radiant energy obtained from the analysis surface is:

$$Q_{env} = \sum_{j=1}^{n} B_{ji} \alpha_j A_j (Q_{Bj} + Q_{Dj} + Q_{Lj}) \tag{4.24}$$

Where α is the albedo of surface j, Q_{Bj} is the direct beam radiation received on the surface j, Q_{Dj} is the diffuse radiation received on surface j and Q_{Lj} is the long-wave radiation received on surface j.

At this time, in order to calculate the amount of reflected radiation received in a certain area, the average value of all radiation in this area is introduced, and according to Equations 4.19 and 4.20, Equation 4.24 can be expressed as:

$$Q_{env} = A_i \alpha_{ave} Q_{ave} (1 - SVF) \tag{4.25}$$

Where α_{ave} is the average albedo of the area and Q_{ave} the average value of all radiation in the area.

The average energy intensity Q_{ave} is obtained by calculating the energy value received by each pixel from different directions based on the raster data zonal operation and then taking the average value, which is also used to calculate the average albedo α_{ave}. The specific implementation process is described in section 4.2.1. In simple terms, a zonal raster file is created to divide the raster area to be analysed into different blocks. Then, the average of the raster data within its extent based on this zonal raster can be calculated. With the help of the above method, various average parameters and the received radiant energy of the building environment in the specified area can be easily summarised. Generally, after all the above-calculated grid layers are superimposed and calculated in an orderly manner through the process shown in Figure 1, the solar radiation energy distribution of buildings in the neighbourhood can be quickly analysed.

4.3 Model validation

As an essential part of numerical model development, it is important to validate numerical models of urban radiation. Unless validated, it is difficult to ensure the reliability of developed models in reproducing and predicting the distribution of solar radiation on urban surfaces. Therefore, in order to verify the correctness of the physical model of the radiation simulation of the building complex and its combination with the raster analysis, this chapter will compare the simulated data with the actual observed data. The built environment model for the simulations will be based on the field observation area. Other climatic conditions will also be configured to suit the specific circumstances at the time of the observation. Finally, this study is validated by comparing field measurement results by Shahrestani *et al.*

(2015) for the microclimate in central London with the simulation results from the proposed model.

4.3.1. Experimental site and instruments in London

Figure 4.21 shows the actual urban morphology condition (including buildings, streets and vegetation distribution) of the field measurement site. This field survey campaign was carried out in London in summer (from July 21 to July 26, 2010) with a total of 6 survey points. These measurement locations are labelled from 1 to 6 (specific locations are numbered in Figure 4.21). At each site, several microclimatic variables including the air temperature, the wind speed and direction, the air humidity and the global solar radiation (the sum of the direct radiation and diffuse radiation components in the horizontal plane) were measured at a height of 4m. The accuracy of the integrated sensor suite (ISS) used in the weather station for measuring each climatic variable is 0.56°C (air temperature), ± 5% (the wind speed), ± 7 degrees (the wind direction), ± 3% (the air humidity) and ± 5% (the solar radiation). The measurements were logged locally on a continuous basis at five-

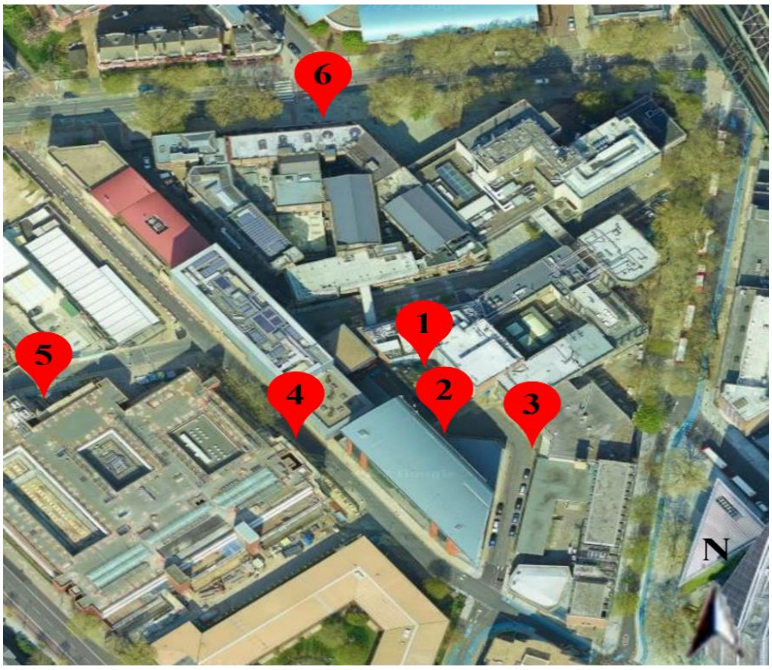

Figure 4.21: London field measurement site at Elephant and Castle, United Kingdom. Source: Google Earth.

minute intervals at each site. Furthermore, for studying the influence of long-wave radiation in the building environment, the surface temperature of the ground and two walls were also recorded at experimental site 4 on July 21. Since this study mainly simulates the radiation distribution in the building complex, only the measured results of the global solar radiation and surface temperatures are used for validation. In addition, considering that this experiment was conducted in 2010, the DEM data and other input parameters will be set according to specific conditions in 2010.

4.3.2. Comparison of the model outputs with the experimental results

(1) Solar radiation distribution results

For the purpose of validating the solar radiation results, the above-mentioned data from measurements in a real built environment were used to compare the results produced by the proposed model to calculate the mean absolute percentage error (MAPE) and the root mean square error (RMSE). These two indicators can be used to quantify the quality of the estimated results, which can reveal the gap between the predicted results and the actual observed results. It should be noted that the simulation results are compared by extracting the same 6 points as the experimental site. All indicators of precision statistics (including the values of all 6 measurement points) are shown in Table 4.2. The results presented in Table 4.2 indicate that the percentage MAPE values for all estimates is relatively low (below 3). Meanwhile, the root-mean-square error (RMSE) also shows a relatively low range (below 110). Since most of the estimates for radiation simulation usually reflected the RMSE in a range from about 80-140w/m^2 (Zhang *et al.*, 2017), the simulation results are considered reliable.

Table 4.2: Statistical results of simulated and measured data.

Experimental Site	*1*	*2*	*3*	*4*	*5*	*6*	*Overall*
Mean (W/m^2)	**204.78**	**36.58**	**81.39**	**165.13**	**266.39**	**95.62**	**141.65**
MAPE (%)	**1.7**	**1.75**	**2.4**	**1.16**	**0.98**	**0.87**	**1.48**
RMSE (W/m^2)	**93.19**	**79.64**	**82.37**	**58.79**	**110.21**	**80.79**	**85.58**

At the same time, the scatter diagram generated in Figure 4.22 can more intuitively represent the relationship between the simulated data and the observed data, wherein the x-coordinate and the y-coordinate represent the simulated solar radiation distribution and the actual measured value, respectively. Clearly, as can be seen from Figure 4.22, the variables simulated using the proposed model are similar to the actual observed results, as all the scattering data are close to the 1-1 line. Furthermore, the quantitative indicators (Table 4.2) were consistent with the results in the scatterplot (Figure 4.22).

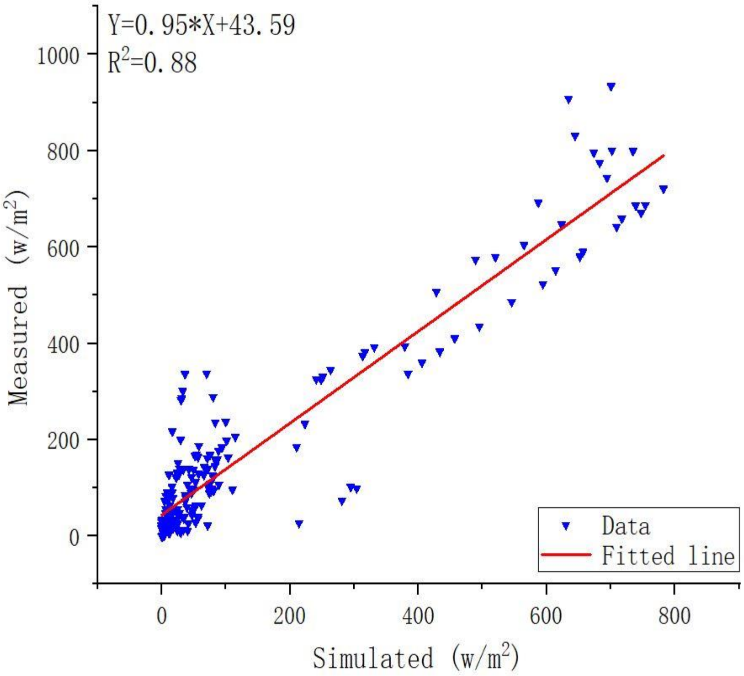

Figure 4.22: Scatter plot of comparison between the measured data and the simulated results of global solar radiation.

(2) Surface net radiation results

Finally, the reliability of the surface net radiation simulation output is verified by comparing the value of the simulation output with the net radiation value converted from the surface temperature results from the experimental measurements at site 4. In the summer (July 21), the comparison of the net surface radiation budget based on simulation and the actual measurement is shown in Figure 4.23 and, overall, the simulated value has a similar trend to the actual measurement. It is evident from the figure that the results calculated from the actual measured values are more variable than the simulated values. In addition, the RMSE value is calculated to be relatively high around 150 w/m^2. However, since the model is intended to assist in the early design stages, the representation of trending results is more important than precise results. Thus, the model predictions are considered acceptable and directional.

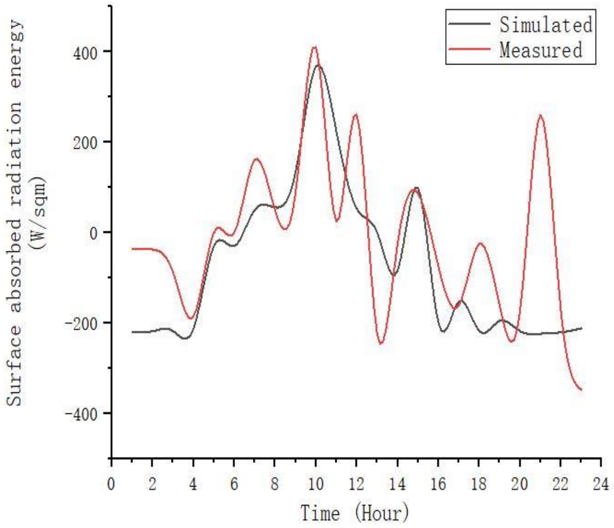

Figure 4.23: Comparison of the simulated value of the net surface radiation budget with the measured value (the ground surface at site 4).

4.4 Results and discussions

Through the above-mentioned raster computing-based model, a new method that can efficiently present the radiation distribution in the built environment is proposed. At the same time, the output of the proposed model was demonstrated to be plausible by comparing the results simulated by the proposed model with those actually observed. With the new proposed model, solar radiation in a neighbourhood can be quickly determined. The output includes solar direct radiation, solar diffuse radiation and a net surface radiation budget. These results are discussed further below.

4.4.1 Solar direct radiation results

The results for direct solar radiation obtained by applying the method described in Section 4.2 can be output as shown in Figure 4.24. All the direct solar radiation energy distribution in the building complex in Figure 4.16 is considered at the ground-based position which involves a certain approximation. In other words, the shadow distribution in the building complex is different from the actual terrain, which will lead to a certain difference between the direct radiation energy distribution on the actual terrain and the direct radiation energy distribution based on the plane of the ground. However, this paper is mainly aimed at the early stage of building design in neighbourhoods so the above difference can be ignored, along with the assumption that the distribution of solar radiation in the vertical direction of the entire building complex is uniform. In addition, due to the introduction of the vertical surface layer, the model can not only solve the direct radiation energy

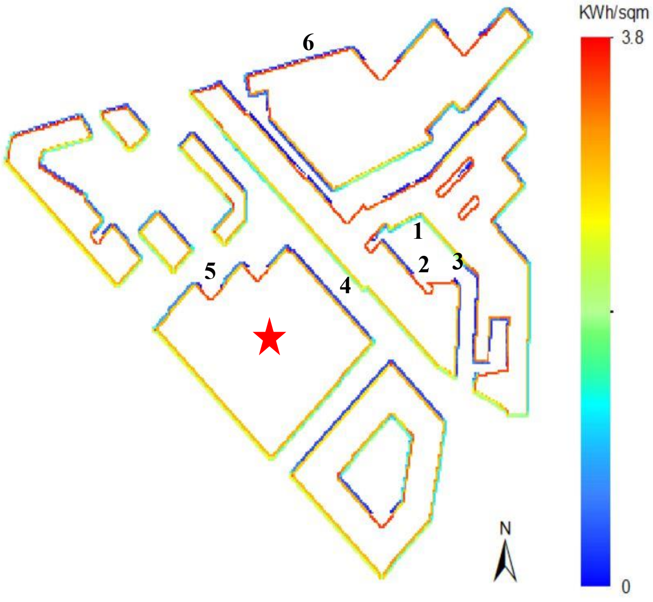

Figure 4.24: Distribution map of direct solar radiation energy in the vertical plane of the building complex in a whole day (simulated time: 2010.07.21).

distribution at each pixel position on the horizontal plane, but also know the radiation value at any time on the wall (combined with the height on the pixel) and the cumulative value over a period. Therefore, the direct radiation results of the model can be suitable for any time and any place and it can also analyse the direct solar radiation in any period - a map of the direct radiant energy distribution in an hour is shown in Figure 4.16. The same method can be used for the analysis of the direct radiant energy for a whole year. At the same time, the vertical layer introduced in this paper emphasizes the distribution of direct solar radiation on the façade for a whole day which can be mapped in Figure 4.24. Take the building marked with a five-pointed star in Figure 4.24 as an example, after extracting its four different facing surfaces (southwest, southeast, northwest and northeast), the direct solar radiation energy it receives throughout the day can be obtained in Figure 4.25.

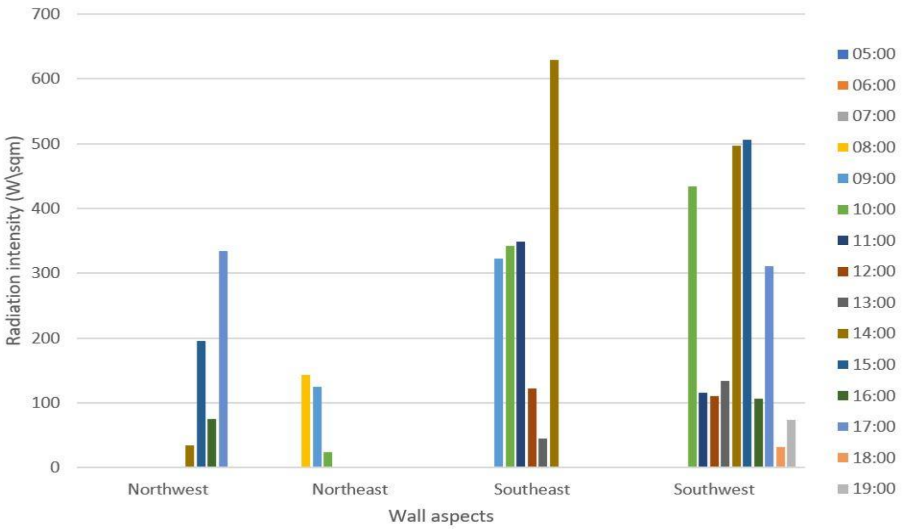

Figure 4.25: Example building facades all-day direct solar radiation energy (simulated time: 2010.07.21).

4.4.2 Solar diffuse radiation

The calculation method of solar diffuse radiation has been described in detail in Section 4.2.2 (4) and the output results are presented in Figure 4.19. At the same time, from the calculation process of solar diffuse radiation described in Section 4.2.2 (4), it can be clearly seen that the calculation of the SVF value will directly affect the diffuse radiation simulation results. Thus, sensitivity analysis of the Sky

View Factor (SVF) calculation results can help with the parameter settings for diffuse radiation simulation. In addition, the result of the SVF calculation is highly dependent on the grid resolution and fixed search radius when it is calculated. Since this study adopts a fixed high resolution of 1m for all raster files, determining the appropriate search radius is the key to the SVF calculation. The building group in Figure 4.24 is also used for example analysis. The basic situation of the buildings for the analysis is: the average building height is about 12m (range 17m to 7m). By setting different constant search radii, the value of the viewing angle coefficient of the ground facing the sky with the search radius of 5m, 10m, 20m and 50m is clearly shown in Figure 4.26 based on a 1m SVF resolution. It can be seen from Figure 4.26 that in the densely built area, the viewing angle coefficient is significantly reduced, while the angle coefficient can be close to 1 in places far from the building area and on the roof of a building, that is, it is basically not affected by the building. In addition, in the open space surrounded by buildings, it can be clearly seen that there are slight gaps in the SVF results under different search radii. Table 4.3 can

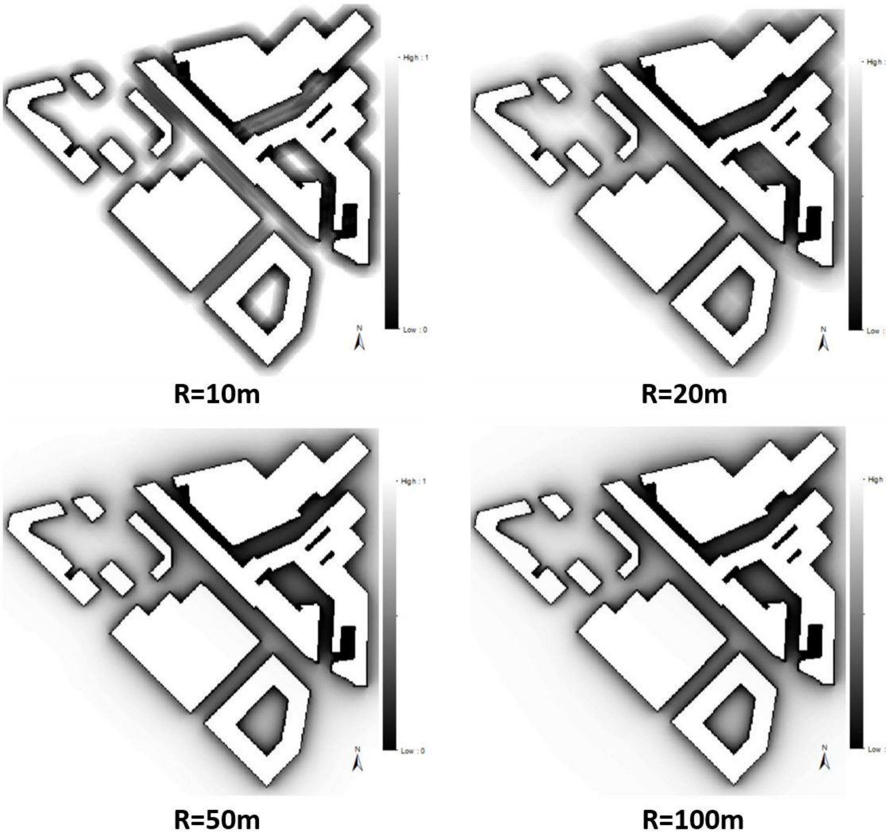

R=10m R=20m

R=50m R=100m

Figure 4.26: Result of calculating the SVF value under different search radii with 1m resolution.

be obtained by extracting the results for the same position as the measuring point label in Figure 4.24. It shows in more detail the effect of different search radii on SVF results. It can be seen from Table 4.3 that when in narrow streets, the size of the search radius has little effect on the calculation results (such as in experimental site 3). Meanwhile, when located in a relatively open area, the search radius will significantly affect the output results. However, when the search radius is greater than 20m, the change in the results will no longer be obvious. Generally, the setting of the search radius is mainly determined according to the requirements for solving practical problems. If the analysis area has many tall buildings or wide streets, the search radius needs to be larger. In this paper, a search radius is 20m can meet the simulation requirements.

Table 4.3: Comparison of SVF values calculated under different search radii.

Search Radius	***Site 1***	***Site 2***	***Site 3***	***Site 4***	***Site 5***	***Site 6***
10m	0.65	0.52	0.39	0.63	0.91	0.63
20m	0.47	0.48	0.34	0.52	0.73	0.6
50m	0.41	0.36	0.31	0.49	0.72	0.59
100m	0.41	0.36	0.31	0.49	0.71	0.59

4.4.3 Surface net radiation budget

In addition to the evaluation of solar radiant energy, the net radiant energy on the surface of the building complex also needs to be quantitatively analysed, which is essential for the analysis of the outdoor thermal environment in the early design stage, especially for summer nights. As mentioned in section 4.1.1, the current radiant energy analysis tools for neighbourhood environments mainly focus on calculating solar radiation. Therefore, the raster data model not only analyses the direct solar radiation and scattered radiation but also analyses the long-wave radiation and the reflected radiation in the environment by introducing the surface physical property layer. During the net radiant energy analysis, the ground and building roof planes are subjected to a radiant energy balance analysis for each unit (pixel) in the raster data. On the other hand, the analysis of the building facade maintenance structure is to find out the position of the facade structure, which is similar to the method for direct radiant energy analysis. To perform a net radiation analysis on each underlying surface unit in a building complex, obtaining a grid distribution of the underlying surface albedo parameters is essential. For existing physical building groups, these data can be obtained through field research or bird's-eye image analysis; if it is a building group in the design process, these parameters can be obtained from the design information and stored in the corresponding pixel positions. By using the method introduced in Section 4.2, the net surface radiated energy of buildings in different time periods can be obtained, as shown in Figure

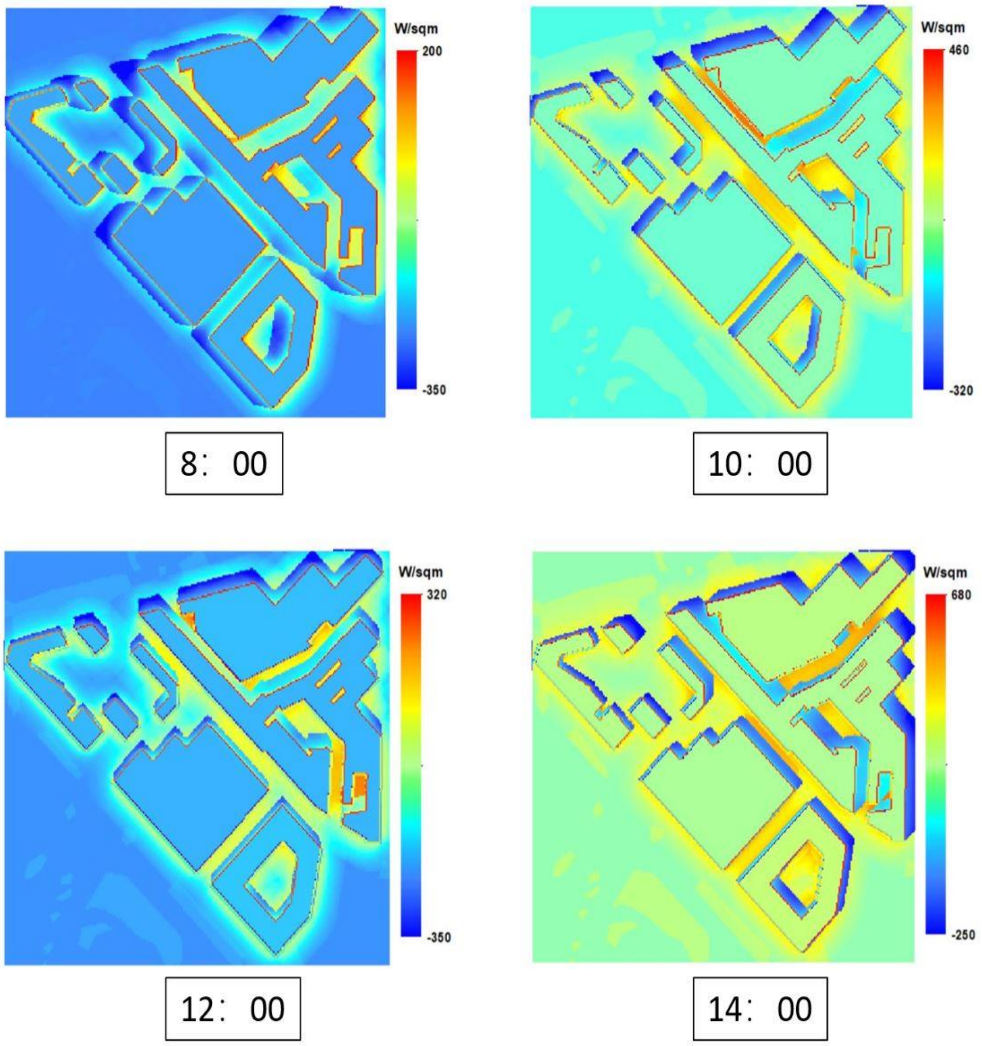

Figure 4.27: The net surface radiated energy of buildings in different time periods.

4.27. In addition, since the proposed model adds facades layer information to the traditional 2.5D elevation model, it is possible to transform the plane data to display the result in 3D vision.

4.5 Summary and conclusions

In order to quickly analyse the distribution of solar radiation in a building complex, this chapter develops a new radiation simulation model based on raster data operations. It allows numerical modelling to more effectively help designers to manage the exchange of thermal radiation in the environment in the early design phase. To validate the reliability of the model results, the simulation results are compared with the actual measured results and are carefully discussed. Overall, the observed and simulated results show a high degree of agreement with a correlation coefficient of 0.88. Thus, this model can meet the reference role for the analysis of the outdoor radiation conditions within the building complex at the early planning stage.

By building a radiation model based on raster data operations, the proposed model has the following features:

- The model theoretically calculates direct solar radiation and isotropic radiation by combining the raster data operation method and basic physical models.
- Fast processing of large amounts of fixed position data by means of raster data operations for efficient solar radiation analysis.
- Comprehensive radiation calculations are made with the help of multi-level raster data for land surface properties.
- A new vertical raster layer has been added to the existing 2.5D geometry model. It adds dimensionality to the calculation of the radiation distribution based on DEM data.

The benefits of the above features are obvious: (1) Numerical models built using raster operations as a base framework save time in simulation operations which allows the designer to quickly predict the radiant distribution within the neighbourhood. (2) The rasterised representation of the urban surface makes the model more flexible for multi-scene comparisons in the early design phase. (3) Multi-band geographic information synergy offers further possibilities for analysis based on 2.5D models. It takes advantage of the multi-band data structure of the raster data to enrich the information in the 2.5D data. (4) The combination of mathematical modelling and raster data analysis methods offers new solutions for modelling similar environmental problems.

In general, the proposed model can be used in comparative studies to assess the variation between different scenarios to provide a more scientific approach to managing the radiation exchange through architecture and landscape design. It can also be further combined with the urban surface climate model to provide a more complete urban outdoor thermal environment simulation (described in Chapter 5).

Chapter 5

A Novel Raster-Based Outdoor Thermal Climate Simulation Model

5.1 Introduction

According to a review of the existing models in Chapter 2, it is obvious that the models currently used mainly for microclimate analysis are UCMs and building-resolving models coupled with CFD. However, due to their characteristics (oversimplified city form or overly complicated models), both models are difficult to use in early-stage urban planning strategy analysis. Thus, inspired by the method developed by Yao *et al.* (2011), this study will use a network of nodes to construct multiple air zones. However, unlike previous studies, the construction of this node network will be built on top of a raster data structure. Each node will correspond to a raster element, and node-to-node interaction will be accomplished through the operations of raster analysis. The basic raster operations have been described in Chapter 4. This chapter focuses on the process of developing an urban climate model by combining raster operations based on the urban surface energy balance. As described in Chapter 4, the introduction of raster operations allows the proposed numerical model to perform a wide range of energy budget calculations in a short time. Meanwhile, by combining raster data operations, the proposed model is therefore able to assess the impact of different urban design elements (e.g., building-geometry, road width, trees, etc.) on the outdoor urban thermal environment in the early urban design process. Thus, this chapter will also use raster data operations as a framework for building numerical models of outdoor thermal climate simulations. The model is expected to assist in strategic urban planning by optimising the planning of the built environment in relation to the outdoor thermal climate in the early design/update phase. In order to build microclimate simulation models that can be used to parameterise urban surfaces, it is fundamental to understand the energy exchange processes on urban surfaces.

Understanding and predicting the precise impact of the urban built environment on the surface microclimate usually uses the surface energy balance equation. For this reason, the surface energy balance (SEB) is the basic starting point for modelling the urban climate. It is a formula for the conservation of energy on surfaces and volumes and is not limited by spatial or temporal scales. It can therefore be used to measure energy transfer and storage within urban systems and between them and the atmosphere. This includes, but is not limited to, roofs, walls, roads, human bodies, vegetation, the entire surface-atmosphere interface, or selected layers of the urban atmosphere. In general, both the urban elements immersed in the urban atmosphere and the system as a whole can be used to create energy balances.

5.1.1 Basic urban energy transfer and balance theory

(1) Surface energy balance on flat areas

In short, changes in SEB are key to driving changes in the surface climate. It describes the net result of surface thermal exchange (flux density in W/m^2). This

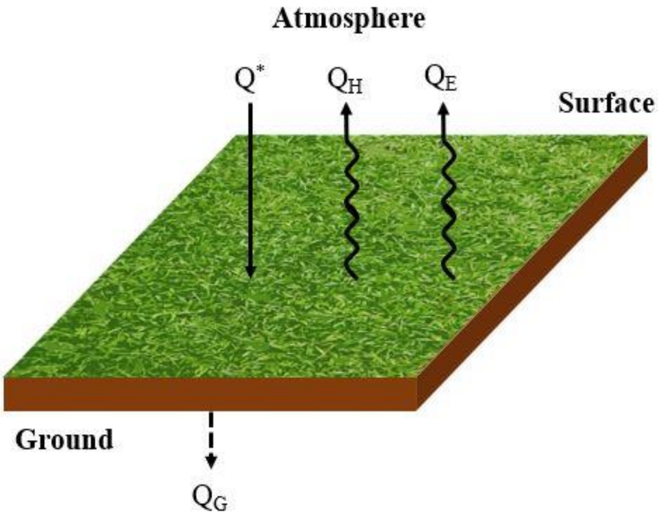

Figure 5.1: Schematic representation of the fluxes in the surface energy balance for a flat area. Arrows are drawn in the direction considered to be positive in the corresponding flux.

thermal exchange can take place in a small plane, in the elements or between the ground and the atmosphere by conduction, convection and radiation. Figure 5.1 shows an ideal case where all heat flux densities are restricted to the vertical direction. It is essentially a one-dimensional view of the horizontally extended plane. Complicated results due to horizontal heat transfer from distinctly different upwind surfaces can be avoided by choosing such broad planes. The energy balance of a flat surface can therefore be represented in the following Equation 5.1.

The flat surface energy balance equation:

Thus, a one-dimensional heat transfer energy balance equation at a flat surface can be expressed as:

$$Q^{*} = Q_H + Q_E + Q_S \tag{5.1}$$

Where Q^{*} is net all-wave radiation, Q_H is the density of turbulent sensible heat flow exchanged between the surface and the atmosphere, Q_E is the density of turbulent latent heat flow exchanged between the surface and the atmosphere and Q_S is the density of heat flow stored by the ground, which transfers sensible heat to the substrate by conduction.

In the above formula, the flux must be balanced on the surface to achieve the state of energy conservation. Note that Equation 5.1 is a true balance statement, unlike the equation used to configure the surface radiation budget in Chapter 4. This is because radiation is not a complete representation of the total energy of the system (it only represents one of the forms of energy). In simple terms, in a budget, it is not necessary for the sum always to be zero, it can have a surplus or deficit. However, in a conservation system, the sum of all terms, including the sign, must be zero.

(2) Surface energy balance in urban systems

In an urban environment, however, there is usually not a simple large flat area but a complex of numerous street valleys. For example, Figure 5.2 shows a relatively extreme street canyon situation within the urban canopy layer (UCL) in which all surfaces are impervious. In such a street valley, hard and impermeable man-made materials make up the entire surface. As mentioned in Chapter 3, the aerodynamics and radiation exchange in the upper atmosphere depend on the canyon patterns formed by buildings and roads. In such a street, water cannot be transferred properly from the substrate to the atmosphere. There are no plants to transfer water through the plant root system and stomata. In addition, the sealing of the underlying surface material also prevents its moisture from being replenished through the surface. Pipes for energy and water supply to and from buildings on both sides of the street (e.g., cables and pipes) are also usually present in such urban streets. In some tropical or hot summer regions, most buildings also have additional air conditioning units on their facades. The air conditioning system is used to create a comfortable indoor climate while increasing the accumulation of outdoor energy. The modifications to the ground cover brought about by the construction activities of these urban dwellers will affect the energy balance of the urban surface. Several fundamental transformations of SEB that accompany urbanization are also shown in this figure.

Figure 5.2: An extreme example, an alley where all natural materials are replaced by man-made ones.

As in the case of the street valley shown in Figure 5.2, urban development leads to a marked change in the surface energy balance. In contrast to the case shown in

Figure 5.2, the more complex surface structure also makes the energy balance process more tedious. In urban environments, artificial materials are often introduced to remove, replace or modify natural surface materials (e.g., soil and vegetation). The more three-dimensional surface structure of the city is also very different from the flat surface structure. The physical material properties and spatial structure of these urban elements result in changes in radiation, aerodynamics, thermal and humidity properties compared to natural surfaces. This also makes the micro- and meso-climates of the surface and Atmospheric Boundary Layer (ABL) very different. This chapter will focus on how to simulate changes in these properties, processes and phenomena based on raster analysis algorithms to achieve efficient urban surface climate predictions.

The urban surface energy balance equation:

For any single element of the urban surface (e.g., roofs, walls and roads) the energy balance can be constructed using a similar approach to Equation 5.1. However, as mentioned above, this single-surface treatment becomes impossible or inappropriate when dealing with some three-dimensional units joined together by multiple surfaces (e.g., a single building, a street valley or an entire city). This is because it has to deal with the possible sources of energy or energy sink factors

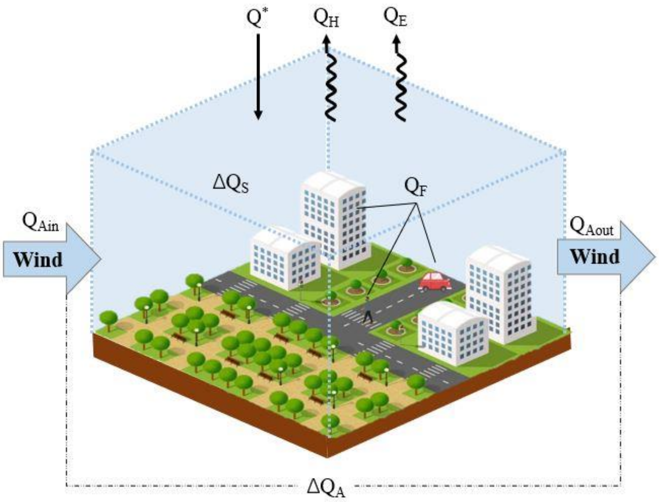

Figure 5.3: Schematic representation of the fluxes in the urban surface energy balance. Arrows are drawn in the direction considered to be positive in the corresponding flux.

affecting the whole city. In such an urban context it needs to be considered that each surface is individually coupled to the atmosphere. This will no longer be a simple calculation of the sum of the energy balances at the component surfaces. Their energy balance can also change due to the coupling of radiation, wind and turbulence effects on multiple surfaces. In addition, the energy content of the entire volume may change internally as a result of the warming or cooling of the material, air etc. Therefore, consideration of the energy-coupling between different urban elements is the basis for the development of surface urban climate models.

This formulation of the volumetric energy balance representing the response of the whole urban environmental system, as shown in Figure 5.3, has three new assumptions (Oke *et al.*, 2017c). First, it is necessary to consider the energy sources and energy sinks generated by the elements within the city. Secondly, energy exchange can occur not only at the top but on any other façade. Finally, there is an interaction between the facets. These assumptions are very different from the one-dimensional transfer approach expressed in Equation 5.1. The above assumptions largely restore the energy conservation of the three-dimensional city surface, but also increase the complexity of its expression. In practice, therefore, an integrated urban environmental system (a block or a whole city) is usually defined as an entire energy concept. The volume of this energy block concept is usually determined by the purpose and scale of the research (refer specifically to the description of scale in Chapter 2). The balance of such urban surface energy can be expressed as:

$$Q^* + Q_F = Q_H + Q_E + \Delta Q_S + \Delta Q_A + S \tag{5.2}$$

Where Q^* is net all-wave radiation, Q_F is the anthropogenic heat fluxes (It is the heat released in a volume by human activity, which is usually related to population density, traffic conditions and building type. See section 5.2.2 (2) for details), Q_H is the turbulent sensible heat fluxes, Q_E is the turbulent latent heat fluxes, ΔQ_S is the heat storage which represents the net change in heat storage of all elements of the city. Unlike Equation 5.1, it includes not only the heat storage in the ground but also the energy of other façades such as building materials and trees (see section 5.2.2 (4) for details), ΔQ_A is the net advected flux (the net energy added to or subtracted from the volume energy by windborne transport (see section 5.2.2 (5) for details)) and S is all other energy sources and sinks.

The above energy balance equation reveals the main processes of energy exchange in an urban environment. By calculating and modelling the energy term in the above equation, it can effectively predict the thermal climate of urban surfaces. This chapter focuses on developing an approach to urban climate analysis based on a raster data analysis model combined with urban surface energy balance equations. By introducing raster operations, (1) a new urban surface climate model similar to the raster-based algorithm in Chapter 4 was developed. (2) The newly proposed method uses multiple raster-based data operations to optimize the calculation of the variety of energy terms in the urban surface energy balance equation. (3) This also provides a more flexible and practical simulation method for modelling surface thermal climate conditions in different urban environments. It integrates the urban surface climate modelling process more effectively, enabling fast and brief simulations of the near-surface urban thermal climate.

5.2 A new raster-based urban energy balance simulation model

In order to create a fast simulation solution, the climate model builds physical processes based on the laws governing raster operations. The main physical processes to be connected are the same as those described in Chapter 4 and will be based on local raster data operations (See Chapter 4 for details). However, as there are some specific physical processes that require unique raster processes, these are described separately for each specific physical process. The entire numerical model is constructed as follows:

5.2.1 Input data for urban climate simulation

The main role of numerical models is to simulate real-world phenomena. This simulation process is achieved by establishing a link between a set of properties (e.g., temperature, material heat capacity, etc.) and a physical process (e.g., heat flux density). Therefore, when building a numerical model, it is essential to determine the necessary property data in addition to constructing a reasonable physical process. These sets of property data act as the input data for the numerical model. For urban climate models, there are usually two types of input data: meteorological files used to determine climate boundary conditions and urban surface properties files used to characterise urban morphology. This study therefore establishes the required input data for the constructed model as follows:

(1) Input weather data

Since the volumetric energy model assumed in Equation 5.2 is used to predict the exchange of energy, mass and momentum at the urban surface, the boundary conditions of the urban surface climate model are determined by the atmospheric state (Predictions from mesoscale atmospheric models can also be used as input values.). Therefore, the initial meteorological data ultimately required for the study were air temperature at ABL, wind speed, wind direction and global solar radiation. All input meteorological data in this study are derived from publicly available weather station data corresponding to the simulated cities. In addition, since the final results of the model are hourly outputs, these input data are also in an hourly time step.

(2) Input urban surface properties in raster form

As described in Chapter 3, the urban climate is strongly influenced by building geometry. The combined factors of the shape and orientation of the surfaces of buildings, roads and other artificial structures can affect the mechanical, thermal and radiative properties of the atmosphere. The values of these parameters depend on the shape and materials of the building, the thermal structure, the vegetation coverage on the roof and road, the sky view factor and the heating source inside the building, which is different for different building shapes, sizes and types. This also illustrates the importance of accurate and more detailed descriptions of urban information for urban climate modelling, which highlights the need to generate homogeneous descriptions of urban surface properties at fine resolution for input into urban climate models. Therefore, this study has constructed a dataset for characterizing urban surfaces based on the raster data structure mentioned in Chapter 3. This raster representation of the city's surface properties enables not only a high-resolution description but also the storage of multidimensional content, which also provides the base-line data for climate models based on raster operations analysis. This section summarises the input parameters required for the study, taking into account the urban information parameters obtained in Chapter 3 and the urban surface energy balance described in Equation 5.2. These input parameters used to describe the surface properties of the city can be summarised in three major categories, as shown in Table 5.1.

Table 5.1: Recognized parameters from satellite images for urban microclimate modelling.

General classification	Subcategory for each category	Parameter settings
Land surface classification	Buildings Roads Trees Grasses Bare soil Waterbody	Surface materials’ albedos Surfaces thermal conductivity Surface materials’ densities Surface materials’ specific heat capacities Surface materials’ potential evaporation rates Surface materials’ emissivity

Buildings geometry	Height of buildings Footprint of buildings	Wall positions Sky view factors (SVFs)
Buildings use types	Public Residential Commercial	Heat emission profiles of buildings Wall albedos Wall thermal conductivities Wall densities Wall specific heat capacities Wall emissivity

5.2.2 Development of the numerical climate model

Due to the three-dimensional geometry of the city, total solar radiation is unevenly distributed over the city's surface area. Generally, the net solar radiation and the anthropogenic heat flux balance the sensible heat flux, latent heat flux, net advected flux and conducted heat flux between the surface layer and the underlying layers. Therefore, after ignoring other sources and sinks of energy that are less influential in Equation 5.2, a general energy balance equation for an urban surface is:

$$Q^* + Q_F = Q_H + Q_E + \Delta Q_S + \Delta Q_A \tag{5.3}$$

Where Q^* is the net all-wave radiation, Q_F is the anthropogenic heat fluxes, Q_H is the turbulent sensible heat fluxes, Q_E is the turbulent latent heat fluxes, ΔQ_S is the heat storage and ΔQ_A is the net advected flux.

The energy balance equation above serves as the framework for the most basic physical process in this numerical model. Each energy term in Equation 5.3 will be calculated according to its own characteristics in combination with the above input data and reasonable raster operations. The operations of each energy term are described in detail below:

(1) Urban radiation budget

Solar radiation plays a major role in outdoor comfort and surface energy balance. The net total radiation in an urban microclimate is affected by the geometry (i.e. the location, orientation and shape of the building) (Shishegar, 2013). The total net solar radiation received on the surface is:

$$Q_R = K\downarrow - K\uparrow + L\downarrow - L\uparrow \tag{5.4}$$

Where Q_R is net radiation, $K\downarrow$ is incoming direct and diffuse short-wave radiation, $K\uparrow$ is reflected short-wave radiation, $L\downarrow$ is incoming long-wave radiation from the atmosphere and $L\uparrow$ is outgoing long-wave radiation from the surface.

Additionally, the net radiation energy absorbed by a canyon surface could be expressed as:

$$Q_R = (1-\alpha)(Q_{BH} + Q_D + Q_{env}) + Q_L \tag{5.5}$$

Where Q_R is net radiation, α is the surface albedo, Q_{BH} is the direct beam radiation on a horizontal surface, Q_D is diffuse radiation, Q_{env} is the reflection of radiation from the surrounding urban environment and Q_L is surface-absorbed long-wave radiation.

As this study has already developed a mature solar radiation simulation model based on raster operations, the specific calculation process is not repeated in this section (See Chapter 4 for details). In addition, the results of the developed radiation model can be used directly in the calculation of the surface energy balance. They are both stored and operated in a raster form data structure.

(2) The anthropogenic heat fluxes

Anthropogenic heat flux usually depends on the population density of the city. Furthermore, the seasonal temperature variability also tends to affect the heat flux from human activities. For instance, in some areas, more energy is used for ventilation whilst in other areas with cold winters, more energy is used for heating, especially at high altitudes. Similarly, the anthropogenic heat flux has a huge impact on the modelling of the urban energy flux as it accounts for at least 10% of urban surface energy (Grimmond, 1992). However, the amount of energy released by human activities such as space heating, transportation, air conditioning and industrial waste is not easily available. Thus, the value of anthropogenic heat is mostly obtained by estimations or indirect measurements (Yogeswaran, 2015). For estimation, the two most commonly used methods are top-down and bottom-up approaches.

The top-down approach is essentially a regional statistical method, which provides detailed statistics on all energy use in a city. These energy data are usually derived from official or publicly available reports or databases. The thermal equivalent in a region is then assessed by estimating the conversion process of the consumed energy to thermal energy. As these data are aggregated values, the data collection requires long time periods and low resolution at spatial scales. Therefore, when it is necessary to determine energy emissions at the micro-scale it is often necessary to match other information for determining the situation in time and space. This also allows the method to be commonly used for the assessment of total energy release over a large geographical area (e.g., a country or city) and over a long time period (e.g., a year). Therefore, this study does not use this approach to estimate anthropogenic heat.

The bottom-up approach explores the typical elements of an urban ecosystem, usually considering vehicles, people and buildings. The composition of the anthropogenic heat can be written as the following equation:

$$Q_F = Q_{FV} + Q_{FM} + Q_{FB} \tag{5.6}$$

Where Q_{FV}, Q_{FM} and Q_{FB} represent vehicular, human metabolic and building heat emissions, respectively.

Taking building energy consumption estimation as an example, the use of the building energy model (BEM) tool is a common approach. This tool is used to assist in the energy design of buildings. It takes into account, on the one hand, the electricity and fuel consumption arising from the internal heating and cooling needs of the building, appliances, lighting, etc. On the other hand, it takes into account the external energy balance (including climatic conditions and solar geometry) caused by the internal spatial structure, the building materials and the activity patterns of the occupants. Finally, it calculates a time-series energy consumption profile for a particular building type by coupling this range of internal and external building conditions. Such a method allows the estimation of energy consumption not only on fine spatial scales but also over shorter time steps. In addition, in order to simplify the calculation of the BEM in practice, it is common to quantify the energy released by a representative group of building types. In addition, in order to simplify the calculation of a practical estimation of the BEM, some studies have used quantifications of the energy released by a representative set of building types (Sailor, 2011). As this study aims to model surface energy processes more efficiently, the estimation of anthropogenic heat is also calculated by quantifying a representative set of categories. Thus, the anthropogenic heating of the buildings is estimated based on the building types obtained in Chapter 3. In addition, as traffic conditions and population density data are highly dependent on temporal and spatial variations, the data are not extracted in advance in Chapter 3. They need to be considered separately once the location and timing of the study have been determined. The process of estimating these three components of anthropogenic heat is described in detail below.

Vehicle heat emissions

In the past, due to the lack of detailed information on changes in traffic density over time and changes in the heat emissions of different vehicle types, a relatively simple method was often used to quantify traffic heat (Yogeswaran, 2015). This method was later refined to examine hourly spatial changes in heat emissions from traffic by disaggregating data using a top-down approach. Furthermore, Smith *et al.* (2009) proposed a bottom-up, high-resolution, estimation method by analysing traffic flow data. The corresponding calculation method can be expressed as:

$$Q_{FV}(t) = n_m(t) * L * EF_m \tag{5.7}$$

Where n_m is equal to the number of vehicles of type m, t is the hour of the day, L is the length of the road and EF_m is a speed-dependent fuel consumption emission factor, which is available from the UK Transport Research Laboratory (Boulter *et al.*, 2009).

From Equation 5.7 it can be found that the heat generated by the vehicle mainly lies in the estimation of the traffic flow and speed. Thanks to our previous research in a spatial-and-temporal-based method for rapid particle concentration, it is now possible to estimate traffic flow based on existing traffic data (Xiong *et al.*, 2020). The data obtained to represent the traffic situation in the city (see Figure 5.4) shows the traffic conditions coloured green, orange, red and black to represent smooth,

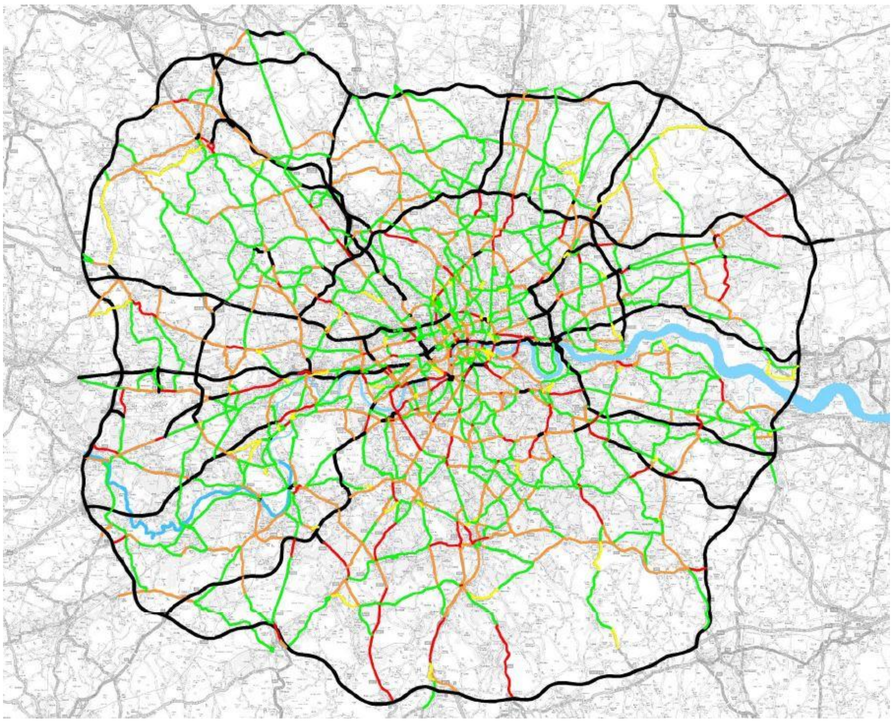

Figure 5.4: Statistical map of average daily vehicle traffic in 2010, Source: UK Department for Transport National Road Traffic Census Counts (NRTCC).

slow, congested and severely congested respectively. Therefore, this study estimates the number of vehicle types and driving speeds in different congestion states through real-time traffic conditions. It should be noted that the values represented by the colours of traffic data from different sources may be slightly different. The actual traffic estimation will be implemented according to the specific situation represented by the data. In addition, in areas where traffic data is not available, estimated values can also be assigned based on actual conditions.

Metabolic heat emissions

Metabolic heat emissions are usually estimated based on demographic data. Allen *et al.* (2011) assert that the waste heat generated by humans can be determined by assuming the value of the average human metabolic rate combined with population data. Therefore, the metabolic heat emission calculation will be combined with the human population map from the GIS data. WorldPop (www.worldpop.org, an open-source database of global population densities) has access to GIS data on population (Lloyd *et al.*, 2019). Taking London as an example, the population data obtained is shown in Figure 5.5 (The data is displayed in the form of raster data with a spatial resolution of 100m). The calculation formula can be expressed as:

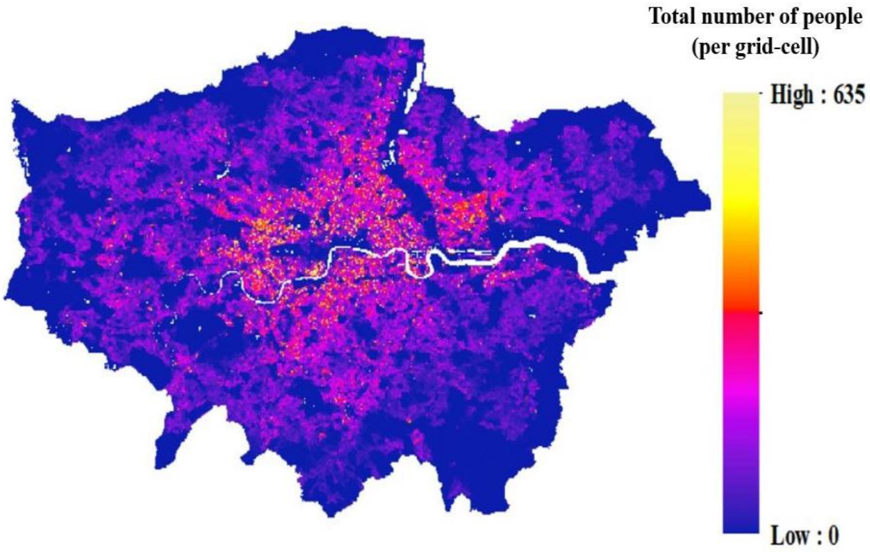

Figure 5.5: Statistical map of population in 2010, London (Resolution in 100m), Source: DOI: 10.5258/SOTON/WP00645.

$$Q_{FM}(t) = n(t) * POP \tag{5.8}$$

Where t is the hour of the day, n is equal to the number of people and POP is the human metabolic rate.

Building heat emissions

Anthropogenic heat generated by buildings accounts for the majority of total heat emissions (Hamilton *et al.*, 2009). Its calculation has had a major impact on the results of the anthropogenic heat budget. As described above, both top-down and bottom-up methods are used to estimate the waste heat emission from buildings. The top-down approach typically uses annual energy statistics from large areas and then distributes the statistics over the year based on time and season, while the bottom-up approach uses more detailed energy data for individual buildings (Usually hourly). Since a simple classification of building types has been performed during data input in this study, a bottom-up approach by connecting the energy consumption of different building types will be used. The heat emission from buildings can be calculated using the following equation introduced by Smith *et al.* (2009) with different Urban Morphology Types (UMTs):

$$Q_{FB} = \frac{\sum A_{UMT} Blt_{UMT} H_{UMT}}{A_i} \tag{5.9}$$

Where A_{UMT} is the area covered by each UMT within grid square i, Blt_{UMT} is the proportional built surface covered by each UMT, H_{UMT} is the typical heat emission by each UMT and A_i is the area of grid square i.

Therefore, based on the equation above, the daily anthropogenic heat profile of UK buildings can be presented as in Figure 5.6. In addition, since locations used for the simulation are all within the university area, the calculation of anthropogenic heat is only based on the energy used by the education building. In other words, the user needs to adjust the energy consumption for anthropogenic heat calculation based on the type of buildings in the simulated area, which could refer to the energy consumption profiles of different buildings (Kilpatrick and Banfill, 2011; Pombeiro *et al.*, 2012).

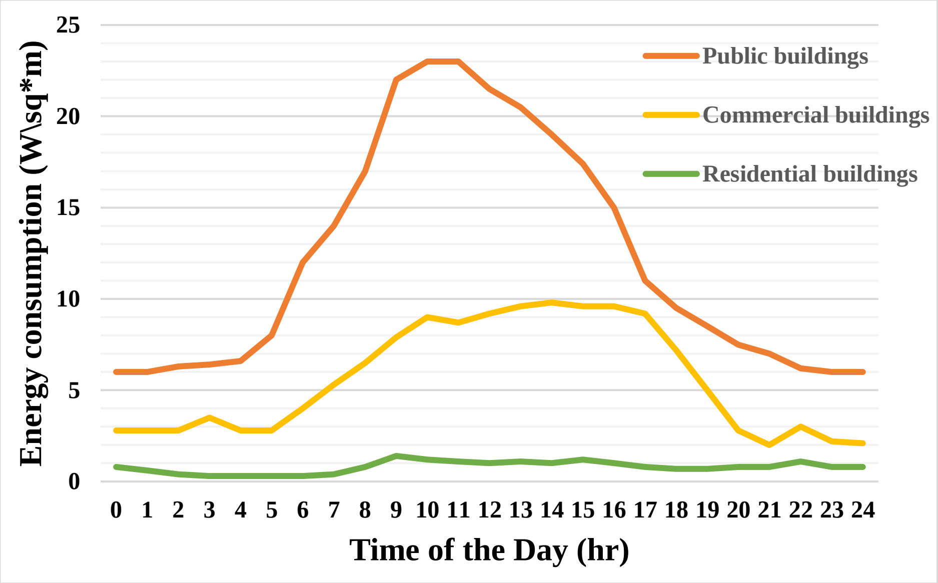

Figure 5.6: Daily Energy consumption profile of three building types for anthropogenic heat emission calculations.

(3) The density of latent heat fluxes

Latent heat fluxes affect soil water dynamics, surface runoff and the overlying atmosphere, which plays an important role in urban energy balance (Koster, 2015). However, Gentine *et al.* (2016) claimed that precise measurements and estimates of urban latent heat flux and evapotranspiration are sparse in both time and space. Meanwhile, due to the lower albedo and surface absorption of buildings and roads, urban surfaces have higher sensible heat fluxes rather than latent heat. Therefore, this study will use the SLUCM method to estimate the latent heat flux which means that this source of the energy is only roughly estimated based on the properties of different surface materials without too much discussion. According to Yang *et al.* (2015), the turbulent latent heat fluxes at the surface of natural/artificial landscapes can be expressed as:

$$Q_{Eveg} = -C_H E_p \tag{5.10a}$$

$$Q_{Eart} = -\frac{\delta}{d_{eng}} \emptyset E_p \tag{5.10b}$$

Where Q_{Eveg}, Q_{Eart} are the latent heat fluxes for natural/artificial landscapes respectively, C_H is the exchange coefficient, E_p is the potential evaporation rate, δ is the porosity of engineered materials, d_{eng} is the maximum water-holding depth dependent on pavement materials and $\emptyset$ is the water retention depth.

Since this study is mainly concerns simulations in the early planning stages, it does not take into account rainfall or water accumulation on the road. The latent heat energy generated by man-made materials in Equation 5.10b will be ignored in this study. All the above physical parameters are assigned by combining the results of surface material classification from Chapter 3. In addition, the vegetation evaporation rate used in this study was determined by referring to studies conducted by Moreo *et al.* (2007) and Moss *et al.* (2019).

(4) The heat storage

As mentioned earlier, there is a heat exchange between the urban building fabric and the outdoor air. During the day, the urban surface absorbs solar radiant heat which heats solid materials such as the ground, buildings, plants and water bodies. After the temperature of the underlying surface rises, the heat stored inside the underlying surface dissipates heat to the surrounding air and sky through convection and radiation. The heat received during the day is usually released at night. In this process, the underlying surface is the most important energy conversion site. Its temperature is related to the effects of various energy exchanges. However, urban development has seen the replacement of large quantities of natural materials (e.g., soil or vegetation) by building materials (e.g., bricks, wood, cement, etc.). The impact of this urbanization process is particularly prominent in the changing thermal properties of the underlying surface of the city. This also complicates the thermal properties of the urban subsurface. In this way, the thermal conductivity and heat capacity of urban ground are larger than those in the suburbs. This difference in the thermophysical properties of the underlying surface materials in urban and suburban areas results in significantly higher ground heat storage in urban rather than suburban areas. Therefore, it is important to take reasonable account of the heat stored by the urban surface when estimating urban surface energy.

In this study, the focus will be on the heat stored in the building envelope and the urban ground. Material differences in building facades and ground coverings are also assigned values based on different rasterised representations of building types and surface classifications. Ultimately, the stored energy is represented by constructing the energy conservation equation at the buildings' outer surface or the ground surface.

Surface energy model

The heat transfer through the surface can be calculated by the one-dimensional heat conduction equation for each cell:

$$\rho c \frac{\partial T}{\partial \tau} = \frac{\partial}{\partial x}(\lambda \frac{\partial T}{\partial x}) \tag{5.11}$$

Where T is the temperature, ρ is the physical property density, c is the physical property specific heat capacity, τ is the time step and λ is the thermal conductivity.

Therefore, the energy balance model of the wall and the ground surfaces, which is used to calculate the surface temperature, can be expressed as:

$$-\lambda \frac{\partial T_{sur}}{\partial x} = Q_{cond} + Q_{conv} + Q_R + Q_{Lsur} \tag{5.12}$$

Where T_{sur} represents the surface temperature, λ represents the thermal conductivity, Q_{cond} represents the conducted heat from the wall/underground temperature control point to the surface, Q_{conv} represents convective heat transfer between air and surface, Q_R represents net radiation heat absorbed by the surface and Q_{Lsur} represents long-wave radiant heat from the surface itself.

The energy terms Q_{cond} , Q_{conv} and Q_{Lsur} in the above equation can be expressed respectively as:

$$Q_{cond} = U(T_{conrol} - T_{sur}) \tag{5.13a}$$

$$Q_{conv} = h(T_i - T_{sur}) \tag{5.13b}$$

$$Q_{Lsur} = -\varepsilon\sigma T_{sur}^{4} \tag{5.13c}$$

Where T_{sur} represents the surface temperature, T_{conrol} represents the temperature at the control point of the underlying surface (the control point in the wall is the surface of the inner wall of the building) and is 20m underground. T_i represents the air temperature corresponding to air zone i, U represents the heat transfer coefficient of the underlying surface, h represents the convective heat transfer coefficient, ε represents the emissivity of the emitting body and σ represents the Stefan-Boltzmann constant. The specific calculation of the energy of Q_R has been discussed in detail in Chapter 4.

(5) Turbulent transfer in the atmosphere

As mentioned in the previous section, building shapes, pedestrian sidewalks, the street H/W ratio, building orientations, urban corridors and green spaces are all parameters that affect the heat dissipation of the urban surface. Hence, understanding the details of airflow plays a key role in exploring how heat can be exchanged between street canyons and their surroundings. In many studies, CFD models are the technology of choice for this purpose (Tominaga *et al.*, 2015; Derakhshan and Shaker, 2017). The CFD could clearly analyse turbulence at multiple scales from a single building to the boundary layer and represents a more realistic impact of the city on the atmosphere. However, as described in Chapter 2, it requires considerable computing resources and huge initial and boundary conditions, which is inconsistent with the purpose of this study. In contrast, the UCM uses a pattern that decouples the airflow model from the energy budget equation. By adopting a similar method to the UCM, the air velocity is assumed to be the same, which is provided by the weather data for this area. Additionally, the airflow zone is set up based on the image pixels in GIS and each cell represents an airflow zone. In addition, since turbulent heat fluxes are generated by the presence of gradients of relevant thermal properties in the air, a simple way to establish suitable gradient fields is also required in this study. When established, this gradient field can be used to better analyse the direction of heat flow in the air. Therefore, a simplified approach to wind analysis is provided in this study, taking into account the directional characteristics of the raster data. The entire airflow analysis is constructed as follows:

Wind corridor judgment based on raster surface watershed analysis

In GIS analysis, it is very common to analyse the characteristics of a surface through the digital surface model (i.e., DEM) constructed from raster data, such as slope, hillside orientation, visibility, etc. The watershed analysis is one of the main uses of surface models in GIS. A watershed is a catchment area where surface water discharges to a common outlet. In other words, its main use is to analyse the flow of water through the terrain. For example, important tasks such as estimating the volume of water flowing in rivers and accumulating in reservoirs, flood hazard assessment and the extent of soil erosion all require knowledge of how water moves across surfaces. The principle of this analysis is to simulate the direction in which water will pass over a specific surface. Therefore, when the surface model analysis object is changed from water flow to airflow, it is possible to achieve an analysis of the surface wind direction.

Taking the analysis of water flow direction as an example, DEM is a raster model often used in flow direction raster data analysis since the DEM data presents the elevation of the ground surface (the main factor for judging the direction of water flow) in a simple structural way. The key to modelling water flow through a plane is to determine the direction in which water will flow from each DEM cell. This is obtained by considering all the pixel values in the local 3*3 neighbourhood range, that is, the application of the neighbourhood operation introduced in Chapter 4. The simplest approach is to assume that the water will flow to the adjacent cell with the steepest slope from the centre cell. This will gradually become the lowest estimate using neighbourhood operations. However, since the adjacent diagonals are slightly further from the centre cell than the rest, this method is unsuitable for practical calculations. Specifically, the downhill grid point does not represent the main downhill direction from the centre point. The 3*3 virtual DEM grid in Figure 5.7 shows terrain with a slope of about 180° (i.e., south). However, following the above assumptions, the water flow from the centre cell will be towards the southeast cell (a direction of approximately 135°).

150	149	147
130	126	120
110	108	98

Figure 5.7: A fictitious 3*3DEM data grid (values represent virtual elevation values). This terrain slope is almost due south; however, water from each cell will flow approximately southeast.

Strictly speaking, the fluid does not flow from one planar point to another and the local neighbourhood cell must be taken into account. For example, Figure 5.8 shows a model of water flowing from the element around each cell. Thus, a more refined approach is usually based on the following two points of view:

i. Water coming out of a cell is always in the same direction. However, this does not force water directly into neighbouring cells. Unless water flows directly into adjacent cells, water will be dispersed into some adjacent cells.

ii. The water originates from a face rather than a point and may not follow the same direction. In a case where water runs off the top of the hill, this may result in water being distributed to all neighbouring cells.

Algorithms for different flow directions will differ from complex algorithms that require each cell to be calculated. However, the complexity will be the square of the total number of cells, since each point needs to be calculated. A more efficient comparison is the single-flow approach. The 8-direction method (D8) is a widely used single-flow method which assigns the flow direction of a cell to point to one of the surrounding 8 cells. The direction of flow is determined by the direction of the steepest slope or the direction of the greatest descent for each cell. Therefore, the formula for calculating the flow direction is as follows:

$$Direction_{flow} = \Delta Z/distance \tag{5.14}$$

Where $Direction_{flow}$ is the direction of the steepest descent, that is, the direction of water flow, ΔZ is the elevation difference between the centre cell and the calculation cell and $distance$ is the centre distance between the centre cell and the calculation cell.

If multiple cells have the same maximum drop in direction, the adjacent cells will be enlarged. This process will continue until the steepest descent direction is found. If all neighbouring cells are higher than the processing cell, it is considered noise and will be filled with the lowest value of its neighbours and there will be flow to that cell. However, if a one-cell sink is adjacent to a physical edge of the raster or has at least one NoData cell as a neighbour, it will not be filled. This is due to insufficient information about neighbouring cells. For a cell to be considered a true one-cell sink, all neighbourhood information must be present. The raster analysis method for the D8 flow direction is shown in Figure 5.8. As shown in the figure, by calculating the distance-weighted slope between the central cell and the other 8 adjacent cells, the flow direction of the central cell in (A) is determined. For the four closely adjacent cells (i.e., up, down, left and right), the calculation of the slope is to divide the elevation difference between the central cell and the adjacent cell by 1. For adjacent cells at the four corners, the slope is calculated by dividing the elevation difference by √2 (As shown in Figure 5.8 (B)). The final result shows that the steepest slope is from the centre cell to its right cell (as shown in Figure 5.8 (C)).

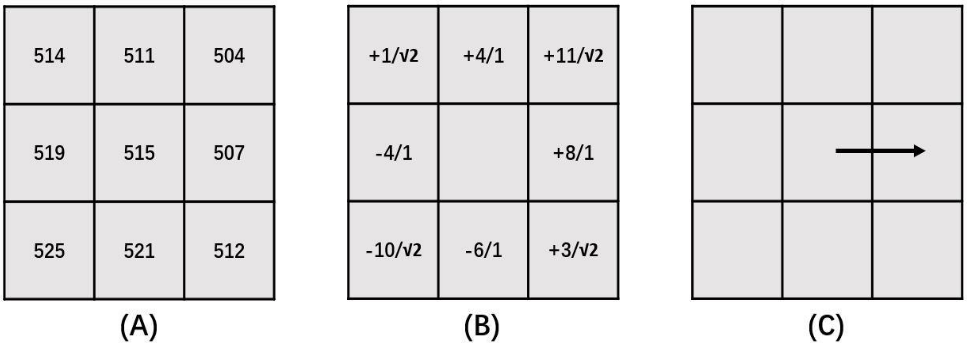

Figure 5.8: Schematic diagram of D8 (8-direction method) flow direction raster algorithm. (A) is a fictitious DEM raster data that needs to judge the flow direction of its central cell; (B) is the result of judging the distance weight slope of the surrounding 8 cells according to equation 5.15 (The left side of the fraction is the height difference between the centre cell and this cell, and the right side of the fraction is the distance from the centre cell to this cell); (C) is the fluid flow direction of the central pixel judged according to the calculation results of (B).

The above is the process of judging water flow based on DEM raster data. It is obvious that in the above method, DEM data is the basic input data for flow surface analysis. This is because it physically determines the direction of water flow. Therefore, in this study, it is essential to construct surface data that can represent wind potential in a similar way to DEM data. As mentioned in Appendix I, a large number of urban morphological parameters have been used to study their relationship with environmental parameters such as temperature and wind in the city. Among them, FAI and the SVF index are the parameters most related to wind speed and wind direction. This section will focus on SVF, since it has been discussed and calculated in Chapter 4. Existing studies have shown a high spatial correlation between wind conditions and SVF in urban environments (Yang *et al.*, 2013; He *et al.*, 2020). Therefore, some studies have used it as a criterion for evaluating urban ventilation performance in cities (Ren *et al.*, 2018; Lai *et al.*, 2021). In general, the higher the SVF value in the city the better the ventilation performance and the more the wind tends to pass through it. Therefore, it can be determined that in the same direction, the air tends to flow to the area with a large SVF value. There are many methods for estimating the SVF and the methods used in this study are described in detail in Chapter 4. The research will establish DEM-like wind force raster data based on the SVF value to judge the wind direction. For this reason, in this study, the raster with wind forces from high to low was first established according to the wind direction. The established method is mainly determined according to the x and y coordinates of the position of each cell. For example, in a 3*3 grid as shown in Figure 5.9, each cell has (x, y) coordinates to represent its position. When the wind direction is α, each cell can generate a gradient grid in this direction according to Equation 5.15. Then, after superimposing the calculated gradient grid and the calculated SVF grid data, a new grid can be generated. This raster data is an SVF value with a gradient generated according to the wind direction. Unlike traditional SVF data, this result reflects the general direction of the wind. Finally, applying this raster to the above-mentioned D8 flow direction analysis, the direction of the wind in the built environment can quickly be determined.

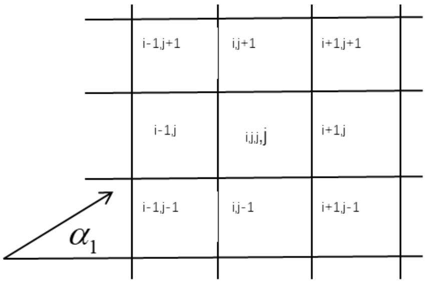

Figure 5.9: Schematic diagram of air area division.

$$G_{wind} = x * cos\alpha + y * sin\alpha \tag{5.15}$$

Where x, y are the coordinates of the cell.

After determining the trend of the wind in the built environment, the individual air zone for each cell is established as the basis for the analysis of the thermal value of each cell.

Raster-based airflow zone

As the raster data consists of cells, each cell has its own space. The airflow zone is set up based on the raster cells and each cell represents an airflow zone (see Figure

5.9). Since the study expects to reflect the effect of wind more simply, the wind speed, which is provided by the meteorological data in advance, is assumed to be the same for all air zones. According to the wind velocity and direction of the weather data, the velocity along the X and Y coordinates is calculated:

$$U_X = U * \cos \alpha \tag{5.16a}$$

$$U_Y = U * \sin \alpha \tag{5.16b}$$

Where α is the angle between the wind direction and the X coordinate and U is the wind speed at each pixel.

The mass balance for each air zone can be expressed by the following equations:

$$m_{X(i,j)} = \rho_{X(i,j)} * A_{X(i,j)} * U_{X(i,j)} \tag{5.17a}$$

$$m_{Y(i,j)} = \rho_{Y(i,j)} * A_{Y(i,j)} * U_{Y(i,j)} \tag{5.17b}$$

Where A_X is the opening area along the X coordinate, A_Y is opening area along the Y coordinate, ρ is air density and i, j is the number of the airflow zone.

The total mass balance for a pixel or airflow zone $(i, j)\ is$:

$$m_{(i,j)} = m_{X(i,j)} + m_{Y(i,j)} \tag{5.18}$$

Where m_X is mass of air along the X coordinate and m_Y is the mass of air along Y coordinate. The energy contained in the air is removed from one airflow zone to another zone with the movement of the mass of air. Hence, the amount of energy is based on the mass flow of $m_{X(i,j)} m_{Y(i,j)}$, which is calculated from the mass balance equations.

The heat transfer by airflow can be calculated using the following equation:

$$\Delta Q_A = Q_{AX} + Q_{AY} \tag{5.19}$$

Where Q_{AX} is the heat exchange due to the airflow along the X coordinate and Q_{AY} is the heat exchange due to the airflow along the Y coordinate.

The heat exchange due to the airflow through openings is:

$$Q_{AX} = C_P m_{X(i-1,j)} T_{(i-1,j)} - C_P m_{X(i,j)} T_{(i,j)} \tag{5.20a}$$

$$Q_{AY} = C_P m_{Y(i,j-1)} T_{(i,j-1)} - C_P m_{Y(i,j)} T_{(i,j)} \tag{5.20b}$$

Where C_p is the heat capacity, T is the air temperature at the airflow zone, m_X is the mass of air along the X coordinate, m_Y is the mass of air along the Ycoordinate and i, j is the number of the airflow zone.

(6) Heat balance in the air zone

Once all the above energy terms have been analysed, an energy balance equation can be established within each air zone (i.e., each cell) built on the basis of the raster. The heat balance of each air zone can be expressed using the following equation:

$$Q_i = Q_{Conv} + Q_F + Q_E + \Delta Q_A \tag{5.21}$$

Where Q_{Conv} is the convective heat flux density transfer from surfaces, Q_F is the anthropogenic heat flux density, Q_E is the latent heat flux density and ΔQ_A is the net heat flux density transferred by airflow.

As the air has the capability to store heat to change its temperature, the heat stored in the airflow zone can be expressed by:

$$Q_i = \rho_i C_{pi} V_i \frac{\partial T_i}{\partial t} \tag{5.22}$$

Where ρ is density, C_p is heat capacity, V is volume, T is temperature, i is the number of the air zone and t is time.

To resolve all the above equations, the finite difference method has been implemented. The solution technique in this method is based on the Urban Surface Energy Balance (SEB) equation and the solution program has been compiled using map algebra based on raster operations. Additionally, all the above physical parameters will be assigned by combining the results of urban surface information in the raster format obtained in Chapter 4. After synthesizing all the above urban processes, the simulation flowchart shown in Figure 5.10 can be obtained.

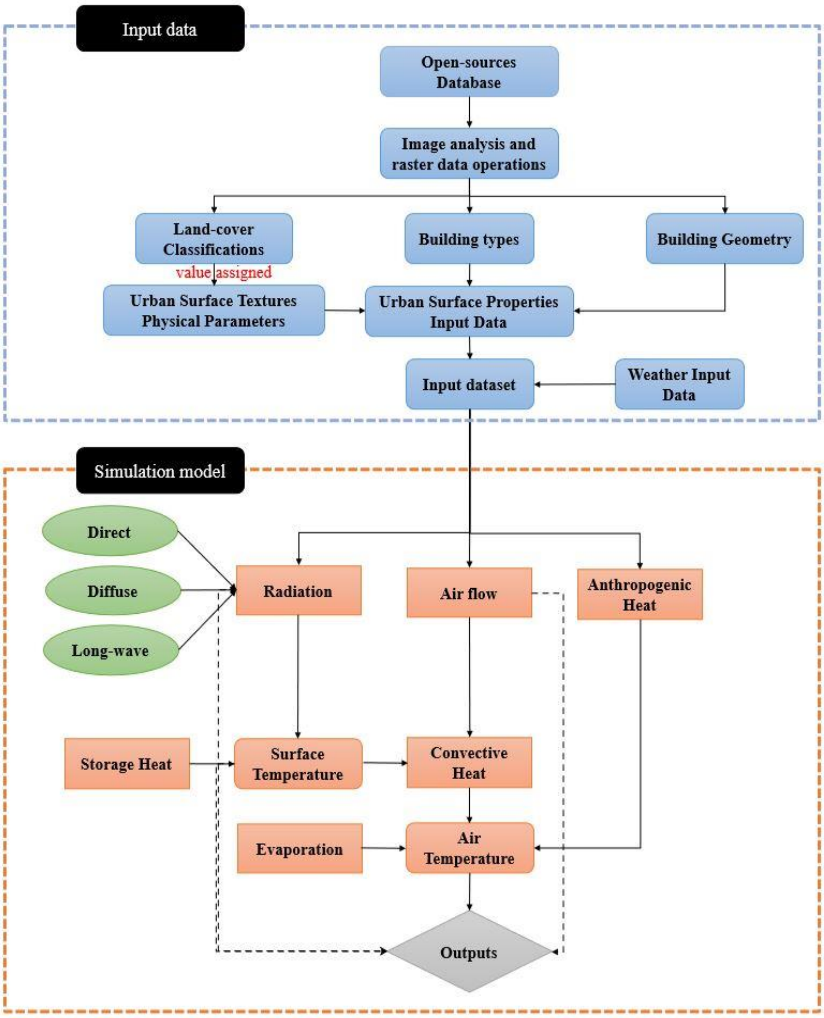

Figure 5.10: A brief framework of proposed numerical method for urban climate simulations based on raster operations.

5.3 Model validation

As mentioned in Chapter 4, it is important to validate numerical models against observations. Validation is indispensable in ensuring that the proposed model can be relied upon to accurately reproduce and predict urban surface climate characteristics. To do this, the study used microclimate data collected at two different sites in the UK for comparison. The two different experimental datasets were chosen for validation mainly because they have different properties. This will be described in the subsequent model validation. First, the proposed climate model was validated using the same microclimate data for London that were used in Chapter 4.

5.3.1 Data validation in London

To understand how this model performs in an urban centre, a data comparison between simulated data and measured data was conducted for the London area. The site chosen for comparison in London is shown in Figure 5.11, which is the same measurement point as that used in Chapter 4. The experimental configurations and instrument parameters involve the experimental scenarios described in Chapter 4. By modelling and simulating the areas in Figure 5.11, the results of the temperature simulations at the measurement locations can be obtained. Comparing the simulation results for the six points with the measurements at the same locations gives the results in Figure 5.12. As can be seen from the graph, overall, the simulation results for all six points correspond closely with the measured results. Despite the absolute values of the simulated and measured results occasionally varying considerably at some points in time, the results are still considered reliable

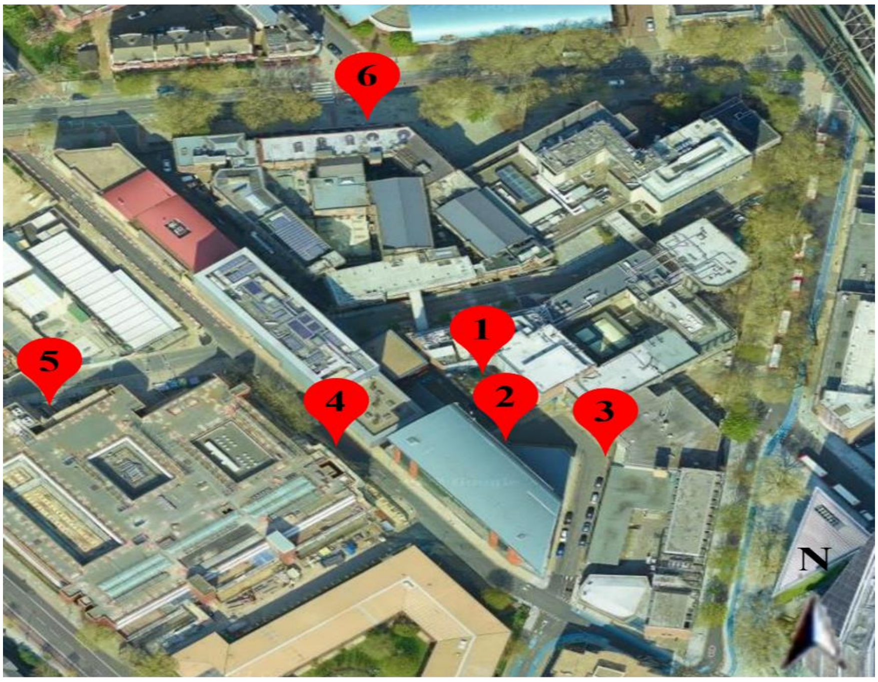

Figure 5.11: London field measurement site at Elephant and Castle, United Kingdom. Source: Google Earth.

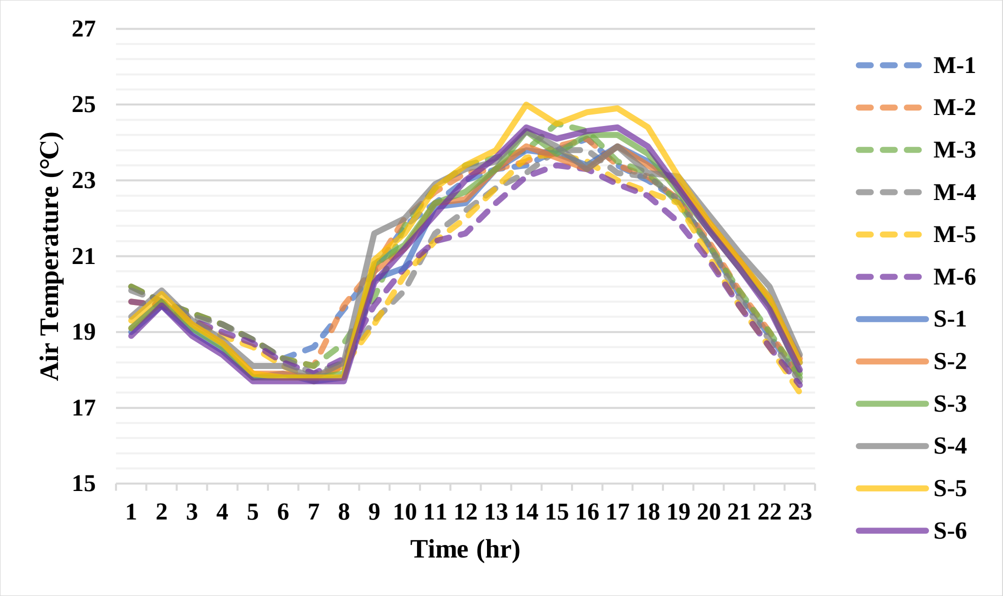

Figure 5.12: Comparison of measured and simulated results for six measurement locations (July 21, 2010). In the figure, M represents the measurement results and S represents the simulation results. Numbers 1-6 correspond to the respective locations of the measurement points in Figure 5.11.

since the pattern of variation is the same. In addition, a linear fit (Figure 5.13) to all measurement points also showed a high degree of agreement between the measured and simulated results.

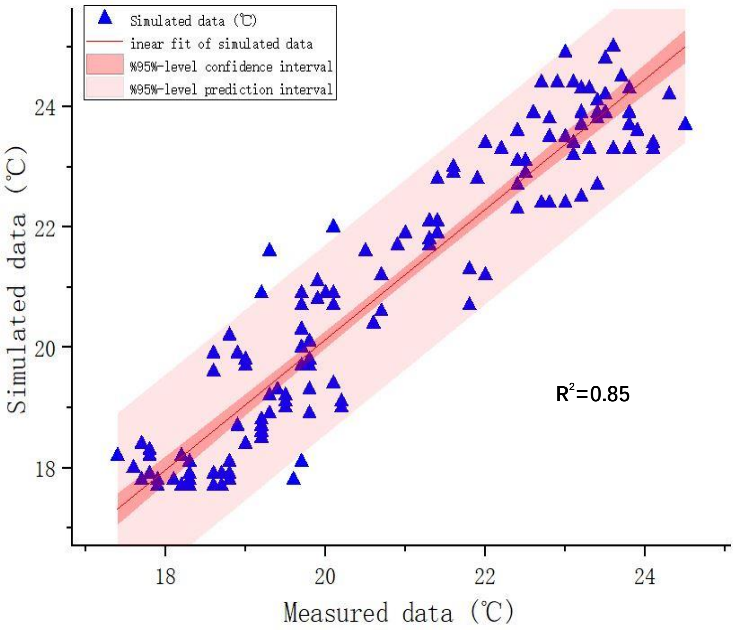

Figure 5.13: Air temperature comparison at the London experimental site on July 21, 2010.

5.3.2 Data validation at the University of Reading

For validation purposes, continuous observation data is important. In order to further explore the stability of the proposed model, a more continuous set of data covering a wider range of climatic conditions was used for comparison. This dataset was collected at the University of Reading and covers a full year of microclimate data. The details of the experiment are as follows:

The experimental site at the University of Reading

The simulation results are validated against our experimental data obtained from a field campaign carried out on the University of Reading campus, thanks to the EPSRC EP / N009797/1 project led by Yao (2009). Figure 5.14 shows the building complex where the outdoor experiment was conducted. The complex covers the same area as the simulated place (350 x 300m^2) and there are a total of six buildings considered in the simulation. Their dimensions, orientations and surrounding conditions are given in Figure 5.14. The building heights vary between 6.2m and 11.6m. While only one building has concrete walls, the other buildings' walls are made of bricks. The ground surface is mainly a grass lawn with asphalt pedestrian footpaths and access roads to buildings. The vegetation cover on the site is also displayed in Figure 5.14.

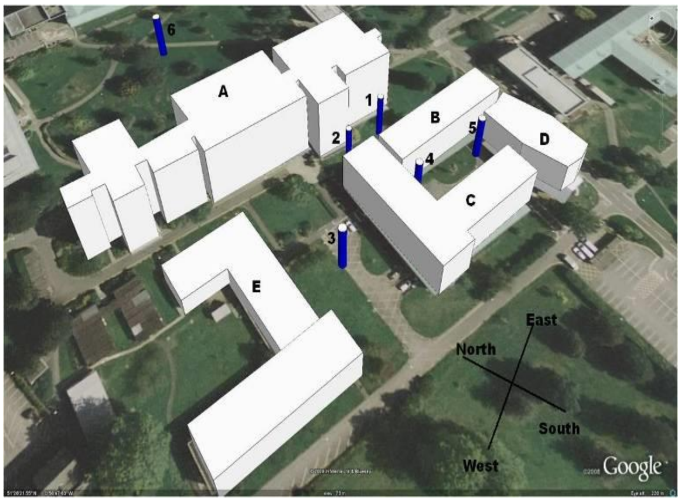

Figure 5.14: Layout of the building complex for simulation at the University of Reading, United Kingdom. Source: EPSRC EP / N009797/1 project led by Yao (2009).

The microclimatic variables of the air temperature, the wind speed and direction, the air humidity and the global solar radiation (the total value of the direct and diffused components on a horizontal surface) were measured at a height of 4m at several locations within the building complex. The six locations of weather stations at the Reading site are displayed in Figure 5.14. These measurement locations are labelled as Mast-1, Mast-2, Mast-3, Mast-4, Mast-5 and Mast-6. The accuracy of the integrated sensor suite (ISS) of the weather station for measuring each climatic variable is 0.56°C for air temperature, ± 5% for the wind speed, ± 7 degrees for the wind direction, ± 3% for the air humidity and ± 5% for the solar radiation. These measurements were logged locally at each mast, at five-minute intervals, again on a continuous basis. The distance between them varies from 20m to 116m. The weather data for different seasons were chosen to validate our model. This allows for a better exploration of its stability in different seasonal conditions.

Data comparison for different seasons

As mentioned above, measured data and data calculated by the simulation program were chosen for comparison in the data validation. The results of these comparisons are shown in Figure 5.15 and Figure 5.16. Overall, the time profile in Figure 5.15 shows that the simulated and measured data show a consistent trend. Nevertheless, the Figure 5.15 shows that although the overall trend is extremely similar, the absolute errors are relatively large for some time periods. Using the data in Figure 5.15 from 0100 to 0600 hours on 4 January as an example, it can be seen that the overall simulated trend for this time period is generally consistent with the actual measured values. However, the simulated values are overall higher than the measured data. This is mainly due to the fact that the meteorological input data for the study used local weather station data as input for the meteorological boundary conditions. Specifically, when the weather station measurements differ significantly from the climatic conditions at the actual simulated site, the simulations usually produce some quantitative deviation in the results. This use of weather station data

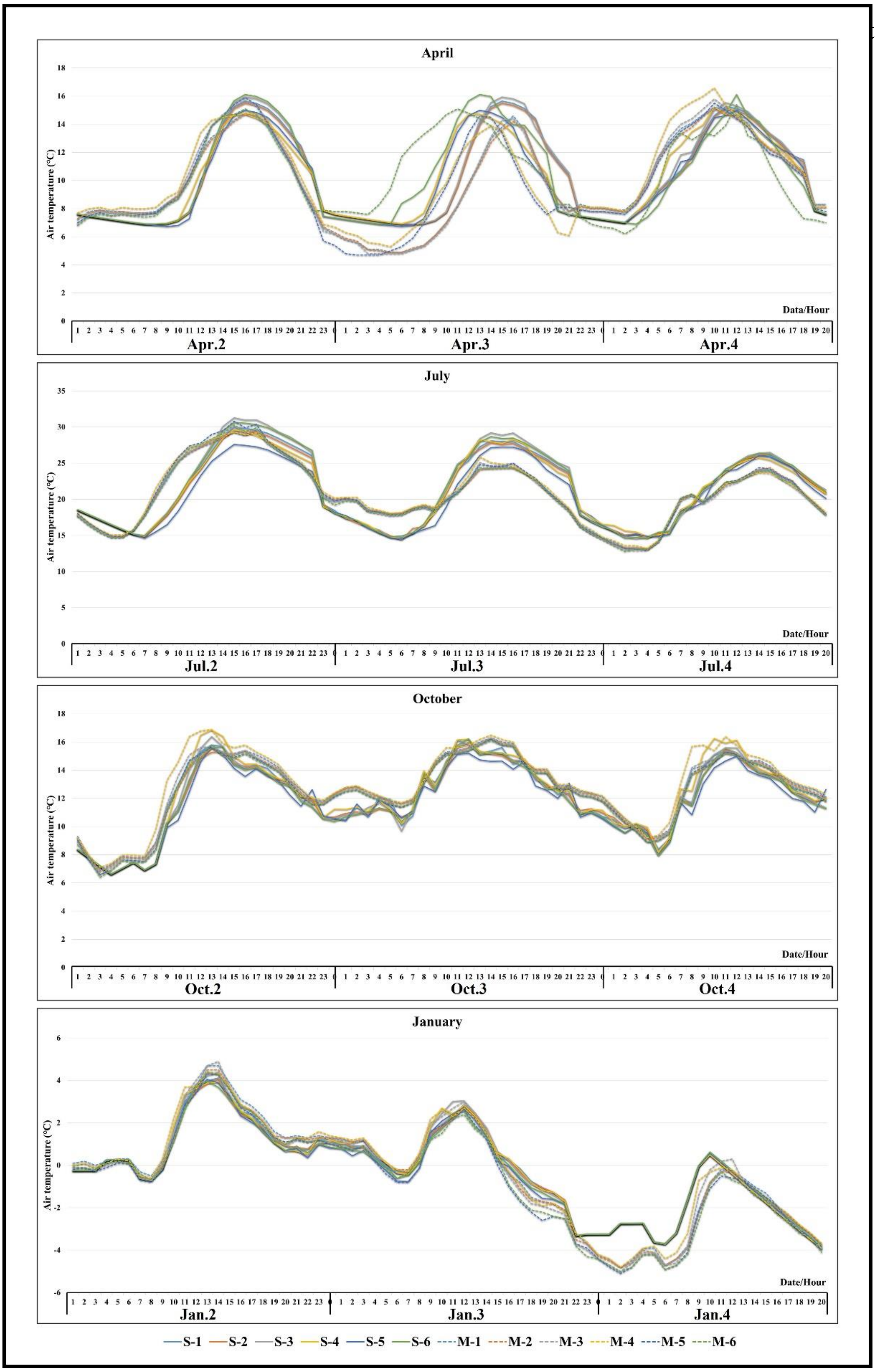

Figure 5.15: Comparison of measured and simulated results for six measurement locations in London for different seasons (2009). In the figure, M represents the measurement results and S represents the simulation results. Numbers 1-6 correspond to the respective locations of the measurement points in Figure 5.14.

the main purpose of the urban climate model is to quickly represent the microclimate temperature trends designed for the urban environment. Such deviations that do not affect the overall trend representation are acceptable. Indeed, in future studies, it would be helpful if detailed climate boundary conditions could be provided in a concise manner for the corresponding simulated locations, which would further improve the simulation accuracy of the model.

To verify the reliability of the method, the results for different seasons are compared separately to draw conclusions. As can be seen from Figure 5.16, the data for the four different months of April, July, October and January, corresponding to the four

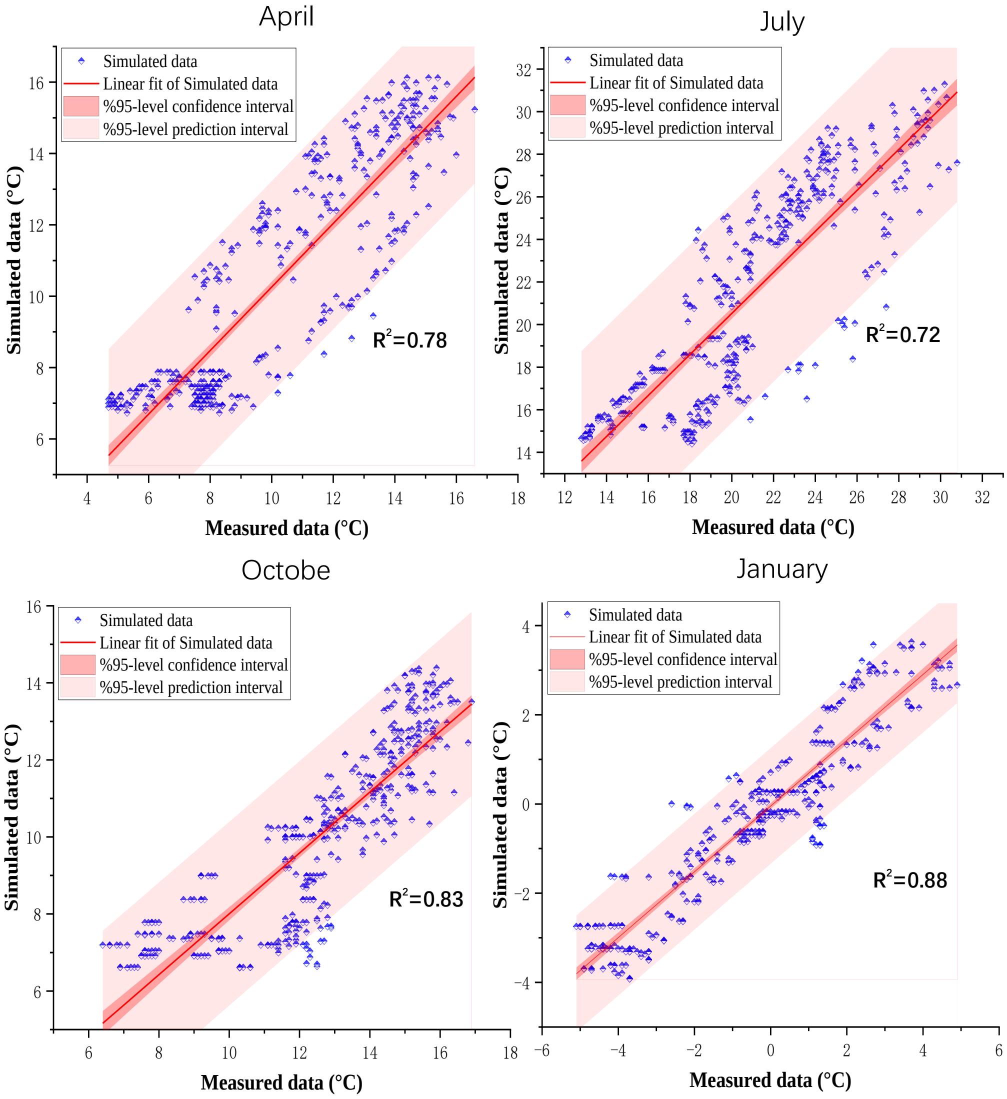

Figure 5.16: Air temperature comparison in four different seasons at University of Reading site.

seasons of spring, summer, autumn and winter, are classified and compared. In addition, a total of three days of data were used for comparison in each month. In general, comparative results for all seasons have relatively high consistency. To be more specific, the results for January and October have a confidence level above 80% and April's fit is also close to 80%. Although July's confidence level is lower than the other three months, the confidence level still exceeds 70%. Considering that the main purpose of this method is to give certain reference opinions at the beginning of planning, credibility higher than 70% is acceptable.

Furthermore, the main reason for the reliability of the simulation data in July being slightly lower than in other months may be related to the simplification of this method. Specifically, this method does not currently consider reflections and long-wave radiation inside the building in order to obtain results quickly, which may have a greater impact on the microclimate in summer. On the other hand, the scatter plot results of July show that the temperature trend is not a simple increase, as there is a curve relationship compared with other months' results. In order to find out the specific cause of the curve trend, we compared the data for each day in July. After comparison, it was found that the comparison result on July 2nd is the reason for the curve. Therefore, we verified the simulation data on July 2nd separately as shown in Figure 5.17. Compared to the experimental data and simulation data in detail, it can be found that the high-temperature value at the Mast-5 station on July 2, caused the simulation results to be relatively lower than the measurement results and showed a curve trend in results. Considering the geographical location of different stations, the reason may arise from the strong solar radiation at that station at that time (due to different cloud conditions). However, the transmission and diffusion values used in all simulation areas are the same. Therefore, the accuracy of the simulation will decrease when this special case occurs. In addition, since solar radiation under different cloud conditions is considered in this method, it can be used to simulate cloudy and sunny conditions except when the cloud relationship in the same area is too complicated.

Thus, this model can simulate the outdoor temperature distribution at different times at a neighbourhood scale. Since the model calculation is based on different surface materials, it can more intuitively reflect the impact of the combination of different architectural elements on the microclimate of the simulated area. Additionally, by calculating direct solar radiation, diffuse radiation, long-wave radiation and heat in the air under the different urban textures (the computer program is made using the Map Algebra base in raster data operations), the relationship between the microclimate and urban structures can be calculated. The calculated results are restored in raster format as output images. The attributes of the different textures' parameters have been referred from the published manuals and the value has been adjusted to approximately meet the actual conditions which should ensure the parameter inputs into the model for simulating the building complex on the selected area are correct. Furthermore, the model can not only simulate the actual urban climate conditions through satellite images but also achieve comparative simulations for different city designs by simply modifying the raster data.

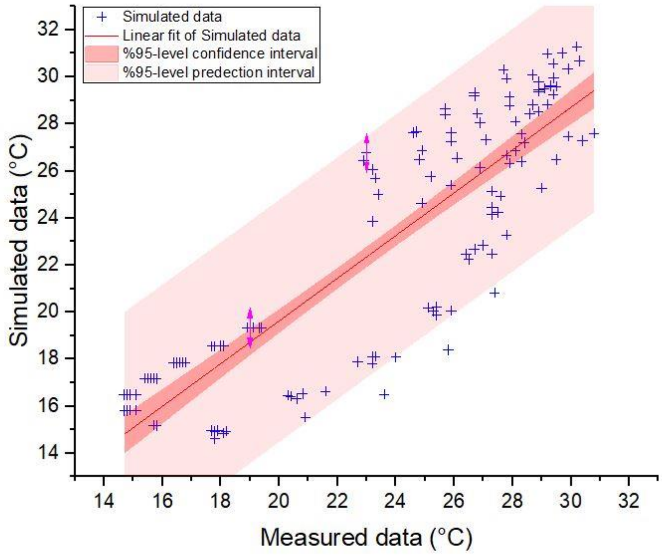

Figure 5.17: Air temperature comparison at the University of Reading site on July 02. 2010.

5.4 Results and discussions

Through the above-mentioned model, a new method that can efficiently present the outdoor thermal conditions in the built environment is proposed. This model is similar to the radiation model proposed in Chapter 4. Both of these numerical methods are built up using raster operations analysis. As in Chapter 4, the verification results of this model will also be discussed by comparing them with measured data. This section also focuses on the results that the newly proposed climate model can produce and their characteristics. Note that as the radiation-related simulation result has already been discussed in Chapter 4, it will not be repeated in this section. This section will only discuss wind corridors, surface temperatures and outdoor thermal environment results.

5.4.1 Wind corridor

In this chapter, a new and simple method of wind corridor analysis is proposed by means of a flow direction algorithm that combines raster data. This calculation method has been described in section 5.2.2 (5). The airflow in the city under certain wind boundary conditions is shown in Figure 5.18. This method is a very simple flow direction algorithm to quickly represent the airflow in a city. At the same time, it is clear from the analysis process of the wind corridor described in 5.2.2 (5) that the simulation results of the wind direction in each cell are directly influenced by the SVF results. It is of interest to carry out a sensitivity analysis of the wind simulation by inputting the results of different search radius sky view factor (SVF) calculations. This is because the raster resolution and fixed search radius determine the quality of the SVF calculation results (see Chapter 4 for details). As this study uses a fixed high resolution of 1m for all raster files, determining the appropriate search radius is key to the SVF calculation. The same building blocks from Chapter 4 are used here for the example analysis. The basic geometry of the buildings analysed is therefore the same: the highest building height is approximately 17m, the lowest building height is approximately 7m and the average building height is approximately 12m. In addition, the SVF results entered during the sensitivity test were also set to a constant search radius of 5m, 10m, 20m and 50m for different cases. This is also set up to be consistent with the sensitivity test of the SVF results. The results of the input SVF are therefore consistent with those shown in Figure 4.22 (resolution of 1m). In the analysis in Chapter 4, it was already known that the difference in the search radius of the SVF results mainly affects the values in the more open areas. Therefore, in order to investigate the impact of different SVF input values on the wind corridor analysis, six main points in more open areas were extracted for comparison. The exact locations of these six points are shown in Figure 5.18(A). Extract the wind direction results of the pixels at the same positions marked in Figure 5.18 and the results in Table 5.2 can be obtained. From these results, it can be seen that the results for all 6 points are not greatly affected by the change in SVF value. Considering that the wind direction is mainly determined by the wind direction gradient established by the SVF value, the change of the SVF

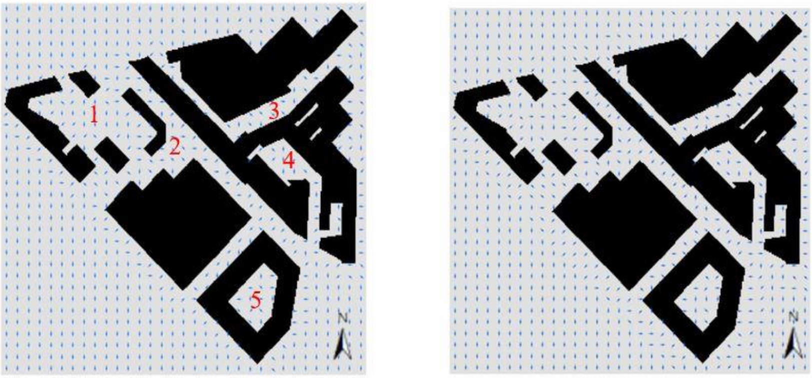

(A) R=10m (B) R=20m

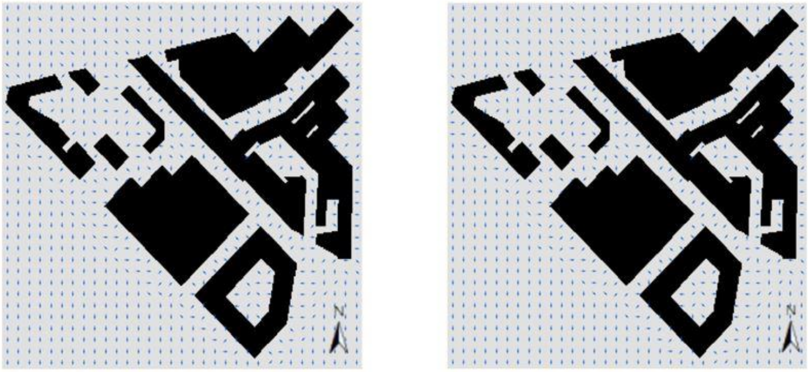

(C) R=50m (D) R=100m

Figure 5.18: Result of airflow directions calculated by SVF value for different search radii with 1m resolution.

value search radius will change this trend when it is less than 10m. This is because the SVF value of wider streets cannot be truly represented when the search radius is too small. This also allows the wind corridor results calculated based on the SVF search radius metric to be unaffected when it satisfies the basic conditions for representing street characteristics. Therefore, the search radius of 20m set in this paper will not affect the simulation results.

Table 5.2: Comparison of airflow direction values calculated under different SVF search radii.

Search Radium	***Site 1***	***Site 2***	***Site 3***	***Site 4***	***Site 5***
10m	45°	270°	90°	90°	90°
20m	0°	270°	315°	45°	90°
50m	0°	270°	315°	45°	90°
100m	0°	270°	315°	45°	90°

5.4.2 Surface temperature

Since this study has established an energy balance formula based on the surface of each pixel, the temperature of the surface can also be output as a result. As described in Section 5.2.2 (4), the heat conduction process is based on a single cell volume in the raster data. Therefore, the associated radiation raster analysis results will be incorporated during the calculation of the surface temperature based on the raster conduction analysis. Since solar radiation is the main factor affecting the outdoor thermal environment of buildings, the distribution of solar radiation directly affects the quality of their outdoor thermal environment. For the calculation model, the analysis of the distribution of solar radiation energy in the building complex is the first task (see Chapter 4). After obtaining the radiation conditions in the building group, how to compare these data with the different material properties of the underlying surface of the building group and establish calculations becomes the key. In order to obtain the initial physical attribute data of the entity building group, an indirect assignment method was carried out for the classification of the solid surface and the type of building obtained in Chapter 3. The thermal physical parameters (including density, thermal conductivity, specific heat, etc.) of each material on the surface or underlying surface are assigned to the classification through the grid operation and they are stored in the form of digital information in the raster data (See Chapter 3) and make their own raster data files as the basic information of the heat conduction analysis process, which is convenient for unified calling in the mathematical model. After the data files required in the calculation process of cell heat conduction are completed through the grid analysis process, each cell body in the building group grid contains this information. The energy balance mathematical model in Section 5.2.2 for each cell in the raster is called and solved separately. The temperature distribution obtained from the solution is also kept in the temperature distribution raster data file of the underlying surface and provides data for calculating the convective heat transfer between the underlying surface and the air in the flow area, thus integrating the energy balance mathematical model with the grid operation analysis process.

5.4.3 Outdoor thermal climate

Finally, the model can quickly simulate the outdoor thermal climate in the environment of the building group by coupling all the energy models. In the specific solution process, first, a grid digital model of the building group is established

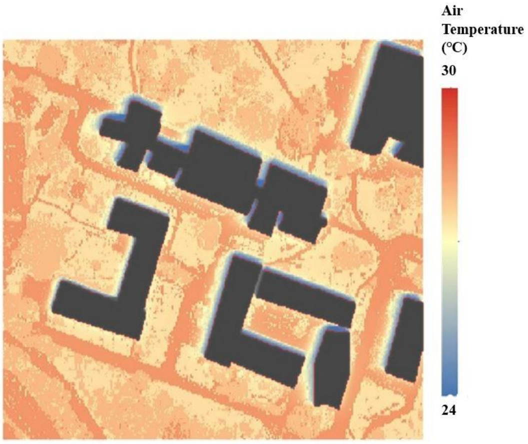

Figure 5.19: Examples of simulation results for outdoor thermal climate conditions of building groups at the University of Reading site at 12 o’clock. (The black parts are buildings).

according to the planning map or actual geographic information. The respective data on building layout, height, building materials, greening and other factors are stored as raster data. Secondly, according to the layout characteristics of the building, the model constructs a raster-based multiple flow area network model which realizes the combination of the raster operation process and the solution of the flow process, that is, information such as the size and position of the airflow zone is realized through the basic information stored in the grid data. While providing this information to each flow model, these flow models also provide the calculated air temperature and other information to the raster data which is stored as additional information and used when calculating the temperature of the underlying surface. In addition, due to the fixed cell position of raster data, the flow area of each position in the cell can be automatically matched. In this way, the mutual call of grid analysis technology and the mathematical model is realized and the analysis of the outdoor thermal process for the entire building complex is completed. Finally, the regional air temperature and outdoor thermal environment conditions of the building group can efficiently be obtained, as shown in Figure 5.19.

5.5 Summary and conclusions

This chapter presents a raster-based numerical method for simulating the urban outdoor thermal climate. By combining the urban surface properties information model based on raster data, the geographic information data-processing method and the urban Surface Energy Balance (SEB) equation, a high-resolution microclimate rapid analysis integration model based on raster data units is directly established. In order to validate the credibility of the proposed climate model, two sets of UK-based field measurements were used for comparison to validate the model. All validation results show good agreement, which proves that the model can effectively and quickly simulate the urban outdoor thermal climate. At the same time, since the entire proposed model is built within a rasterised data framework (all data storage and analysis operations), it is clear that it presents the following features:

- All urban surface properties information is stored and represented as raster data in multiple bands. This unique way of representing geographic information allows for faster construction of urban information models for urban climate modelling and data input for the description of urban surfaces. At the same time, this more flexible and easier-to-build urban surface information model also facilitates comparative simulation for different scenarios.
- The model does not require a separate spatial coordinate system for calculations between individual nodes. This is because raster data in a GIS-based framework has a unique coordinate reference system.
- The raster data analysis operation is used to connect different energy balance models. It provides an efficient and fast mode for practical simulation operations, mainly thanks to the special map overlay algorithm for raster data.
- Similarly, based on its structural properties, raster data consists of an infinite number of grids with numerical information. In this study, separate thermal climate zones are created directly from each cell of the raster data. This allows the model to calculate the surface temperature simply by combining the DEM data with the surface information raster matrix. Such rasterised data processing also allows the model to output high-resolution simulation results as they are calculated independently on the basis of each raster cell.
- Additionally, based on raster data analysis operations for flow directions, the model has proposed a new multi-zone method for airflow analysis. The proposed method enables the simplified analysis of wind corridors in urban building complexes with the help of raster data flow analysis principles. This provides additional data support for thermal climate analysis in urban environments.
- Building this rasterised model based on a GIS platform allows the method to quickly visualise the simulation results. This allows scenario models to be

compared more quickly and can be used in practice to evaluate design options in the early planning stages. The most obvious advantage of the proposed model is its ability to rapidly perform high-resolution urban thermal climate simulations.

Taking into account the features of the model mentioned above, this method is very suitable for rapid urban microclimate simulation to support urban design in both urban construction and renewal as it facilitates early urban design evaluation. The tool can calculate the urban air temperature, ground surface temperatures, solar radiation falling on the ground, etc. using the simplified physical model. The program is sufficiently powerful to provide information on climate variables at any location with satellite images. The simulated local climate data can be used for building-energy simulations and outdoor thermal comfort analysis. The model can be applied to the research area with specific building information and the network nodes are relatively coarse with less information on spatial heat distribution. Hence, it provides useful information for sustainable architectural design, urban planning and outdoor comfort assessment. At the same time, a simple case study also demonstrated its practicality. This simple case study is detailed in Chapter 6. In general, this chapter presents a new approach to the analysis of urban surface thermal climate environments by comprehensively combining raster data manipulation with urban surface energy balance processes.

Chapter 6

Case Study and Discussions

6.1 Preamble

The newly developed model allows rapid high-resolution assessment of urban thermal climate environments at the neighbourhood scale. It can be seen as an intermediate model between the Urban Canopy Model (UCM) and the CFD-based microclimate model. The numerical model structure is designed for a more effective and practical assessment of the design of urban environments in relation to microclimate at an early planning stage. In current urban developments, data on outdoor microclimatic features including air temperature and surface temperature are desired for outdoor thermal comfort assessment and also for the design of low energy buildings. The method developed in this thesis can provide microclimate data to engineers and building designers. In the planning and design phase, this model offers urban designers and planners the opportunity to modify their ideas by iterating the simulation of changes with ease and within a modest time frame. The essence of this novel method is its flexibility and ease of operation. Consequently, it helps planners improve their design in the context of assessing urban microclimates. This chapter uses the newly developed model to carry out case studies in two different scenarios and discusses the potential application of the model. One of the case studies is an outdoor thermal climate simulation in an existing urban context, which can provide a quantitative reference for urban renewal work related to the thermal environment. Another case study is a simulation analysis of a construction project under design which can be used to optimise the design of the built environment in relation to the thermal climate.

6.2 Case study for the existing urban context

6.2.1 Basic information for the study area

An important feature of the newly developed model is the ability to quickly assess the outdoor thermal climate environment at the neighbourhood scale. This allows the model to quickly provide quantitative parameters for thermal environment-related assessments in urban renewal work at an early planning stage. In order to demonstrate more intuitively the function and role of the proposed model in specific application scenarios, several microclimate simulations in different neighbourhood contexts are performed in this section. Three 1km*1km areas have been chosen for this case study, using London (51°N, 0°E) as an example. Figure 6.1 shows the specific locations of three selected regions in London which are numbered 1, 2 and 3 respectively: Area 1 is west of central London, Area 2 in north London and Area 3 northeast of London. The three areas were selected regarding two main indicators of building: Volume Density (BVD) and Fractional Vegetation Cover (FVC), both of which directly affect the urban thermal environment (Isa *et al.*, 2020; Qi *et al.*, 2022).

Figure 6.1: The 3 selected case site locations in London.

The specific calculation process for these two indicators is as follows. Firstly, the BVD indicator can be obtained with the help of Formula I.2 in Appendix I. According to this formula, the BVD mainly reflects the ratio of the building volume to the corresponding land area. Thus, the BVD can be obtained by zonal statistical analysis (See Chapter 4 for details) of Digital Elevation Model (DEM) (1m resolution) data for the whole London area. DEM data is produced using the open-source data provided by the UK Environment Agency (2015). The results in Figure 6.2a show the BVD values for the whole of London for a partition of 1km*1km. Secondly, the FVC index is calculated using the Normalized Difference Vegetation Index (NDVI) according to Equation 6.1a. NDVI is a standardised index used to

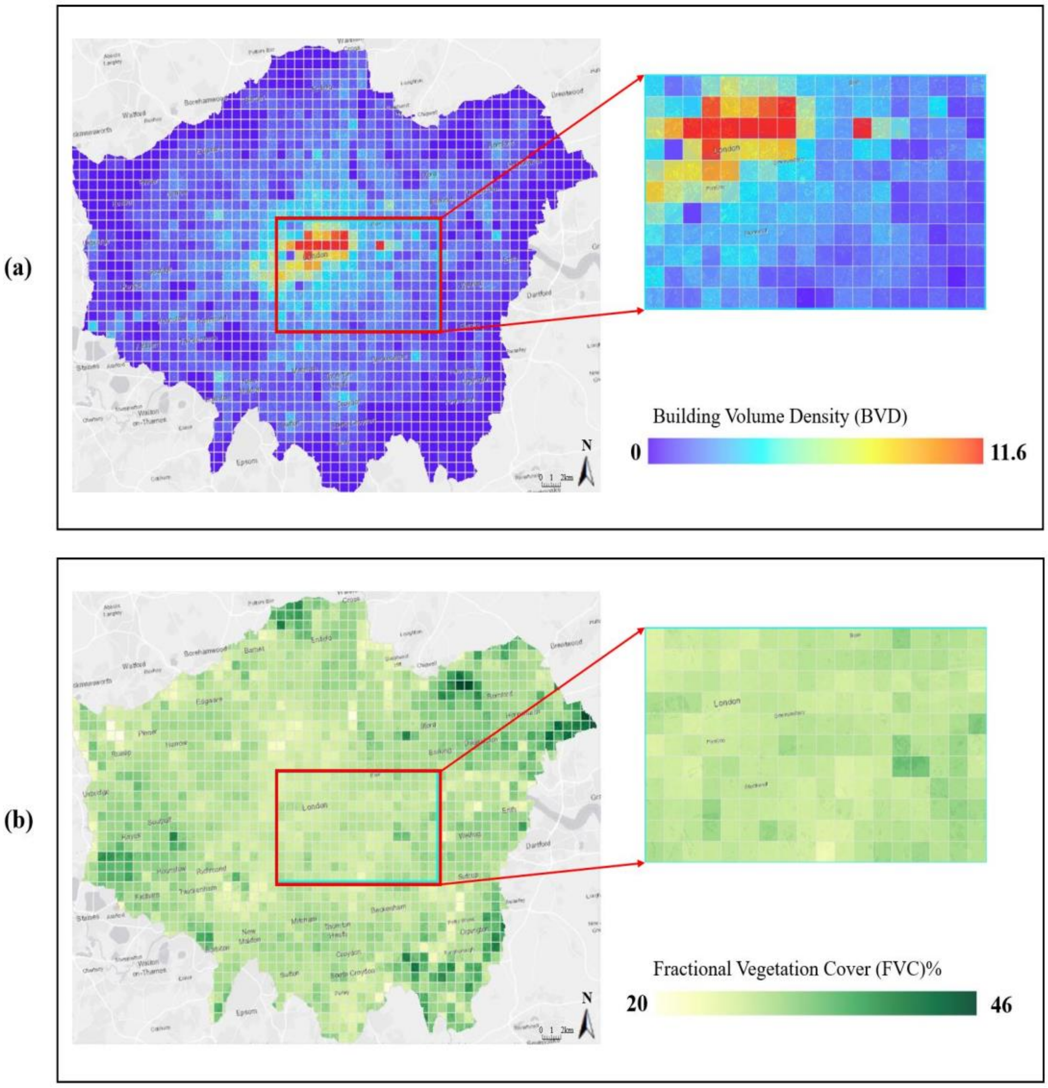

Figure 6. 2: The BVD and FVC values for London with 1km*1km resolutions. (a) shows BVD values calculated based on London DEM data. (b) shows FVC values calculated based on London NDVI values for July 21, 2020.

generate images showing the amount of vegetation. This index is usually obtained from remote sensing images in the red and near infrared red (NIR) bands according to Equation 6.1b acquired by Landsat 8 (Jeevalakshmi, Reddy and Manikiam, 2016). As the calculation of FVC and NDVI is well established and has been discussed in numerous studies (e.g. Song *et al.*, 2017; Anees *et al.*, 2022), it will not be repeated in this section. Similarly, zonal statistics for the FVC values for London give the average value of a 1km*1km grid as shown in Figure 6.2b.

$$FVC = \frac{NDVI-NDVI_{min}}{NDVI_{max}-NDVI_{min}} \tag{6.1a}$$

$$NDVI = \frac{NIR-R}{NIR+R} \tag{6.1b}$$

Where $NDVI_{min}$ is the normalized value of pure soil cells, $NDVI_{max}$ is the normalized value of pure vegetation cells, NIR is the cell value for NIR band images and R is the cell value for red band images.

Table 6.1: Basic morphology indicators of the 3 selected case sites.

Area Number	Fractional Vegetation Cover (FVC)%	Building Volume Density (BVD)	Building Coverage Ratio (BCR)%	Number of Buildings	Mean Height of Buildings (m)	Centre Coordinates
Area 1	36	2.86	23	365	10	0.19°E,51.52°N
Area 2	25	1.76	25	521	6.2	0.01°E,51,56°N
Area 3	38	1.82	25	480	7.5	0.12°E,51.57°N

After filtering based on the BVD and FVC values calculated in Figure 6.2, the three areas shown in Figure 6.1 were selected. The urban morphology parameters for the three selected regions are shown in Table 6.1. Whilst Areas 1 and 3 have similar vegetation cover, Area 1 has a higher building volume than Area 3. Conversely, the building volumes in Areas 2 and 3 are almost identical, but vegetation cover is much lower in Area 2 than in Area 3. Once the simulation areas have been determined, the environment is modelled according to the method described in Chapter 3. The numerical model in Chapter 5 is then used to obtain the corresponding outdoor thermal climate predictions. A typical summer day (July 21, 2020) is selected as the meteorological data input for this case study simulation. The selection of the meteorological data time refers to the date of the remote sensing data used for the NDVI calculation.

6.2.2 Estimation of outdoor thermal climates

Hourly air temperatures were calculated for the three selected 1km*1km areas using the model developed for this study. Figure 6.3 shows the daily variation in predicted air temperature for Area 1 with a resolution of 1m. Its results show significant daily variations in temperature in urban street valleys in both the temporal and spatial domains. The maximum air temperature was around 28°C at 4.00p.m. The air temperature at 10.00a.m. local time was around 10°C lower compared to the maximum temperature. At the same time, comparing the map of air temperature

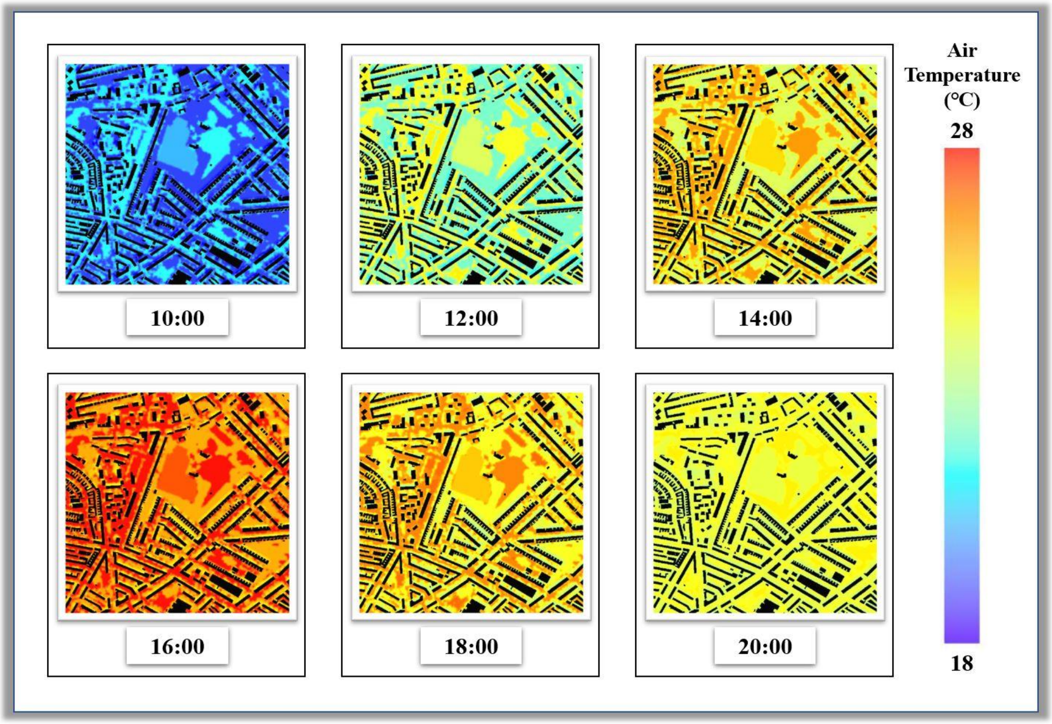

Figure 6.3: The daily variation of predicated air temperature for selected Area 1 in London on July 21, 2020. (The black parts are buildings).

distribution at different times, it can be seen that not only is the temperature at 16:00 the highest, but the temperature difference within the region is also quite large. Such mapping helps to quickly screen the area for possible high-temperature areas and optimise them. Thus, the output of the model can quickly provide high-resolution outdoor thermal climate quantification data for a neighbourhood area. This will help urban planners to assess outdoor thermal climate conditions in existing urban environments more visually and efficiently.

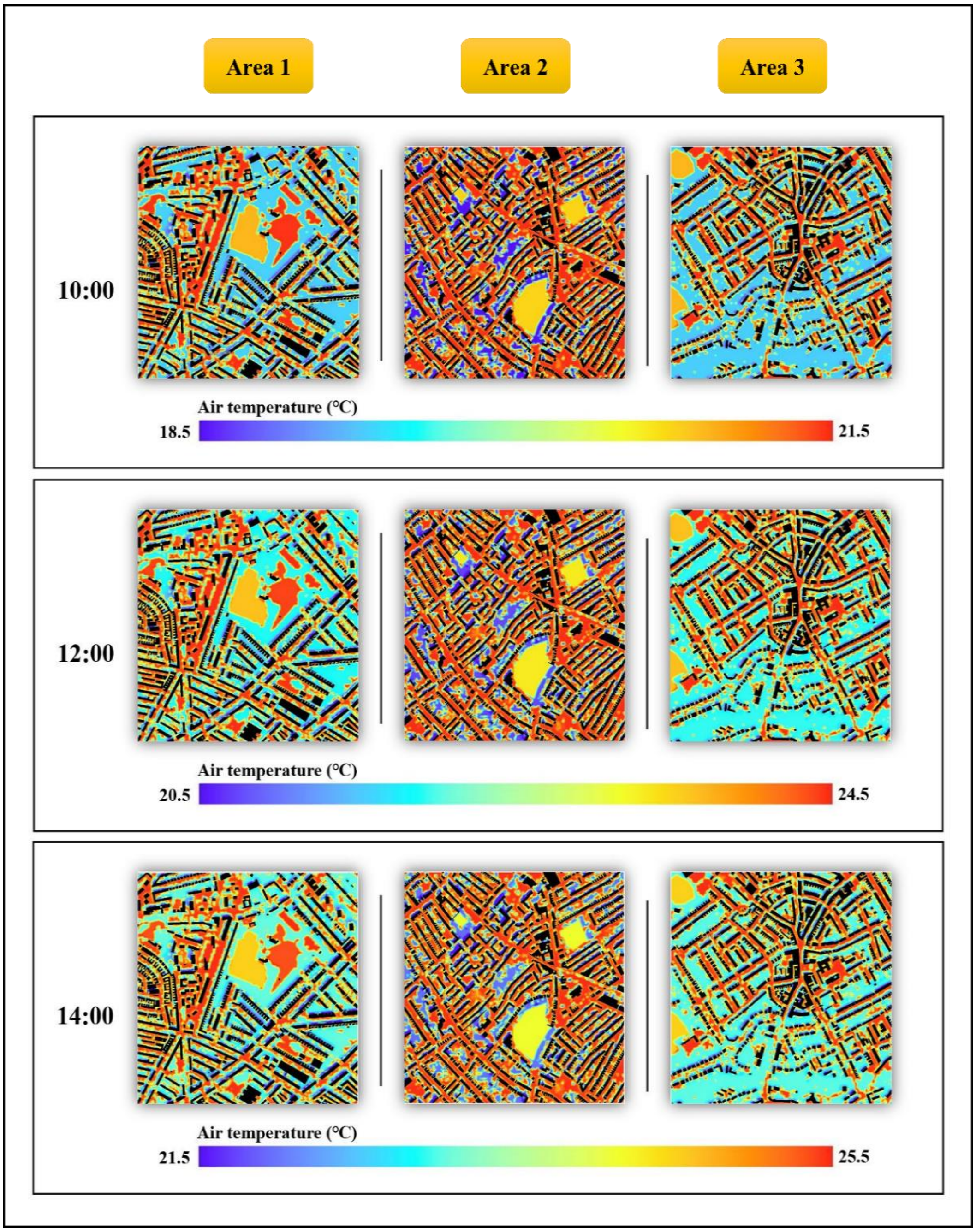

Figure 6.4: Predicted air temperature for three selected areas in London at 10.00,12.00 and 14.00hrs respectively on July 21, 2020. (The black parts are buildings).

In addition, the results of the model can be used for the cross-sectional detection of outdoor thermal characteristics in different building environments. Figure 6.4 shows the predicted air temperature distributions for the selected Areas 1, 2 and 3 at 10.00, 12.00 and 14.00hrs respectively. By comparing the temperature distribution of the 3 regions at a uniform time, it can be seen that the area occupied by the high-temperature region is larger in Area 2 compared to Area 1 and Area 3. Combined with the parameters in Table 6.1, it is known that Area 2 represents a lower building and less green area. The research of Perini and Magliocco (2014) shows that shorter buildings and sparser vegetation cover will lead to an increase in outdoor heat effects. This makes it clear that the model's simulation results are informative. Therefore, based on the simulation results of Figure 6.4, it is recommended that the environment of Area 2 could be improved with additional shading measures or more green areas in the hot areas of mapping to improve the summer heat situation. To further explore the effect of different neighbourhood environments on the outdoor thermal climate, the time-by-time results for the three selected areas were averaged. Figure 6.5 shows the simulated average air temperatures for the three selected areas for the whole day. From the results of the

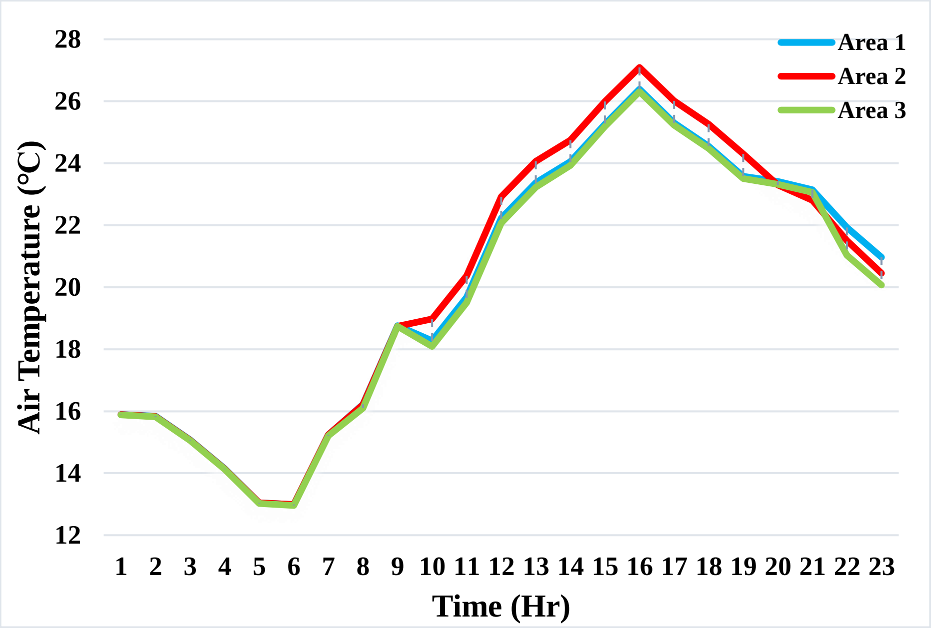

Figure 6.5: Average predicted air temperature for three selected areas in London on July 21, 2020.

linear plot, it can be seen that the temperature in Area 2 is quite high during the day. However, at night Area 1 shows a relatively high-temperature trend. This could be attributed to its high building volume. At the same time, the simulation results of this case study show a consistent trend with the results of other London thermal climate distribution studies (Taylor *et al.*, 2015; Schneider dos Santos, 2020).

The final calculation time for each area is around 4 hours for an output condition with a resolution of 1m*1m. The entire simulation was done with a laptop with 8GB of RAM and a 2.20GHz 8th generation i7 CPU. This is a new method for rapid, high-resolution, neighbourhood-scale, outdoor thermal climate estimation. It suggests that the proposed model is an effective method for rapidly estimating the outdoor thermal climate at the neighbourhood scale for different environmental patterns.

6.3Case study for a new development

6.3.1 Basic information for the construction project

In order to further demonstrate and explore the use of the proposed new climate model in practical built environment design and planning projects, this section presents a case study of a building project in the planning and design phase. The researcher's thanks go to the Sichuan Institute of Building Research for providing information on the relevant construction projects. This construction project is the second office park construction plan of the Sichuan Institute of Building Research. The construction project aims to explore and build a new green and intelligent office park with a demonstration effect. The construction project is located in the New Industry Park in Tianfu New Area, Chengdu, Sichuan Province, China, 20 kilometres from the headquarters of the Sichuan Institute of Building Research. The project has a planned total construction area of 62,907m^2, of which 53,176m^2 is above ground. Six single buildings are planned for the ground level, with the following building scale:

- **Building 1:** Construction area: 27,290.56m^2; Total building height: 44.25m; Number of storeys: 10/1 (above/below ground); Building usage type: offices.
- **Building 2:** Construction area: 2114.53m^2; Total building height: 10.65m; Number of storeys: 2/1 (above/below ground); Building usage type: canteens.
- **Building 3:** Construction area: 10091.27m^2; Total building height: 23.95m; Number of storeys: 7/0 (above/below ground); Building usage type: accommodation.
- **Building 4:** Construction area: 9298.32m^2; Total building height: 21.9m; Number of storeys: 4/0 (above/below ground); Building usage type: offices.
- **Building 5:** Construction area: 4296.43m^2; Total building height: 19.55m; Number of storeys: 4/0 (above/below ground); Building usage type: offices.
- **Building 6:** Construction area: 85.22m^2; Total building height: 3m; Number of storeys: 1/0 (above/below ground); Building usage type: municipal facilities.

The general planning of the project is shown in Figure 6.6.

Figure 6.6: Project construction plan for the second office park of the Sichuan Institute of Building Research

6.3.2 Establishment of the built environment model

As the study proposes a new way of modelling the built environment (see Chapter 3 for details), the case study will also use the newly proposed rasterization approach to model the thermal environment for simulation purposes. It is important to note that as this is a project in planning and design, its built environment has been modelled in detail using BIM software. The rasterised model of the built environment used in this case study can be built directly from the CAD file. This transformation has been achieved thanks to two main reasons: first, the CAD file and the GIS file have already achieved a certain degree of information interoperability; second, the physical model of the environment developed for this study required only a small amount of information about the built environment, mainly building geometry and land cover type. As a result, the CAD file can be converted directly into a rasterised model of the built environment using ArcGIS Pro software or FME (model conversion software). The converted model is also a multi-band raster data file with three main categories of information: (1) the building geometry information (format as DEM); (2) the land surface classification; (3) the building use type classification (As shown in Figure 6.7). All other physical parameters are assigned specific values based on the three types of information mentioned above (see Chapter 5 for details).

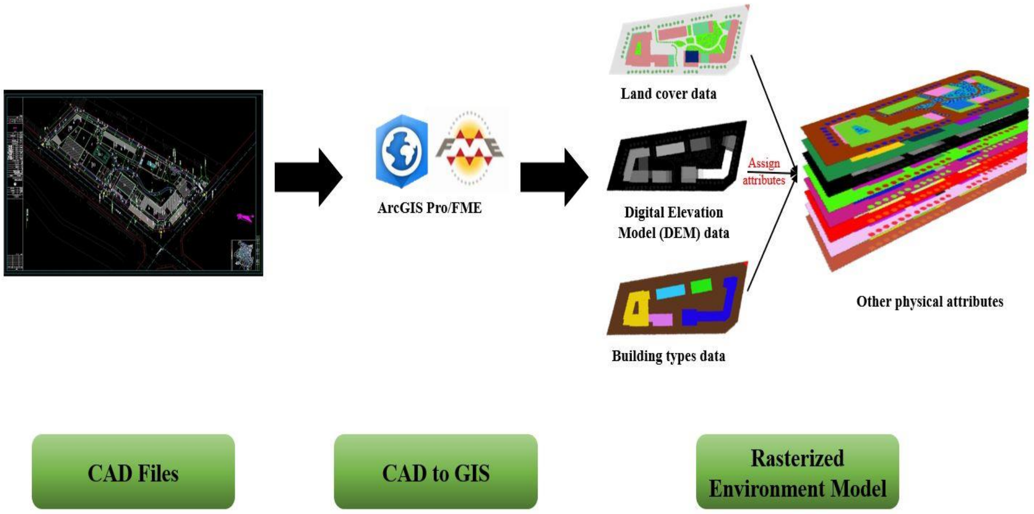

Figure 6.7: Schematic diagram of the process establishing the rasterized environmental model based on BIM models.

In addition, the rasterised approach to environment modelling facilitates the modification of the physical model. As a result, the model can quickly provide multiple comparison scenarios for comparative analysis during the design phase of a construction project. As the main building design of the project has already been determined, this case study focuses on the thermal climate in its changing outdoor environment. In total, three different scenarios were set up for the simulation. The specific rasterised model for these three scenarios is shown in Figure 6.8. Scenario 1 is an outdoor environment modelled with reference to the plan in Figure 6.6. The remaining two scenarios are two extreme cases for comparison. Scenario 2 is a case of a fully impermeable surface with no vegetation cover. Scenario 3 is a FVC surface covered by a large amount of vegetation.

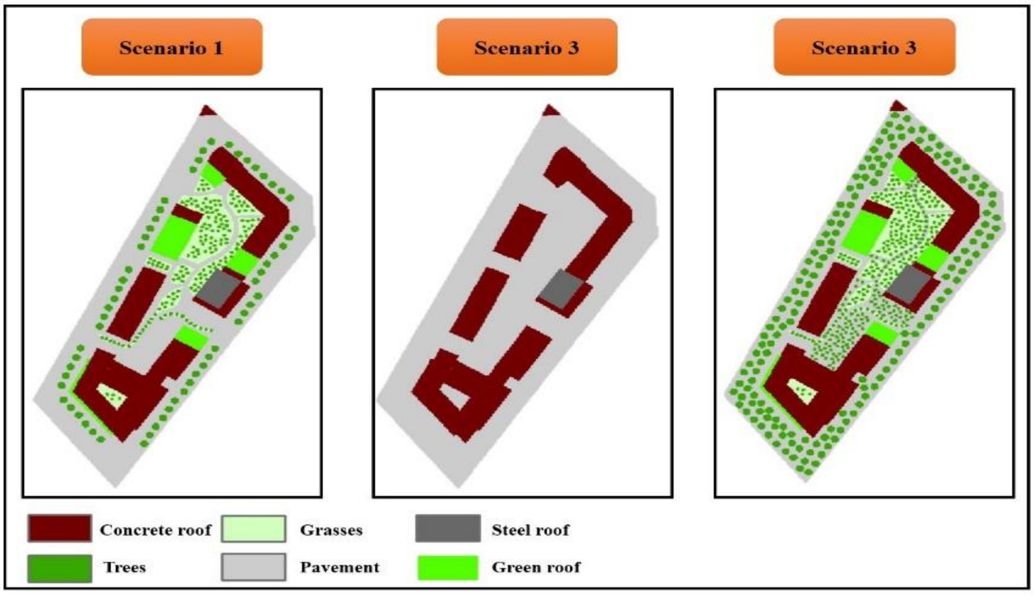

Figure 6.8: The 3 proposed scenarios for the construction projects.

6.3.3 Outdoor thermal climate analysis

Once the basic building environment model has been established, the case study simulates the outdoor thermal climate based on the Typical Meteorological Year (TMY) parameters of the construction site. The specific parameters are shown in Table 6.2.

Table 6.2: Typical Meteorological Year (TMY) parameters for Chengdu.

Time (hr)	Dry bulb temperature (°C)	Global Horizontal Irradiance (GHI) (W/m^2)	Direct Normal Irradiation (DNI) (W/m^2)	Wind Velocity (m/s)	Prevailing Winds
0	24.3	0.00	0.00	0.9	North by Northwest
1	23.5	0.00	0.00	1.0	
2	23.3	0.00	0.00	1.0	
3	22.9	0.00	0.00	0.9	
4	22.7	0.00	0.00	0.9	
5	22.5	0.00	0.00	0.9	
6	22.4	0.00	0.00	0.9	
7	22.5	7.77	6.77	0.9	
8	22.9	74.37	66.60	0.9	
9	23.8	200.91	164.28	1.1	
10	24.8	348.54	241.98	1.3	
11	25.8	476.19	309.69	1.5	
12	26.6	541.68	355.20	1.7	
13	27.2	521.70	380.73	1.8	
14	27.6	475.08	377.40	1.9	
15	27.9	399.60	334.11	2.0	
16	28.1	301.92	256.41	2.0	
17	27.9	209.79	179.82	1.9	
18	27.5	98.79	89.91	1.8	
19	26.8	15.54	14.43	1.5	
20	26.0	0.00	0.00	1.2	
21	25.3	0.00	0.00	1.1	

22	24.7	0.00	0.00	1.0	
23	24.7	0.00	0.00	1.0	
Average	25.1	152.99	115.76	1.3	

The results of the calculation of some of the architectural design indicators based on TMY conditions and environmental modelling conditions are as follows:

1)Windward area of the building

Table 6.3: Calculated windward area ratio of buildings for the construction site.

Building Number	Windward area (m^2)	Maximum possible windward area (m^2)	Maximum possible windward area (°)	Windward area ratio
Building 1	3446.31	5440.11	60	0.634
Building 2	432.76	554.79	20	0.780
Building 3	1546.10	1766.58	30	0.875
Building 4	1518.82	2034.93	20	0.746
Building 5	904.26	1019.22	10	0.887
Building 6	38.17	47.37	40	0.806
The average windward area ratio	0.788			

2)Outdoor site shade coverage

Table 6.4: Calculated outdoor shaded area ratio for the construction site.

Site	The shaded area (m^2)	Site area (m^2)	Shade coverage (%)
Scenario 1	17982	38610	46.6
Scenario 2	15659		40.1
Scenario 3	23569		61.0

3)Green space area

Table 6.5: Calculated green area ratio of buildings for the construction site.

Building Number	Area of vegetation (m^2)	Area of green roof (m^2)	Site area (m^2)	Green space ratio (%)
Scenario 1	0	0	38610	0
Scenario 2	6626	2265		23.0
Scenario 3	10969	2265		34.3

4)Predicted air temperature for the construction site

Similar to the previous example, the model can be used to quickly mapping the outdoor thermal climate by entering specific environmental models and climate parameters. Figure 6.9 shows the predicted outdoor thermal climate at noon for Scenario 1 based on the meteorological data in Table 6.2. The final calculation of the average outdoor thermal climate for three scenarios, based on the input meteorological data, is shown in Figure 6.10. It is clear from the figure that the average daytime temperature in Scenario 2 is significantly higher than in the other scenarios. Conversely, Scenario 3 has the most pronounced cooling effect due to its abundant greenery cover. However, in the context of Table 6.4, it can be seen that Scenario 3 is overshadowed by the abundance of greenery. Scenario 1 is therefore

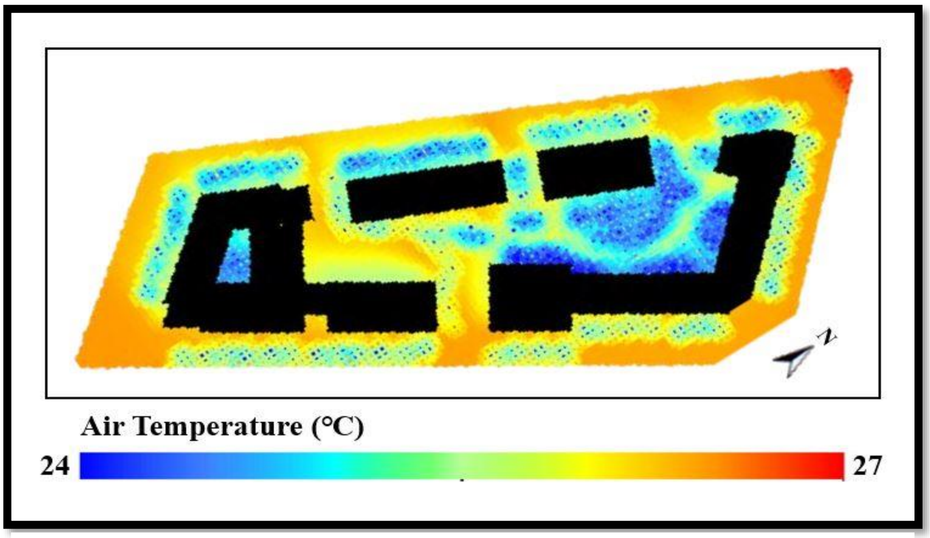

Figure 6.9: Predicted air temperature for Scenario 1 at noon based on TMY data.

significantly more balanced than the extreme cases of Scenarios 2 and 3. It not only controls the outdoor thermal climate to a certain extent but also ensures that the area of sunlight in the park is maintained. Such a comparison of scenarios can help designers to adjust and decide on the design of outdoor environments in a more intuitive and scientific way.

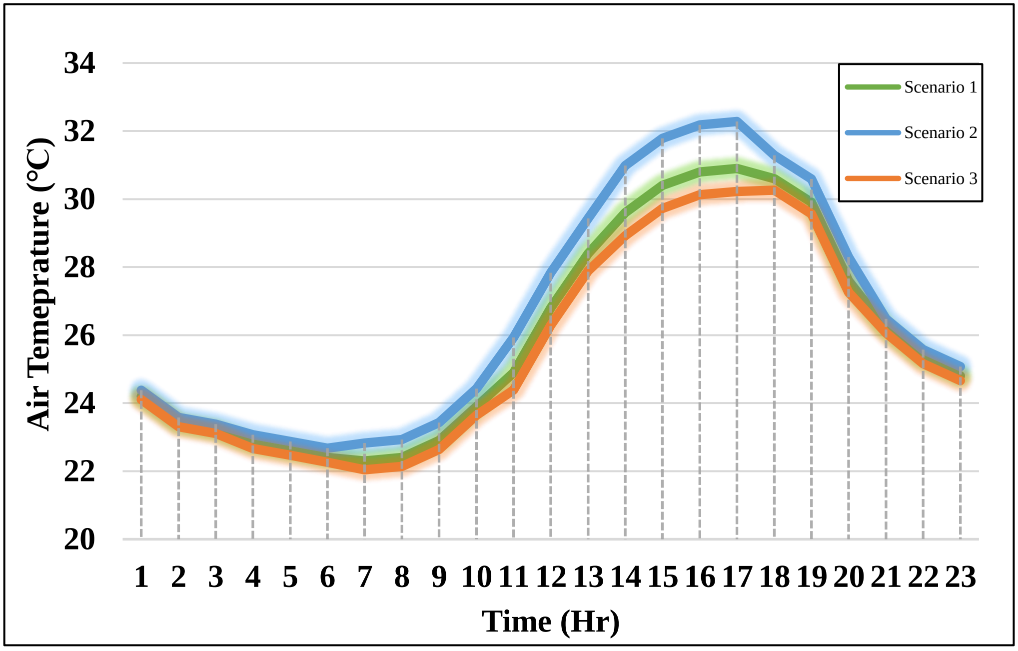

Figure 6.10: Average predicted air temperature for three scenarios based on TMY data.

In general, the model offers the advantage of raster operations not only to provide statistical functions related to design parameters but also to quickly quantify outdoor thermal climate conditions. The results of these calculations show that this urban climate model can quickly and effectively provide quantitative building design parameters and thermal climate assessment results for the design of urban thermal environments.

6.3.4 Combination of the status model and the design model

In addition, as the proposed urban climate model is based on a rasterised data model, this increases the flexibility of modelling the physical environment. This is because multiple raster data can be overlaid with maps to reintegrate the required information. Such an operation is also known as raster data combine in GIS operations. It allows multiple input raster layers to be combined into a new raster according to certain rules. This also opens up the possibility of combining the planning model with the current situation model in the actual planning and design analysis. Such a fusion will use the status model as a base. The status model in the same position is then overwritten with the planning model. The fused model can then be used to analyse the environmental impact of the planning model more fully on the current scenario. Thanks to the new approach to modelling the current state of the urban surface proposed in this study, it is possible to quickly model the current state with the help of geographic information data such as satellite images. Therefore, the approach proposed in this study also allows for a more comprehensive integration model based on a combination of the current and planning models in the actual modelling and analysis of the built environment. This integrated model of the built environment also provides more comprehensive information for relevant environmental analysis. For example, Figure 6.11 shows the analysis of shading conditions in the overall environment after the fusion of the planning model and the status model for this construction project. The darker the area in the graph, the longer it has been covered by shadows. It reflects the joint impact of the planned building and the existing building on the environment. This

Figure 6.11: Calculation of shading conditions based on the environmental model after the fusion of the status and planning models of the construction site.

approach takes a more holistic view of the interaction between the planned project and the surrounding environment.

6.4Summary

This section explores the prospects of applying the proposed raster-data-format-based urban climate model in real planning/building projects with the help of case studies of two different applications. The advantages of this new approach to urban climate modelling in practice are now evident through this simple case illustration. It presents the following advantages from the pre-modelling to the output of the post-results:

- The model proposed in this study allows the rapid creation of environmental models for climate simulation from existing building design models. This is mainly due to the compatibility of existing GIS data platforms for a wide range of data and the proposed representation of the physical model of the environment based on the raster data format in GIS. This allows for effective savings in upfront model processing time in the evaluation of real projects. This can increase the efficiency of the assessment of the project.
- The new raster data operations-based urban climate simulation solution provides reliable and efficient results. It enables a rapid high-resolution assessment of the outdoor thermal climate at a neighbourhood scale. This provides planners and designers with visual and quantitative data for assessing the urban thermal environment in the early planning stages. It not only provides relevant thermal climate simulation data but also provides relevant building design indices for reference. This is all thanks to the excellent regional statistical power of raster data operations.
- The flexible data clipping and combining capabilities of the raster data also provide additional possibilities for the creation of environmental models. They allow the integration of the status model with the planning model in the modelling of the actual environment. This provides more comprehensive

information for urban climate modelling. It also provides a more comprehensive response to the possible interaction of the planning model with existing scenarios.

In general, the proposed model is a robust and practical numerical simulation model for the urban microclimate. It can be used in a variety of scenarios to assist in the assessment of urban planning/building design projects related to the outdoor thermal environment. These two case studies briefly demonstrate some of the functions that can be used in the planning and design phase. Further use scenarios and application directions can be explored in future work.

Chapter 7

Conclusion and Contributions

7.1 Contributions

The primary aim of this thesis is identified in Chapter 1. In order to develop a more practical urban climate model to assist in the design of the built environment at the early planning stages, this study makes three main contributions in two aspects of novel input data generation and numerical simulation algorithms. First, the new multi-band rasterized environmental model building method greatly improves efficiency and flexibility when modelling urban environments. Second, the newly developed numerical urban climate model based on raster operations for the simulation of solar radiation and energy exchange in the urban environment offers the possibility of fast, high-resolution, urban thermal climate simulations.

Chapter 3 presents a new method of representing and modelling the urban surface environment for urban climate simulation in a GIS-based raster data format. The newly proposed approach to environmental modelling combines a raster data model structure with multiple GIS data source processing techniques. This makes a variety of contributions to the urban environment modelling aspect of the pre-data-processing phase of urban climate modelling. Firstly, the use of raster data structures and multi-source fusion analysis methods has resulted in a more concise and comprehensive collection of data for presenting and storing information on urban surface properties. The multi-band storage structure of the raster data brings together many types of geographic information data more simply and easily. Almost all the required basic urban surface information units can also be obtained by means of multi-source data analysis. Secondly, with the collaboration of image analysis methods and multi-source geographic information data analysis, the newly proposed approach to urban environment modelling is able to provide information about the urban surface that is closer to the real situation. Thirdly, such an approach to environmental modelling and representation provides a low-cost means of obtaining information on urban surface properties in urban climate modelling. This low-cost feature is mainly due to the use of fully open-source data and rasterised data representation. Fourthly, such a data representation and storage system aims to provide a systematic and uniform data format for the construction of a complete raster dataset of urban surface properties. This involves significantly more time in input data pre-processing but can be used directly with other urban climate models. Overall, the new urban surface properties acquisition and representation scheme not only contains basic surface environment information but also succeeds in simplifying the process of describing surface properties. These contributions provide the underlying data information and structural framework for subsequent efficient and practical urban climate simulation models.

Chapter 4 develops a new numerical model for the rapid analysis of solar radiation distribution in building complexes based on raster data operations, which contributes to the improvement of the simulation of radiation distribution in urban environments in several ways by using an enhanced 2.5D elevation model. Firstly, the model theoretically calculates direct solar radiation and isotropic radiation by linking the underlying physical equations with raster data operations. This numerical model, built on the framework of raster operations, saves a great deal of time in simulation operations by allowing the overlaying of raster data maps. This allows the prediction of the radiation distribution in the neighbourhood to be done in a short time. Secondly, the representation mode of the raster data offers the possibility of more flexible modelling of the environment. This is mainly due to the clipping and combining characteristics of the raster data. For practical applications, such a contribution is more convenient in comparing multiple scenarios in the early design phase. Thirdly, the model differs from models that calculate radiation distributions based on traditional DEM data by adding a new vertical raster layer. It adds dimension to the calculation of the radiation distribution based on 2.5D data. This allows the radiation distribution calculated based on the 2.5D model to still include the results of vertical surfaces. This collaborative implementation of enhanced 2.5D models through multi-band geographic information offers further possibilities for numerical modelling based on DEM data. Fourthly, it presents an integrated radiation calculation using a combination of multi-level raster data on surface properties. Such a simulation approach offers new problem-solving ideas for modelling similar environmental problems. Overall, the proposed new model contributes to the application of numerical modelling to help designers manage the heat radiation exchange in the environment at an early design stage more effectively. At the same time, to complete a more comprehensive simulation of the urban outdoor thermal environment, it can also provide relevant radiation data for urban surface energy models.

Chapter 5 develops a new numerical model for simulating the urban outdoor thermal climate based on raster data operations. The proposed model directly builds an integrated model for rapid microclimate analysis of multiple air zones based on raster data cells by linking basic physical models with raster data operations. Such a modelling approach offers a variety of contributions to fast and efficient urban surface microclimate simulations: [1] it uses raster data in the form of multiple bands to represent urban surface properties. This provides the basic framework for faster construction of urban surface environment models for urban climate simulations. [2] based on the existing coordinate reference system of the raster data in the GIS framework, the model does not need to establish a coordinate system for the calculation between the individual nodes. [3] a special map overlay algorithm for raster data is used to link the different energy balance models. This provides an efficient and fast model for urban climate simulation operations. [4] the model implements a climate simulation that combines DEM data with a raster matrix of surface information to calculate surface temperatures. It also creates individual thermal climate zones directly from each image element of the raster data used in making the model. This independent calculation mode based on each raster image allows the model to output high-resolution simulation results. [5] it proposes a new approach to multi-area airflow analysis. This flow-direction-based raster data analysis operation proposes a simplified approach for the analysis of wind corridors in urban building complexes. Overall, the proposed new numerical model allows for the rapid execution of high-resolution urban thermal climate simulations. This allows the model to be used in practice to evaluate design options in the early planning stages and to perform quick comparisons between different scenarios.

In general, the entire numerical model is well suited to the rapid simulation of urban microclimates. The simulation results can be used to support the assessment of urban design options in the early planning stages of urban construction or renewal. It provides useful information for sustainable building design, urban planning and outdoor amenity assessment.

7.2 Future work

The developments presented in this thesis offer many opportunities to rapidly explore the neighbourhood-wide interactions of weather, climate, urban form, urban materials, vegetation, building types and human behaviour. The proposed model has been developed in the hope that it will be useful for planners and designers to investigate some of these interactions in the early planning stages. However, as the proposed numerical model for urban climate simulation is still in its infancy, its application and improvement in the subsequent stages need to be further explored. Considering the characteristics of the current model, subsequent work can improve it in the following ways. Firstly, the model currently only considers outdoor weather under sunny/cloudy conditions. For a more comprehensive climate analysis, more simulations of different climatic conditions, such as the effects of rain and snow, could be included in the future. Secondly, anthropogenic heat caused by buildings is one of the main contributors to the urban heat island effect. More detailed modelling of the heat released by buildings can therefore help to improve the accuracy of urban climate models. In future research, links to other Building Energy Models (BEM) could be attempted to provide more detailed building energy information for climate modelling. At the same time, the simulation results of this urban climate model can provide data on basic climate conditions for the BEM. Finally, due to development time constraints, the current program is mainly scripted for data entry interfaces. This type of interaction is not user-friendly at the moment. Thus, some user interaction will need to be added in subsequent improvements.

7.3 Concluding remarks

This thesis introduces raster data analysis techniques to address the outdoor thermal environment of urban building complexes, taking into account a number of influencing factors. It establishes a rasterised urban environment description scheme, an enhanced DEM data-based radiation analysis model and an urban surface energy analysis model based on raster data operations. A mathematical model of the thermal convection, heat transfer and radiant energy balance of the building, the ground and the air is also developed on this basis. At the same time, mathematical models of thermal convection, conduction and radiation were written using raster data map algebra, and a tool for analysing the outdoor thermal environment of building complexes was developed based on GIS. To verify the reliability of the mathematical model, this study validates the results of the urban surface properties acquisition model, the raster-based solar radiation model, and the final integrated microclimate model respectively. For the surface properties model, the indices of the accuracy statistics (shown in Table 3.1) indicate that all of the estimated results had relatively low-percentage AAD values (below 0.1) compared with the actual observations data and also presented high correlation coefficients (above 0.85) with the actual parameters. This validation result shows that the urban surface properties information for microclimate simulations processed in this study is credible. In addition, for the validation of the radiation model, all indicators of accuracy statistics (shown in Table 4.2) indicate that the estimated values are relatively low (below 3) in terms of percentage MAPE to the measured values. At the same time, the RMSE shows a relatively low range (below 110). The simulation results of this radiation model are reliable considering that the estimated values of the radiation simulation usually reflect the RMSE in the range of approximately 80-140 w/m2 (Zhang *et al.*, 2017). Finally, to verify the reliability of the integrated urban climate model, experimental tests were carried out during four seasons: spring, summer, autumn and winter, and the simulation results were compared with the measured results. The comparative results for all seasons have relatively high consistency (shown in Figure 5.16). To be more specific, the results for autumn and winter have a confidence level above 80%. The confidence level of spring and summer is also higher than 70%. This credibility (above 70%) is acceptable to give certain reference opinions at the beginning of planning. Thus, all validation results show that the results calculated using the mathematical model do not differ significantly from the experimental results and that the simulation results present a temperature variation pattern that is generally consistent with the measured results. Therefore, the new raster-based urban climate model proposed in this thesis can serve as a reference for planning the outdoor thermal environment of building complexes in the early planning process.

Appendix I: Review of Several Urban Morphological Parameters

Building coverage ratio (BCR):

The ratio of the area covered by the building to the total area of the land is the building coverage ratio (BCR). It can be calculated by the following equation:

$$BCR = \frac{\sum_{n=1}^{N} C_n}{S_L} \tag{I.1}$$

Where C_n is the area of building n, S_L is the total area of land, and N is the total number of buildings.

Building Coverage Ratio (BCR) plays an important role in changes in urban thermal and wind environments (Mortezazadeh *et al.*, 2021). asserted that when the BCR value is higher, the value of wind speed tends to lower (Yoshie *et al.*, 2006).

Building height (BH):

Building height (BH) is the most basic form index in urban geometric elements, which has a significant impact on wind speed. Ng *et al.* (2011) indicate that air circulation in low/medium-density areas can be improved by controlling building heights. Additionally, building height information also affects the urban thermal environment, specifically, too low building height may increase the urban temperature during the day (Loughner *et al.*, 2012).

Building volume density (BVD):

Building Volume Density (BVD) is the ratio of the volume of a building to the area of the land. Unlike BCR, BVD contains height information of buildings. The calculation method of BVD is as follows:

$$BVD = \frac{\sum_{n=1}^{N} (C_n * H_n)}{S_L} \tag{I.2}$$

Where C_n is the area of building n, H_n is the height of building n, S_L is the total area of land, and N is the total number of buildings.

The urban thermal environment is clearly influenced by changes in the BVD (Zhan *et al.*, 2015). Isa *et al.* (2020) points out that higher BVD can lead to higher ambient temperatures in city centres and worsen urban thermal comfort.

Frontal area index (FAI):

Frontal area index (FAI) refers to the frontal area of a building, which is closely related to urban ventilation at the pedestrian level. The FAI of a wind direction can be calculated by the following equation:

$$FAI(\theta) = \frac{\sum_i A_F(\theta)}{S_L} \tag{I.3}$$

Where $A_F(\theta)$ is the frontal area of building i in the wind direction θ, S_L is the total area of land.

It is commonly used to quantify resistance as a function of building height by researchers in plant canopy and urban canopy communities. Chen and Ng (2011) studied the spatial variation of the wind environment affected by the building volume by means of numerical simulation, which shows that the FAI value is inversely proportional to the wind speed.

Roughness length (RL):

The Roughness length (RL) plays a crucial role in the study of the urban surface wind environment. It can effectively determine the wind speed value on the surface, by linking the turbulent exchange process with the surface roughness in the meteorological model. According to Xu *et al.* (2017), its basic calculation model is as follows:

$$RL = H_{ave} * \frac{C_d}{0.74} * \left(1 - \frac{Z_d}{H_{ave}}\right)^2 * \frac{FAI}{BCR} \tag{I.4}$$

where H_{ave} is the volume average building height, C_d is the obstacle resistance coefficient, Z_d is the zero-displacement height, FAI is the frontal area index, and BCR is the building coverage.

Sky view factor (SVF):

The sky view factor (SVF) is one of the most concerned urban morphological parameters and is often used to describe the three-dimensional geometric structure of the city. It is defined as the fraction of radiative flux that leaves the surface at one point and reaches the atmosphere above the urban canopy (Oke *et al.*, 2017c). According to Dirksen *et al.*(2019), from a 3D perspective, the SVF of a point on the grid is calculated as:

$$SVF = \int_{\theta=0}^{2\pi} COS^2(\beta_{svf}(R.\theta))d\theta \qquad (I.5)$$

Where $\beta_{svf}(R.\theta)$ is the angle from the centre point to the maximum obstacle height at the maximum constant search radius (R) distance in search direction θ. When integrating this formula in all directions (dθ) from 0 to 2π, the SVF for the entire hemisphere can be obtained.

A large number of studies have shown that the heat island effect is negatively correlated with SVF (Oke, 1981; Unger, 2004; Radhi, Fikry *et al.*, 2013); the surface temperature is also affected by SVF (Scarano and Sobrino, 2015; Baghaeipoor and Nasrollahi, 2019). Therefore, it is of great significance to accurately extract the SVF of the complex underlying surface in urban areas.

Appendix II: Associated works

II.1 Journal articles

Published:

A holistic investigation into the seasonal and temporal variations of window opening behavior in residential buildings in Chongqing, China. Du. C, Yu. W, Ma. Y, Cai. Q, Li. B, Li. N, Wang. W, Yao. R,. (2021). Energy Build 231:110522. https://doi.org/10.1016/j.enbuild.2020.110522.

A spatial-and-temporal-based method for rapid particle concentration estimations in an urban environment. Xiong. J, Yao. R, Wang. W, Yu. W, Li. B,. (2022). J Clean Prod 256:120331. https://doi.org/10.1016/j.jclepro.2020.120331.

A mathematical model for a rapid calculation of the urban canyon albedo and its applications. Zhang. H, Yao. R, Luo. Q, Wang. W,. (2022). Renew Energy 197:836–851. https://doi.org/10.1016/j.renene.2022.07.110.

Preparing:

A rasterised urban surface properties model establishing method based on open-source data for urban climate simulation input.

A novel raster based mathematical model for solar potential and environmental radiation analysis at neighbourhoods.

A GIS-based Urban microclimate model to support early-stage design with image-recognition of urban surface properties.

II.2 Computational code

All code for this study was developed in Python based on the ArcMap API. This research and development program is therefore used in conjunction with ArcMap software. In addition, the program uses an object-oriented compilation model. The entire program is completed by several subroutines linked together. The specific code is as follows:

The main file (This file is the main file for parameter settings and simulation runs):

```
# Name: main.py:
#Description: Combine all calculation together Calculate the ground temperature with different layers by heat transfer equations
# Requirements: Spatial Analyst Extension

# Import system modules
import arcpy
from arcpy import env
from arcpy.sa import *
import Hcal
import QrRS
import gc

#set initial input parameters
emissivity=arcpy.Raster(r"D:\Document\Mengwei\UHI-project\programe\initial_p\eimissivity.tif") #emissivity of surface materials
print("Emissivity has read")
beta=arcpy.Raster(r"D:\Document\Mengwei\UHI-project\programe\initial_p\beta.tif") #albedo of surface materials
print("Albedo has read")
pcs=arcpy.Raster(r"D:\Document\Mengwei\UHI-project\programe\initial_p\pcs.tif") #density*heat capacity of surface
ks=arcpy.Raster(r"D:\Document\Mengwei\UHI-project\programe\initial_p\ks.tif") #heat conduction coefficient of surface
hs=1.72 #heat convection coefficient used 5.7
dt=120 #time step
dx=1 #deep of each ground layer
pc=1500*1480 #density*heat capacity of ground
k=1 #heat conduction of ground
wins=[0.9,1.0,1.0,0.9,0.9,0.9,0.9,0.9,1.1,1.3,1.5,1.7,1.8,1.9,2.0,2.0,1.9,1.8,1.5,1.2,1.1,1.0,1.0] #wind speed
wind=[320,320,320,320,320,320,320,320,320,45,45,45,45,45,45,45,45,45,45,45,45,45,45,45] #wind direction
Qanthr=[1.72,1.58,1.47,1.55,1.43,1.57,2.21,2.74,3.56,4.76,4.94,4.81,4.69,4.74,4.56,4.5,4.12,3.5,2.88,2.34,1.87,1.66,1.99,1.6] #anthropogenic heat
Qet=arcpy.Raster(r"D:\Document\Mengwei\UHI-project\programe\initial_p\Qe.tif") #vegetation evaporation
day=190 #simulated date
diff=0.3 #diffuseProp for radiation calculation
```

```
trans=[0.1,0.1,0.1,0.1,0.1,0.1,0.1,0.7,0.7,0.7,0.7,0.7,0.7,0.7,0.7,0.7,0.7,0.5,0.1,0.1,0.1,0.1,0.1,0.1]
#transmittivity for radiation calculation
print("Parameters (hs,dt,dx,pcs,ks,pcs,k,ws,wd,Qa) have setted")
Ts=emissivity*0+298.3 #initial surface temp
Ta=emissivity*0+297.3 #initial air temp
#initial ground temp
Tg1=emissivity*0+298
Tg2=emissivity*0+297.8
Tg3=emissivity*0+297.6
Tg4=emissivity*0+295.2
Tg5=emissivity*0+292.7
Tg6=emissivity*0+290.5
Tg7=emissivity*0+288.3
Tg8=emissivity*0+287.1
Tg9=emissivity*0+286
Tg10=emissivity*0+286

#save initial temp parameters
Ts.save(r"D:\Document\Mengwei\UHI-
project\programe\move_temp\Temperature_temp\Ts_1.tif")
Ta.save(r"D:\Document\Mengwei\UHI-
project\programe\move_temp\Temperature_temp\Ta_1.tif")
Tg1.save(r"D:\Document\Mengwei\UHI-
project\programe\move_temp\Temperature_temp\Tg1_1.tif")
Tg2.save(r"D:\Document\Mengwei\UHI-
project\programe\move_temp\Temperature_temp\Tg2_1.tif")
Tg3.save(r"D:\Document\Mengwei\UHI-
project\programe\move_temp\Temperature_temp\Tg3_1.tif")
Tg4.save(r"D:\Document\Mengwei\UHI-
project\programe\move_temp\Temperature_temp\Tg4_1.tif")
Tg5.save(r"D:\Document\Mengwei\UHI-
project\programe\move_temp\Temperature_temp\Tg5_1.tif")
Tg6.save(r"D:\Document\Mengwei\UHI-
project\programe\move_temp\Temperature_temp\Tg6_1.tif")
Tg7.save(r"D:\Document\Mengwei\UHI-
project\programe\move_temp\Temperature_temp\Tg7_1.tif")
Tg8.save(r"D:\Document\Mengwei\UHI-
project\programe\move_temp\Temperature_temp\Tg8_1.tif")
Tg9.save(r"D:\Document\Mengwei\UHI-
project\programe\move_temp\Temperature_temp\Tg9_1.tif")
Ts.save(r"D:\Document\Mengwei\UHI-project\programe\move_temp\QrTs.tif")
Ta.save(r"D:\Document\Mengwei\UHI-project\programe\move_temp\QrTa.tif")
print("Initial temp parameters has been generated")
#save files off
```

```python
#files for identying buildings
ib=arcpy.Raster(r"D:\Document\Mengwei\UHI-project\programe\initial_p\id_b\identy_b.tif")
ibw=arcpy.Raster(r"D:\Document\Mengwei\UHI-project\programe\initial_p\id_b\identybw.tif")
ibe=arcpy.Raster(r"D:\Document\Mengwei\UHI-project\programe\initial_p\id_b\identybe.tif")
ibn=arcpy.Raster(r"D:\Document\Mengwei\UHI-project\programe\initial_p\id_b\identybn.tif")
ibs=arcpy.Raster(r"D:\Document\Mengwei\UHI-project\programe\initial_p\id_b\identybs.tif")
print("Files of buildings identify have read")

for i in range(0,23):
    ws=wins[i]
    wd=135
    Qa=Qanthr[i]*1.8
    if 9<=i<=18:
        Qe=Qet
    else:
        Qe=0
    QrRS.RQr(i,emissivity,beta,day,diff,trans[i])
    Hcal.Hourlycal(i,Tg10,hs,dt,dx,pcs,ks,pc,k,ws,wd,ib,ibw,ibe,ibn,ibs,Qa,Qe)
    gc.collect()
    print("Calculation at hour "+str(i+1)+"has finished")

arcpy.Delete_management(r"D:\Document\Mengwei\UHI-project\programe\move_temp\Temperature_temp\Ts_1.tif")
arcpy.Delete_management(r"D:\Document\Mengwei\UHI-project\programe\move_temp\Temperature_temp\Ta_1.tif")
arcpy.Delete_management(r"D:\Document\Mengwei\UHI-project\programe\move_temp\Temperature_temp\Tg1_1.tif")
arcpy.Delete_management(r"D:\Document\Mengwei\UHI-project\programe\move_temp\Temperature_temp\Tg2_1.tif")
arcpy.Delete_management(r"D:\Document\Mengwei\UHI-project\programe\move_temp\Temperature_temp\Tg3_1.tif")
arcpy.Delete_management(r"D:\Document\Mengwei\UHI-project\programe\move_temp\Temperature_temp\Tg4_1.tif")
arcpy.Delete_management(r"D:\Document\Mengwei\UHI-project\programe\move_temp\Temperature_temp\Tg5_1.tif")
arcpy.Delete_management(r"D:\Document\Mengwei\UHI-project\programe\move_temp\Temperature_temp\Tg6_1.tif")
arcpy.Delete_management(r"D:\Document\Mengwei\UHI-project\programe\move_temp\Temperature_temp\Tg7_1.tif")
arcpy.Delete_management(r"D:\Document\Mengwei\UHI-project\programe\move_temp\Temperature_temp\Tg8_1.tif")
arcpy.Delete_management(r"D:\Document\Mengwei\UHI-project\programe\move_temp\Temperature_temp\Tg9_1.tif")
```

```
arcpy.Delete_management(r"D:\Document\Mengwei\UHI-project\programe\move_temp\QrTa.tif")
arcpy.Delete_management(r"D:\Document\Mengwei\UHI-project\programe\move_temp\QrTs.tif")
```

Other files (Other subroutine code used to implement individual functions):

Name: Qrcal.py:

```
# Description: Derives incoming solar radiation from a raster surface, Outputs a global radiation
raster and optional direct, diffuse and rasters, Generate total radiation absorbed by surface.
# Requirements: Spatial Analyst Extension

# Import system modules
import arcpy
from arcpy import env
from arcpy.sa import *
import math

# Set environment settings
env.workspace = r"D:\Document\PhD\Radiation_revise\Data"

# Check out the ArcGIS Spatial Analyst extension license
arcpy.CheckOutExtension("Spatial")

def calqrn(day,Tst,IB,ID,temp,surtemp): #,ID,Ta,beta,emissivity,SVF):
    #Set local variables
    inRaster = arcpy.Raster(r"D:\Document\PhD\Radiation_revise\Data\LSB_DEM_vali.tif")
    if Tst==12:
        Tst=11.9
    Tave = temp
    Tsur = surtemp
    beta_ave=arcpy.Raster(r"D:\Document\PhD\Radiation_revise\Data\LSB_albedo.tif")
    #beta_ave = arcpy.GetRasterProperties_management(beta, 'MEAN')
    eave= 0.95

emissivity=arcpy.Raster(r"D:\Document\PhD\Radiation_revise\Data\LSB_emmissivity.tif.tif")
    SVF=arcpy.Raster(r"D:\Document\PhD\Radiation_revise\Data\Intersect\SVF_R20m.tif")
    latitude=51*math.pi/180
    a=5.67*pow(10,-8) #Boltzmann’s Constant
    b=2*math.pi*(day-1)/365
    sundeclination=0.006918-0.399912*math.cos(b)+0.070257*math.sin(b)-
0.006758*math.cos(2*b)+0.000907*math.sin(2*b)-
0.002697*math.cos(3*b)+0.00148*math.sin(3*b)
    Sunt=(Tst-12)*math.pi/12

Hs=math.asin(math.sin(latitude)*math.sin(sundeclination)+math.cos(latitude)*math.cos(sundeclin
ation)*math.cos(Sunt))
```

```
    As=math.acos((math.sin(Hs)*math.sin(latitude)-math.sin(sundeclination))/(math.cos(Hs)*math.cos(latitude)))
    if Tst<=12:
        As=-As

    #Execute aspect
    outAspect = Aspect(inRaster)
    #outback=outAspect
    Asg=As*180/math.pi+180
    #print("Hs:"+str(Hs))
    #print("As:"+str(As))

    if Tst==11.9:
        Tst=12
    print("Radiation at"+str(Tst)+"start")

    #Chose back
    outback=~((outAspect>=(Asg-90))&(outAspect<=(Asg+90)))&(outAspect>=0)
    outfront=((outAspect>=(Asg-90))&(outAspect<=(Asg+90)))&(outAspect>=0)
    #outback.save(r"D:\Document\PhD\Radiation_revise\Data\wall_back.tif")
    #outfront.save(r"D:\Document\PhD\Radiation_revise\Data\wall_front.tif")
    Backdem=inRaster*outback
    AspectfrontSA=Asg-outAspect*outfront
    #Execute Shade
    if 0<Hs<90:
        outHillShade = Hillshade(Backdem, Asg, Hs*180/math.pi, "SHADOWS", 1)
        outVerticalfacede=Con(outfront*outHillShade>0,1,0)
        buildings=Con(inRaster>0,1,0)
        outHillShade=Con(outHillShade+buildings>0,1,0)
        #outHillShade.save(r"D:\Document\PhD\Radiation_revise\Data\shade_"+str(Tst)+".tif")
        #Execute Radiation
        DirectRadH=Con(outHillShade==1,IB*math.sin(Hs),0)
        DirectRadV=IB*math.cos(Hs)*arcpy.sa.Cos(AspectfrontSA*math.pi/180)*outVerticalfacede
        DirectRad=Con(DirectRadV>0,DirectRadV,DirectRadH)
        DirectRad.save(r"D:\Document\PhD\Radiation_revise\Data\Results\Direct\directRad_"+str(int(Tst*2))+".tif")
        DiffuseRad=ID*SVF
        DiffuseRad.save(r"D:\Document\PhD\Radiation_revise\Data\Results\Diffuse\diffuseRad_"+str(int(Tst*2))+".tif")
        GlobalRad=DirectRad+DiffuseRad
```

```
GlobalRad.save(r"D:\Document\PhD\Radiation_revise\Data\Results\Global\GlobalRad_"+str(int(
Tst*2))+".tif")
        else:
                DirectRad=0
                DiffuseRad=0
                GlobalRad=DirectRad+DiffuseRad

        LongwaveRad=eave*a*(Power(Tave,4))*(1-SVF)

#LongwaveRad.save(r"D:\Document\PhD\Radiation_revise\Data\Longwave_"+str(Tst)+".tif")
        envRad=(DirectRad+DiffuseRad+LongwaveRad)*beta_ave
        LongRad=(LongwaveRad-emissivity*a*(Power(Tsur,4)))
        Radave = arcpy.GetRasterProperties_management(envRad, 'MEAN')
        Rad_ave=str(Radave)
        Radave=float(Rad_ave)
        RefelectRad=Radave*(1-SVF)
        outNetRad=(DirectRad+DiffuseRad+RefelectRad)

        locals()['Qr'+str(Tst)]=(1-beta_ave)*outNetRad+LongRad

locals()['Qr'+str(Tst)].save(r"D:\Document\PhD\Radiation_revise\Data\Results\net\AbsorRad_"+st
r(int(Tst*2))+".tif")
        print("Radiation energy at time "+str(Tst)+" has calculated")
        return locals()['Qr'+str(Tst)]
        '''
        #DirectRadH.save("D:\Document\Mengwei\UHI-project\programe\DRH.tif")
        #DirectRadV.save("D:\Document\Mengwei\UHI-project\programe\DRV.tif")
        DirectRad.save("D:\Document\Mengwei\UHI-project\programe\DR.tif")
        print("DirectRad at"+str(Tst)+"finished")
        DiffuseRad=ID*SVF
        LongwaveRad=eave*a*(Power(Tave,4))*(1-SVF)
        outRad=DirectRad+DiffuseRad+LongwaveRad
        Radave = arcpy.GetRasterProperties_management(outRad, 'MEAN')
        RefelectRad=beta_ave*Radave*(1-SVF)
        outGlobalRad=DirectRad+DiffuseRad+RefelectRad
        locals()['Qr'+str(Tst)]=(1-beta)*outGlobalRad+LongwaveRad
        print("Radiation energy at time "+str(Tst)+" has calculated")
        return locals()['Qr'+str(Tst)]
        '''
for i in range(0,48):
        Tst=float(i)/2
```

```
IB=[0,0,0,0,1,1,1,1,1,1,2,11,26,113,104,264,304,364,479,509,553,639,683,724,325,771,263,229,802,780,749,716,158,123,505,445,62,220,212,143,81,30,3,0,0,0,0,0]

ID=[0,0,0,0,0,0,0,0,0,0,0,2,6,24,22,57,65,78,103,109,119,138,147,156,70,166,57,49,172,168,161,154,34,26,109,96,13,47,45,31,18,6,1,0,0,0,0,0]

temp=[22.77,22.77,23.27,23.27,23.23,23.23,22.07,22.07,20.53,20.53,20.9,20.9,20.87,20.87,22.07,22.07,22.5,22.5,23.57,23.57,26.83,26.83,27.07,27.07,28.67,28.67,27.43,27.43,28.37,28.37,29.87,29.87,29.2,29.2,26.27,26.27,25.47,25.47,24.67,24.67,22.63,22.63,24.93,24.93,23.2,23.2,20.63,20.63]

surtemp=[22.7,22.7,23.6,23.6,23.3,23.3,22.6,22.6,21.1,21.1,21.1,21.1,21.1,21.1,22.4,22.4,22.8,22.8,23.5,23.5,26.8,26.8,27,27,29.1,29.1,27.3,27.3,27.1,27.1,27.8,27.8,27.2,27.2,25.9,25.9,25.7,25.7,24.4,24.4,23,23,25.1,25.1,23.7,23.7,20.9,20.9]
    calqrn(202,Tst,IB[i],ID[i],temp[i]+273,surtemp[i]+273)
```

```
# Name: QrRun.py:
#Description: Run radiation part and save output
# Requirements: Spatial Analyst Extension



# Import system modules
import arcpy
from arcpy import env
from arcpy.sa import *
import Qrcal

def RQr(i,emissivity,beta,day,diff,trans):

    Ta=arcpy.Raster(r"D:\Document\Mengwei\UHI-project\programe\move_temp\QrTa.tif")
    Ts=arcpy.Raster(r"D:\Document\Mengwei\UHI-project\programe\move_temp\QrTs.tif")
    Qr=Qrcal.calqr(i,i+1,emissivity,beta,Ts,Ta,day,diff,trans)
    Qr.save(r"D:\Document\Mengwei\UHI-project\programe\move_temp\Qr"+str(i)+".tif")
    del Qr
    arcpy.Delete_management(r"D:\Document\Mengwei\UHI-project\programe\move_temp\QrTa.tif")
    arcpy.Delete_management(r"D:\Document\Mengwei\UHI-project\programe\move_temp\QrTs.tif")
```

```
# Name: SVFcal.py:
# Description: Derives sky view factor (SVF) from a digital elevation model(DEM). Outputs a SVF raster.
# Requirements: Spatial Analyst Extension
```

```
# Import system modules
import arcpy
from arcpy import env
from arcpy.sa import *
import math

# Set environment settings
env.workspace = r"D:\Document\Mengwei\UHI-project\programe"

# Check out the ArcGIS Spatial Analyst extension license
arcpy.CheckOutExtension("Spatial")

def calSVF(DEM):
    #Convert Raster to features
    inRaster = DEM
    arcpy.RasterToPolygon_conversion(inRaster,"D:\Document\Mengwei\UHI-project\programe\move_temp\DEMpolygon_temp.shp","NO_SIMPLIFY","VALUE")
    Buildings=r"D:\Document\Mengwei\UHI-project\programe\move_temp\DEMpolygon_temp.shp"
    #Create centre point
    env.outputCoordinateSystem = arcpy.SpatialReference("NAD 1983 UTM Zone 11N")
    outfishnet=r"D:\Document\Mengwei\UHI-project\programe\move_temp\fishnet.shp"
    Centre=r"D:\Document\Mengwei\UHI-project\programe\move_temp\DEMpoint_temp.shp"
    # Set the origin of the fishnet
    originCoordinate = '1037.26 4145.81'
    # Set the orientation
    yAxisCoordinate = '1037.26 4155.81'
    # Enter 0 for width and height - these values will be calcualted by the tool
    cellSizeWidth = '20'
    cellSizeHeight = '20'
    # Number of rows and columns together with origin and opposite corner
    # determine the size of each cell
    numRows =    '20'
    numColumns = '20'
    oppositeCoorner = '19273.61 18471.17'
    # Create a point label feature class
    labels = 'LABELS'
    # Extent is set by origin and opposite corner - no need to use a template fc
    templateExtent = '#'
    # Each output cell will be a polygon
    geometryType = 'POLYGON'
    arcpy.CreateFishnet_management(outfishnet, "", "", cellSizeWidth, cellSizeHeight, numRows, numColumns, "", labels, templateExtent, geometryType)
```

```
    ExtractValuesToPoints(r"D:\Document\Mengwei\UHI-
project\programe\move_temp\fishnet_label.shp",
DEM,Centre,"INTERPOLATE","VALUE_ONLY")
    print("Centre point created")
    #Create Buffer
    outBuffer=r"D:\Document\Mengwei\UHI-project\programe\move_temp\CentreBuffer.shp"
    sideType="FULL"
    endType="ROUND"
    dissolveType="NONE"
    arcpy.Buffer_analysis(Centre, outBuffer, "10 Meters", sideType, endType, dissolveType)
    print("Buffer created")
    #Intersect Buffer & Buildings
    outIntersect = r"D:\Document\Mengwei\UHI-
project\programe\move_temp\CentreInersect.shp"
    arcpy.Intersect_analysis([outBuffer, Buildings], outIntersect,"ALL", "", "INPUT")
    print("Intersect finished")
```

Name: TacalC.py:

#Description: Calculate the air temperature by heat transfer equations, Calculate the heat transfer by airflow fot air temperature calculation, Calculate the convective heat transfer for air temperature calculation.

Requirements: Spatial Analyst Extension

```
# Import system modules
import arcpy
from arcpy import env
from arcpy.sa import *
import math
import Tacal
import MoveQf
import Qfcal

# Set environment settings
env.workspace = r"D:\Document\Mengwei\UHI-project\programe"

# Check out the ArcGIS Spatial Analyst extension license
arcpy.CheckOutExtension("Spatial")



def calTaC(ws,wd,Ta,ib,ibw,ibe,ibn,ibs,Ts,dt,Qa,Qe,hs,n,i):

    p=1.29
```

```
    cp=1000
    height=2
    Qfx,Qfy=MoveQf.moveqf(ws,wd,Ta,p,cp,dt)
    #Qfx.save(r"D:\Document\UHI-project\programe\results\Qfx"+str(i)+".tif")
    f="move"+str(n)
    print(f)
    Qf=Qfcal.calQf(Ta,Qfx,Qfy,wd,ib,ibw,ibe,ibn,ibs)
    #Qf.save(r"D:\Document\UHI-project\programe\results\Qf"+str(i)+".tif")
    f1="Qf"+str(n)
    print(f1)
    Tacal.calTa(Ta,Ts,dt,Qa,Qf,Qe,hs,p,cp,height,n,i)
    print("Ta")
    #path=r"D:\Document\UHI-project\programe\move_temp\Ta_secondscal"+str(i)+".tif"
    #locals()['Ta'+str(i)].save(path)
    #path1=r"D:\Document\UHI-project\programe\move_temp\Ta_secondscal"+str(i-1)+".tif"
    pathw1=r"D:\Document\Mengwei\UHI-project\programe\move_temp\Qfw.tif"
    pathe1=r"D:\Document\Mengwei\UHI-project\programe\move_temp\Qfe.tif"
    pathn1=r"D:\Document\Mengwei\UHI-project\programe\move_temp\Qfn.tif"
    paths1=r"D:\Document\Mengwei\UHI-project\programe\move_temp\Qfs.tif"
    arcpy.Delete_management(pathw1)
    arcpy.Delete_management(pathe1)
    arcpy.Delete_management(pathn1)
    arcpy.Delete_management(paths1)
    return
```

Name: Tacal.py:

```
#Description: Calculate the air temperature by heat transfer equations, Calculate the heat transfer by airflow fot air temperature calculation, Calculate the convective heat transfer for air temperature calculation
# Requirements: Spatial Analyst Extension

# Import system modules
import arcpy
from arcpy import env
from arcpy.sa import *
import math
import os

# Set environment settings
env.workspace = r"D:\Document\Mengwei\UHI-project\programe"

# Check out the ArcGIS Spatial Analyst extension license
arcpy.CheckOutExtension("Spatial")
```

```
def calTa(Ta,Ts,dt,Qa,Qf,Qe,hs,p,cp,height,n,i):

    arcpy.env.overwriteOutput = True

Tsur=[23.5,23.3,22.9,22.7,22.5,22.4,22.5,22.9,23.8,24.8,25.8,26.6,27.2,27.6,27.9,28.1,27.9,27.5,26.8,26,25.3,24.7,24.7]
    Qf=(Qf*dt)/(height*p*cp)
    Qc=(hs*(Ts-Ta)*dt)/(height*p*cp)
    Qa=(Qa*dt)/(height*p*cp)
    Qe=(Qe*dt)/(height*p*cp)
    Qa=(Qa*dt)/(height*p*cp)
    Ta=Qf+Qc+Qa-Qe+Ta
    Qs=8*(Ta-Tsur[i]-273)*dt/(height*p*cp)
    Ta=Ta-Qs
    #Ta=((hs*(Ts-Ta)+Qa+height*Qf)*dt)/(height*p*cp)+Ta
    if n==(3600/dt):
        Ta.save(r"D:\Document\Mengwei\UHI-project\programe\move_temp\Temperature_temp\Ta_1.tif")
        Ta.save(r"D:\Document\Mengwei\UHI-project\programe\move_temp\QrTa.tif")
        Ta.save(r"D:\Document\Mengwei\UHI-project\programe\results\air\Ta_"+str(i+1)+".tif")
    else:
        Ta.save(r"D:\Document\Mengwei\UHI-project\programe\move_temp\Temperature_temp\Ta_"+str(n+1)+".tif")
    Return
```

 # Name: TGcal.py:

```
#Description: Calculate the surface temperature by heat transfer equations, Calculate the ground temperature with different layers by heat transfer equations
# Requirements: Spatial Analyst Extension

# Import system modules
import arcpy
from arcpy import env
from arcpy.sa import *

# Set environment settings
env.workspace = r"D:\Document\Mengwei\UHI-project\programe"

# Check out the ArcGIS Spatial Analyst extension license
arcpy.CheckOutExtension("Spatial")

def calTs(Qr,pcs,ks,dt,dx,Ta,Ts,Tg1,hs):
```

```
    Ts=(2*dt*hs)/(dx*pcs)*(Ta-Ts)-(2*dt*ks)/(pow(dx,2)*pcs)*(Ts-Tg1)+(2*Qr*dt)/(pcs+dx)+Ts
    return Ts

def calTg1(Ts,Tg1,Tg2,ks,dt,dx,pc,k):

    f01=(ks*dt)/(pc*pow(dx,2))
    f02=(k*dt)/(pc*pow(dx,2))
    Tg1=f01*(Ts-Tg1)+f02*(Tg2-Tg1)+Tg1
    return Tg1

def calTg2(Tg1,Tg2,Tg3,dt,dx,pc,k):

    f0=(k*dt)/(pc*pow(dx,2))
    Tg2=f0*(Tg1-Tg2+Tg3-Tg2)+Tg2
    return Tg2

def calTg3(Tg2,Tg3,Tg4,dt,dx,pc,k):

    f0=(k*dt)/(pc*pow(dx,2))
    Tg3=f0*(Tg2-Tg3+Tg4-Tg3)+Tg3
    return Tg3

def calTg4(Tg3,Tg4,Tg5,dt,dx,pc,k):

    f0=(k*dt)/(pc*pow(dx,2))
    Tg4=f0*(Tg3-Tg4+Tg5-Tg4)+Tg4
    return Tg4
def calTg5(Tg4,Tg5,Tg6,dt,dx,pc,k):

    f0=(k*dt)/(pc*pow(dx,2))
    Tg5=f0*(Tg4-Tg5+Tg6-Tg5)+Tg5
    return Tg5

def calTg6(Tg5,Tg6,Tg7,dt,dx,pc,k):

    f0=(k*dt)/(pc*pow(dx,2))
    Tg6=f0*(Tg5-Tg6+Tg7-Tg6)+Tg6
    return Tg6

def calTg7(Tg6,Tg7,Tg8,dt,dx,pc,k):

    f0=(k*dt)/(pc*pow(dx,2))
    Tg7=f0*(Tg6-Tg7+Tg8-Tg7)+Tg7
```

```
    return Tg7

def calTg8(Tg7,Tg8,Tg9,dt,dx,pc,k):

    f0=(k*dt)/(pc*pow(dx,2))
    Tg8=f0*(Tg7-Tg8+Tg9-Tg8)+Tg8
    return Tg8

def calTg9(Tg8,Tg9,Tg10,dt,dx,pc,k):

    f0=(k*dt)/(pc*pow(dx,2))
    Tg9=f0*(Tg8-Tg9+Tg10-Tg9)+Tg9
    return Tg9
```

```
# Name: Qfcal.py:
#Description: Calculate the heat transfer by airflow fot air temperature calculation.
# Requirements: Spatial Analyst Extension



# Import system modules
import arcpy
from arcpy import env
from arcpy.sa import *
import math
import os
import gc

# Set environment settings
env.workspace = r"D:\Document\Mengwei\UHI-project\programe"

# Check out the ArcGIS Spatial Analyst extension license
arcpy.CheckOutExtension("Spatial")

def calQf(Ta,Qfx,Qfy,wd,ib,ibw,ibe,ibn,ibs):
    pathw=r"D:\Document\Mengwei\UHI-project\programe\move_temp\Qfw.tif"
    pathe=r"D:\Document\Mengwei\UHI-project\programe\move_temp\Qfe.tif"
    pathn=r"D:\Document\Mengwei\UHI-project\programe\move_temp\Qfn.tif"
    paths=r"D:\Document\Mengwei\UHI-project\programe\move_temp\Qfs.tif"
    Qfw=arcpy.Raster(pathw)
    Qfe=arcpy.Raster(pathe)
    Qfn=arcpy.Raster(pathn)
    Qfs=arcpy.Raster(paths)

    Qfw=(Qfw-Qfx)*ibw
```

```
    Qfe=(Qfe-Qfx)*ibe
    Qfn=(Qfn-Qfy)*ibn
    Qfs=(Qfs-Qfy)*ibs
    arcpy.env.extent = Ta
    if 90<=wd<=270:
        Qfx=Con(IsNull(Qfe),0,Qfe)*ib
    else:
        Qfx=Con(IsNull(Qfw),0,Qfw)*ib
    if 0<=wd<=180:
        Qfy=Con(IsNull(Qfs),0,Qfs)*ib
    else:
        Qfy=Con(IsNull(Qfn),0,Qfn)*ib
    Qf=(Qfx+Qfy)
    return Qf
```

Name: MoveQf.py:

```
#Description: Opetare move for calculation Qf.
# Requirements: Spatial Analyst Extension

# Import system modules
import arcpy
from arcpy import env
from arcpy.sa import *
import math

# Set environment settings
env.workspace = r"D:\Document\Mengwei\UHI-project\programe"

# Check out the ArcGIS Spatial Analyst extension license
arcpy.CheckOutExtension("Spatial")

def moveqf(ws,wd,Ta,p,cp,dt):

    mx=abs(ws*math.sin((wd/180)*math.pi)*p*2)
    my=abs(ws*math.cos((wd/180)*math.pi)*p*2)
    Qfx=cp*mx*Ta/3600
    Qfy=cp*my*Ta/3600
    pathw=r"D:\Document\Mengwei\UHI-project\programe\move_temp\Qfw.tif"
    pathe=r"D:\Document\Mengwei\UHI-project\programe\move_temp\Qfe.tif"
    pathn=r"D:\Document\Mengwei\UHI-project\programe\move_temp\Qfn.tif"
    paths=r"D:\Document\Mengwei\UHI-project\programe\move_temp\Qfs.tif"
    arcpy.Shift_management(Qfx,pathw,-1,0)
    arcpy.Shift_management(Qfx,pathe,1,0)
    arcpy.Shift_management(Qfy,pathn,0,1)
```

```
    arcpy.Shift_management(Qfy,paths,0,-1)
    return Qfx,Qfy
```

Name: Lcal.py:

```
#Description: Combine all calculation together, Calculate the ground temperature with different layers by heat transfer equations.
# Requirements: Spatial Analyst Extension

# Import system modules
import arcpy
from arcpy import env
from arcpy.sa import *
import TGcal
import TacalC
import gc
import os

# Set environment settings
env.workspace = r"D:\Document\Mengwei\UHI-project\programe"

# Check out the ArcGIS Spatial Analyst extension license
arcpy.CheckOutExtension("Spatial")

#Run cal Ta
def fininalcal(Ts,Ta,Tg1,Tg2,Tg3,Tg4,Tg5,Tg6,Tg7,Tg8,Tg9,Tg10,hs,dt,dx,pcs,ks,pc,k,ws,wd,ib,ibw,ibe,ibn,ibs,Qa,Qe,Qr,n,i):
    Ts=TGcal.calTs(Qr,pcs,ks,dt,dx,Ta,Ts,Tg1,hs)
    Tg1=TGcal.calTg1(Ts,Tg1,Tg2,ks,dt,dx,pc,k)
    Tg2=TGcal.calTg2(Tg1,Tg2,Tg3,dt,dx,pc,k)
    Tg3=TGcal.calTg3(Tg2,Tg3,Tg4,dt,dx,pc,k)
    Tg4=TGcal.calTg4(Tg3,Tg4,Tg5,dt,dx,pc,k)
    Tg5=TGcal.calTg5(Tg4,Tg5,Tg6,dt,dx,pc,k)
    Tg6=TGcal.calTg6(Tg5,Tg6,Tg7,dt,dx,pc,k)
    Tg7=TGcal.calTg7(Tg6,Tg7,Tg8,dt,dx,pc,k)
    Tg8=TGcal.calTg8(Tg7,Tg8,Tg9,dt,dx,pc,k)
    Tg9=TGcal.calTg9(Tg8,Tg9,Tg10,dt,dx,pc,k)
    if n==(3600/dt):
        Ts.save(r"D:\Document\Mengwei\UHI-project\programe\move_temp\Temperature_temp\Ts_1.tif")
        Tg1.save(r"D:\Document\Mengwei\UHI-project\programe\move_temp\Temperature_temp\Tg1_1.tif")
        Tg2.save(r"D:\Document\Mengwei\UHI-project\programe\move_temp\Temperature_temp\Tg2_1.tif")
```

```
        Tg3.save(r"D:\Document\Mengwei\UHI-project\programe\move_temp\Temperature_temp\Tg3_1.tif")
        Tg4.save(r"D:\Document\Mengwei\UHI-project\programe\move_temp\Temperature_temp\Tg4_1.tif")
        Tg5.save(r"D:\Document\Mengwei\UHI-project\programe\move_temp\Temperature_temp\Tg5_1.tif")
        Tg6.save(r"D:\Document\Mengwei\UHI-project\programe\move_temp\Temperature_temp\Tg6_1.tif")
        Tg7.save(r"D:\Document\Mengwei\UHI-project\programe\move_temp\Temperature_temp\Tg7_1.tif")
        Tg8.save(r"D:\Document\Mengwei\UHI-project\programe\move_temp\Temperature_temp\Tg8_1.tif")
        Tg9.save(r"D:\Document\Mengwei\UHI-project\programe\move_temp\Temperature_temp\Tg9_1.tif")
        Ts.save(r"D:\Document\Mengwei\UHI-project\programe\results\surface\Ts_"+str(i+1)+".tif")
        '''
        Tg1.save(r"D:\Document\Mengwei\UHI-project\programe\results\ground\Tg1_"+str(i+1)+".tif")
        Tg2.save(r"D:\Document\Mengwei\UHI-project\programe\results\ground\Tg2_"+str(i+1)+".tif")
        Tg3.save(r"D:\Document\Mengwei\UHI-project\programe\results\ground\Tg3_"+str(i+1)+".tif")
        Tg4.save(r"D:\Document\Mengwei\UHI-project\programe\results\ground\Tg4_"+str(i+1)+".tif")
        Tg5.save(r"D:\Document\Mengwei\UHI-project\programe\results\ground\Tg5_"+str(i+1)+".tif")
        Tg6.save(r"D:\Document\Mengwei\UHI-project\programe\results\ground\Tg6_"+str(i+1)+".tif")
        Tg7.save(r"D:\Document\Mengwei\UHI-project\programe\results\ground\Tg7_"+str(i+1)+".tif")
        Tg8.save(r"D:\Document\Mengwei\UHI-project\programe\results\ground\Tg8_"+str(i+1)+".tif")
        Tg9.save(r"D:\Document\Mengwei\UHI-project\programe\results\ground\Tg9_"+str(i+1)+".tif")
        '''
        Ts.save(r"D:\Document\Mengwei\UHI-project\programe\move_temp\QrTs.tif")
    else:
        Ts.save(r"D:\Document\Mengwei\UHI-project\programe\move_temp\Temperature_temp\Ts_"+str(n+1)+".tif")
        Tg1.save(r"D:\Document\Mengwei\UHI-project\programe\move_temp\Temperature_temp\Tg1_"+str(n+1)+".tif")
        Tg2.save(r"D:\Document\Mengwei\UHI-project\programe\move_temp\Temperature_temp\Tg2_"+str(n+1)+".tif")
```

```
        Tg3.save(r"D:\Document\Mengwei\UHI-project\programe\move_temp\Temperature_temp\Tg3_"+str(n+1)+".tif")
        Tg4.save(r"D:\Document\Mengwei\UHI-project\programe\move_temp\Temperature_temp\Tg4_"+str(n+1)+".tif")
        Tg5.save(r"D:\Document\Mengwei\UHI-project\programe\move_temp\Temperature_temp\Tg5_"+str(n+1)+".tif")
        Tg6.save(r"D:\Document\Mengwei\UHI-project\programe\move_temp\Temperature_temp\Tg6_"+str(n+1)+".tif")
        Tg7.save(r"D:\Document\Mengwei\UHI-project\programe\move_temp\Temperature_temp\Tg7_"+str(n+1)+".tif")
        Tg8.save(r"D:\Document\Mengwei\UHI-project\programe\move_temp\Temperature_temp\Tg8_"+str(n+1)+".tif")
        Tg9.save(r"D:\Document\Mengwei\UHI-project\programe\move_temp\Temperature_temp\Tg9_"+str(n+1)+".tif")
    print("Ground temperature calculation at "+str(n*dt)+" seconds finished")
    TacalC.calTaC(ws,wd,Ta,ib,ibw,ibe,ibn,ibs,Ts,dt,Qa,Qe,hs,n,i)
    print("Air temperature calculation at "+str(n*dt)+" seconds finished")
```

Name: Hcal.py:

```
#Description: The finial function for calculating energy balance for each hour.
# Requirements: Spatial Analyst Extension

# Import system modules
import arcpy
from arcpy import env
from arcpy.sa import *
import RScal

def Hourlycal(i,Tg10,hs,dt,dx,pcs,ks,pc,k,ws,wd,ib,ibw,ibe,ibn,ibs,Qa,Qe):
        Qr=arcpy.Raster(r"D:\Document\Mengwei\UHI-project\programe\move_temp\Qr"+str(i)+".tif")
        for n in range(1,(3600+dt)/dt):
            RScal.RS(Tg10,hs,dt,dx,pcs,ks,pc,k,ws,wd,ib,ibw,ibe,ibn,ibs,Qa,Qe,Qr,n,i)
        arcpy.Delete_management(r"D:\Document\Mengwei\UHI-project\programe\move_temp\Qr"+str(i)+".tif")
```

Name: RScal.py:

```
#Description: Read and save files of results for loop of calculation.
# Requirements: Spatial Analyst Extension

# Import system modules
import arcpy
from arcpy import env
from arcpy.sa import *
```

```
import Lcal
import Qrcal
import gc

def RS(Tg10,hs,dt,dx,pcs,ks,pc,k,ws,wd,ib,ibw,ibe,ibn,ibs,Qa,Qe,Qr,n,i):

        Ts=arcpy.Raster(r"D:\Document\Mengwei\UHI-project\programe\move_temp\Temperature_temp\Ts_"+str(n)+".tif")
        Ta=arcpy.Raster(r"D:\Document\Mengwei\UHI-project\programe\move_temp\Temperature_temp\Ta_"+str(n)+".tif")
        Tg1=arcpy.Raster(r"D:\Document\Mengwei\UHI-project\programe\move_temp\Temperature_temp\Tg1_"+str(n)+".tif")
        Tg2=arcpy.Raster(r"D:\Document\Mengwei\UHI-project\programe\move_temp\Temperature_temp\Tg2_"+str(n)+".tif")
        Tg3=arcpy.Raster(r"D:\Document\Mengwei\UHI-project\programe\move_temp\Temperature_temp\Tg3_"+str(n)+".tif")
        Tg4=arcpy.Raster(r"D:\Document\Mengwei\UHI-project\programe\move_temp\Temperature_temp\Tg4_"+str(n)+".tif")
        Tg5=arcpy.Raster(r"D:\Document\Mengwei\UHI-project\programe\move_temp\Temperature_temp\Tg5_"+str(n)+".tif")
        Tg6=arcpy.Raster(r"D:\Document\Mengwei\UHI-project\programe\move_temp\Temperature_temp\Tg6_"+str(n)+".tif")
        Tg7=arcpy.Raster(r"D:\Document\Mengwei\UHI-project\programe\move_temp\Temperature_temp\Tg7_"+str(n)+".tif")
        Tg8=arcpy.Raster(r"D:\Document\Mengwei\UHI-project\programe\move_temp\Temperature_temp\Tg8_"+str(n)+".tif")
        Tg9=arcpy.Raster(r"D:\Document\Mengwei\UHI-project\programe\move_temp\Temperature_temp\Tg9_"+str(n)+".tif")

Lcal.fininalcal(Ts,Ta,Tg1,Tg2,Tg3,Tg4,Tg5,Tg6,Tg7,Tg8,Tg9,Tg10,hs,dt,dx,pcs,ks,pc,k,ws,wd,ib,ibw,ibe,ibn,ibs,Qa,Qe,Qr,n,i)
        del Ts,Ta,Tg1,Tg2,Tg3,Tg4,Tg5,Tg6,Tg7,Tg8,Tg9
        gc.collect()
        arcpy.Delete_management(r"D:\Document\Mengwei\UHI-project\programe\move_temp\Temperature_temp\Ts_"+str(n)+".tif")
        arcpy.Delete_management(r"D:\Document\Mengwei\UHI-project\programe\move_temp\Temperature_temp\Ta_"+str(n)+".tif")
        arcpy.Delete_management(r"D:\Document\Mengwei\UHI-project\programe\move_temp\Temperature_temp\Tg1_"+str(n)+".tif")
        arcpy.Delete_management(r"D:\Document\Mengwei\UHI-project\programe\move_temp\Temperature_temp\Tg2_"+str(n)+".tif")
        arcpy.Delete_management(r"D:\Document\Mengwei\UHI-project\programe\move_temp\Temperature_temp\Tg3_"+str(n)+".tif")
```

```
        arcpy.Delete_management(r"D:\Document\Mengwei\UHI-project\programe\move_temp\Temperature_temp\Tg4_"+str(n)+".tif")
        arcpy.Delete_management(r"D:\Document\Mengwei\UHI-project\programe\move_temp\Temperature_temp\Tg5_"+str(n)+".tif")
        arcpy.Delete_management(r"D:\Document\Mengwei\UHI-project\programe\move_temp\Temperature_temp\Tg6_"+str(n)+".tif")
        arcpy.Delete_management(r"D:\Document\Mengwei\UHI-project\programe\move_temp\Temperature_temp\Tg7_"+str(n)+".tif")
        arcpy.Delete_management(r"D:\Document\Mengwei\UHI-project\programe\move_temp\Temperature_temp\Tg8_"+str(n)+".tif")
        arcpy.Delete_management(r"D:\Document\Mengwei\UHI-project\programe\move_temp\Temperature_temp\Tg9_"+str(n)+".tif")
```

Name: Imagereclass.py:

```
#Description: Generate parametes in raster format for calculation
# Requirements: Spatial Analyst Extension

# Import system modules
import arcpy
from arcpy import env
from arcpy.sa import *
import math
import os

# Set environment settings
env.workspace = r"D:\Document\Mengwei\UHI-project\programe"
arcpy.env.overwriteOutput = True

# Set local variables
inRaster = arcpy.Raster(r"D:\Document\Mengwei\UHI-project\programe\SI.tif")
sigFile = r"D:\Document\Mengwei\UHI-project\programe\demo\uortestarea_rs.gsg"
probThreshold = "0.0"
aPrioriWeight = "EQUAL"
aPrioriFile = ""
outConfidence = r"D:\Document\Mengwei\UHI-project\programe\uorconfmlc.tif"

# Check out the ArcGIS Spatial Analyst extension license
arcpy.CheckOutExtension("Spatial")

# Execute
mlcOut = MLClassify(inRaster, sigFile, probThreshold, aPrioriWeight,
                    aPrioriFile, outConfidence)

# Save the output
```

```
mlcOut.save(r"D:\Document\Mengwei\UHI-project\programe\uorfeatures1.tif")
f=arcpy.Raster(r"D:\Document\Mengwei\UHI-project\programe\uorfeatures1.tif")
f1=arcpy.Raster(r"D:\Document\Mengwei\UHI-project\programe\DEM_UoR.tif")
f1=Con(f1==0,1,0)
f=f*f1
f=Con(f==4,2,Con(f==3,3,Con(f==2,2,Con(f==1,1,Con(f==0,4,0)))))
f.save(r"D:\Document\Mengwei\UHI-project\programe\uorfeatures.tif")
arcpy.Delete_management(r"D:\Document\Mengwei\UHI-project\programe\uorfeatures1.tif")
```

Name: Generateparameter.py:

```
#Description: Generate parametes in raster format for calculation.
# Requirements: Spatial Analyst Extension

# Import system modules
import arcpy
from arcpy import env
from arcpy.sa import *
import math
import os

# Set environment settings
env.workspace = r"D:\Document\Mengwei\UHI-project\programe"

# Check out the ArcGIS Spatial Analyst extension license
arcpy.CheckOutExtension("Spatial")

f=arcpy.Raster(r"D:\Document\Mengwei\UHI-project\programe\uorfeatures.tif")
#generate beta
a1=0.18
a2=0.2
a3=0.26
a4=0.27
a5=0.3
beta=Con(f==1,a1,Con(f==2,a2,Con(f==3,a3,Con(f==4,a4,Con(f==5,a5,0)))))
beta.save(r"D:\Document\Mengwei\UHI-project\programe\initial_p\beta.tif")
#generate eimissivity
b1=0.92
b2=0.99
b3=0.9
b4=0.96
b5=0.89
eimissivity=Con(f==1,b1,Con(f==2,b2,Con(f==3,b3,Con(f==4,b4,Con(f==5,b5,0)))))
eimissivity.save(r"D:\Document\Mengwei\UHI-project\programe\initial_p\eimissivity.tif")
#generate ks
```

```
c1=0.7
c2=0.3
c3=1.1
c4=1.21
c5=1.0
ks=Con(f==1,c1,Con(f==2,c2,Con(f==3,c3,Con(f==4,c4,Con(f==5,c5,0)))))
ks.save(r"D:\Document\Mengwei\UHI-project\programe\initial_p\ks.tif")
#generate pcs
d1=1330000
d2=690*2300
d3=2800000
d4=1950000
d5=1500*1480
pcs=Con(f==1,d1,Con(f==2,d2,Con(f==3,d3,Con(f==4,d4,Con(f==5,d5,0)))))
pcs.save(r"D:\Document\Mengwei\UHI-project\programe\initial_p\pcs.tif")
#generate Qe
tree=2456*0.019
grass=2456*0.005
gf=2456*0.01
Qe=Con(f==2,tree,Con(f==3,grass,Con(f==6,gf,0)))
Qe.save(r"D:\Document\Mengwei\UHI-project\programe\initial_p\Qe.tif")

#generate identy_b
idb=Con(f==1,1,Con(f==2,1,Con(f==3,1,Con(f==4,0,0))))
idb.save(r"D:\Document\Mengwei\UHI-project\programe\initial_p\id_b\identy_b.tif")

ib=arcpy.Raster(r"D:\Document\Mengwei\UHI-project\programe\initial_p\id_b\identy_b.tif")
arcpy.Shift_management(ib,r"D:\Document\Mengwei\UHI-
project\programe\initial_p\id_b\identybw.tif",-1,0)
arcpy.Shift_management(ib,r"D:\Document\Mengwei\UHI-
project\programe\initial_p\id_b\identybe.tif",1,0)
arcpy.Shift_management(ib,r"D:\Document\Mengwei\UHI-
project\programe\initial_p\id_b\identybn.tif",0,1)
arcpy.Shift_management(ib,r"D:\Document\Mengwei\UHI-
project\programe\initial_p\id_b\identybs.tif",0,-1)
```

Some of the input parameters appearing in the above code are examples and should be changed by the user to suit their needs.

Appendix III: Physical Parameters of Urban Surfaces for Reference

Surface	Albedo[a]	Emissivity[a]	Thermal Conductivity $(w*m^{-1}*K^{-1})$[b]	Specific Heat Capacity $(J*kg^{-1}*K^{-1})$
Natural surfaces				
Bare ground				
Soil (dark, wet → light, dry)	0.05-0.45	0.98-0.89	0.52	1840
Sand and rock	0.2-0.45	0.84-0.92	0.27	800
Low vegetation				
Grass (long → short)	0.16-0.26	0.98-0.90	1.10	2600
Crops	0.18-0.25	0.90-0.99	-	-
Trees	0.13-0.20	0.90-0.99	0.02-0.6	1255-3586
Water	0.03-0.5	0.92-0.97	0.59	4200
Artificial surface materials				
Roads				
Asphalt	0.05-0.27	0.89-0.96	0.062	920
Concrete	0.10-0.35	0.85-0.97	1.4	880
Walls				
Concrete	0.10-0.35	0.85-0.97	1.4	880
Bricks (colour, red - white)	0.20-0.60	0.90-0.92	1.0-2.3	835-1130
Stone	0.40-0.64	0.85-0.95	2.15-2.90	745-830
Wood	0.22	0.90	0.11-0.19	2385-2805
Roofs				
Tile	0.10-0.35	0.90	0.08-0.17	1300
Tar and gravel	0.08-0.18	0.92	0.09-0.15	1170-1380
Slate	0.10-0.14	0.90	2.0	760
Corrugate iron	0.10-0.16	0.13-0.28	204	1400
Galvanized steel	0.37-0.45	0.25	52	480

a. Oke *et al.* (2017)

b. Incropera and Dewitt (1998)

Appendix IV: Nomenclature

IV.1 Symbols

A_s	The solar azimuth angle
A_{wall}	The orientation of the wall
B_t	The buildings use types
C_p	The heat capacity
E_p	The potential evaporation rate
E_{sat}	The satellite elevation angle
G_x	The gradient in the x-axis direction
G_y	The gradient in the y-axis direction
H_n	The building height
H_s	The solar zenith angle
I_B	The direct radiation intensity on a horizontal plane
I_D	The diffuse radiation intensity
L_{AB}	The length of the building height reflecting on the view panel of the satellite
Q^*	The net all-wave radiation
Q_B	The direct beam radiation on a plane surface
Q_{BH}	The direct solar radiation energy received by the horizontal surface
Q_{BV}	The intensity of direct solar radiation received on the vertical plane
Q_D	The diffuse radiation
Q_E	The density of turbulent latent heat flow exchanged between the surface and the atmosphere
Q_{Eart}	The latent heat fluxes for artificial landscapes
Q_{Eveg}	The latent heat fluxes for natural landscapes
Q_F	The anthropogenic heat fluxes
Q_{FB}	The building heat emissions
Q_{FM}	The human metabolic heat emissions
Q_{FV}	The vehicular heat emissions
Q_H	The density of turbulent sensible heat flow exchanged between the surface and the atmosphere
Q_L	The surface-absorbed long-wave radiation
Q_{Lsur}	The long-wave radiant heat from the surface itself
Q_R	The net radiation absorbed by the surface
Q_S	The density of heat flow stored by the ground
Q_{cond}	The conducted heat from the wall/underground temperature control point to the surface
Q_{conv}	The convective heat transfer between air and surface

Q_{env}	The radiation reflected from the surrounding urban environment
Q_i	The heat stored in the airflow zone
$Sobel_x(x,y)$	The Sobel operator in the x-axis direction
$Sobel_y(x,y)$	The Sobel operator in the y-axis direction
T_{conrol}	The temperature at the control point of the underlying surface
T_{env}	The effective environment temperature of surrounding objects
T_i	The air temperature corresponding to air zone
T_{sur}	The surface temperature
lat_{site}	The site latitude in degrees
lon_{sat}	The satellite's longitude in degrees
lon_{site}	The site longitude in degrees
$m_{(i,j)}$	The total mass balance for a pixel
θ_{grad}	The direction of the gradient
θ_{polar}	The angle between ρ and the x-axis
σ_G	The standard deviation of the Gaussian distribution
$\emptyset$	The geographic latitude
ΔQ_A	The net advected flux
ΔQ_s	The heat storage which represents the net change in heat storage of all elements of the city
G	The magnitude of the gradient
S	The all other energy sources and sinks
x	The x-axis coordinate of the pixel in the image
y	The y-axis coordinate of the pixel in the image
BS	The building shape index
$G(x,y)$	The two-dimensional Gaussian function
$K\uparrow$	The reflected short-wave radiation
$K\downarrow$	The incoming direct and diffuse short-wave radiation
$L\uparrow$	The outgoing long-wave radiation from the surface
$L\downarrow$	The incoming long-wave radiation from the atmosphere
$POIc$	The closest POI value
$POIi$	The intersect POI value
V	The volume
t	Time
α	The surface albedo
δ	The sun declination
ε	The emissivity of the emitting body
ρ	The geometrical perpendicular to the line
ρ	The density
σ	The Stefan-Boltzmann constant

IV.2 Abbreviations

AAD	Average Absolute Deviation
ABL	Atmospheric Boundary Layer
ALOS	Advanced Land Observing Satellite
API	Application Programming Interface
BCR	Building Coverage Ratio
BEM	Building Energy Model
BEP	Building Effect Parameterization
BH	Building Height
BVD	Building Volume Density
CAD	Computer-aided design
CC	correlation coefficient
CFD	Computational Fluid Dynamics
CTTC	Cluster Thermal Time Constant
DEM	Digital Elevation Model
DSM	Digital Surface Model
DTM	Digital Terrain Model
FAI	Frontal Area Index
FCN	Full Convolutional Network
FVC	Fractional Vegetation Cover
GIS	Geographical Information System
ISS	Integrated Sensor Suite
LiDAR	Light Detection and Ranging
LST	Land Surface Temperature
MAPE	Mean Absolute Percentage Error
MCM	The Microclimate Model
MLUCM	Multi-Layer Urban Canopy Model
nDSM	normalized Digital Surface Model
NDVI	Normalized Difference Vegetation Index
NIR	Near Infrared Red
POI	Points of Interest
RL	Roughness Length
RMSE	root mean squared error
SAR	Synthetic Aperture Radar
SEB	Surface Energy Balance
SLUCM	Single-Layer Urban Canopy Model
SUNtool	Sustainable Urban Neighbourhood modelling tool
SVF	Sky View Factor
TEB	Town Energy Budget
TMY	Typical Meteorological Year
TUF-IOBES	Temperature of Urban Facets Indoor–Outdoor Building Energy Simulator
UBL	Urban Boundary Layer
UCL	Urban Canopy Layer

UCM	Urban Canyon Model
UFZ	Urban function zone
UHI	Urban Heat Island

References

Agency, E. (2015) *The Environment Agency National LIDAR Programme*. Available at: https://www.data.gov.uk/dataset/f0db0249-f17b-4036-9e65-309148c97ce4/national-lidar-programme#licence-info (Accessed: 21 March 2023).

Allen, L., Lindberg, F. and Grimmond, C. S. B. (2011) ‘Global to city scale urban anthropogenic heat flux: Model and variability’, *International Journal of Climatology*, 31(13), pp. 1990–2005. doi: 10.1002/joc.2210.

Alves, E. D. L. and Lopes, A. (2017) ‘The urban heat island effect and the role of vegetation to address the negative impacts of local climate changes in a small Brazilian City’, *Atmosphere*, 8(2). doi: 10.3390/atmos8020018.

Anees, S. A. *et al.* (2022) ‘Estimation of fractional vegetation cover dynamics based on satellite remote sensing in pakistan: A comprehensive study on the FVC and its drivers’, *Journal of King Saud University - Science*. The Author(s), 34(3), p. 101848. doi: 10.1016/j.jksus.2022.101848.

Arnfield, A. J. (2000) ‘A simple model of urban canyon energy budget and its validation’, *Physical Geography*, 21(4), pp. 305–326. doi: 10.1080/02723646.2000.10642712.

Arya, S. P. (2001) *Introduction to micrometeorology*. Academic Press.

Azevedo, J. A., Chapman, L. and Muller, C. L. (2016) ‘Quantifying the daytime and night-time urban heat Island in Birmingham, UK: A comparison of satellite derived land surface temperature and high resolution air temperature observations’, *Remote Sensing*, 8(2). doi: 10.3390/rs8020153.

Baghaeipoor, G. and Nasrollahi, N. (2019) ‘The effect of sky view factor on air temperature in high-rise urban residential environments’, *Journal of Daylighting*, 6(2), pp. 42–51. doi: 10.15627/jd.2019.6.

Baklanov, A. *et al.* (2005) ‘Approaches for urbanization of DMI-HIRLAM NWP model’, *HIRLAM Newsletter*, 49, pp. 61–75.

Beckers, B. and Rodríguez, D. (2009) ‘Helping architects to design their personal daylight’, *WSEAS Transactions on Environment and Development*, 5(7), pp. 467–477.

Best, M. J. (2005) ‘Representing urban areas within operational numerical weather prediction models’, *Boundary-Layer Meteorology*, 114(1), pp. 91–109. doi: 10.1007/s10546-004-4834-5.

Best, M. J. and Grimmond, C. S. B. (2016) ‘Modeling the partitioning of turbulent fluxes at urban sites with varying vegetation cover’, *Journal of Hydrometeorology*, 17(10), pp. 2537–2553. doi: 10.1175/JHM-D-15-0126.1.

Bokaie, M. *et al.* (2016) ‘Assessment of Urban Heat Island based on the relationship between land surface temperature and Land Use/ Land Cover in Tehran’, *Sustainable Cities and Society*. Elsevier Ltd, 23, pp. 94–104. doi: 10.1016/j.scs.2016.03.009.

Bonacquisti, V. *et al.* (2006) ‘A canopy layer model and its application to Rome’, *Science of the Total Environment*, 364(1–3), pp. 1–13. doi: 10.1016/j.scitotenv.2005.09.097.

Boulter, P. G., Barlow, T. J. and Mccrae, I. S. (2009) *Emission factors 2009: Report 3-exhaust emission factors for road vehicles in the United Kingdom*.

Bragança, L., Vieira, S. M. and Andrade, J. B. (2014) 'Early stage design decisions: The way to achieve sustainable buildings at lower costs', *The Scientific World Journal*, 2014. doi: 10.1155/2014/365364.

Brito, M. C. *et al.* (2012) 'Photovoltaic potential in a Lisbon suburb using LiDAR data', *Solar Energy*, 86(1), pp. 283–288. doi: 10.1016/j.solener.2011.09.031.

Brown, M. (2000) 'Urban Parameterizations for Mesoscale Meteorological Models', *Mesoscale Atmospheric Dispersion, WIT Press*, (193–255).

Bruse, M. and Fleer, H. (1998) 'Simulating surface-plant-air interactions inside urban environments with a three dimensional numerical model', *Environmental Modelling and Software*, 13(3–4), pp. 373–384. doi: 10.1016/S1364-8152(98)00042-5.

Buyadi, S. N. A., Mohd, W. M. N. W. and Misni, A. (2013) 'Green Spaces Growth Impact on the Urban Microclimate', *Procedia - Social and Behavioral Sciences*. Elsevier B.V., 105, pp. 547–557. doi: 10.1016/j.sbspro.2013.11.058.

Campbell, S. *et al.* (2018) 'Heatwave and health impact research: A global review', *Health and Place*. Elsevier Ltd, 53(August), pp. 210–218. doi: 10.1016/j.healthplace.2018.08.017.

Carneiro, C. M. (2011) 'Extraction of Urban Environmental Quality Indicators using LiDAR-Based Digital Surface Models', 5050, p. 321.

Chen, F. *et al.* (2011) 'The integrated WRF/urban modelling system: Development, evaluation, and applications to urban environmental problems', *International Journal of Climatology*, 31(2), pp. 273–288. doi: 10.1002/joc.2158.

Chen, L. and Ng, E. (2011) 'Quantitative urban climate mapping based on a geographical database: A simulation approach using Hong Kong as a case study', *International Journal of Applied Earth Observation and Geoinformation*. Elsevier B.V., 13(4), pp. 586–594. doi: 10.1016/j.jag.2011.03.003.

Chow, A., Fung, A. S. and Li, S. (2014) 'GIS modeling of solar neighborhood potential at a fine spatiotemporal resolution', *Buildings*, 4(2), pp. 195–206. doi: 10.3390/buildings4020195.

Clough, S. A. and Iacono, M. J. (1995) 'Line-by-line calculation of atmospheric fluxes and cooling rates 2. Application to carbon dioxide, ozone, methane, nitrous oxide and the halocarbons', *Journal of Geophysical Research*, 100(D8).

Compagnon, R. (2004) 'Solar and daylight availability in the urban fabric', *Energy and Buildings*, 36(4), pp. 321–328. doi: 10.1016/j.enbuild.2004.01.009.

Coseo, P. and Larsen, L. (2014) 'How factors of land use/land cover, building configuration, and adjacent heat sources and sinks explain Urban Heat Islands in Chicago', *Landscape and Urban Planning*. Elsevier B.V., 125, pp. 117–129. doi: 10.1016/j.landurbplan.2014.02.019.

Czmoch, I. and Pękala, A. (2014) 'Traditional Design versus BIM Based Design', *Procedia Engineering*, 91(TFoCE), pp. 210–215. doi: 10.1016/j.proeng.2014.12.048.

Debbage, N. and Shepherd, J. M. (2015) 'The urban heat island effect and city contiguity', *Computers, Environment and Urban Systems*. Elsevier B.V., 54, pp. 181–194. doi: 10.1016/j.compenvurbsys.2015.08.002.

Deilami, K., Kamruzzaman, M. and Liu, Y. (2018) 'Urban heat island effect: A systematic review of spatio-temporal factors, data, methods, and mitigation measures', *International*

Journal of Applied Earth Observation and Geoinformation. Elsevier, 67(November 2017), pp. 30–42. doi: 10.1016/j.jag.2017.12.009.

Derakhshan, S. and Shaker, A. (2017) ‘Numerical study of the cross-ventilation of an isolated building with different opening aspect ratios and locations for various wind directions’, *International Journal of Ventilation*. Taylor & Francis, 16(1), pp. 42–60. doi: 10.1080/14733315.2016.1252146.

Desthieux, G. *et al.* (2018) ‘Solar energy potential assessment on rooftops and facades in large built environments based on lidar data, image processing, and cloud computing. Methodological background, application, and validation in geneva (solar cadaster)’, *Frontiers in Built Environment*, 4(March). doi: 10.3389/fbuil.2018.00014.

Development, C. C. of H. and U.-R. (2021) ‘Chongqing Green Building “14th Five-Year Plan”’. Available at: http://zfcxjw.cq.gov.cn/zwxx_166/gsgg/202201/t20220110_10286992.html.

Dirksen, M. *et al.* (2019) ‘Sky view factor calculations and its application in urban heat island studies’, *Urban Climate*. Elsevier, 30(February), p. 100498. doi: 10.1016/j.uclim.2019.100498.

Doick, K. J., Peace, A. and Hutchings, T. R. (2014) ‘The role of one large greenspace in mitigating London’s nocturnal urban heat island’, *Science of the Total Environment*. Elsevier B.V., 493, pp. 662–671. doi: 10.1016/j.scitotenv.2014.06.048.

Du, H. *et al.* (2016) ‘Influences of land cover types, meteorological conditions, anthropogenic heat and urban area on surface urban heat island in the Yangtze River Delta Urban Agglomeration’, *Science of the Total Environment*. Elsevier B.V., 571, pp. 461–470. doi: 10.1016/j.scitotenv.2016.07.012.

Duffie, J. A. and Beckman, W. A. (2013) *Solar Engineering of Thermal Processes, 4th Edition*. 4th edn. Available at: https://www.wiley.com/en-us/Solar+Engineering+of+Thermal+Processes%2C+4th+Edition-p-9780470873663.

Dupont, S. *et al.* (2006) ‘Parameterization of the urban water budget with the submesoscale soil model’, *Journal of Applied Meteorology and Climatology*, 45(4), pp. 624–648. doi: 10.1175/JAM2363.1.

Dupont, S. and Mestayer, P. G. (2006) ‘Parameterization of the urban energy budget with the submesoscale soil model’, *Journal of Applied Meteorology and Climatology*, 45(12), pp. 1744–1765. doi: 10.1175/JAM2417.1.

Dupont, S., Otte, T. L. and Ching, J. K. S. (2004) ‘Simulation of meteorological fields within and above urban and rural canopies with a mesoscale model’, *Boundary-Layer Meteorology*, 113(1), pp. 111–158. doi: 10.1023/B:BOUN.0000037327.19159.ac.

Ekici, B. B. and Aksoy, U. T. (2009) ‘Prediction of building energy consumption by using artificial neural networks’, *Advances in Engineering Software*. Elsevier Ltd, 40(5), pp. 356–362. doi: 10.1016/j.advengsoft.2008.05.003.

Erdélyi, R. *et al.* (2014) ‘Three-dimensional SOlar RAdiation Model (SORAM) and its application to 3-D urban planning’, *Solar Energy*, 101, pp. 63–73. doi: 10.1016/j.solener.2013.12.023.

Evins, R. (2013) ‘A review of computational optimisation methods applied to sustainable building design’, *Renewable and Sustainable Energy Reviews*. Elsevier, 22, pp. 230–245. doi: 10.1016/j.rser.2013.02.004.

Fernando, H. J. S. *et al.* (2001) ‘Urban Fluid Mechanics: Air Circulation and Contaminant Dispersion in Cities’, *Environmental Fluid Mechanics*, 1(1), pp. 107–164. doi: 10.1023/A:1011504001479.

Fortuniak, K. (2005) ‘Application of a slab surface energy balance model to determine surface parameters for urban areas’, *Lund eRep. Phys. Geog.*, 5(September 2016), pp. 90–91. Available at: http://www.nateko.lu.se/Elibrary/LeRPG/LeRPG5Article.pdf.

Fu, P. and Rich, P. M. (1999) ‘Design and Implementation of the Solar Analyst: an ArcView Extension for Modeling Solar Radiation at Landscape Scales’, *19th Annual ESRI User Conference*, (February), pp. 1–24.

Fuller, R. *et al.* (2022) ‘Pollution and health: a progress update’, *The Lancet Planetary Health*, 6(6), pp. e535–e547. doi: 10.1016/S2542-5196(22)00090-0.

Gentine, P. *et al.* (2016) ‘Evaporation estimates using weather station data and boundary layer theory’, *Geophysical Research Letters*, 43(22), pp. 11,661-11,670. doi: 10.1002/2016GL070819.

Von Glasow, R. *et al.* (2013) ‘Megacities and large urban agglomerations in the coastal zone: Interactions between atmosphere, land, and marine ecosystems’, *Ambio*, 42(1), pp. 13–28. doi: 10.1007/s13280-012-0343-9.

Grenfell, T. C. *et al.* (1994) ‘Reflection of solar radiation by the Antarctic snow surface at ultraviolet , visible , and near-infrared wavelengths results were obtained at Vostok Station The albedo has a uniformly high value across the UV and visible spectrum , nearly independent of s’, *Journal of Geophysical Research,* 99(D9), pp. 18 669-18 684.

Grimmond, C. S. B. (1992) ‘The suburban energy balance: Methodological considerations and results for a mid-latitude west coast city under winter and spring conditions’, *International Journal of Climatology*, 12(5), pp. 481–497. doi: 10.1002/joc.3370120506.

Grimmond, C. S. B. and Oke, T. R. (2002) ‘Turbulent heat fluxes in urban areas: Observations and a local-scale urban meteorological parameterization scheme (LUMPS)’, *Journal of Applied Meteorology*, 41(7), pp. 792–810. doi: 10.1175/1520-0450(2002)041<0792:THFIUA>2.0.CO;2.

Guan, Q. and Clarke, K. C. (2010) ‘A general-purpose parallel raster processing programming library test application using a geographic cellular automata model’, *International Journal of Geographical Information Science*, 24(5), pp. 695–722. doi: 10.1080/13658810902984228.

Gunawardena, K. R., Wells, M. J. and Kershaw, T. (2017) ‘Utilising green and bluespace to mitigate urban heat island intensity’, *Science of the Total Environment*. The Author(s), 584–585, pp. 1040–1055. doi: 10.1016/j.scitotenv.2017.01.158.

Haghighat, F. and Mirzaei, P. A. (2011) ‘Impact of non-uniform urban surface temperature on pollution dispersion in urban areas’, *Building Simulation*, 4(3), pp. 227–244. doi: 10.1007/s12273-011-0035-6.

Hamdi, R. and Masson, V. (2008) ‘Inclusion of a drag approach in the Town Energy Balance (TEB) scheme: Offline 1D evaluation in a street canyon’, *Journal of Applied Meteorology and Climatology*, 47(10), pp. 2627–2644. doi: 10.1175/2008JAMC1865.1.

Hamdi, R. and Schayes, G. (2007) ‘Validation of Martilli’s urban boundary layer scheme with measurements from two mid-latitude European cities’, *Atmospheric Chemistry and Physics*, 7(17), pp. 4513–4526. doi: 10.5194/acp-7-4513-2007.

Hamilton, I. G. *et al.* (2009) 'The significance of the anthropogenic heat emissions of London's buildings: A comparison against captured shortwave solar radiation', *Building and Environment*, 44(4), pp. 807–817. doi: 10.1016/j.buildenv.2008.05.024.

Hao, L., Zhang, Y. and Cao, Z. (2016) 'Building extraction from stereo aerial images based on multi-layer line grouping with height constraint', in *2016 IEEE International Geoscience and Remote Sensing Symposium (IGARSS)*. IEEE, pp. 445–448. doi: 10.1109/IGARSS.2016.7729110.

Harman, I. N., Barlow, J. F. and Belcher, S. E. (2004) 'Scalar fluxes from urban street canyons. Part II: Model', *Boundary-Layer Meteorology*, 113(3), pp. 387–409. doi: 10.1023/B:BOUN.0000045526.07270.a3.

Harman, I. N. and Belcher, S. E. (2006) 'The surface energy balance and boundary layer over urban street canyons', *Quarterly Journal of the Royal Meteorological Society*, 132(621), pp. 2749–2768. doi: 10.1256/qj.05.185.

He, B. J., Ding, L. and Prasad, D. (2020) 'Outdoor thermal environment of an open space under sea breeze: A mobile experience in a coastal city of Sydney, Australia', *Urban Climate*. Elsevier, 31(October 2019), p. 100567. doi: 10.1016/j.uclim.2019.100567.

Herath, H. M. P. I. K., Halwatura, R. U. and Jayasinghe, G. Y. (2018) 'Evaluation of green infrastructure effects on tropical Sri Lankan urban context as an urban heat island adaptation strategy', *Urban Forestry and Urban Greening*. Elsevier, 29(March 2017), pp. 212–222. doi: 10.1016/j.ufug.2017.11.013.

Hertwig, D. *et al.* (2021) 'High-resolution global climate simulations: Representation of cities', *International Journal of Climatology*, 41(5), pp. 3266–3285. doi: 10.1002/joc.7018.

Hidalgo, J., Lemonsu, A. and Masson, V. (2019) 'Between progress and obstacles in urban climate interdisciplinary studies and knowledge transfer to society', *Annals of the New York Academy of Sciences*, 1436(1), pp. 5–18. doi: 10.1111/nyas.13986.

Hirano, Y. and Fujita, T. (2012) 'Evaluation of the impact of the urban heat island on residential and commercial energy consumption in Tokyo', *Energy*. Elsevier Ltd, 37(1), pp. 371–383. doi: 10.1016/j.energy.2011.11.018.

Hofierka, J. and Kaňuk, J. (2009) 'Assessment of photovoltaic potential in urban areas using open-source solar radiation tools', *Renewable Energy*, 34(10), pp. 2206–2214. doi: 10.1016/j.renene.2009.02.021.

Hofierka, J. and Súri, M. (2002) 'The solar radiation model for Open source GIS: implementation and applications', *Open source GIS - GRASS users conference*, (September), pp. 11–13. Available at: http://www.ing.unitn.it/~grass/conferences/GRASS2002/proceedings/proceedings/pdfs/Hofierka_Jaroslav.pdf.

Hraška, J. (2019) 'Approaches, Methods and Tools of Rights of Access to Sunlight around the World', *Slovak Journal of Civil Engineering*, 27(4), pp. 45–52. doi: 10.2478/sjce-2019-0031.

Huszar, P. *et al.* (2014) 'Regional climate model assessment of the urban land-surface forcing over central Europe', *Atmospheric Chemistry and Physics*, 14(22), pp. 12393–12413. doi: 10.5194/acp-14-12393-2014.

Incropera, F. P. and Dewitt, D. P. (1998) *Fundamentals of Heat and Mass Transfer*. 6th edn.

Isa, N. A. *et al.* (2020) ‘Building Volume Effects on Ambient Temperature in the Kuala Lumpur City’, *IOP Conference Series: Earth and Environmental Science*, 489(1). doi: 10.1088/1755-1315/489/1/012011.

Jeevalakshmi, D., Reddy, S. N. and Manikiam, B. (2016) ‘Land cover classification based on NDVI using LANDSAT8 time series: A case study Tirupati region’, *International Conference on Communication and Signal Processing, ICCSP 2016*. IEEE, 560056, pp. 1332–1335. doi: 10.1109/ICCSP.2016.7754369.

Jones, P. D. and Lister, D. H. (2009) ‘The urban heat island in Central London and urban-related warming trends in Central London since 1900’, *Weather*. John Wiley & Sons, Ltd, 64(12), pp. 323–327. doi: 10.1002/wea.432.

Kakon, A. and Nobuo, M. (2009) ‘The Sky View Factor Effect on the Microclimate of a City Environment: A Case Study of Dhaka City’, *7th International Conference on Urban Climate*, (April 2008), pp. 7–10. Available at: http://www.ide.titech.ac.jp/~icuc7/extended_abstracts/pdf/384760-1-090513144446-003.pdf.

Kamari, A., Kotula, B. M. and Schultz, C. P. L. (2022) ‘A BIM-based LCA tool for sustainable building design during the early design stage’, *Smart and Sustainable Built Environment*. doi: 10.1108/SASBE-09-2021-0157.

Kambezidis, H. D. *et al.* (2017) ‘Meteorological Radiation Model (MRM v6.1): Improvements in diffuse radiation estimates and a new approach for implementation of cloud products’, *Renewable and Sustainable Energy Reviews*. Elsevier Ltd, 74(February), pp. 616–637. doi: 10.1016/j.rser.2017.02.058.

Khodakarami, J. and Ghobadi, P. (2016) ‘Urban pollution and solar radiation impacts’, *Renewable and Sustainable Energy Reviews*. Elsevier, 57, pp. 965–976. doi: 10.1016/j.rser.2015.12.166.

Kikegawa, Y. *et al.* (2003) ‘Development of a numerical simulation system toward comprehensive assessments of urban warming countermeasures including their impacts upon the urban buildings’ energy-demands’, *Applied Energy*, 76(4), pp. 449–466. doi: 10.1016/S0306-2619(03)00009-6.

Kilpatrick, R. A. R. and Banfill, P. F. G. (2011) ‘Energy Consumption In Non-Domestic Buildings: A Review of Schools’, *Proceedings of the World Renewable Energy Congress – Sweden, 8–13 May, 2011, Linköping, Sweden*, 57, pp. 1008–1015. doi: 10.3384/ecp110571008.

Kondo, H. *et al.* (2005) ‘Development of a multi-layer urban canopy model for the analysis of energy consumption in a big city: Structure of the urban canopy model and its basic performance’, *Boundary-Layer Meteorology*, 116(3), pp. 395–421. doi: 10.1007/s10546-005-0905-5.

Koster, R. (2015) ‘“Efficiency space”: A framework for evaluating joint evaporation and runoff behavior’, *Bulletin of the American Meteorological Society*, 96(3), pp. 393–396. doi: 10.1175/BAMS-D-14-00056.1.

Krayenhoff, S. E. and Voogt, J. A. (2007) ‘A microscale three-dimensional urban energy balance model for studying surface temperatures’, *Boundary-Layer Meteorology*, 123(3), pp. 433–461. doi: 10.1007/s10546-006-9153-6.

Kusaka, H. *et al.* (2001) ‘A Simple Single-Layer Urban Canopy Model For Atmospheric

Models: Comparison With Multi-Layer And Slab Models’, *Boundary-Layer Meteorology*, 101(3), pp. 329–358. doi: 10.1023/A:1019207923078.

Kusaka, H. and Kimura, F. (2004) ‘Coupling a single-layer urban canopy model with a simple atmospheric model: Impact on urban heat island simulation for an idealized case’, *Journal of the Meteorological Society of Japan*, 82(1), pp. 67–80. doi: 10.2151/jmsj.82.67.

Lai, S. *et al.* (2021) ‘Characteristics of daytime land surface temperature in wind corridor: A case study of a hot summer and warm winter city’, *Journal of Building Engineering*. Elsevier Ltd, 44(866), p. 103370. doi: 10.1016/j.jobe.2021.103370.

Lauzet, N. *et al.* (2019) ‘How building energy models take the local climate into account in an urban context – A review’, *Renewable and Sustainable Energy Reviews*. Elsevier Ltd, 116(February), p. 109390. doi: 10.1016/j.rser.2019.109390.

Lee, K. and Levermore, G. J. (2020) ‘Estimation of surface solar irradiation using sky view factor, sunshine factor and solar irradiation models according to geometry and buildings’, *Advances in Building Energy Research*. Taylor & Francis, 14(2), pp. 189–201. doi: 10.1080/17512549.2019.1591299.

Lee, K., Yoo, H. and Levermore, G. J. (2013) ‘Quality control and estimation hourly solar irradiation on inclined surfaces in South Korea’, *Renewable Energy*. Elsevier Ltd, 57, pp. 190–199. doi: 10.1016/j.renene.2013.01.028.

Lee, S. H. and Park, S. U. (2008) ‘A vegetated urban canopy model for meteorological and environmental modelling’, *Boundary-Layer Meteorology*, 126(1), pp. 73–102. doi: 10.1007/s10546-007-9221-6.

Lemonsu, A. *et al.* (2012) ‘Inclusion of vegetation in the Town Energy Balance model for modelling urban green areas’, *Geoscientific Model Development*, 5(6), pp. 1377–1393. doi: 10.5194/gmd-5-1377-2012.

Lemonsu, A. and Masson, V. (2002) ‘Simulation of a summer urban breeze over Paris’, *Boundary-Layer Meteorology*, 104(3), pp. 463–490. doi: 10.1023/A:1016509614936.

Li, D., Malyshev, S. and Shevliakova, E. (2016) ‘Exploring historical and future urban climate in the Earth System Modeling framework: 2. Impact of urban land use over the Continental United States’, *Journal of Advances in Modeling Earth Systems*, 8(2), pp. 936–953. doi: 10.1002/2015MS000579.

Li, G. *et al.* (2018) ‘Urban heat island effect of a typical valley city in China: Responds to the global warming and rapid urbanization’, *Sustainable Cities and Society*. Elsevier, 38(October 2017), pp. 736–745. doi: 10.1016/j.scs.2018.01.033.

Li, J. juan *et al.* (2009) ‘Remote sensing evaluation of urban heat island and its spatial pattern of the Shanghai metropolitan area, China’, *Ecological Complexity*. Elsevier, 6(4), pp. 413–420. doi: 10.1016/j.ecocom.2009.02.002.

Lin, P. *et al.* (2017) ‘The Impact of Urban Design Descriptors on Outdoor Thermal Environment: A Literature Review’, *Energies*, 10(12), p. 2151. doi: 10.3390/en10122151.

Lindberg, F. *et al.* (2018) ‘Urban Multi-scale Environmental Predictor (UMEP): An integrated tool for city-based climate services’, *Environmental Modelling and Software*, 99, pp. 70–87. doi: 10.1016/j.envsoft.2017.09.020.

Liu, X. *et al.* (2017) ‘Evaluation of an urban canopy model in a tropical city: The role of tree evapotranspiration’, *Environmental Research Letters*, 12(9). doi: 10.1088/1748-9326/aa7ee7.

Lloyd, C. T. *et al.* (2019) ‘Global spatio-temporally harmonised datasets for producing high-resolution gridded population distribution datasets’, *Big Earth Data*, 3(2), pp. 108–139. doi: 10.1080/20964471.2019.1625151.

Loughner, C. P. *et al.* (2012) ‘Roles of urban tree canopy and buildings in urban heat island effects: Parameterization and preliminary results’, *Journal of Applied Meteorology and Climatology*, 51(10), pp. 1775–1793. doi: 10.1175/JAMC-D-11-0228.1.

Mahmoud Eldesoky, A. H., Colaninno, N. and Morello, E. (2019) ‘An integrated, agile approach for estimating solar radiation on building facades in complex urban environments’, *Journal of Physics: Conference Series*, 1343(1). doi: 10.1088/1742-6596/1343/1/012015.

Mardaljevic, J. and Rylatt, M. (2003) ‘Irradiation mapping of complex urban environments: An image-based approach’, *Energy and Buildings*, 35(1), pp. 27–35. doi: 10.1016/S0378-7788(02)00077-4.

Martilli, A., Clappier, A. and Rotach, Mathias W. (2002) ‘An urban surface exchange parameterisation for mesoscale models’, *Boundary-Layer Meteorology*, 104(2), pp. 261–304. doi: 10.1023/A:1016099921195.

Martilli, A., Clappier, A. and Rotach, Mathias W (2002) ‘Mesoscale Models’, *Boundary-Layer Meteorology*, 104, pp. 261–304. doi: 10.1023/A:1016099921195.

Masson, V. (2000) ‘A physically-based scheme for the urban energy budget in atmospheric models’, *Boundary-Layer Meteorology*, 94(3), pp. 357–397. doi: 10.1023/A:1002463829265.

Masson, V., Grimmond, C. S. B. and Oke, T. R. (2002) ‘Evaluation of the Town Energy Balance (TEB) scheme with direct measurements from dry districts in two cities’, *Journal of Applied Meteorology*, 41(10), pp. 1011–1026. doi: 10.1175/1520-0450(2002)041<1011:EOTTEB>2.0.CO;2.

Matzarakis, A., Rutz, F. and Mayer, H. (2007) ‘Modelling radiation fluxes in simple and complex environments - Application of the RayMan model’, *International Journal of Biometeorology*, 51(4), pp. 323–334. doi: 10.1007/s00484-006-0061-8.

Mauree, D. *et al.* (2017) ‘On the coherence in the boundary layer: Development of a Canopy Interface Model’, *Frontiers in Earth Science*, 4(January). doi: 10.3389/feart.2016.00109.

Mavrogianni, A. *et al.* (2011) ‘The comfort, energy and health implications of London’s urban heat island’, *Building Services Engineering Research and Technology*, 32(1), pp. 35–52. doi: 10.1177/0143624410394530.

Méndez Echenagucia, T. *et al.* (2015) ‘The early design stage of a building envelope: Multi-objective search through heating, cooling and lighting energy performance analysis’, *Applied Energy*. Elsevier Ltd, 154, pp. 577–591. doi: 10.1016/j.apenergy.2015.04.090.

Menut, L. *et al.* (1999) ‘Urban boundary-layer height determination from lidar measurements over the Paris area’, *Applied Optics*, 38(6), p. 945. doi: 10.1364/ao.38.000945.

Michaelides, S. *et al.* (2009) ‘Precipitation: Measurement, remote sensing, climatology and modeling’, *Atmospheric Research*. Elsevier B.V., 94(4), pp. 512–533. doi: 10.1016/j.atmosres.2009.08.017.

Miguet, F. and Groleau, D. (2002) ‘A daylight simulation tool for urban and architectural spaces-application to transmitted direct and diffuse light through glazing', *Building and Environment*, 37(8–9), pp. 833–843. doi: 10.1016/S0360-1323(02)00049-5.

Mills, G. (2008) 'Luke Howard and The Climate of London', *Weather*, 63(6), pp. 153–157. doi: 10.1002/wea.195.

Montavez, J. P., Jimenez, J. I. and Sarsa, A. (2000) 'A Monte Carlo model of the nocturnal surface temperatures in urban canyons', *Boundary-Layer Meteorology*, 96(3), pp. 433–452. doi: 10.1023/A:1002600523841.

Moreo, M. T., Laczniak, R. J. and Stannard, D. I. (2007) 'Evapotranspiration Rate Measurements of Vegetation Typical of Ground-Water Discharge Areas in the Basin and Range Carbonate-Rock Aquifer System , White Pine County , Nevada and Adjacent Areas in Nevada and Utah , September 2005 – August 2006', *U.S. Geological Survey Scientific Investigations Report 2007-5078*, (August 2006), p. 36.

Morille, B., Lauzet, N. and Musy, M. (2015) 'SOLENE-microclimate: A tool to evaluate envelopes efficiency on energy consumption at district scale', *Energy Procedia*. Elsevier B.V., 78, pp. 1165–1170. doi: 10.1016/j.egypro.2015.11.088.

Mortezazadeh, M., Jandaghian, Z. and Wang, L. L. (2021) 'Integrating CityFFD and WRF for modeling urban microclimate under heatwaves', *Sustainable Cities and Society*. Elsevier Ltd, 66(December 2020), p. 102670. doi: 10.1016/j.scs.2020.102670.

Moss, J. L. *et al.* (2019) 'Influence of evaporative cooling by urban forests on cooling demand in cities', *Urban Forestry and Urban Greening*. Elsevier, 37(July 2017), pp. 65–73. doi: 10.1016/j.ufug.2018.07.023.

Myrup, L. O., McGinn, C. E. and Flocchini, R. G. (1993) 'An analysis of microclimatic variation in a suburban environment', *Atmospheric Environment. Part B, Urban Atmosphere*, 27(2), pp. 129–156. doi: 10.1016/0957-1272(93)90001-M.

Nault, E. *et al.* (2015) 'Review and critical analysis of early-design phase evaluation metrics for the solar potential of neighborhood designs', *Building and Environment*. Elsevier Ltd, 92, pp. 679–691. doi: 10.1016/j.buildenv.2015.05.012.

Negendahl, K. (2015) 'Building performance simulation in the early design stage: An introduction to integrated dynamic models', *Automation in Construction*. Elsevier B.V., 54, pp. 39–53. doi: 10.1016/j.autcon.2015.03.002.

Ng, E. *et al.* (2011) 'Improving the wind environment in high-density cities by understanding urban morphology and surface roughness: A study in Hong Kong', *Landscape and Urban Planning*. Elsevier B.V., 101(1), pp. 59–74. doi: 10.1016/j.landurbplan.2011.01.004.

Ngarambe, J. *et al.* (2021) 'Influences of wind speed, sky conditions, land use and land cover characteristics on the magnitude of the urban heat island in Seoul: An exploratory analysis', *Sustainable Cities and Society*. Elsevier Ltd, 71(December 2020), p. 102953. doi: 10.1016/j.scs.2021.102953.

Nguyen, H. T. and Pearce, J. M. (2012) 'Incorporating shading losses in solar photovoltaic potential assessment at the municipal scale', *Solar Energy*. Elsevier Ltd, 86(5), pp. 1245–1260. doi: 10.1016/j.solener.2012.01.017.

Noro, M. and Lazzarin, R. (2015) 'Urban heat island in Padua, Italy: Simulation analysis and mitigation strategies', *Urban Climate*. Elsevier B.V., 14, pp. 187–196. doi: 10.1016/j.uclim.2015.04.004.

Oke, T. R. (1979) *Review of Urban Climatology 1973-1976*. 1st edn, *WMO Technical Note*

No. 169. 1st edn. Geneva: Organization, Secretariat of the World Meteotological.

Oke, T. R. (1981) ‘Canyon geometry and the nocturnal urban heat island: Comparison of scale model and field observations’, *Journal of Climatology*, 1(3), pp. 237–254. doi: 10.1002/joc.3370010304.

Oke, T. R. (1988) ‘The urban energy balance’, *Progress in Physical Geography*, 12(4), pp. 471–508. doi: 10.1177/030913338801200401.

Oke, T. R. *et al.* (2017a) *Urban Climates*. Cambridge: Cambridge University Press. doi: 10.1017/9781139016476.

Oke, T. R. *et al.* (2017b) *Urban Climates*. 1st edn. Cambridge: Cambridge University Press. doi: 10.1017/9781139016476.

Oke, T. R. *et al.* (2017c) *Urban Climates*. Cambridge: Cambridge University Press. doi: 10.1017/9781139016476.

Oleson, K. W. *et al.* (2008) ‘An urban parameterization for a global climate model. Part 1: Formulation and evaluation for two cities’, *Journal of Applied Meteorology and Climatology*, 47(4), pp. 1038–1060. doi: 10.1175/2007JAMC1597.1.

Otte, T. L. *et al.* (2004) ‘Implementation of an urban canopy parameterization in a mesoscale meteorological model’, *Journal of Applied Meteorology*, 43(11), pp. 1648–1665. doi: 10.1175/JAM2164.1.

Perini, K. and Magliocco, A. (2014) ‘Effects of vegetation, urban density, building height, and atmospheric conditions on local temperatures and thermal comfort’, *Urban Forestry and Urban Greening*. Elsevier GmbH., 13(3), pp. 495–506. doi: 10.1016/j.ufug.2014.03.003.

Peuquet, D. J. and Duan, N. (1995) ‘An event-based spatiotemporal data model (ESTDM) for temporal analysis of geographical data’, *International Journal of Geographical Information Systems*, 9(1), pp. 7–24. doi: 10.1080/02693799508902022.

Pombeiro, H., Pina, A. and Silva, C. (2012) ‘Analyzing residential electricity consumption patterns based on Consumer’s segmentation’, *CEUR Workshop Proceedings*, 923, pp. 29–38.

Qi, Y. *et al.* (2022) ‘A Case Study of the Relationship Between Vegetation Coverage and Urban Heat Island in a Coastal City by Applying Digital Twins’, *Frontiers in Plant Science*, 13(April), pp. 1–15. doi: 10.3389/fpls.2022.861768.

Qin, Q. *et al.* (2022) ‘Urban Functional Zone Identification By Considering the Heterogeneous Distribution of Points of Interests’, *ISPRS Annals of the Photogrammetry, Remote Sensing and Spatial Information Sciences*, V-4–2022(June), pp. 83–90. doi: 10.5194/isprs-annals-v-4-2022-83-2022.

Radhi, H., Fikry, F. and Sharples, S. (2013) ‘Impacts of urbanisation on the thermal behaviour of new built up environments: A scoping study of the urban heat island in Bahrain’, *Landscape and Urban Planning*. Elsevier B.V., 113, pp. 47–61. doi: 10.1016/j.landurbplan.2013.01.013.

Redweik, P., Catita, C. and Brito, M. (2013) ‘Solar energy potential on roofs and facades in an urban landscape’, *Solar Energy*. Elsevier Ltd, 97, pp. 332–341. doi: 10.1016/j.solener.2013.08.036.

Reichstein, M. *et al.* (2019) ‘Deep learning and process understanding for data-driven Earth system science’, *Nature*. Springer US, 566(7743), pp. 195–204. doi: 10.1038/s41586-

019-0912-1.

Ren, C. *et al.* (2018) ‘Creating breathing cities by adopting urban ventilation assessment and wind corridor plan – The implementation in Chinese cities’, *Journal of Wind Engineering and Industrial Aerodynamics*. Elsevier Ltd, 182(October), pp. 170–188. doi: 10.1016/j.jweia.2018.09.023.

RIZWAN, A. M., DENNIS, L. Y. C. and LIU, C. (2008) ‘A review on the generation, determination and mitigation of Urban Heat Island’, *Journal of Environmental Sciences*, 20(1), pp. 120–128. doi: 10.1016/S1001-0742(08)60019-4.

Robinson, D. *et al.* (2007) ‘SUNtool - A new modelling paradigm for simulating and optimising urban sustainability’, *Solar Energy*, 81(9), pp. 1196–1211. doi: 10.1016/j.solener.2007.06.002.

Rotach, M. W. (1993) ‘Turbulence close to a rough urban surface part I: Reynolds stress’, *Boundary-Layer Meteorology*, 65(1–2), pp. 1–28. doi: 10.1007/BF00708816.

Sailor, D. J. (2011) ‘A review of methods for estimating anthropogenic heat and moisture emissions in the urban environment’, *International Journal of Climatology*, 31(2), pp. 189–199. doi: 10.1002/joc.2106.

Salamanca, F. *et al.* (2010) ‘A new building energy model coupled with an urban canopy parameterization for urban climate simulations-part I. formulation, verification, and sensitivity analysis of the model’, *Theoretical and Applied Climatology*, 99(3–4), pp. 331–344. doi: 10.1007/s00704-009-0142-9.

Salata, F. *et al.* (2017) ‘Relating microclimate, human thermal comfort and health during heat waves: An analysis of heat island mitigation strategies through a case study in an urban outdoor environment’, *Sustainable Cities and Society*. Elsevier B.V., 30, pp. 79–96. doi: 10.1016/j.scs.2017.01.006.

Salleh, S. A. *et al.* (2013) ‘Factors Contributing to the Formation of an Urban Heat Island in Putrajaya, Malaysia’, *Procedia - Social and Behavioral Sciences*. Elsevier B.V., 105, pp. 840–850. doi: 10.1016/j.sbspro.2013.11.086.

Santamouris, M. (2014) ‘On the energy impact of urban heat island and global warming on buildings’, *Energy and Buildings*. Elsevier B.V., 82, pp. 100–113. doi: 10.1016/j.enbuild.2014.07.022.

Santamouris, M. (2016) ‘Cooling the buildings – past, present and future’, *Energy and Buildings*. Elsevier B.V., 128, pp. 617–638. doi: 10.1016/j.enbuild.2016.07.034.

Scarano, M. and Sobrino, J. A. (2015) ‘On the relationship between the sky view factor and the land surface temperature derived by Landsat-8 images in Bari, Italy’, *International Journal of Remote Sensing*. Taylor & Francis, 36(19–20), pp. 4820–4835. doi: 10.1080/01431161.2015.1070325.

Schneider dos Santos, R. (2020) ‘Estimating spatio-temporal air temperature in London (UK) using machine learning and earth observation satellite data’, *International Journal of Applied Earth Observation and Geoinformation*. The Author, 88(February), p. 102066. doi: 10.1016/j.jag.2020.102066.

Seaman, N. L. *et al.* (1989) ‘Numerical studies of urban planetary boundary-layer structure under realistic synoptic conditions’, *Journal of Applied Meteorology*, pp. 760–781. doi: 10.1175/1520-0450(1989)028<0760:NSOUPB>2.0.CO;2.

Shahrestani, M. *et al.* (2015) ‘A field study of urban microclimates in London’, *Renewable*

Energy. Elsevier Ltd, 73, pp. 3–9. doi: 10.1016/j.renene.2014.05.061.

Shashua-Bar, L. and Hoffman, M. E. (2002) ‘The Green CTTC model for predicting the air temperature in small urban wooded sites’, *Building and Environment*, 37(12), pp. 1279–1288. doi: 10.1016/S0360-1323(01)00120-2.

Shishegar, N. (2013) ‘Street Design and Urban Microclimate: Analyzing the Effects of Street Geometry and Orientation on Airflowand Solar Access in Urban Canyons’, *Journal of Clean Energy Technologies*, 1(1), pp. 52–56. doi: 10.7763/jocet.2013.v1.13.

Smith, C., Lindley, S. and Levermore, G. (2009) ‘Estimating spatial and temporal patterns of urban anthropogenic heat fluxes for UK cities: The case of Manchester’, *Theoretical and Applied Climatology*, 98(1–2), pp. 19–35. doi: 10.1007/s00704-008-0086-5.

Sobstyl, J. M. *et al.* (2018) ‘Role of City Texture in Urban Heat Islands at Nighttime’, *Physical Review Letters*, 120(10), pp. 1–5. doi: 10.1103/PhysRevLett.120.108701.

Song, W. *et al.* (2017) ‘Estimating fractional vegetation cover and the vegetation index of bare soil and highly dense vegetation with a physically based method’, *International Journal of Applied Earth Observation and Geoinformation*. Elsevier B.V., 58, pp. 168–176. doi: 10.1016/j.jag.2017.01.015.

Stavropulos-Laffaille, X. *et al.* (2018) ‘Improvements to the hydrological processes of the Town Energy Balance model (TEB-Veg, SURFEX v7.3) for urban modelling and impact assessment’, *Geoscientific Model Development*, 11(10), pp. 4175–4194. doi: 10.5194/gmd-11-4175-2018.

Su, M. A. *et al.* (2021) ‘Empirical evidence on the impact of urban overheating on building cooling and heating energy consumption’, *iScience*. Elsevier Inc., 24(5), p. 102495. doi: 10.1016/j.isci.2021.102495.

Sun, R. *et al.* (2013) ‘Assessing the stability of annual temperatures for different urban functional zones’, *Building and Environment*. Elsevier Ltd, 65, pp. 90–98. doi: 10.1016/j.buildenv.2013.04.001.

Swaid, H. and Hoffman, M. E. (1990) ‘Prediction of urban air temperature variations using the analytical CTTC model’, *Energy and Buildings*, 14(4), pp. 313–324. doi: 10.1016/0378-7788(90)90094-Y.

Tadono, T. *et al.* (2014) ‘Precise Global DEM Generation by ALOS PRISM’, *ISPRS Annals of the Photogrammetry, Remote Sensing and Spatial Information Sciences*, II–4(May), pp. 71–76. doi: 10.5194/isprsannals-ii-4-71-2014.

Taha, H. (1999) ‘Modifying a mesoscale meteorological model to better incorporate urban heat storage: A bulk-parameterization approach’, *Journal of Applied Meteorology*, 38(4), pp. 466–473. doi: 10.1175/1520-0450(1999)038<0466:MAMMMT>2.0.CO;2.

Takebayashi, H. and Moriyama, M. (2009) ‘Study on the urban heat island mitigation effect achieved by converting to grass-covered parking’, *Solar Energy*, 83(8), pp. 1211–1223. doi: 10.1016/j.solener.2009.01.019.

Tan, J. *et al.* (2010) ‘The urban heat island and its impact on heat waves and human health in Shanghai’, *International Journal of Biometeorology*, 54(1), pp. 75–84. doi: 10.1007/s00484-009-0256-x.

Tao, W. (2013) ‘Interdisciplinary urban GIS for smart cities: Advancements and opportunities’, *Geo-Spatial Information Science*, 16(1), pp. 25–34. doi: 10.1080/10095020.2013.774108.

Taylor, J. *et al.* (2015) 'Mapping the effects of urban heat island, housing, and age on excess heat-related mortality in London', *Urban Climate*. Elsevier B.V., 14, pp. 517–528. doi: 10.1016/j.uclim.2015.08.001.

Teller, J. and Azar, S. (2001) 'Townscope II - A computer systems to support solar access decision-making', *Solar Energy*, 70(3), pp. 187–200. doi: 10.1016/S0038-092X(00)00097-9.

Thielen, J. *et al.* (2000) 'The possible influence of urban surfaces on rainfall development: A sensitivity study in 2D in the meso-γ-scale', *Atmospheric Research*, 54(1), pp. 15–39. doi: 10.1016/S0169-8095(00)00041-7.

Tian, W. *et al.* (2007) 'Effect of building integrated photovoltaics on microclimate of urban canopy layer', *Building and Environment*, 42(5), pp. 1891–1901. doi: 10.1016/j.buildenv.2006.02.022.

Tominaga, Y. *et al.* (2015) 'Air flow around isolated gable-roof buildings with different roof pitches: Wind tunnel experiments and CFD simulations', *Building and Environment*. Elsevier Ltd, 84, pp. 204–213. doi: 10.1016/j.buildenv.2014.11.012.

Toparlar, Y. *et al.* (2017) 'A review on the CFD analysis of urban microclimate', *Renewable and Sustainable Energy Reviews*. Elsevier Ltd, 80(September 2016), pp. 1613–1640. doi: 10.1016/j.rser.2017.05.248.

Treitz, P. M., Howarth, P. J. and Peng Gong (1992) 'Application of satellite and GIS technologies for land-cover and land-use mapping at the rural-urban fringe: a case study', *Photogrammetric Engineering & Remote Sensing*, 58(4), pp. 439–448.

Trusilova, K. *et al.* (2013) 'Implementation of an urban parameterization scheme into the regional climate model COSMO-CLM', *Journal of Applied Meteorology and Climatology*, 52(10), pp. 2296–2311. doi: 10.1175/JAMC-D-12-0209.1.

Tsou, J. *et al.* (2017) 'Urban Heat Island Assessment Using the Landsat 8 Data: A Case Study in Shenzhen and Hong Kong', *Urban Science*. MDPI AG, 1(1), p. 10. doi: 10.3390/urbansci1010010.

Unger, J. (2004) 'Intra-urban relationship between surface geometry and urban heat island: Review and new approach', *Climate Research*, 27(3), pp. 253–264. doi: 10.3354/cr027253.

United Nations (2019) *World Urbanization Prospects The 2018 Revision*.

United Nations (2022) *World Population Prospects*, *World Population Prospects 2022*. UN. doi: 10.18356/cd7acf62-en.

Vahmani, P. and Ban-Weiss, G. A. (2016) 'Impact of remotely sensed albedo and vegetation fraction on simulation of urban climate in WRF-urban canopy model: A case study of the urban heat island in Los Angeles', *Journal of Geophysical Research*, 121(4), pp. 1511–1531. doi: 10.1002/2015JD023718.

Wang, D. *et al.* (2020) 'An advanced geometric model to simulate thermal anisotropy time-series for simplified urban neighborhoods (GUTA-T)', *Remote Sensing of Environment*, 237(November 2019). doi: 10.1016/j.rse.2019.111547.

Wang, Y., Berardi, U. and Akbari, H. (2016) 'Comparing the effects of urban heat island mitigation strategies for Toronto, Canada', *Energy and Buildings*. Elsevier B.V., 114, pp. 2–19. doi: 10.1016/j.enbuild.2015.06.046.

Ward, H. C. *et al.* (2016) 'Surface Urban Energy and Water Balance Scheme (SUEWS):

Development and evaluation at two UK sites', *Urban Climate*. The Authors, 18, pp. 1–32. doi: 10.1016/j.uclim.2016.05.001.

Weng, Q. (2009) 'Thermal infrared remote sensing for urban climate and environmental studies: Methods, applications, and trends', *ISPRS Journal of Photogrammetry and Remote Sensing*. Elsevier B.V., 64(4), pp. 335–344. doi: 10.1016/j.isprsjprs.2009.03.007.

Weng, W. and Zhu, X. (2021) 'INet: Convolutional Networks for Biomedical Image Segmentation', *IEEE Access*, 9, pp. 16591–16603. doi: 10.1109/ACCESS.2021.3053408.

Whitehand, J. W. R. *et al.* (2011) 'Urban morphology and conservation in China', *Cities*. Elsevier Ltd, 28(2), pp. 171–185. doi: 10.1016/j.cities.2010.12.001.

Wimmer, R. and Wack, A. (2002) 'Digital terrain models from airborne laser scanner data – a grid based approach', *International Archives of Photogrammetry and Remote Sensing*. Available at: http://citeseerx.ist.psu.edu/viewdoc/summary?doi=10.1.1.221.9114.

Wong, K. V., Paddon, A. and Jimenez, A. (2013) 'Review of World Urban Heat Islands: Many Linked to Increased Mortality', *Journal of Energy Resources Technology, Transactions of the ASME*. doi: 10.1115/1.4023176.

Xiao, R. *et al.* (2007) 'Spatial pattern of impervious surfaces and their impacts on land surface temperature in Beijing, China', *Journal of Environmental Sciences*, 19(2), pp. 250–256. doi: 10.1016/S1001-0742(07)60041-2.

Xiong, J. *et al.* (2020) 'A spatial-and-temporal-based method for rapid particle concentration estimations in an urban environment', *Journal of Cleaner Production*. Elsevier Ltd, 256, p. 120331. doi: 10.1016/j.jclepro.2020.120331.

Xu, Y. *et al.* (2017) 'Urban morphology detection and computation for urban climate research', *Landscape and Urban Planning*. Elsevier, 167(May), pp. 212–224. doi: 10.1016/j.landurbplan.2017.06.018.

Yaghoobian, N. and Kleissl, J. (2012) 'An indoor-outdoor building energy simulator to study urban modification effects on building energy use - Model description and validation', *Energy and Buildings*. Elsevier B.V., 54, pp. 407–417. doi: 10.1016/j.enbuild.2012.07.019.

Yang, F., Qian, F. and Lau, S. S. Y. (2013) 'Urban form and density as indicators for summertime outdoor ventilation potential: A case study on high-rise housing in Shanghai', *Building and Environment*. Elsevier Ltd, 70, pp. 122–137. doi: 10.1016/j.buildenv.2013.08.019.

Yang, J. *et al.* (2015) 'Enhancing Hydrologic Modelling in the Coupled Weather Research and Forecasting–Urban Modelling System', *Boundary-Layer Meteorology*, 155(1), pp. 87–109. doi: 10.1007/s10546-014-9991-6.

Yang, X., Li, Y. and Yang, L. (2012) 'Predicting and understanding temporal 3D exterior surface temperature distribution in an ideal courtyard', *Building and Environment*. Elsevier Ltd, 57, pp. 38–48. doi: 10.1016/j.buildenv.2012.03.022.

Yao, R., Luo, Q. and Li, B. (2011) 'A simplified mathematical model for urban microclimate simulation', *Building and Environment*. Elsevier Ltd, 46(1), pp. 253–265. doi: 10.1016/j.buildenv.2010.07.019.

Yogeswaran, N. (2015) 'Anthropogenic heat flux estimation over Hong Kong : a multi modelling approach’. The Hong Kong Polytechnic University.

YOSHIE, R. *et al.* (2006) ‘CFD Prediction of Wind Environment around a High-rise Building Located in an Urban Area’, *CFD Prediction of Wind Environment around a High-rise Building Located in an Urban Area*, 1(108), pp. 129–132.

Yu, Z. *et al.* (2021) ‘A new urban functional zone-based climate zoning system for urban temperature study’, *Remote Sensing*, 13(2), pp. 1–17. doi: 10.3390/rs13020251.

Yuan, C. *et al.* (2020) ‘Mitigating intensity of urban heat island by better understanding on urban morphology and anthropogenic heat dispersion’, *Building and Environment*. Elsevier Ltd, 176(April), p. 106876. doi: 10.1016/j.buildenv.2020.106876.

Yusuf, Y. A., Pradhan, B. and Idrees, M. O. (2014) ‘Spatio-temporal Assessment of Urban Heat Island Effects in Kuala Lumpur Metropolitan City Using Landsat Images’, *Journal of the Indian Society of Remote Sensing*. Springer India, 42(4), pp. 829–837. doi: 10.1007/s12524-013-0342-8.

Zhan, Q., Meng, F. and Xiao, Y. (2015) ‘Exploring the relationships between land surface temperature, ground coverage ratio and building volume density in an urbanized envronment’, *International Archives of the Photogrammetry, Remote Sensing and Spatial Information Sciences - ISPRS Archives*, 40(7W3), pp. 255–260. doi: 10.5194/isprsarchives-XL-7-W3-255-2015.

Zhang, J. *et al.* (2017) ‘A critical review of the models used to estimate solar radiation’, *Renewable and Sustainable Energy Reviews*. Elsevier, 70(November 2016), pp. 314–329. doi: 10.1016/j.rser.2016.11.124.

Zhang, Y., Gu, Z. and Yu, C. W. (2018) ‘Review on numerical simulation of airflow and pollutant dispersion in urban street canyons under natural background wind condition’, *Aerosol and Air Quality Research*, 18(3), pp. 780–789. doi: 10.4209/aaqr.2017.09.0303.

Zhao, J. *et al.* (2020) ‘Assessing the thermal contributions of urban land cover types’, *Landscape and Urban Planning*. Elsevier, 204(19), p. 103927. doi: 10.1016/j.landurbplan.2020.103927.

Zhao, Y. (2003) ‘Principles and Methods of Remote Sensing Application Analysis’. Beijing: Peking: Science Press.

Zhou, D. *et al.* (2016) ‘Spatiotemporal trends of urban heat island effect along the urban development intensity gradient in China’, *Science of the Total Environment*. Elsevier B.V., 544(219), pp. 617–626. doi: 10.1016/j.scitotenv.2015.11.168.

Zhou, W., Huang, G. and Cadenasso, M. L. (2011) ‘Does spatial configuration matter? Understanding the effects of land cover pattern on land surface temperature in urban landscapes’, *Landscape and Urban Planning*. Elsevier B.V., 102(1), pp. 54–63. doi: 10.1016/j.landurbplan.2011.03.009.

Zhu, S. *et al.* (2013) ‘Influence of sky temperature distribution on sky view factor and its applications in urban heat island’, *International Journal of Climatology*, 33(7), pp. 1837–1843. doi: 10.1002/joc.3660.